IMPERIAL

Selective Nanopore Sensing of miRNA with DNA-based Carrier

Liquan Long

Department of Chemistry

Imperial College London

A thesis submitted in partial fulfilment of the requirement for the degree of

Doctor of Philosophy

May 2025

Abstract

The advancement of biosensor technology, particularly single-molecule sensing, is driving the development of ultrasensitive detection methods. Nanopore sensing, with its high sensitivity and specificity, is particularly promising for detecting biomarkers at the single-molecule level. This thesis focuses on enhancing solid-state nanopore sensing for the detection of small biomolecules like microRNA (miRNA). Key innovations include molecular carrier design, reconfigurable DNA nanostructures, and cost-effective nanopore fabrication, addressing challenges in sensitivity and selectivity.

First, a double-stranded DNA (dsDNA)-based molecular carrier system was developed using a sandwich hybridisation strategy. A 9.1 kbp dsDNA scaffold with multiple miRNA-specific receptor sequences, labeled with streptavidin-modified probes, enhanced signal resolution during nanopore translocation. This system enabled the detection of single and multiplexed miRNAs, including clinically relevant targets such as miRNA-141-3p, miRNA-7-5p, and miRNA-382-5p, showing promise for diagnostic applications.

Second, a reconfigurable DNA origami hinge was designed as a molecular carrier for nanopore-based detection of miRNA-141-3p. Upon binding to the target, the hinge undergoes a controlled transition from a closed to an extended conformation, producing distinct ionic current signatures during translocation. This approach achieved detection at nanomolar concentrations with excellent sequence selectivity, effectively distinguishing miRNA-141-3p from similar sequences. These results highlight the suitability of DNA nanostructure-based nanopore sensing for ultrasensitive and selective biomarker detection in complex biological environments.

Both molecular carrier systems—linear dsDNA-based carriers and reconfigurable DNA hinge structures—were successfully applied in different nanopore platforms, including nanopipette-based platforms and solid-state nanopores fabricated by the controlled breakdown method. The

results demonstrate the structural versatility and adaptability of the two designs across varied experimental setups.

In conclusion, this research advances solid-state nanopore sensing by introducing DNA-based molecular carrier strategies for selective detection of miRNAs. These methods offer promising solutions for clinical diagnostics, thereby broadening the applicability of nanopore biosensing in precision medicine.

Declaration of Originality

I, the author, declare that the work presented in this thesis is original and performed by me; otherwise, it is cited and acknowledged. This work has not previously been submitted in any form to satisfy any degree requirements at this or any other university.

Copyright Declaration

The copyright of this thesis rests with the author. Unless otherwise indicated, its contents are licensed under a Creative Commons Attribution-Non Commercial 4.0 International Licence (CC BY-NC).

Under this licence, you may copy and redistribute the material in any medium or format. You may also create and distribute modified versions of the work. This is on the condition that: you credit the author and do not use it, or any derivative works, for a commercial purpose.

When reusing or sharing this work, ensure you make the licence terms clear to others by naming the licence and linking to the licence text. Where a work has been adapted, you should indicate that the work has been changed and describe those changes.

Please seek permission from the copyright holder for uses of this work that are not included in this licence or permitted under UK Copyright Law.

Acknowledgment

First and foremost, I would like to express my sincerest gratitude to my supervisors, Dr Aleksandar Ivanov, Prof. Joshua Edel and Prof. Lorenzo Di Michele, for their exceptional guidance, unwavering support, and invaluable mentorship throughout my PhD journey. Each of them brought a unique perspective to my work, and their encouragement and expertise have been instrumental in shaping both my research and my development as a scientist. Alex and Josh, you introduced me to the world of nanopore sensing four years ago, and I can still remember the first moment I began working on nanopore research when I was amazed by the magic of this tiny device. Additionally, your profound knowledge, innovative ideas, kindness, and enthusiasm have empowered me to take my own small step forward in this field. Lorenzo, I deeply appreciate your guidance and support in the DNA origami aspect of my research; you have always been kind and responsive.

I would like to acknowledge my collaborator, Dr Joshua Johnson. Joshua, our work on the reconfigurable DNA origami molecular carrier is truly amazing, and you have provided me with immense assistance in understanding DNA origami as well as in making DNA origami and nanopore sensing compatible.

A special thanks to my colleagues in the Edel Group and Ivanov Group. I would like to give a big thank you to Ren and Shenglin, who guided me at the beginning of my PhD research. Their inspiring ideas, extensive experimental experience, and kind words have had a great impact on me. I also want to thank Yaxian and Xiaoyi for their guidance during my master's studies. Charlotte, Annie, Yilin, and Oliver, I am grateful that you are always willing to help in the lab. Alfie, thank you for answering my questions about confocal microscopy; I will never forget your warm-hearted encouragement. To Aleksandra, you are an amazing demonstrator in CBD—thank you for your patience. And to Micol, Long, Caroline, Tony, Ben, Zoe, Javier, Jiayu, Xixian, and Bank, it has been wonderful to know you during my PhD journey, and I truly appreciate your company.

Acknowledgment

To my friends—Olivia and Peno, the story of our happy and lovely white city family will never end. Tandy, my soulmate, life isn't always easy in a foreign country, but it will lead us to find our own way. Peng, we have known each other for almost ten years, and there have been countless times when just a few messages from you have made my day. Meimei, Yu, Kevin, and beloved little CoCo, it was such a pleasure living with you, and I will always be happy to be your housemate again in the future.

Most importantly, to my family—Mum and Dad, thank you for your unconditional love and support. Your open-mindedness and inclusive attitude are the most precious gifts I could ever receive, just as invaluable as the gift of life and growth. To my grandparents, uncle, and everyone else, I am so grateful to have you as my family.

I would love to end this acknowledgement with my favourite quote from *Siddhartha*— "To let it be as it was and to love it and be happy to belong to it."

Amor fati.
April 2025

Table of Contents

Abstract **2**

Declaration of Originality **4**

Copyright Declaration **5**

Acknowledgment **6**

Table of Contents **8**

List of Figures **14**

List of Tables **28**

Abbreviation **29**

Chapter 1 Introduction **31**

1.1 miRNA 33

1.1.1 miRNA Functions and Applications 33

1.1.2 miRNA Quantification Methods 34

1.2 Nanopore Technology 38

1.2.1 Single-molecule Sensing 38

1.2.2 Origin of Nanopore Technology 39

1.2.3 Biological Nanopores 41

1.2.4 Solid-state Nanopores 42

1.2.4.1 Membranes 43

1.2.4.2 Nanopipettes 44

1.3 Nanopore Sensing Principles 46

1.3.1 Ionic Current 46

1.3.2 Surface Charges 48

1.3.3 Electrophoretic and Electroosmotic Flows 50

1.3.4 Conductance Modulation by Charged Molecules 52

1.4 Selective Nanopore Sensing 54

1.4.1 Receptor-functionalised Nanopores 55

1.4.2 Molecular Carriers 57

1.5 DNA Origami Technology 60

1.5.1 DNA Origami in Nanopore Sensing 63

1.6 Summary of Dissertation 66

1.7 References 67

Chapter 2 Methodology 77

2.1 Nanopore Fabrication and Characterisation 79

2.1.1 Nanopipette 79

2.1.1.1 Nanopipette Fabrication 79

2.1.1.2 Nanopipette Characterisation 81

2.1.3 CBD Nanopore 83

2.2 Nanopore Translocation Experiment 86

2.2.1 Ag/AgCl Electrode 86

2.2.2 Buffer Solution 87

2.2.3 Translocation Setup and Ionic Current Measurement 88

2.3 DNA-based Carrier Preparation 90
2.3.1 dsDNA Carrier 90
2.3.2 DNA Origami Hinge 92

2.4 Data Analysis 93
2.4.1 Binding Analysis 99
2.4.1.1 Fractional Subpeak Position Threshold 100
2.4.1.2 Peak Current Threshold 101

2.5 References 101

Chapter 3 Nanopore Detection of miRNA with dsDNA Carrier 103

3.1 Introduction 105

3.2 Methods 107
3.2.1 dsDNA Carrier Preparation 107
3.2.2 DNA Carrier–miRNA–Streptavidin Probe Complex Preparation 109

3.3 Results and Discussion 110
3.3.1 Nanopipette Characterisation 110
3.3.2 dsDNA Carrier Characterisation 111
3.3.2.1 Gel Electrophoresis 111
3.3.2.2 Nanopore Study of dsDNA Carrier 112
3.3.3 Detection of miRNA with dsDNA Carrier 113
3.3.3.1 Direct Detection of miRNA-141 114
3.3.3.2 Translocation Buffer Selection 114
3.3.3.3 Detection of miRNA-141 with dsDNA Carrier 116
3.3.3.4 Multiplexed Detection of miRNA-7 and miRNA-382 with dsDNA Carrier 118
3.3.3.5 miRNA Binding Optimisation 120

3.4 Conclusion 122

3.5 References 122

Chapter 4 Reconfigurable DNA Origami Nanostructure and Nanopore Characterisation 126

4.1 Introduction 128

4.2 Methods 130

4.2.1 DNA Origami Hinge Preparation 130

4.2.2 Bulk Fluorescence Characterisation 131

4.3 Results and Discussion 131

4.3.1 DNA Origami Hinge 131

4.3.1.1 Hinge Mechanism 131

4.3.1.2 Bulk Fluorescence Assays 133

4.3.1.3 TEM Analysis 135

4.3.2 Nanopore Characterisation of DNA Origami Hinge 136

4.3.2.1 Nanopipette Characterisation 136

4.3.2.2 Closed Hinge vs Extended Hinge 138

4.2.3.3 Voltage Dependant 140

4.2.3.4 Open Hinge 144

4.4 Conclusion 145

4.5 References 146

Chapter 5 Nanopore Detection of miRNA with Reconfigurable DNA Origami Carrier 149

5.1 Introduction 151

5.2 Methods 153

5.2.1 Kinetic Assays 153
5.2.2 Hinge-miRNA Binding Preparation 154
5.2.3 Sigmoidal Trend Fitting 154

5.3 Results and Discussion 155
5.3.1 DNA Origami Hinge Carrier 155
5.3.1.1 Hinge Mechanism and miRNA Binding 155
5.3.1.2 Kinetic Assays 157
5.3.1.3 TEM Analysis 160
5.3.2 DNA Origami Hinge Carrier for Nanopore Detection of miRNA 161
5.3.2.1 Direct Detection of miRNA-141 161
5.3.2.2 Nanopore Study of Binding Dynamic Mechanism 162
5.3.2.3 Nanopore Study of Binding Mechanism 167
5.3.2.4 Detection in Human Serum 168
5.3.2.5 Dual Detection of miRNA-141 and miRNA-375 171

5.4 Conclusion 173

5.5 References 174

Chapter 6 CBD Nanopore and Detection 177

6.1 Introduction 179

6.2 Methods 181
6.2.1 CBD Pore Formation 181
6.2.2 Pore Expansion 182

6.3 Results and Discussion 183
6.3.1 CBD Nanopore Fabrication 183
6.3.2 Detection with CBD Nanopore 185
6.3.2.1 Detection of dsDNA 185

6.3.2.2 Detection of miRNA with dsDNA Carrier 187

6.3.2.3 Detection of DNA Origami Hinge 188

6.4 Conclusion 190

6.5 References 190

Chapter 7 Conclusion and Future Work 193

7.1 Aims 195

7.2 Achievements 195

7.3 Future Works 197

7.3.1 Protein Biomarker Detection 197

7.3.2 Multiplexed Biomarker Detection 199

7.3.3 Multi-nanopore Sensing 200

7.4 Conclusion 202

7.5 References 202

Appendices 204

Appendix 1 Copyright Permission 204

Appendix 2 Ethics Statement 218

Appendix 3 Publication 219

List of Figures

Figure 1.1 Overview of potential miRNA biomarkers for human cancer..... 34

Figure 1.2 Methods of miRNA quantification by RT-qPCR. **a.** A single miRNA is first reverse transcribed using a gene-specific stem-loop primer. The resulting complementary DNA (cDNA) is then amplified by quantitative real-time PCR using a mixture of specific primers and a hydrolysis probe. During the extension process, *Taq* polymerase displaces and cleaves the probe, leading to the separation of the fluorophore from the quencher. The accumulation of fluorescence signal is measured in real time and reflects the amount of amplified product. **b.** Alternatively, all miRNAs can be polyadenylated by poly(A) polymerase. The tailed miRNAs are then reverse transcribed using an oligo dT primer strategy. The resulting cDNA is subsequently amplified with specific primers. The PCR reaction is monitored in real time using a dye that fluoresces upon binding to double-stranded DNA. Figure adapted and reprinted with permission from reference 22. 35

Figure 1.3 Schematic illustration of the Coulter counting and nanopore sensing principles. **a.** Experimental setup for Coulter counting or nanopore recording. **b.** Application of a transmembrane potential drives a steady ionic current through the pore. **c.** Transient current blockades occur when analytes pass through the pore. **d.** Analyte binding to engineered recognition sites within the pore produces characteristic current fluctuations. Figure adapted and reprinted with permission from reference 52. 40

Figure 1.4 Ribbon representations of α-hemolysin (αHL). The side and top views of the two major domains of αHL reveal its structural features. The cap domain has a height of approximately 7 nm and an outer diameter of up to 10 nm. Within this domain, the vestibule measures around 2.6 nm, and the adjacent nanocavity spans approximately 4.6 nm. The stem domain extends about 5.2 nm in length and terminates in a β-barrel with a constriction diameter of ~1.4 nm. Figure adapted and reprinted with permission from reference 58. 41

Figure 1.5 Methods of fabricating small and thin nanopores. **a.** Focused electron/ion-beam milling of free-standing membranes. The pore size and shape can be monitored in real time during fabrication. **b.** Controlled dielectric breakdown can be used to fabricate pores in membrane. Figure adapted and reprinted with permission from reference 76. 44

Figure 1.6 Representative micrographs of quartz nanopipettes. **a.** Schematic illustration of a quartz nanopipette showing key structural components, including the stem, shoulder, shank, and tip. **b.** Optical micrograph of a dye-filled nanopipette, highlighting the internal channel for visualisation. **c.** SEM of a nanopipette viewed from the tip, clearly revealing the nanopore opening at the apex. Figure adapted and reprinted with permission from reference 85..... 45

Figure 1.7 Real-time ionic current recording during analyte translocation. **a.** The schematic displays the ionic current recorded over time and the interpretation of analyte translocation events. When an analyte passes through the pore, it causes a decrease in the steady-state ionic current. The current returns to its original level after the molecule exited the pore. **b.** Two key parameters are commonly used to characterize the translocation process through a nanopore: (i) Dwell time: the duration for which a molecule resides within the nanopore during translocation. (ii) Peak amplitude: the magnitude of current change, defined as the difference between the open-pore current and the current during molecular passage. In addition, capture rate: the frequency of translocation events. Figure adapted and reprinted with permission from reference 94..... 47

Figure 1.8 Schematic description of the ion distribution in the electric double layer at a charged solid/liquid interface with Stern and diffuse layers according to the Gouy-Chapman-Stern model, including the local potential distribution. Figure adapted and reprinted with permission from reference 107..... 49

Figure 1.9 Salt-dependent conductance variations during DNA bundle translocation at 600 mV, pH 8. **a.** Representative ionic current traces of 4HB (four-helix bundle) translocations recorded at varying KCl concentrations in the presence of 75 μM PEG 8000. Baseline currents were subtracted for clarity. Each trace shows a 450 μs segment of the translocation event. At low salt concentrations, increased counterion density leads to current enhancement, whereas at high salt, frictional effects dominate, resulting in current blockades. **b.** Conductance change as a function of KCl concentration for dsDNA (blue circles), 4HB (orange triangles), and 16HB (green squares). Linear regression reveals crossover concentrations of ~126 mM for 4HB (95% CI: [59, 174] mM), ~183 mM for 16HB (95% CI: [150, 201] mM), and ~310 mM for dsDNA. Each data point and associated error bar denote the mean ± standard deviation across multiple nanopores, with and without PEG. The light green diamond indicates a 16HB measurement at

pH 5. The inset highlights the conductance behaviour near the crossover regions. Figure adapted and reprinted with permission from reference 119. 53

Figure 1.10 Examples of receptor-functionalised nanopore platforms. **a. i.** Schematic of a gold-coated nanopore functionalised with a combination of matrix thiols ($SC_{15}EG_3$) and receptor thiols (NTA). A Ni^{2+} (green) loaded NTA receptor (black) specifically binds to His_6-tagged proteins (red). **ii.** Current versus time trace with rapid protein A/G/L translocations through a 28 nm pore modified with $SC_{15}EG_3$ matrix thiols (no NTA). **iii.** Current versus time trace of a 26 nm pore functionalised with 2 mol% bisNTA after the addition of 180 nM His_6-tagged protein A/G/L shows discrete, long-lasting binding events. **b. i.** Solid-state nanopore functionalised with hairpin-loop (HPL) DNA molecules. Current–time representative data for **ii.** 1 base mismatched (1MM) DNA and **iii.** perfect complementary (PC) DNA translocation through the functionalised nanopore. A higher number of narrower and deeper pulses are observed for the PC-DNA. Figure adapted and reprinted with permission from references 102 and 125. 56

Figure 1.11 Examples of molecular carriers for selective nanopore sensing. **a.** α-Syn oligomers in CSF are captured by DNA carriers modified with aptamers, forming a complex between the carrier and the protein. These DNA-bound α-Syn oligomer complexes are then translocated through a nanopore, where they can be recognised by a distinct subpeak signal. The subpeak ratio, indicating the proportion of signals with subpeaks relative to the total signal count, is indicative of the concentration of oligomeric forms in the clinical sample. **b.** Monomeric and dimeric nanoparticles translocated though the nanopore, the ionic current signal can be used to differentiate between Au nanoparticles monomers and dimers and as a result selectively determine the concentration of target analytes. Monomeric nanoparticles (17–20 nm) modified with antibodies can be used to initiate self-assembly and dimerisation in the presence of an antigen. A similar strategy can be used for the selective detection of miRNA, two populations of nanoparticles can be modified to contain half of the complementary miRNA sequence. **c.** Multiplexed detection of viral proteins and RNAs from patients' samples. SARS-CoV-2 virus is lysed into S protein, N protein, and RNA fragments, which can be selectively determined by the nanopore when bound to their corresponding encoded DNA molecular probes. Figure adapted and reprinted with permission from references 131, 132 and 133. 59

Figure 1.12 DNA origami technology. **a.** Principle of classic DNA origami. A long single-stranded scaffold DNA is annealed with multiple short staples (blue). The staples can bring together distant regions of the scaffold via base pairing (pairing sequences are marked red, orange, green and blue, for example), resulting in a prescribed shape. **b.** DNA nanostructure-enabled applications. DNA origami, 2D and 3D DNA structures and their applications in nanofabrication, biosensing, drug delivery, and DNA computing and storage. Figure adapted and reprinted with permission from references 135 and 139. 62

Figure 1.13 Examples of DNA origami hybrid nanopores. **a.** Hybrid nanopores formed by trapping DNA origami onto a solid state nanopore. **i.** Schematic representation of the DNA origami structure with the double-stranded overhang. Double helices are presented as rods. **ii.** Top: Side view of the nanopore section of the DNA origami structure with helices shown as cylinders. **b.** DNA origami nanopores inserted into lipid bilayers. **i.** Schematic representation of a DNA nanopore composed of six interconnected duplexes represented as cylinders. **ii.–iV.** Nanopores are structurally stable in lipid bilayer membranes and support a constant transmembrane current. Single channel current trace of a DNA-nanopore in 1 M KCl, 50 mM Tris, pH 5.0 at +100 mV (**ii**), 0 mV (**iii**), and −100 mV (**iv**) relative to the side of the membrane to which the DNA solution was added. Figure adapted and reprinted with permission from references 149 and 153. 64

Figure 1.14 Examples of DNA origami molecular carriers for nanopore sensing. **a. i.** Schematic representation of the DNA nanostructure-based biosensing concept exploiting translocation through nanopipettes as the sensing mechanism. **ii.** Typical ion current signatures upon translocation of (C-reactive protein) CRP molecules, CRP–DNA aptamer complexes, unoccupied carriers and CRP-bound occupied carriers. The scale bars represent 20 pA and 1 ms, respectively. **b.** Enzymatic regulation on surface modification to influence the origami carrier translocation. **i.** Design of ribbon-4 with 10 aptamers on the surface. Addition of adenosine monophosphate (AMP) to ribbon-4 forms ribbon-7. The addition of the enzyme adenosine deaminase (ADA) converts AMP to inosine monophosphate (IMP), which dissociates from the aptamers, and the ribbon-7 is recovered back to ribbon-4. **ii.** Scatter plots of translocation events using a 20 nm nanopore at 500 mV. Figure adapted and reprinted with permission from references 156 and 157. 65

Figure 2.1 Schematic of the fabrication of nanopipettes from capillaries using laser assisted pulling method by two-line protocol. 80

Figure 2.2 I-V characterisation of a nanopipette. **a.** I-t measurement of the nanopipette under the voltage of ±400 mV in 1M KCl buffer solution. **b.** I-V curve of the nanopipette. 81

Figure 2.3 a. SEM image of the side view of a typical nanopipette fabricated by Protocol 1. (scale bar: 10 um) **b.** SEM image of the cross-section of the nanopipette. (scale bar: (i) 20 nm, (ii) 20 nm). The diameter of nanopipettes measured by SEM is 15 ± 3 nm (n = 5). Figure adapted and reprinted with permission from reference 2. 83

Figure 2.4 a. SEM image of the top view of a typical nanopipette fabricated by Protocol 2. **b.** SEM image of the side view of the nanopipette. The diameter of nanopipettes measured by SEM is 22 ± 3 nm (n = 5). Figure adapted and reprinted with permission from reference 3. 83

Figure 2.5 Schematic representation of the SiN_x chip structure. **a.** Lateral view of the multilayered chip. **b.** Vertical view of the chip, showing a thinner window exposed at the centre of the chip. 84

Figure 2.6 The setup of Ag/AgCl electrode preparation. 87

Figure 2.7 Schematic illustration of the nanopore translocation setup and ionic current measurement. **a.** Nanopipette translocation setup. **b.** Devices used in ionic current measurement. **c.** CBD nanopore translocation setup. 89

Figure 2.8 Schematic illustration of the 9.1 kbp dsDNA carrier. **a.** Nicking step to create single-stranded regions, the 0.5 site by Nb.BtsI and the 0.2 site by Nt.BsmAI. **b.** Hybridisation step of the receptor sequences with the single-stranded regions. **c.** T4 ligase step. **d.** Digestion step to excise the 9.1 kbp carrier from the lambda DNA. 90

Figure 2.9 The caDNAno scaffold routing of the DNA origami hinge. 93

Figure 2.10 Data loading and refiltering in 'The Nanopore App'. 94

Figure 2.11 Baseline tracking and threshold defining in 'The Nanopore App'. 95

Figure 2.12 Peak finding in 'The Nanopore App'. 96

Figure 2.13 Peak statistics in 'The Nanopore App'. 97

Figure 2.14 Subpeak Analysis in 'The Nanopore App'. 99

Figure 3.1 Design and nanopore sensing of miRNAs using a 9.1 kbp dsDNA carrier. **a.** The 9.1 kbp dsDNA carrier (0-1) enables the formation of a DNA carrier–miRNA–streptavidin probe

sandwich structure. The 0.2 and 0.5 sites can be used to detect different miRNAs. **b.** Schematic of the nanopore sensing platform. **c.** Representative nanopore translocation event of the miRNA-bound dsDNA carrier. 107

Figure 3.2 Enzymes used for 9.1 kbp dsDNA carrier preparation. 108

Figure 3.3 Sequences used for detection of miRNAs. **a.** Schematic representations of 0.5 site 9.1 kbp dsDNA carrier used for detection of miRNA-141-3p. **b.** Schematic representation of 0.2 and 0.5 sites 9.1 kbp dsDNA carrier used for multiplexed detection of miRNA-7-5p and miRNA-382-5p..... 109

Figure 3.4 I-V characterisation of the nanopipettes fabricated using Protocol 1. The measurements were performed in 2 M LiCl, 5 mM $MgCl_2$, 10 mM Tris, 1 mM EDTA, pH = 8. The conductance of the quartz nanopore was 18.7 ± 3.1 nS (n = 8), calculated from the ohmic region (± 100 mV). The error band represents one standard deviation. 111

Figure 3.5 Gel electrophoresis of the 9.1 kbp dsDNA carrier after all enzyme and hybridisation reactions (lane 1: reaction product; lane 2: 1 kbp extended DNA ladder). 112

Figure 3.6 Nanopore translocation study of 9.1 kbp dsDNA carrier. **a.** Current-time trace and typical events. Experiments were performed in 2 M LiCl, 5 mM $MgCl_2$, 10 mM Tris, 1 mM EDTA, pH = 8, and at a voltage bias of 300 mV. **b.** Dwell time and peak current statistics.. 113

Figure 3.7 Nanopore sensing of miRNA-141-3p (500 pM). Experiments were performed in 2 M LiCl, 5 mM $MgCl_2$, 10 mM Tris, 1 mM EDTA, pH = 8, and at a voltage bias of 300 mV.. 114

Figure 3.8 Experiments showing the nanopore detection of miRNA-141-3p using the dsDNA carrier in 2 M and 1.5 M LiCl buffer solutions. **a.** Example translocation events for unbound dsDNA carrier and miRNA-141-3p bound dsDNA carrier. **b.** Box plot showing the capture rate for nanopore detection in 2 M and 1.5 M LiCl. The black central line represents the median, the bottom and top edges mark the one standard error, and the whiskers represent 1.5× interquartile range (IQR). The measurements were performed with six independent nanopores. 116

Figure 3.9 Nanopore detection of miRNA-141-3p using dsDNA carrier–miRNA–streptavidin complex strategy. **a.** example events for: (i) receptor sequence modified 9.1 kbp dsDNA carrier, (ii) partially folded dsDNA carrier, (iii) dsDNA carrier–miRNA–streptavidin complex, and (iv) partially folded dsDNA carrier–miRNA–streptavidin complex. **b.** The scatter plot of peak

current and dwell time for the translocation events of the dsDNA carrier (500 pM), reporter sequence (10 nM), and streptavidin (50 nM) in the presence of miRNA-141-3p (50 nM). Events with a bound complex subpeak are highlighted in green. **c.** Statistics of normalised subpeak position. 117

Figure 3.10 Nanopore multiplexed detection of miRNA-7-5p and miRNA-382-5p using dsDNA carrier–miRNA–streptavidin complex strategy. **a.** example events for: (i) streptavidin-miRNA-7-5p bound 9.1 kbp dsDNA carrier, (ii) streptavidin-miRNA-382-5p bound 9.1 kbp dsDNA carrier, (iii) streptavidin-miRNA-7-5p and streptavidin-miRNA-382-5p bound 9.1 kbp dsDNA carrier. **b.** Statistics of normalised subpeak position for bound streptavidin-miRNA-382-5p and bound streptavidin-miRNA-7-5p subpeaks. 120

Figure 3.11 Enhancement of miRNA binding to the 9.1 kbp dsDNA carrier using T4 RNA ligase. **a.** Two-step T4 RNA ligase incubation approach for nanopore detection of miRNA with dsDNA carrier. The receptor sequence and reporter sequence can be ligated by T4 RNA ligase. **b.** Comparison of miRNA binding ratios with versus without the T4 RNA ligase incubation approach. 121

Figure 4.1 Design and nanopore sensing of DNA origami hinge. 130

Figure 4.2 Design of the reconfigurable DNA origami hinge. **a.** Schematic illustration of the DNA hinge reconfiguration. The cross-sectional area of the closed hinge being approximately twice that of the extended hinge. **b.** TEM images of the closed and extended hinge (scale bar: 100 nm). 132

Figure 4.3 Schematic illustration of DNA origami closed hinge and extended hinge, showing the positions of the closer helper strands, latching strands, and extender strands. 133

Figure 4.4 Design of the DNA origami hinge. The hinge in a closed configuration, with the top and bottom arms linked by six closer helper strands. A pair of fluorophores (Alexa488 and Atto550) are positioned on the bottom arm, with a quencher on the top arm, which suppresses Alexa488 fluorescence in the closed state. The extender strands lock the hinge in an extended configuration to ensure irreversible reconfiguration. The quencher is now closer to the Atto550. 134

Figure 4.5 a. Kinetics of hinge reconfiguration of closed hinge using displacer strand and a mixture of displacer and extender strands compared with hinge folded in the closed, open, and extended states. **b.** Endpoint of fluorescence ratio..... 135

Figure 4.6 a. Representative TEM image of closed hinge after 4 hours incubation with 5-fold excess of closer displacer and extender strands (scale bar: 100 nm). Only structures which were clearly identifiable in the closed, open, or extended states were counted while aggregates, overlapping structures, or structures with unclear stain were not included. **b.** Fraction of hinge in closed, open, or extended states counted on TEM images after various incubation times. 136

Figure 4.7 I-V characterisation of the nanopipettes fabricated using Protocol 2. The measurements were performed in 1 M KCl, 12.5 mM $MgCl_2$, 10 mM Tris, 1 mM EDTA, pH = 8. The conductance of the quartz nanopore was 36.8 ± 3.1 nS (n = 20), calculated from the ohmic region (± 100 mV). The error band represents one standard deviation..... 137

Figure 4.8 Nanopore detection of closed and extended DNA origami hinges. **a.** Ionic current analysis of the closed hinge (300 pM): i. Representative current-time trace. ii. Example translocation events. iii. Peak current distribution. **b.** Corresponding data for the extended hinge (300 pM), measured under identical conditions. All experiments were conducted using the same nanopipette in a buffer containing 1 M KCl, 12.5 mM $MgCl_2$, 10 mM Tris, and 1 mM EDTA (pH 8) at a voltage bias of 300 mV..... 138

Figure 4.9 Nanopore detection of closed and extended DNA origami hinges. Dwell time and charge statistics for translocation of **a.** closed hinge (300 pM) and **b.** extended hinge (300 pM). **c.** Scatter plot of peak current vs dwell time for closed and extended hinges, illustrating distinct event distributions. 139

Figure 4.10 Voltage dependant current-time traces for translocation of closed hinge (300 pM) at voltage ranging from 150 mV to 350 mV in 1 M KCl, 12.5 mM $MgCl_2$, 10 mM Tris, 1 mM EDTA, pH = 8. 141

Figure 4.11 Volatge dependant **a.** dwell time, **b.** peak current and **c.** charge statistics for translocation of closed hinge (300 pM) at voltage ranging from 150 mV to 350 mV in 1 M KCl, 12.5 mM $MgCl_2$, 10 mM Tris, 1 mM EDTA, pH = 8. 142

Figure 4.12 Volatge dependant current-time traces for translocation of extended hinge (300 pM) at voltage ranging from 150 mV to 350 mV in 1 M KCl, 12.5 mM $MgCl_2$, 10 mM Tris, 1 mM EDTA, pH = 8. 143

Figure 4.13 Volatge dependant **a.** dwell time, **b.** peak current and **c.** charge statistics for translocation of extened hinge (300 pM) at voltage ranging from 150 mV to 350 mV in 1 M KCl, 12.5 mM $MgCl_2$, 10 mM Tris, 1 mM EDTA, pH = 8. 143

Figure 4.14 Voltage-dependent peak current characteristics for both hinge states. Shaded error bands represent one standard deviation from three independent experiments. 144

Figure 4.15 Voltage-dependant **a.** dwell time and **b.** charge for closed hinge and extended hinge. The error bands represent one standard deviation of three independent repeats..... 144

Figure 4.16 a. Current-time trace, typical events and **b.** peak current statistics for translocation of open hinge (300 pM). Experiments were performed with the same nanopipette (for closed and extended hinges) in 1 M KCl, 12.5 mM $MgCl_2$, 10 mM Tris, 1 mM EDTA, pH = 8, and at a voltage bias of 300 mV. 145

Figure 5.1 Design and nanopore sensing of the reconfigurable DNA origami hinge. **a.** Schematic illustration of the DNA hinge reconfiguration. Upon binding to miRNA, the hinge transitions from a closed to an extended state, with the cross-sectional area of the closed hinge being approximately twice that of the extended hinge. **b.** TEM images of the closed and extended hinge (scale bar: 100 nm). **c.** Schematic of the nanopore sensing platform. The nanopipette is filled with 1 M KCl Tris-EDTA buffer, with DNA hinges initially placed outside. Under an applied positive voltage, electrophoretic force drives the hinges from the outer to the inner chamber of the nanopipette. **d.** Representative nanopore translocation events of closed and extended hinges, showing distinct differences in peak current. 153

Figure 5.2 Schematic of the triggered hinge reconfiguration process: i. The hinge is initially folded in a closed configuration, with the top and bottom arms linked by a target latch and five closer helper strands. A pair of fluorophores (Alexa488 and Atto550) are positioned on the bottom arm, with a quencher on the top arm, which suppresses Alexa488 fluorescence in the closed state. ii. The hinge is primed for target detection after closer helper strands are removed via toehold-mediated strand displacement. iii. The target strand displaces the top arm latching strand, allowing the hinge to relax into an open configuration. The quencher moves away from

the Alexa488. iv. The extender strands lock the hinge in an extended configuration to ensure irreversible reconfiguration. The quencher is now closer to the Atto550. This design allows for the anti-correlation signals from the two fluorophores, facilitating the readout of the hinge state. 157

Figure 5.3 a. Example raw Fluorescence data for Alexa488 and Atto550 dyes collected after adding 500nM of miRNA-375-3p_DNA to closed hinge with a miRNA-375-3p latching strand. **b.** Ratio of raw data (with -1 offset) helps eliminate sample variation and artifacts. 158

Figure 5.4 a. Fluorescence response against different miRNA-141-3p_DNA concentrations over time for closed hinge with a miRNA-141-3p latching strand. **b.** Endpoint fluorescence ratio as a function of miRNA-141-3p_DNA concentration, fitted using a Hill equation, yielding a dissociation constant (K_d) of 5.5 ± 0.3 nM. Error bars indicate one standard deviation from 3 independent experimental repeats. 159

Figure 5.5 a. Fluorescence response against different miR-375-3p_DNA concentrations over time for closed hinge with a miR-375-3p latching strand. **b.** Endpoint of fluorescence ratio against miR-375-3p_DNA concentration. The data were fitted with a Hill equation, the dissociation constant (K_d) was determined to be 45.6 ± 0.5 nM. The error bars represent one standard deviation of independent experimental repeats. 160

Figure 5.6 TEM-based quantification of hinge state distribution across different miRNA-141-3p_DNA concentrations. 160

Figure 5.7 a. Example of TEM image of hinge imaged after adding 500 nM of miR-375-3p_DNA to closed hinge with a miR-375 latching strand and allowing to incubate for 24 hours (scale bar: 100 nm). **b.** Fraction of hinge in closed, open, or extended states counted on TEM images after 24 h incubating with various miR-375-3p_DNA concentrations. 161

Figure 5.8 Nanopore sensing of miR-141-3p (200 nM). The translocation experiment was performed in 1 M KCl, 12.5 mM $MgCl_2$, 10 mM Tris, 1 mM EDTA, pH = 8, and at a volatge bias of 300 mV. 162

Figure 5.9 Study of the binding dynamics between the DNA origami hinge with miRNA-141-3p studied via nanopore sensing. **a.** Peak current distribution of initially closed hinge (1 nM) after incubation with miRNA-141-3p (1 μM) for varying durations (0–16 h). Incubated samples (N = 5) were diluted to a final hinge concentration of 200 pM and a final miRNA-141-3p

concentration of 200 nM before translocation experiments. Histograms were fitted using a Gaussian function. **b.** Schematic illustration of the threshold definition. The mean (μ) and standard deviation (σ) were derived from Gaussian fitting, with 84.1% of reconfigured hinge events included within the mean +1σ threshold. **c.** Reconfigured fraction as a function of incubation time, fitted with a logistic equation. The half-life ($t_1/_2$) and association rate constant (K_{on}) were determined to be 1.27 ± 0.05 h and 606 $M^{-1}{\cdot}s^{-1}$. Error bars represent one standard deviation from 3 independent experiments. 164

Figure 5.10 Methods of defining the binding ratio or reconfigured fraction. **a.** The reconfigured fraction is calculated as the proportion of the area covered by reconfigured events to the total area encompassed by all events. **b.** The reconfigured fraction is determined by dividing the count of reconfigured events by the total number of events. Reconfigured events are identified using a threshold: events with peak current below the mean + 1 sigma (μ + σ) value of the distribution of reconfigured events are considered as reconfigured. Binding ratios, fitted binding dynamic curve and fitted binding dynamic curve corresponding to different defining method. The error bars represent one standard deviation of independent experimental repeats. R-square represents coefficient of determination. 165

Figure 5.11 Methods of defining the binding ratio or reconfigured fraction. The reconfigured fraction is determined by dividing the count of reconfigured events by the total number of events. **a.** Reconfigured events are identified using a threshold: events with peak current below the mean + 2 sigma (μ + 2σ) value of the distribution of reconfigured events are considered as reconfigured. **b.** Reconfigured events are identified using a threshold: events with peak current below the localised minimum value between the distribution of reconfigured events and the distribution of closed hinge events are considered as reconfigured. Binding ratios, fitted binding dynamic curve and fitted binding dynamic curve corresponding to different defining method. The error bars represent one standard deviation of independent experimental repeats. R-square represents coefficient of determination. 166

Figure 5.12 Nanopore analysis of the binding between the closed hinge and miRNA-141-3p. **a.** Peak current distribution for the closed hinge (1 nM) after incubation with varying concentrations of miRNA-141-3p (0–1 μM) for 8 h. Incubated samples were diluted to a final hinge concentration of 200 pM and final miRNA-141-3p concentrations of 0, 200 pM, 2 nM,

20 nM, and 200 nM for translocation experiments. Histograms were fitted using a Gaussian function to determine the fraction of open and closed hinges. **b.** Fraction of reconfigured hinges as a function of miRNA-141-3p concentration, fitted with a Hill equation. The dissociation constant (K_d) was determined to be 11.6 ± 0.4 nM. Error bars represent one standard deviation from four independent experimental repeats (excluding 2% human serum data points). **c.** Fraction of reconfigured hinges for blank control, scrambled miRNA-141-3p, miRNA-200a-3p, and miRNA-141-3p (final concentration: 200 nM). The black central line indicates the median, the lower and upper edges mark one standard error, and whiskers represent 1.5× the interquartile range (IQR). Statistical significance was assessed using one-way analysis of variance (**P < 0.01, ***P < 0.001). Experiments were performed using 3 independent nanopores..... 167

Figure 5.13 Nanopore sensing of closed hinge (200 pM) with human serum at 300 mV. Current-time traces for a range dilution of human serum from 2% to 20% and blank control. Human serum was diluted in 1 M KCl, 12.5 mM $MgCl_2$, 10 mM Tris, 1 mM EDTA, pH = 8 according to the multiplicity and was placed in the bath outside the nanopipette. 170

Figure 5.14 Peak current statistics for closed hinge (1 nM) incubated with 1000 nM miRNA-141-3p and blank control for 8 hours. Incubated samples were diluted with 2% human serum in 1 M KCl, 12.5 mM $MgCl_2$, 10 mM Tris, 1 mM EDTA, pH = 8 at the final hinge concentration at 200 pM and the final miRNA-141-3p concentration at 200 nM for translocation experiments. 171

Figure 5.15 Hinge reconfiguration of closed hinge with dual latching strands. **a.** Closed hinge with one miRNA-141-3p latching strand and one miRNA-375-3p latching strand for miRNA dual sensing. **b.** TEM counting and fluorescence bulk measurement for miRNA dual sensing. **c.** Nanopore sensing for miRNA dual sensing. The error bars represent one standard deviation of three independent experimental repeats. Statistical significance was tested by one-way analysis of variance. (****P < 0.0001; ns, not siganificant) 172

Figure 6.1 Schematic for detection of DNA molecule using CBD solid-state nanopore. The SiN_x membrane with a single nanopore is positioned between two chambers of electrolyte solution. 180

Figure 6.2 Schematic representation of a SiN_x membrane during nanopore fabrication via CBD. 182

Figure 6.3 Schematic representation of a SiN_x membrane during expansion, with a voltage pulse applied in high salt. 182

Figure 6.4 CBD nanopore fabrication of a SiN_x membrane. **a.** Voltage-time plot of the CBD process. The voltage profile consisted of two sequential phases: An initial linear ramp from 0 V to 5 V at 1 V/s, a subsequent slower ramp from 5 V to the breakdown threshold (or 30 V maximum) at 0.025 V/s. **b.** Current-time plot of the CBD process. A termination threshold was set at 50 nA. **c.** I-V measurements before and after CBD process under the voltage of ±400 mV. **d.** Breakdown voltages of SiN_x membranes. The measurements were performed in 1 M KCl, 10 mM Tris, 1 mM EDTA, pH = 8. 183

Figure 6.5 Expansion of a CBD nanopore. **a.** Voltage-time plot of one voltage pulse cycle in the expansion process. Each processing cycle consisted of: Application of 0.5 s pulses at 1/3 of the breakdown voltage, subsequent current measurement at ±100 mV for 0.2 s following each pulse. **b.** Currents measured at ±100 mV. A termination threshold was set at 2.5 nA. **c.** I-V measurements before and after expansion process under the voltage of ±400 mV. The measurements were performed in 3.6 M LiCl, 10 mM Tris, 1 mM EDTA, pH = 8. 184

Figure 6.6 Detection of 10 kbp dsDNA using CBD-fabricated nanopores. **a.** Voltage dependant of capture rate for detection of 2 nM 10 kbps dsDNA in 1 M KCl buffer (1 M KCl, 5 mM $MgCl_2$, 10 mM Tris and 1 mM EDTA, pH 8) and 2 M LiCl buffer (2 M LiCl, 5 mM $MgCl_2$, 10 mM Tris and 1 mM EDTA, pH 8). **b.** Concentration dependant of capture rate for detection in 2 M LiCl buffer at a volatge bias of 300 mV. **c.** Current-time trace, typical events and **d.** peak current statistics for detection of 2 nM 10 kbps dsDNA in 2M LiCl buffer at a volatge bias of 300 mV. 186

Figure 6.7 CBD nanopore sensing of miRNA using a 9.1 kbp dsDNA carrier. **a.** Schematic of the CBD nanopore sensing platform. **b.** Example translocation events for dsDNA carrier–miRNA–streptavidin complex (dsDNA carrier :1 nM, reporter sequence: 20 nM, streptavidin: 100 nM, and in the presence of miRNA-141-3p: 100 nM). All experiments were conducted using a 7 nm nanopore in a buffer containing 2 M LiCl, 5 mM $MgCl_2$, 10 mM Tris, and 1 mM EDTA (pH 8) at a voltage bias of 300 mV. 188

Figure 6.8 CBD nanopore detection of closed and extended DNA origami hinges. **a.** Ionic current analysis of the closed hinge (500 pM): i. Example translocation events. ii. Peak current distribution. **b.** Corresponding data for the extended hinge (500 pM), measured under identical conditions. All experiments were conducted using a 28 nm nanopore in a buffer containing 1 M KCl, 12.5 mM $MgCl_2$, 10 mM Tris, and 1 mM EDTA (pH 8) at a voltage bias of 300 mV.189
Figure 7.1 Schematic design of DNA-based molecular carriers for nanopore detection of protein biomarker. **a. i.** Aptamer sequence integrated 9.1 kbp dsDNA carrier for PSA detection. **ii.** Nanobody integrated 9.1 kbp dsDNA carrier for PSA detection. **b.** Hinge reconfiguration of closed hinge with aptamer sequence integrated latching strand for small protein detection. 198
Figure 7.2 Schematic design of multi-scale reconfigurable DNA origami hinge molecular carriers for multiplexed nanopore detection. **a.** Hinge structures with fixed height parameters (Hinge 1: 18 nm closed state to 8 nm extended state; Hinge 2: 5 nm closed state to 2 nm extended state). **b.** Translocation events for multiplexed detection while maintaining target-responsive conformational changes. 200
Figure 7.3 Schematic design of multi-nanopore sensing. 201

List of Tables

Table 1.1 Comparison of commonly used methods for miRNA quantification..... 36

Table 2.1 Parameters for two-line protocols used for nanopipette fabrication..... 80

Table 2.2 Buffer solutions. 87

Abbreviation

Abbreviation	Full Term
AFM	Atomic force microscopy
AKI	Acute kidney injury
CBD	Colorectal cancer
cDNA	complementary DNA
ClyA	Cytolysin A
CRC	Controlled breakdown
DNA	Deoxyribonucleic acid
dPCR	Digital PCR
dsDNA	Double-stranded DNA
EOF	Electroosmotic flow
EOF	Electrophoretic flow
ELISA	Enzyme linked immunosorbent assay
FraC	Fragaceatoxin C
FRET	Fluorescence resonance energy transfer
GNPs	Gold nanoparticles
HB	Helix bundle
αHL	α-hemolysin
IgG	Immunoglobulin G
IQR	Interquartile range
I-t	Current-time
I-V	Current-voltage

IHP	Inner Helmholtz panel
miRNA	Messenger RNA
MNPs	Magnetic Nanoparticles
mRNA	microRNA
MspA	Mycobacterium smegmatis porin A
OHP	Outer Helmholtz panel
PCa	Prostate cancer
PCR	Polymerase chain reaction
PEG	Polyethylene glycol
PSA	Prostate-specific antigen
QCM	Quartz crystal microbalance
QDs	Quantum dots
qPCR	Quantitative PCR
RNA	Ribonucleic acid
rRNA	Ribosomal RNA
RT-qPCR	Real time-quantitative PCR
SEM	Scanning electron microscopy
SiN_x	Silicon nitride
SiO_2	Silicon dioxide
Small RNA-seq	Small RNA sequencing
SNR	Signal-to-noise ratio
SPR	Surface plasmon resonance
TEM	Transmission electron microscopy
TIRFM	Total internal reflection fluorescence microscopy

Chapter 1 Introduction

Synopsis

This chapter provides an overview of miRNA functions, applications, and quantification methods, followed by an introduction to nanopore technology, including biological and solid-state nanopores. The principles of nanopore sensing, such as ionic current, surface charge effects, electrophoretic and electroosmotic flows, and conductance modulation, are discussed. Strategies for selective nanopore sensing, including receptor-functionalisation nanopores and molecular carriers, are outlined. Finally, the chapter introduces DNA origami technology and its applications in nanopore sensing, concluding with a summary of the dissertation objectives.

Chapter 1 Introduction 31

1.1 miRNA 33

1.1.1 miRNA Functions and Applications 33

1.1.2 miRNA Quantification Methods 34

1.2 Nanopore Technology 38

1.2.1 Single-molecule Sensing 38

1.2.2 Origin of Nanopore Technology 39

1.2.3 Biological Nanopores 41

1.2.4 Solid-state Nanopores 42

1.3 Nanopore Sensing Principles 46

1.3.1 Ionic Current 46

1.3.2 Surface Charges 48

1.3.3 Electrophoretic and Electroosmotic Flows 50

1.3.4 Conductance Modulation by Charged Molecules 52

1.4 Selective Nanopore Sensing 54

1.4.1 Receptor-functionalised Nanopores 55

1.4.2 Molecular Carriers 57

1.5 DNA Origami Technology 60

1.5.1 DNA Origami in Nanopore Sensing 63

1.6 Summary of Dissertation 66

1.7 References 67

1.1 miRNA

1.1.1 miRNA Functions and Applications

MicroRNAs (miRNAs) are small non-coding RNAs that play a vital role in post-transcriptional gene regulation [1, 2]. By binding to complementary sequences on target messenger RNAs (mRNAs), miRNAs can contribute to mRNA degradation or suppress translation, ultimately influencing protein synthesis [3, 4]. Their involvement spans a wide range of biological functions, including cell proliferation, differentiation, apoptosis, inflammatory responses, and embryonic development [5]. Importantly, miRNAs have been closely linked to various diseases, such as cancer, neurodegenerative disorders, and metabolic conditions like diabetes [6-8]. These associations suggest that miRNAs hold potential as both diagnostic biomarkers and therapeutic targets. Moreover, the high degree of evolutionary conservation seen in many miRNAs across species highlights their fundamental roles in biological systems [9].

Given their remarkable stability in biological fluids such as blood, urine, and tissue extracts, miRNAs have gained significant attention as non-invasive biomarkers across a range of diseases, including cancer, cardiovascular conditions, and neurological disorders [10-12]. Among these, their application in oncology has been particularly prominent. Abnormal miRNA expression profiles are commonly observed in various cancer types, enabling early detection, subtype classification, and prognosis evaluation. This diagnostic potential supports miRNAs as valuable tools in the development of cancer-specific biomarkers (**Figure 1.1**).

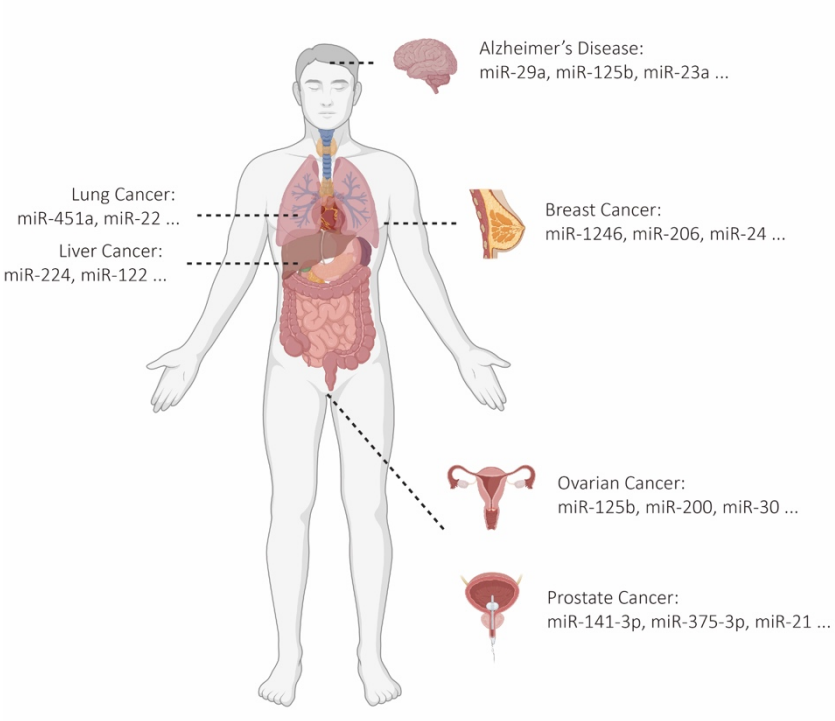


Figure 1.1 Overview of potential miRNA biomarkers for human cancer.

Beyond their diagnostic utility, miRNAs demonstrate considerable therapeutic promise. First, they can serve as direct therapeutic targets, as many diseases exhibit dysregulated expression of specific miRNAs; modulating these aberrant levels may help restore normal cellular function [13, 14]. Second, miRNA replacement therapy offers a potential solution for diseases characterised by miRNA downregulation; synthetic miRNA mimics can be introduced to replenish lost function [15]. Additionally, miRNAs show promise in combination therapies, where they may synergise with conventional treatments, such as chemotherapy or immunotherapy, potentially improving efficacy while minimising side effects [16, 17]. Despite this potential, therapeutic miRNA applications face several challenges, including delivery targeting, specificity, stability, and susceptibility to degradation in biological systems [18].

1.1.2 miRNA Quantification Methods

To enable these applications, researchers have developed diverse analytical techniques for miRNA detection. A major challenge in miRNA quantification lies in their low abundance

within complex biofluid matrices—including serum, plasma, urine, saliva, and cerebrospinal fluid—which demands exceptional sensitivity and specificity from detection methods.

Among available techniques, quantitative reverse transcription PCR (RT-qPCR) and Northern blot represent the most widely employed approaches for miRNA expression analysis. While Northern blot offers reliable detection, its utility for biofluid analysis is limited by two critical factors: its requirement for relatively high miRNA concentrations, and vulnerability to interference from coexisting biomolecules [19]. In comparison, RT-qPCR has emerged as the gold standard due to its superior sensitivity and specificity. The technique generally involves either stem-loop primer-based reverse transcription or poly(A) tailing, followed by real-time PCR amplification [20-22]. Nevertheless, RT-qPCR presents its own challenges, particularly the necessity for miRNA-specific primer design, which substantially increases assay complexity.

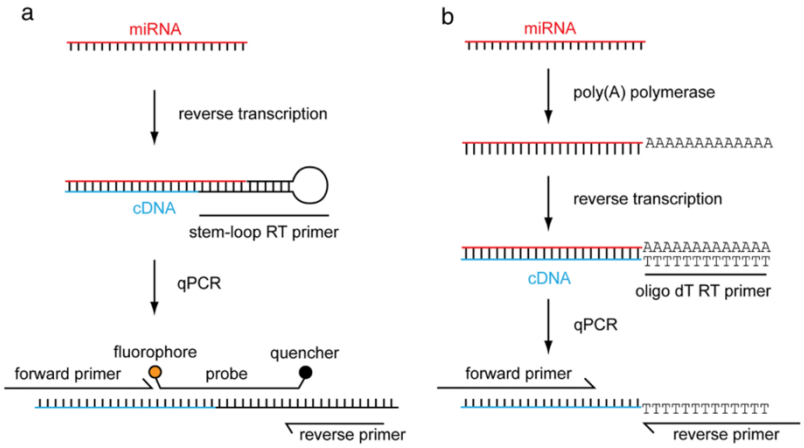


Figure 1.2 Methods of miRNA quantification by RT-qPCR. **a.** A single miRNA is first reverse transcribed using a gene-specific stem-loop primer. The resulting complementary DNA (cDNA) is then amplified by quantitative real-time PCR using a mixture of specific primers and a hydrolysis probe. During the extension process, *Taq* polymerase displaces and cleaves the probe, leading to the separation of the fluorophore from the quencher. The accumulation of fluorescence signal is measured in real time and reflects the amount of amplified product. **b.** Alternatively, all miRNAs can be polyadenylated by poly(A) polymerase. The tailed miRNAs are then reverse transcribed using an oligo dT primer strategy. The resulting cDNA is subsequently amplified with specific primers. The PCR reaction is monitored in real time using a dye that fluoresces upon binding to double-stranded DNA. Figure adapted and reprinted with permission from reference 22.

Beyond conventional methods, several alternative techniques have been developed for miRNA quantification, each with distinct strengths and limitations (**Table 1.1**). Digital PCR (dPCR) enables absolute quantification of low-abundance miRNAs without requiring standard curves or reference genes, making it particularly valuable for analysing complex biofluids [23, 24]. However, its widespread adoption is constrained by high instrumentation costs, technical complexity, and limited scalability for high-throughput applications.

Small RNA sequencing (small RNA-seq) offers comprehensive profiling capabilities, simultaneously detecting all small RNA species, including novel microRNAs (miRNAs) and isomiRs, in a single analysis [25, 26]. While this makes it the method of choice for establishing complete miRNA expression signatures, challenges remain: the low proportion of miRNAs in total RNA from biofluids, interference from abundant ribosomal RNA (rRNA) fragments and other contaminants in plasma or serum, and demanding bioinformatics requirements for data processing.

The microarray technique provides a cost-effective and high-throughput solution for screening known miRNAs across multiple samples [27, 28]. However, their limited sensitivity for detecting low-abundance miRNAs in bodily fluids necessitates subsequent quantitative PCR (qPCR) validation.

Table 1.1 Comparison of commonly used methods for miRNA quantification.

Method	Sensitivity	Specificity	Low-abundance miRNA	High-throughput	Amplification
Northern blot	Low	High	No	No	No
qRT-PCR	High	High	Yes	No	Yes

dPCR	Very high	Very high	Yes	No	Yes
Small RNA-seq	High	High	Yes (requires optimised library prep)	Yes	Yes
Microarray	Medium	Medium	Moderate	Yes	Yes
Nanotechnology-based sensors	High	High	Yes	No	No

Nanotechnology-based approaches have emerged as powerful tools for sensitive and amplification-free detection of miRNAs in biofluids. Inorganic nanoparticles, including magnetic nanoparticles (MNPs), gold nanoparticles (GNPs), and quantum dots (QDs) have been extensively employed in these applications [29-31]. MNPs demonstrate particular utility for isolating and detecting low-abundance miRNAs in complex biological fluids such as urine and blood due to their excellent separation capabilities [32]. GNPs serve as versatile components in both solution-phase and surface-based sensing platforms for miRNA recognition, leveraging their unique plasmonic properties [33]. QDs offer exceptional sensitivity and multiplexing potential through their size-tuneable fluorescence characteristics, although concerns regarding potential toxicity currently limit their clinical translation [34].

The development of carbon-based nanomaterials, including graphene, carbon nanotubes, and carbon dots, has significantly advanced electrochemical miRNA biosensing technology. These materials provide ideal platforms due to their outstanding electrical conductivity, large surface area, and excellent biocompatibility [35]. Notably, carbon dots-based sensors have achieved direct detection of miRNAs in serum samples without requiring RNA extraction procedures [36]. These carbon-based systems enable substantial signal amplification and enhanced sensitivity while maintaining compatibility with portable and cost-effective device formats.

Nanopore technology represents another innovative approach for miRNA analysis, enabling direct, label-free detection at the single-molecule level. This technique operates by monitoring characteristic changes in ionic current as miRNA molecules pass through nanoscale pores, allowing quantitative measurement without target amplification [37, 38]. Recent developments have successfully integrated DNA computing strategies and molecular barcoding techniques with nanopore systems to achieve multiplexed analysis capabilities [39]. However, despite these significant advances, most nanopore-based miRNA detection systems remain at the proof-of-concept stage and will require extensive further validation before clinical implementation.

1.2 Nanopore Technology

1.2.1 Single-molecule Sensing

The convergence of nanotechnology and molecular biology has revolutionised analytical capabilities at the single-molecule level, enabling unprecedented precision in molecular studies. While conventional ensemble measurement techniques remain valuable due to their technical maturity and widespread applicability, their population-averaged outputs inherently mask molecular heterogeneity, thereby obscuring rare events and subtle individual behaviours [40, 41]. Single-molecule approaches overcome this limitation by directly probing individual molecular activities, revealing critical insights into molecular diversity, transient intermediates, and dynamic interaction kinetics [42, 43].

Significant progress has been made in single-molecule methodologies over the past twenty years. Fluorescence-based optical techniques have been particularly instrumental, with total internal reflection fluorescence microscopy (TIRFM) and fluorescence resonance energy transfer (FRET) becoming cornerstone methods for real-time observation of molecular conformations and interactions [44, 45]. Complementary mechanical approaches, including atomic force microscopy (AFM), optical tweezers, and magnetic tweezers, have provided crucial information

about molecular mechanics and structural dynamics [46]. Despite their substantial contributions to understanding biomolecular function, these techniques share common limitations, including the need for sophisticated instrumentation, demanding operational protocols, and frequent requirements for molecular labelling or surface attachment.

Recent technological developments have shifted focus toward label-free detection platforms that combine operational simplicity with enhanced sensitivity for complex biological matrices [47]. Emerging technologies such as nanopore sensing, surface plasmon resonance (SPR), quartz crystal microbalance (QCM), and advanced electrochemical detection systems eliminate the need for fluorescent or enzymatic labels while enabling higher throughput analysis with simplified sample preparation [48-51]. Notably, nanopore technology has emerged as a powerful approach for single-molecule analysis. This technique exploits nanoscale channels to detect characteristic modulations in ionic current as individual molecules translocate through the pore. The label-free nature of this electrical detection scheme, combined with its operational simplicity, rapid response, and exceptional sensitivity, makes nanopore sensing especially attractive for direct single-molecule analysis in minimally processed samples.

1.2.2 Origin of Nanopore Technology

The conceptual foundation of nanopore technology stems from two key scientific advances: the Coulter counter and single-channel current recording [52]. The Coulter counter, developed in the 1950s, detected particles by measuring changes in ionic current as they passed through a microscale aperture [53]. This resistive-pulse sensing principle later inspired molecular-scale detection using nanopores. In the 1970s, single channel current recording further advanced nanopore sensing [54, 55]. Originally used to study ion transport through membrane proteins, this technique measured ionic currents through individual channels. These biological pores demonstrated that nanoscale channels could serve as sensitive, real-time sensors. Unlike Coulter counters, which detect complete translocation events, these devices respond to

molecular interactions through current fluctuations, thereby broadening electrical measurement capabilities.

The first experimental demonstration of nanopore translocation occurred in the early 1990s [56]. Researchers observed synthetic polymers passing through biological pores in lipid bilayers. Soon after, α-hemolysin (αHL) channels detected nucleic acids at single-molecule resolution, where current duration differences revealed molecular length variations [57]. These breakthroughs confirmed nanopores' potential for high-resolution molecular analysis. Since then, nanopore technology has rapidly expanded. It now includes both biological (protein-based) and solid-state (e.g., silicon nitride or glass) nanopores. These platforms offer advantages in sensitivity, speed, and sample versatility. Recently, nanopipette-based solid-state nanopores have gained attention for their structural stability and adaptability.

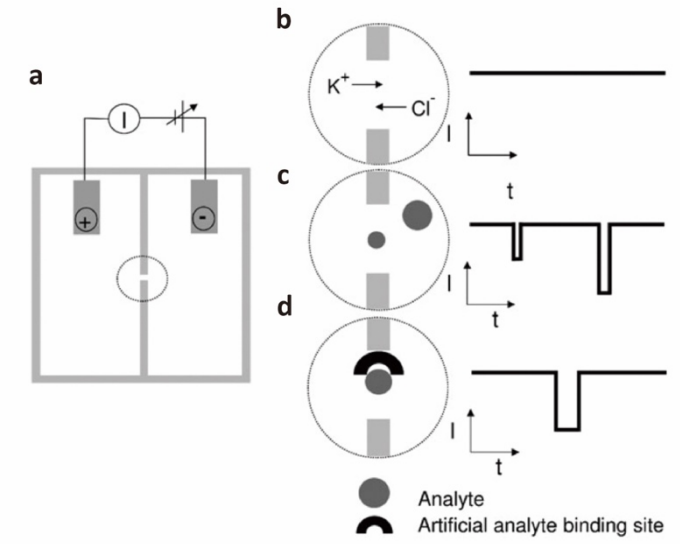


Figure 1.3 Schematic illustration of the Coulter counting and nanopore sensing principles. **a.** Experimental setup for Coulter counting or nanopore recording. **b.** Application of a transmembrane potential drives a steady ionic current through the pore. **c.** Transient current blockades occur when analytes pass through the pore. **d.** Analyte binding to engineered recognition sites within the pore produces characteristic current fluctuations. Figure adapted and reprinted with permission from reference 52.

1.2.3 Biological Nanopores

Biological nanopores are formed by natural membrane proteins that self-assemble into stable nanometre-scale channels within lipid bilayers or artificial membranes. These protein nanopores have been widely used for single-molecule detection, DNA sequencing, and small molecule analysis. Among them, the αHL nanopore is the most thoroughly studied and commonly employed model.

The αHL nanopore originates from Staphylococcus aureus bacteria. As an exotoxin, it forms a stable heptameric pore structure on cell membranes [58]. Its pore size is particularly suitable for studying the translocation of single-stranded DNA, RNA and small molecules. Structurally, the αHL nanopore has a funnel-like shape about 10 nm long, consisting of three main parts: the vestibule at the top, a narrow constriction zone (the sensing region) in the middle, and the β-barrel domain at the bottom (**Figure 1.4**). The narrowest part of the pore has a diameter of approximately 1.4 nm, which is just wide enough for single molecules to pass through.

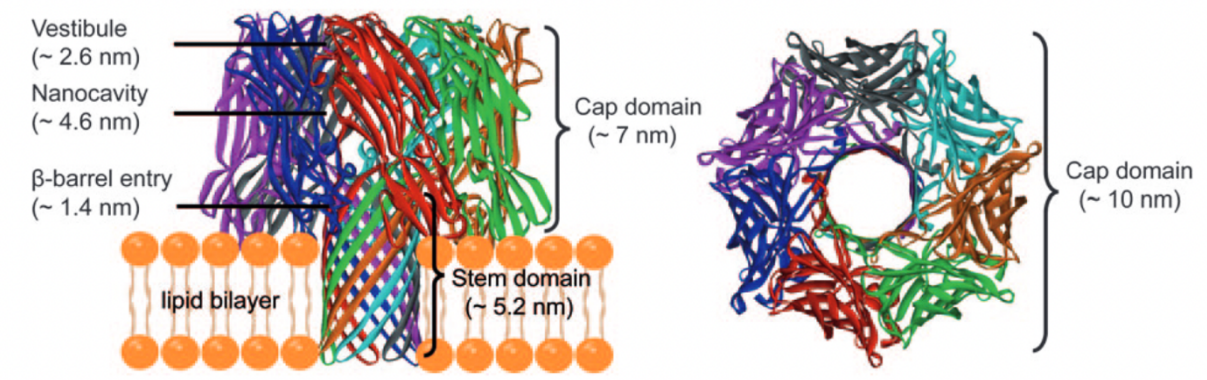


Figure 1.4 Ribbon representations of α-hemolysin (αHL). The side and top views of the two major domains of αHL reveal its structural features. The cap domain has a height of approximately 7 nm and an outer diameter of up to 10 nm. Within this domain, the vestibule measures around 2.6 nm, and the adjacent nanocavity spans approximately 4.6 nm. The stem domain extends about 5.2 nm in length and terminates in a β-barrel with a constriction diameter of ~1.4 nm. Figure adapted and reprinted with permission from reference 58.

Under an applied voltage, charged molecules translocating through the αHL pore cause transient disruptions in the ionic current. The dwell time and blockage amplitude associated with each molecule can be used for molecular identification. αHL exhibits excellent electrical stability, maintaining its structural integrity under relatively high voltages and salt concentrations, which enables long-term and repeated electrochemical measurements. Moreover, the protein can be engineered via site-directed mutagenesis to modify the chemical environment within the pore, thereby enhancing molecular recognition specificity and sensitivity. These features have led to the widespread application of αHL in miRNA detection, DNA mutation analysis, and small-molecule drug screening [59-61].

In addition to αHL, other commonly used biological nanopores include mycobacterium smegmatis porin A (MspA), which features a narrower opening and higher resolution, Aerolysin which is more suitable for peptides and small molecules, Cytolysin A (ClyA) with its larger diameter for protein analysis, and Fragaceatoxin C (FraC) [62-65]. These nanopores provide complementary properties and are often employed to extend the functional capabilities of biological nanopore systems.

Despite their advantages, biological nanopores present several limitations such as sensitivity to environmental conditions, including pH and temperature, poor membrane stability, limited control over pore size, and batch-to-batch variability [66]. These factors may affect their reliability and scalability in practical applications. To overcome these challenges, researchers have increasingly focused on solid-state nanopore systems fabricated from inorganic materials.

1.2.4 Solid-state Nanopores

Biological nanopores typically exhibit diameters ranging from 1 to 5 nanometres, which restricts their application for analysing larger biomolecules such as most proteins. This size limitation has motivated the development of solid-state nanopores to address the constraints inherent to biological nanopores. These artificial nanopores are fabricated from durable

inorganic materials, including silicon nitride (SiN_x), silicon dioxide (SiO_2), aluminium oxide (Al_2O_3), and graphene offering improved mechanical stability and structural integrity [67-70].

Compared to biological nanopores, solid-state versions provide several significant advantages. First, their pore sizes can be precisely controlled and adjusted over a wide range, from a few nanometres to several tens of nanometres, enabling the analysis of a broader size range of analytes, including larger proteins and molecular complexes. Second, they demonstrate superior mechanical strength and maintain stable performance across diverse experimental conditions, including varying pH levels, temperature changes, and different ionic strengths. Finally, solid-state nanopore platforms can be effectively integrated with both electronic and optical detection methods, substantially enhancing their analytical capabilities and application potential [71, 72]. Solid-state nanopores have been extensively employed in the detection and analysis of a wide range of biomolecules, including nucleic acids, proteins, and various small molecules [68, 73-75].

1.2.4.1 Membranes

The nanopore length significantly influences detection performance, as it directly affects both signal amplitude and temporal resolution, parameters that are inversely related to pore length [76]. Consequently, thin solid-state membranes represent the optimal substrate material for nanopore fabrication. These membranes serve dual advantages: they enable the creation of short pores that enhance detection precision while simultaneously replicating the structural features of membrane proteins that give rise to biological nanopores.

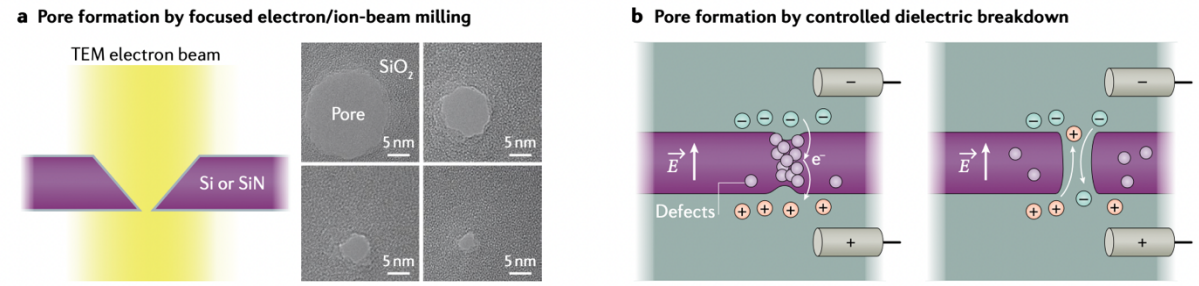


Figure 1.5 Methods of fabricating small and thin nanopores. **a.** Focused electron/ion-beam milling of free-standing membranes. The pore size and shape can be monitored in real time during fabrication. **b.** Controlled dielectric breakdown can be used to fabricate pores in membrane. Figure adapted and reprinted with permission from reference 76.

The established approach for solid-state nanopore fabrication involves focused ion/electron beam milling (**Figure 1.5a.**) [77, 78]. This technique enables precise control over pore dimensions and geometry at specific membrane locations, while allowing real-time monitoring of pore formation. Despite these advantages, the method suffers from several limitations, including high equipment costs, low production throughput, and potential alterations in nanopore geometry when removed from ultra-high vacuum conditions. An emerging alternative is controlled breakdown (CBD), which offers a simpler fabrication process (**Figure 1.5b.**) [79]. In CBD, application of an electric field across an insulating membrane leads to nanopore formation, indicated by a characteristic current spike. This method eliminates the need for sophisticated nanofabrication equipment. Additional fabrication techniques include electrochemical deposition, nanoimprinting, thermal annealing, and chemical etching [80-83]. Each method presents unique advantages and challenges for creating nanopores in solid-state membranes.

1.2.4.2 Nanopipettes

Conventional fabrication of solid-state nanopores typically yields pores with diameters in the sub-10 nm range, often below 5 nm. This process is generally time-consuming, technically challenging, and costly, particularly when attempting to create larger pores. In contrast,

nanopipettes represent an alternative form of solid-state nanopore that offers greater accessibility and cost-effectiveness (**Figure 1.6**). These are produced via laser-assisted pulling methods, enabling rapid and straightforward formation of nanopores with diameters ranging from tens to hundreds of nanometres. Nanopipettes have gained prominence as multifunctional tools for single-molecule detection, intracellular studies, and scanning probe applications [84]. Their straightforward fabrication process, minimal cellular disturbance, and seamless integration with electrochemical analysis techniques have facilitated widespread adoption across analytical chemistry and biomedical research [85].

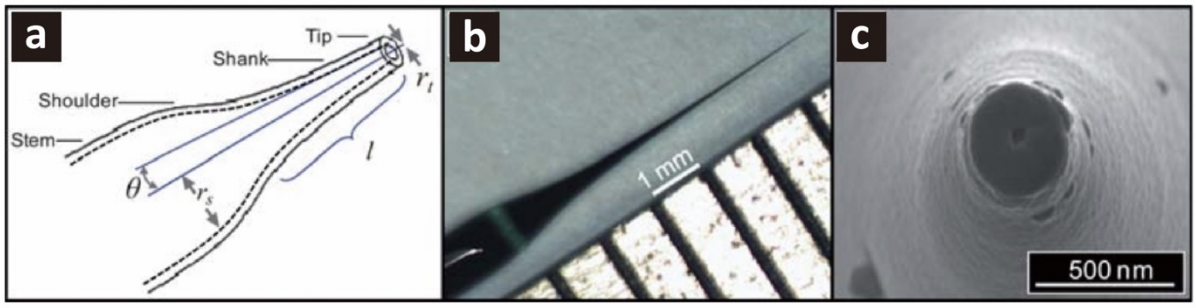


Figure 1.6 Representative micrographs of quartz nanopipettes. **a.** Schematic illustration of a quartz nanopipette showing key structural components, including the stem, shoulder, shank, and tip. **b.** Optical micrograph of a dye-filled nanopipette, highlighting the internal channel for visualisation. **c.** SEM of a nanopipette viewed from the tip, clearly revealing the nanopore opening at the apex. Figure adapted and reprinted with permission from reference 85.

One major application of nanopipettes is in electrochemical and biosensing. Their nanoscale geometry and surface charge properties enable ion current rectification, which serves as a highly sensitive detection mechanism for molecular interactions at the pipette tip [86]. This allows for label-free, real-time detection of various analytes including nucleic acids, proteins, small biomolecules, and nanoparticles [87-89]. Due to their extremely small sensing volume and high signal-to-noise ratio, nanopipettes are particularly suitable for detecting rare biomolecules or low-concentration samples, such as early-stage disease biomarkers. The selectivity of nanopipettes can be specifically modified through surface functionalisation using aptamers, enzymes, antibodies, or synthetic polymers [90-92]. Moreover, when combined with

dielectrophoretic trapping techniques, nanopipettes can preconcentrate analytes at the tip, significantly improving detection sensitivity down to femtomolar levels [93].

1.3 Nanopore Sensing Principles

The basic principle of nanopore sensing depends on the translocation of charged analytes through a nanoscale pore under an applied voltage bias, with continuous monitoring of ionic current as the primary readout. As analytes pass through the nanopore, they cause transient changes in the ionic current, producing characteristic current signatures. However, the underlying principles of this process are considerably more complex. Several key factors deserve mention: (1) the ionic current level, (2) local electrostatics, (3) forces acting on the analyte during translocation, and (4) conductance variations within the nanopore confinement.

1.3.1 Ionic Current

In a standard nanopore sensing setup, two electrolyte-filled reservoirs (typically containing KCl, NaCl, or LiCl) are separated by a nanopore/membrane. The system is connected to an electrometer through Ag/AgCl electrodes. When voltage is applied, the migration of cations and anions through the nanopore generates a steady-state ionic current, completing the electrical circuit [94]. This steady-state ionic current is referred to as the open pore current, occurring when no analytes (only cations and anions) are translocating through the pore.

The system maintains homogeneous electrolyte concentration throughout. However, edge effects—often simplified as access resistance where current converges from bulk electrolyte to the pore entrance—must be considered [95, 96]. The applied voltage predominantly drops across the nanopore because potential losses at electrode/electrolyte interfaces are negligible (using non-polarizable Ag/AgCl electrodes), and the utilised voltages are sufficiently small [97].

Under these conditions, the open pore current i_o for a cylindrical solid-state nanopore can be approximated by [37]:

$$i_o \approx (\mu_+ + \mu_-)ne\left(\frac{4l}{\pi d^2} + \frac{1}{d}\right)^{-1} V \quad 1.1$$

where μ_+ and μ_- represent the electrophoretic mobilities of cation and anion, n denotes the number density of cation or anion, d is the pore diameter, l is the pore length (or membrane thickness), e is the elementary charge, and V is the applied voltage.

For an asymmetric nanopore geometry such as conical nanopores in membranes or nanopipettes, the open pore current i_o can be approximated by [98, 99]:

$$i_o \approx (\mu_+ + \mu_-)ne\left(\frac{4l}{\pi dD} + \frac{8(d+D)}{5dD}\right)^{-1} V \quad 1.2$$

where d and D denote the minor and major diameters (tip and base openings) of the conical nanopore, and access resistance is also included in this model.

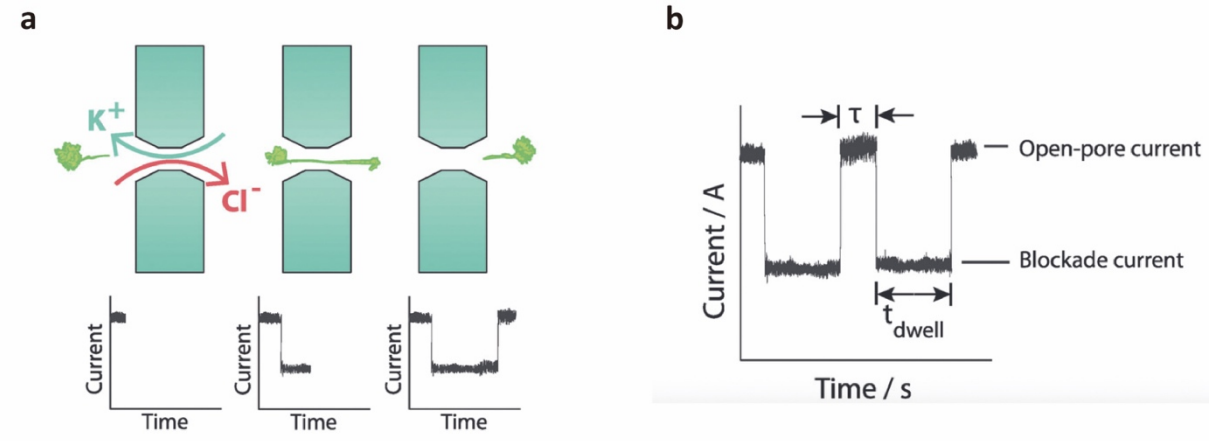


Figure 1.7 Real-time ionic current recording during analyte translocation. **a.** The schematic displays the ionic current recorded over time and the interpretation of analyte translocation events. When an analyte passes through the pore, it causes a decrease in the steady-state ionic current. The current returns to its original level after the molecule exited the pore. **b.** Two key parameters are commonly used to characterize the translocation process through a nanopore: (i) Dwell time: the duration for which a molecule resides within the nanopore during translocation. (ii) Peak amplitude: the magnitude of current change, defined as the difference between the open-

pore current and the current during molecular passage. In addition, capture rate: the frequency of translocation events. Figure adapted and reprinted with permission from reference 94.

During nanopore translocation experiments, the ionic current is recorded as a function of time, yielding current-time traces (**Figure 1.7**). The translocation of analytes through a nanopore results in a transient change in ionic current, which may manifest as either a decrease or an increase, depending on the nature of the molecule. To describe this process, two key parameters of the current signal are commonly evaluated. The first is the dwell time, which indicates the duration that the molecule remains inside the nanopore. The second is the peak current or peak amplitude, which reflects the degree of conductance alteration caused by the translocating species. The integral of the current signal over time provides an estimate of the total charge associated with each analyte during translocation [100]. In addition, the time interval between consecutive translocation events (τ) and the capture rate, usually defined as the number of events per unit time, are used to study the concentration of analytes and their transport behaviour [89, 101]. Analysis of these signal features can reveal important information related to molecular size, shape, charge, and the interaction between the analyte and the nanopore surface [102-104].

1.3.2 Surface Charges

In nanopores, the ion distribution differs from that in bulk electrolyte solutions. This phenomenon arises because the inner surface of the nanopore, when immersed in a polar electrolyte solution, acquires a surface charge. This charge results from the stabilizing interaction between the solvent and ionic species at the solid-liquid interface. For SiN_x and SiO_2 membranes immersed in KCl, NaCl or LiCl electrolyte solutions, the surface typically develops a negative charge due to the ionisation of hydroxyl or oxide groups on the material surface [97]. This charged surface creates an electrostatic environment where: Counterions (positively charged ions in this case) accumulate near the pore walls due to favourable electrostatic attraction; Co-ions (negatively charged ions) are depleted from the near-surface region. These

opposing ion distributions lead to the formation of an electrical double layer at the nanopore/electrolyte interface [105].

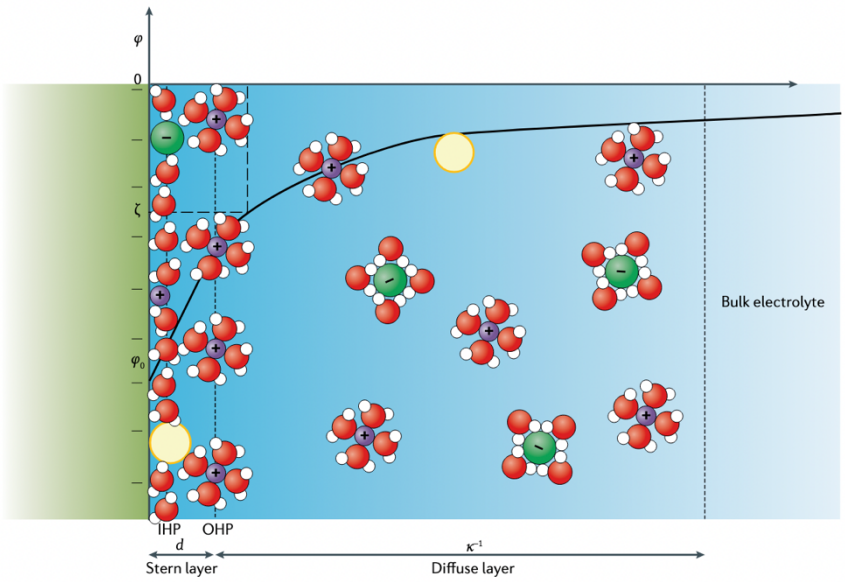


Figure 1.8 Schematic description of the ion distribution in the electric double layer at a charged solid/liquid interface with Stern and diffuse layers according to the Gouy-Chapman-Stern model, including the local potential distribution. Figure adapted and reprinted with permission from reference 107.

The Gouy-Chapman-Stern model provides a fundamental theoretical framework for characterising the formation of electrical double layers at charged interfaces [106]. This three-layer model combines the Stern layer or inner Helmholtz panel (IHP)—where ions and solvent molecules directly adsorbed onto the charged surface; The diffuse or outer Helmholtz panel (OHP)—containing solvated ions that remain mobile due to nonspecific adsorption and long-range electrostatic interactions with the charged surface, allowing their distribution to extend into the diffuse double-layer region; 3) The bulk solution—unaffected by surface charges (**Figure 1.8**) [107]. However, beyond conditions of extremely low electrolyte concentrations, the model exhibits limited quantitative accuracy. This limitation arises from the fundamental simplifications on which the model is based. Although it offers consistent qualitative predictions, its applicability becomes restricted in complex or highly concentrated conditions [108]. The spatial extent of the electrical double layer is quantitatively characterised by the

Debye length, which exhibits a strong concentration dependence, ranging from sub-nanometre scales in concentrated electrolytes to several tens of nanometres in highly dilute solutions [109, 110].

Several models account for both bulk and surface contributions when estimating the open pore current, as the influence of local electrostatic effects cannot be neglected [111]. Nanopore detection is typically performed under high-salt conditions, the negatively charged surface of the nanopore is effectively screened by mobile cations (counterions) that contribute to the overall ionic current [112, 113]. In this case, the total current through the nanopore arises from both the bulk ion concentration and the additional contribution of counterions associated with the surface charge compensation. And open pore current i_o for a cylindrical solid-state nanopore can be approximated by:

$$i_o \approx \frac{\pi d^2}{4l}\left((\mu_+ + \mu_-)ne + \mu_+ \frac{4\sigma_{\text{surf}}}{d}\right)V \qquad 1.4$$

where σ_{surf} is the surface-charge density in the nanopore. It is worth noting that the coupling of local electrostatic effects, geometric structure, and other factors can lead to the rectification effect. For instance, in narrow conical nanopores with surface charges, the activation energy for ion entry into the channel changes depending on the direction of transmission [114].

1.3.3 Electrophoretic and Electroosmotic Flows

The translocation of charged analytes through nanopores is governed by the combined action of multiple forces, with electrophoretic and electroosmotic effects constituting the dominant contributions [94]. Additionally, diffusion plays a non-negligible role, particularly for small globular molecules [115]. Electrophoretic flow (EPF) occurs when ions in solution migrate under an applied electric field. A representative example is the motion of negatively charged DNA molecules through a nanopore toward the positively biased anode during translocation

experiments. The electrophoretic velocity v_{EPF} can be quantified using the Helmholtz-Smoluchowski model [116]:

$$v_{\mathrm{EPF}} = \frac{\varepsilon}{\eta}\zeta_{\mathrm{molecule}}E \qquad 1.5$$

where ε represents the absolute permittivity of the dielectric medium, η denotes the viscosity of the electrolyte solution, E corresponds to the strength of the applied electric field, and $\zeta_{\mathrm{molecule}}$ is the zeta potential of the translocating molecule.

Electroosmotic flow (EOF) develops in nanopores with charged surfaces when an electric field is applied along the channel, causing the electrical double layer that shields the surface charge. The electrical double layer moves the fluid along with it, generating a net flow. As a result, the electroosmotic velocity v_{EOF} is defined by: [110, 115]:

$$v_{\mathrm{EOF}} = -\frac{\varepsilon}{\eta}\zeta_{\mathrm{wall}}E \qquad 1.6$$

where ζ_{wall} is the zeta potential of the nanopore inner wall.

Equation 1.5 and **Equation 1.6** are applicable under the condition that the Debye length is significantly smaller than the channel width, and that a high ionic strength electrolyte is used. By combining the equations for EPF and EOF, an effective velocity v for the molecule inside the pore is obtained [115]:

$$v = v_{\mathrm{EPF}} + v_{\mathrm{EOF}} = \frac{\varepsilon}{\eta}(\zeta_{\mathrm{molecule}} - \zeta_{\mathrm{wall}})E \qquad 1.7$$

EOF can interact with EP in three distinct ways—enhancement, opposition, or reversal of the electrophoretic motion, particularly for moderately charged target molecules. When EOF precisely counterbalances EPF, molecular translocation becomes predominantly diffusion-driven.

1.3.4 Conductance Modulation by Charged Molecules

The translocation of molecules through nanopores leads to changes in ionic current due to modulation of nanopore conductance. This phenomenon stems from two competing mechanisms: first, the physical volume of the molecule excludes ions (G_{block}), reducing conductance; second, mobile counterions that neutralize the molecular charge increase conductance (G_{charge}) [112]. To be precise, these counterions both shield the charged molecule and accompany its movement during translocation [113]. The total change in conductance (ΔG) caused by charged molecule translocation can be calculated by considering the superposition of these two opposing effects:

$$\Delta G = -G_{\text{block}} + G_{\text{charge}} \tag{1.8}$$

$$\Delta G = -(\mu_+ + \mu_-)cF\frac{\pi d_{\text{molecule}}^2}{4l_{\text{pore}}} + \frac{\lambda_q}{l_{\text{pore}}}\mu_{+(-)} \tag{1.9}$$

where d_{molecule} is the diameter of the molecule, l_{pore} is the length of the nanopore, c is the electrolyte concentration, F is the Faraday constant, and λ_q represents the effective charge per unit length of the counter ions screening the nanopore wall.

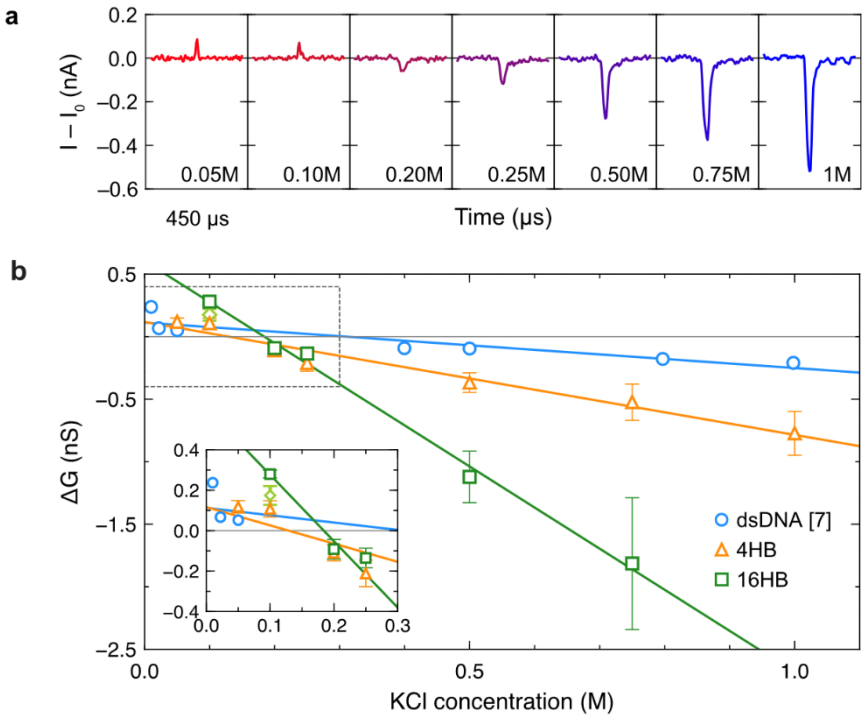


Figure 1.9 Salt-dependent conductance variations during DNA bundle translocation at 600 mV, pH 8. **a.** Representative ionic current traces of 4HB (four-helix bundle) translocations recorded at varying KCl concentrations in the presence of 75 µM PEG 8000. Baseline currents were subtracted for clarity. Each trace shows a 450 µs segment of the translocation event. At low salt concentrations, increased counterion density leads to current enhancement, whereas at high salt, frictional effects dominate, resulting in current blockades. **b.** Conductance change as a function of KCl concentration for dsDNA (blue circles), 4HB (orange triangles), and 16HB (green squares). Linear regression reveals crossover concentrations of ~126 mM for 4HB (95% CI: [59, 174] mM), ~183 mM for 16HB (95% CI: [150, 201] mM), and ~310 mM for dsDNA. Each data point and associated error bar denote the mean ± standard deviation across multiple nanopores, with and without PEG. The light green diamond indicates a 16HB measurement at pH 5. The inset highlights the conductance behaviour near the crossover regions. Figure adapted and reprinted with permission from reference 119.

The translocation of charged analytes through nanopores can result in either ionic current blockade or enhancement, depending on the interplay of molecular properties, nanopore geometry, and electrolyte conditions. The electrolyte composition and concentration significantly influence the translocation signatures. For example, double-stranded DNA (dsDNA) translocating through a nanopore shows different ionic current patterns in various

electrolyte solutions [117, 118]. Even within a single electrolyte type, such as KCl, previous studies have reported concentration-dependent conductance modulation during dsDNA translocation [99, 112]. Specifically, a current enhancement is typically observed at lower electrolyte concentrations, whereas a current reduction becomes apparent at higher concentrations. A transition point, or crossover concentration, has been consistently identified within the range of 0.3 to 0.4 M KCl. This is attributed to counterions following the molecule being more competitive than the ions excluded by the molecule at low concentration.

Molecular structure significantly affects translocation behaviour. A previous study comparing different DNA nanostructures—specifically the four-helix bundle (4HB) and sixteen-helix bundle (16HB)—show distinct current modulation patterns (**Figure 1.9**) [119]. Both structures demonstrate crossover concentrations lower than standard dsDNA (~1HB), confirming that molecular size and shape substantially influence conductance characteristics. In addition, nanopore dimensions critically influence the direction and magnitude of current modulation. A representative example involves the translocation of positively charged nanorods, where both current enhancement and blockade are observed depending on nanopore size [113]. This behaviour arises from overlapping electric double layers between the nanorod and nanopore wall, which modifies local electrostatics and consequently alters the measured current signal.

1.4 Selective Nanopore Sensing

Nanopore sensing demonstrates significant potential for early disease diagnosis due to its unique single-molecule detection capability. However, conventional nanopore systems face substantial selectivity and sensitivity challenges for practical diagnostic applications, primarily because biological fluids like serum, urine, saliva, and cerebrospinal fluid contain complex mixtures of biomolecules. The accurate identification of target analytes is complicated by several factors, including indistinguishable signals from similar molecules, a poor signal-to-noise ratio (SNR) for small molecules, and low capture rates for rare analytes. To overcome these limitations, researchers have successfully incorporated selective components into

nanopore platforms, enhancing their discrimination capabilities while maintaining single-molecule sensitivity. Existing strategies for imparting selectivity to nanopore platforms mainly fall into two categories: functionalisation of the nanopore with analyte-specific receptors, and the introduction of molecular carriers into the electrolyte solution to selectively bind and transport target molecules.

1.4.1 Receptor-functionalised Nanopores

Various strategies have been explored to functionalize nanopores for improved sensing performance, including chemical surface modifications, biomimetic designs based on lipid membranes, and hybrid nanopore systems integrating multiple material properties [120-122]. These approaches primarily focus on optimizing analyte transport while reducing nonspecific adsorption. A particularly successful strategy involves anchoring molecular receptors to the nanopore surface for selective detection [123, 124]. By immobilizing receptors with high specificity and strong binding affinity at the pore interface, the system gains the ability to selectively recognize and capture target molecules from complex mixtures.

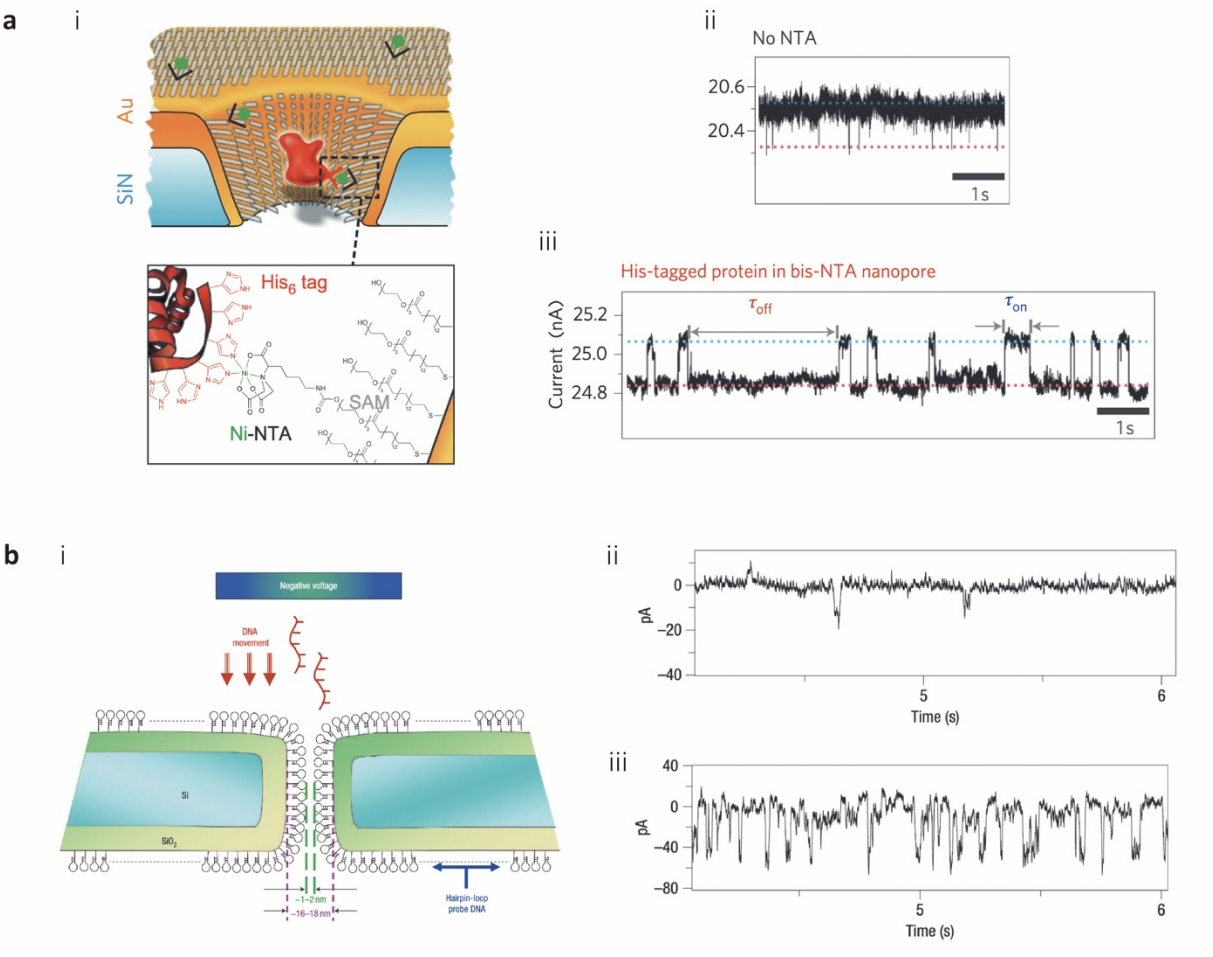


Figure 1.10 Examples of receptor-functionalised nanopore platforms. **a. i.** Schematic of a gold-coated nanopore functionalised with a combination of matrix thiols ($SC_{15}EG_3$) and receptor thiols (NTA). A Ni^{2+} (green) loaded NTA receptor (black) specifically binds to His_6-tagged proteins (red). **ii.** Current versus time trace with rapid protein A/G/L translocations through a 28 nm pore modified with $SC_{15}EG_3$ matrix thiols (no NTA). **iii.** Current versus time trace of a 26 nm pore functionalised with 2 mol% bisNTA after the addition of 180 nM His_6-tagged protein A/G/L shows discrete, long-lasting binding events. **b. i.** Solid-state nanopore functionalised with hairpin-loop (HPL) DNA molecules. Current–time representative data for **ii.** 1 base mismatched (1MM) DNA and **iii.** perfect complementary (PC) DNA translocation through the functionalised nanopore. A higher number of narrower and deeper pulses are observed for the PC-DNA. Figure adapted and reprinted with permission from references 102 and 125.

Several receptor-functionalised nanopore strategies have been developed for selective detection of target nucleic acids and proteins (**Figure 1.10**). Wei et al. developed a gold-coated silicon

nitride nanopore system functionalised with Ni^{2+}-nitrilotriacetic acid (NTA) groups, which enables the selective, single-molecule detection of histidine-tagged proteins [102]. Through site-specific immobilisation of His-tagged protein A within the nanopore, the platform successfully distinguished IgG antibody subclasses based on their characteristic binding dwell times. Iqbal et al. successfully engineered chemically functionalised solid-state nanopores by covalently immobilizing DNA hairpin probes on the pore surface, achieving sequence-specific detection of complementary single-stranded DNA (ssDNA) at the single-molecule level [125]. This platform demonstrated single-nucleotide discrimination capability through characteristic current blockade signatures, establishing an electrically addressable and highly selective nucleic acid sensing methodology. Yusko et al. demonstrated that coating solid-state nanopores with a fluid lipid bilayer enables sub-nanometre tuning of pore diameter and dynamic control of surface chemistry [126]. By incorporating mobile ligands into the bilayer, they achieved selective and time-resolved detection of individual target proteins during translocation.

Despite considerable progress in surface-functionalised nanopores, major challenges persist in achieving controlled receptor placement, reliable target identification in complex biological samples, and sensitive detection of rare analytes. These limitations are especially pronounced for small biomolecules and proteins, whose rapid translocation speeds and low capture rates often exceed current detection capabilities and deviate from classical transport models.

1.4.2 Molecular Carriers

The incorporation of molecular carriers into nanopore sensing systems provides an effective solution to address key limitations in receptor positioning and small biomolecule detection within complex biological samples. These engineered carriers selectively bind target analytes, producing characteristic ionic current signatures that differ from unbound carrier signals (**Figure 1.11**). This strategy offers three principal benefits: (1) translocation velocity modulation that improves temporal resolution by synchronizing target movement with carrier transport, (2) enhanced capture efficiency—particularly for linear DNA molecules due to their extended

conformation—which increases detection sensitivity, and (3) adaptable recognition capabilities through customizable receptor elements that can be tailored for diverse applications.

Recent research has investigated diverse molecular carriers—such as nanoparticles and linear DNA—for enhancing nanopore sensing capabilities [100, 127-130]. These studies have demonstrated notable advancements in applying carrier-based detection to complex biological samples and achieving multiplexed biomolecule analysis. Liu et al. developed an aptamer-modified DNA carrier system for selective detection of α-synuclein oligomers in clinical cerebrospinal fluid using nanopore sensing [131]. The DNA carriers with bound oligomers produced distinct subpeak current signatures and slower translocation, enabling sensitive detection without sample pretreatment. This approach allowed single-molecule discrimination of oligomers in complex biofluids. Ren et al. created DNA molecular probes with position-encoded design for concurrent detection of SARS-CoV-2 proteins and RNA through nanopore sensing [132]. The probes incorporated precisely positioned aptamers and complementary sequences along a DNA scaffold, generating unique signal patterns during translocation that enabled simultaneous identification of viral antigens and genetic variants. This approach achieved specific discrimination between SARS-CoV-2 lineages and characteristic mutations without requiring sequencing. They also developed a single-molecule nanopore assay using gold nanoparticle probes that form dimers upon target binding [133]. The dimerisation event produces distinct translocation signals, enabling differentiation between bound and unbound states. This method achieves sensitive and selective detection without requiring sample amplification or extensive processing.

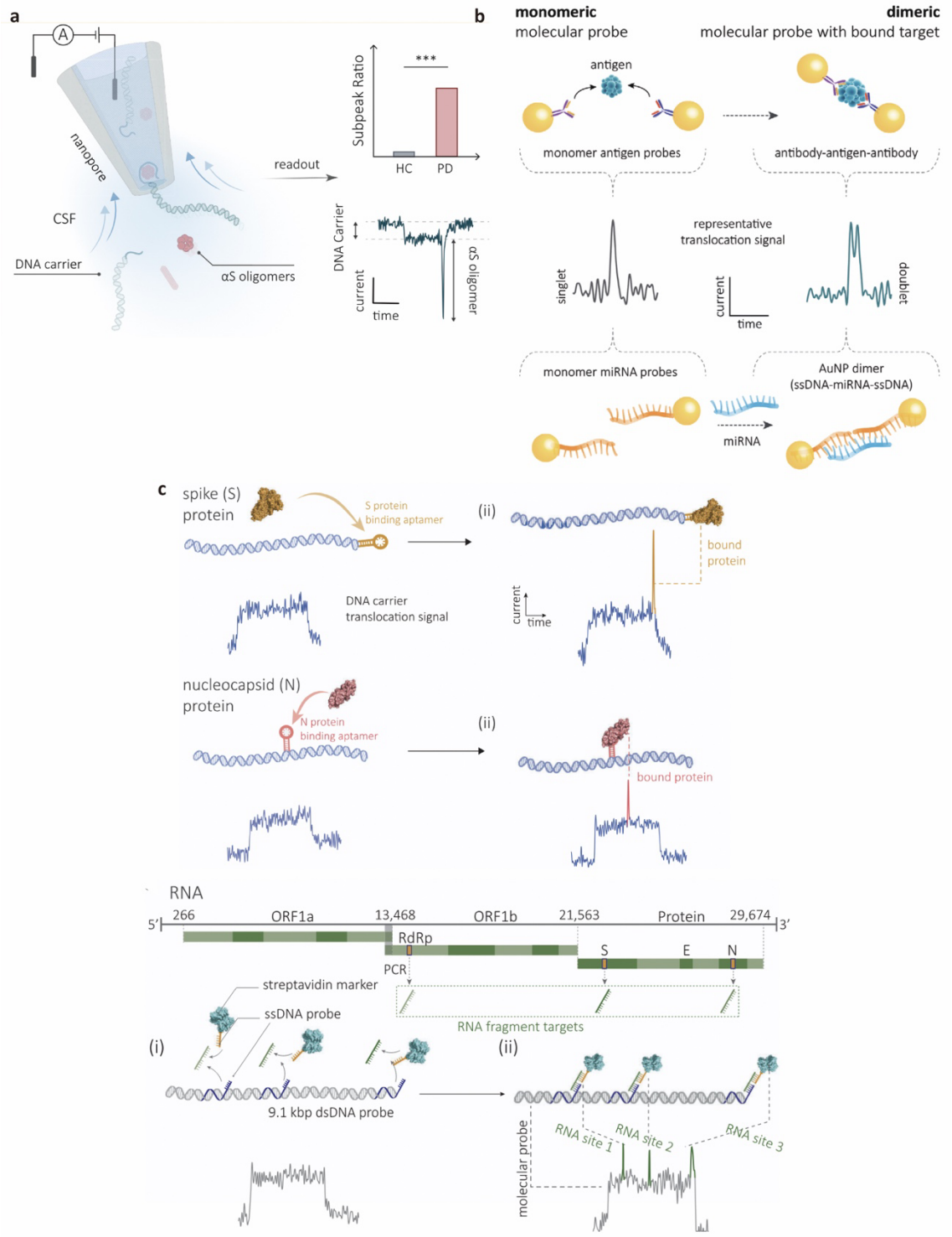


Figure 1.11 Examples of molecular carriers for selective nanopore sensing. **a.** α-Syn oligomers in CSF are captured by DNA carriers modified with aptamers, forming a complex between the carrier and the protein. These DNA-bound α-Syn oligomer complexes are then translocated through a nanopore, where they can be recognised by a distinct subpeak signal. The subpeak ratio, indicating the proportion of signals with subpeaks relative to the total signal count, is indicative of the concentration of oligomeric forms in the clinical sample. **b.** Monomeric and dimeric nanoparticles translocated though the nanopore, the ionic current signal can be used to differentiate

between Au nanoparticles monomers and dimers and as a result selectively determine the concentration of target analytes. Monomeric nanoparticles (17–20 nm) modified with antibodies can be used to initiate self-assembly and dimerisation in the presence of an antigen. A similar strategy can be used for the selective detection of miRNA, two populations of nanoparticles can be modified to contain half of the complementary miRNA sequence. **c.** Multiplexed detection of viral proteins and RNAs from patients' samples. SARS-CoV-2 virus is lysed into S protein, N protein, and RNA fragments, which can be selectively determined by the nanopore when bound to their corresponding encoded DNA molecular probes. Figure adapted and reprinted with permission from references 131, 132 and 133.

These molecular carriers have shown excellent performance in selective nanopore sensing and enabled effective biomolecule detection in complex biological fluids, but several limitations persist. Linear DNA carriers exhibit intrinsic flexibility and tend to fold during nanopore translocation, potentially interfering with the identification of target-associated secondary current peaks. Additionally, linear DNA carrier designs inherently require secondary peak analysis for proper target recognition. In comparison, nanoparticle-based carriers eliminate the need for secondary peak detection but require precise surface charge engineering to ensure nanopore sensing compatibility. The use of DNA nanostructures as molecular carriers presents a promising strategy, as their precisely controlled architectures can enhance structural stability and reduce unwanted folding during translocation through nanopores. Like linear DNA molecules, these nanostructures offer straightforward functionalisation and carry uniform charge distributions.

1.5 DNA Origami Technology

DNA origami is a nanostructure fabrication technique that exploits the highly programmable self-assembly properties of DNA, first introduced by Paul Rothemund in 2006 [134]. The methodology represented a critical advancement in structural DNA nanotechnology, facilitating the fabrication of architecturally complex two- or three-dimensional nanostructures

with sub-nanometre spatial resolution [135]. DNA origami utilises a long single-stranded DNA scaffold, commonly sourced from the M13mp18 bacteriophage, that is precisely folded into predetermined nanostructures through sequence-specific hybridisation with hundreds of short oligonucleotides, termed staple strands (**Figure 1.12**). These staple strands facilitate the folding process by inducing localised base-pairing interactions at specific positions along the scaffold [136]. The DNA origami technique offers a distinct advantage in its unparalleled structural programmability. This capability extends beyond the fabrication of static nanostructures to incorporate dynamic reconfigurability, achieved through precisely controlled strand displacement and hybridisation processes [137, 138].

DNA origami technology presents several fundamental advantages that establish its utility in nanotechnology. First, the technique achieves nanometre-scale spatial precision, enabling exact control over structural dimensions and geometry through programmable sequence design. Second, the intrinsic programmability of DNA facilitates the construction of diverse architectures, ranging from basic geometric motifs to sophisticated three-dimensional frameworks. Third, the inherent biocompatibility of DNA ensures structural stability under physiological conditions, rendering DNA origami particularly suitable for biomedical applications, including targeted drug delivery, high-sensitivity biosensing, and high-resolution cellular imaging. Furthermore, DNA origami structures offer numerous addressable modification sites, allowing for straightforward conjugation with various functional components. These include biomolecules such as antibodies and enzymes, as well as nanomaterials, including plasmonic nanoparticles, quantum dots, and fluorescent dyes.

The unique characteristics of DNA origami have enabled transformative applications across multiple disciplines (**Figure 1.12b.**). In biomedicine, researchers have employed this technology for ultrasensitive biosensing, spatially controlled drug delivery, and high-specificity molecular diagnostics [139, 140]. The field of materials science has utilised DNA origami to construct functional nanomaterials exhibiting programmable optical properties, catalytic activity, and mechanical behaviour [141-143]. Furthermore, this technology has become indispensable for single-molecule studies, where its nanometre-precise patterning capabilities

have significantly enhanced techniques including super-resolution microscopy and single-molecule force spectroscopy [144, 145]. Through enabling unprecedented control over molecular organisation and interactions, DNA origami continues to advance both fundamental biological research and the development of sophisticated nanodevices.

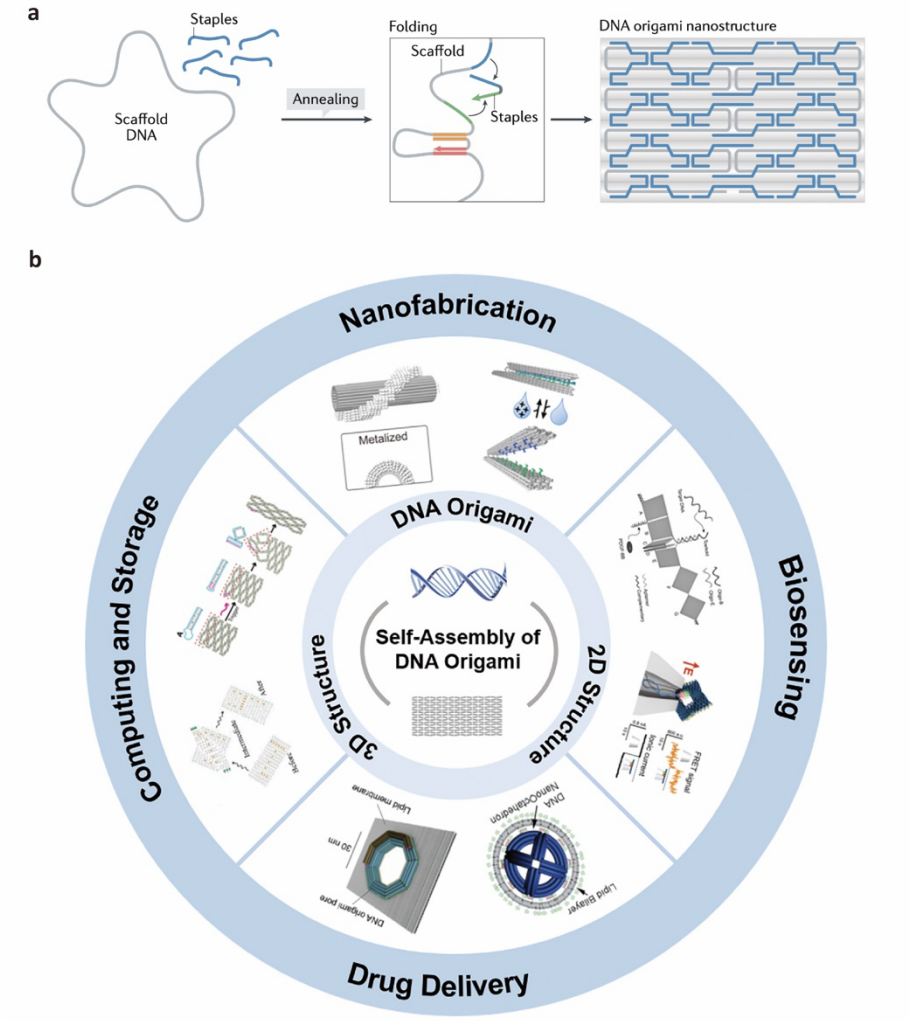


Figure 1.12 DNA origami technology. **a.** Principle of classic DNA origami. A long single-stranded scaffold DNA is annealed with multiple short staples (blue). The staples can bring together distant regions of the scaffold via base pairing (pairing sequences are marked red, orange, green and blue, for example), resulting in a prescribed shape. **b.** DNA nanostructure-enabled applications. DNA origami, 2D and 3D DNA structures and their applications in nanofabrication, biosensing, drug delivery, and DNA computing and storage. Figure adapted and reprinted with permission from references 135 and 139.

1.5.1 DNA Origami in Nanopore Sensing

In nanopore sensing applications, DNA origami technology has been widely adopted through two main approaches: as integrated components in hybrid nanopores, and as programmable molecular carriers, both enabling precise nanoscale manipulation and detection.

Hybrid nanopore systems currently employ two principal DNA origami integration strategies, each offering unique advantages for single-molecule sensing applications. The first approach involves the precise integration of DNA origami nanostructures into solid-state nanopores, where they function as programmable components to regulate molecular translocation dynamics and enhance detection specificity [146-148]. As demonstrated by Bell et al., these hybrid systems enable voltage-controlled insertion and ejection cycles of origami structures within solid-state nanopores, achieving reproducible λ-DNA detection [149]. The second strategy is to incorporate DNA origami directly into lipid bilayers, creating biomimetic nanopores that maintain structural integrity in membrane environments [150-152]. Burns et al. developed this approach through alkyl-phosphorothioate modifications that form a hydrophobic belt around the DNA nanostructure, successfully replicating key functional characteristics of protein pores including stable transmembrane ion conductance [153]. These two strategies provide complementary benefits in structural stability, system adjustability, and platform adaptability, making them suitable for diverse experimental applications.

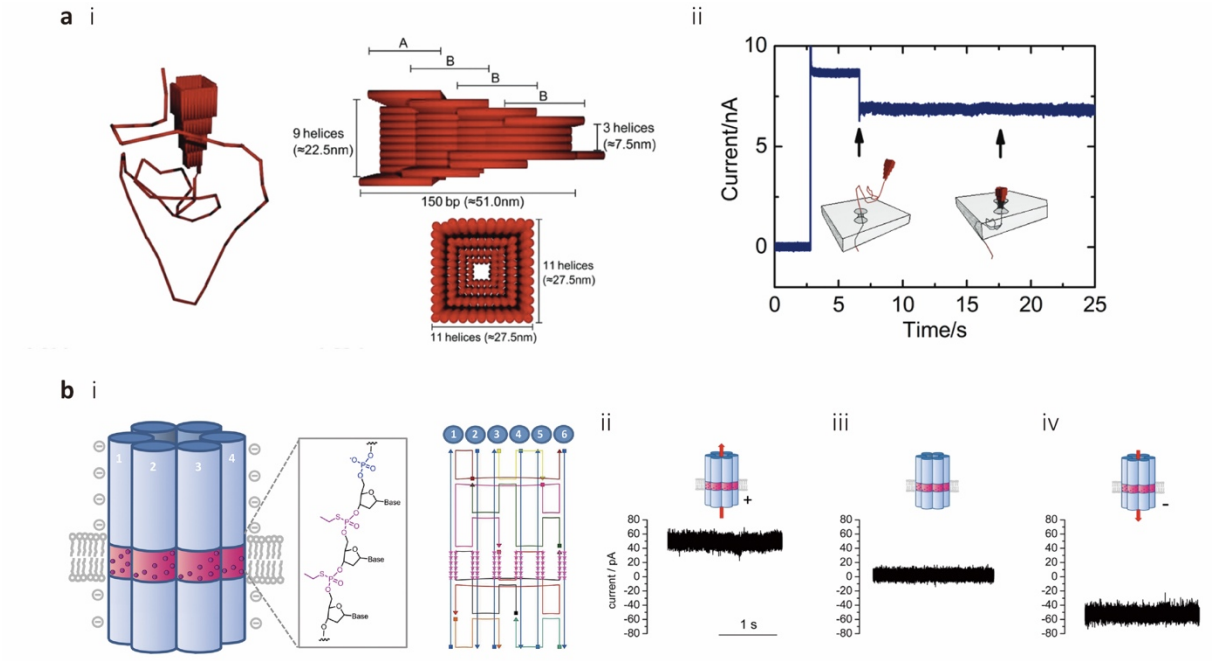


Figure 1.13 Examples of DNA origami hybrid nanopores. **a.** Hybrid nanopores formed by trapping DNA origami onto a solid state nanopore. **i.** Schematic representation of the DNA origami structure with the double-stranded overhang. Double helices are presented as rods. **ii.** Top: Side view of the nanopore section of the DNA origami structure with helices shown as cylinders. **b.** DNA origami nanopores inserted into lipid bilayers. **i.** Schematic representation of a DNA nanopore composed of six interconnected duplexes represented as cylinders. **ii.–iV.** Nanopores are structurally stable in lipid bilayer membranes and support a constant transmembrane current. Single channel current trace of a DNA-nanopore in 1 M KCl, 50 mM Tris, pH 5.0 at +100 mV (**ii**), 0 mV (**iii**), and −100 mV (**iv**) relative to the side of the membrane to which the DNA solution was added. Figure adapted and reprinted with permission from references 149 and 153.

DNA origami has emerged as a powerful platform for developing molecular carriers in nanopore sensing applications (**Figure 1.14**) [87, 154, 155]. Recent work by Raveendran et al. demonstrated this potential through a DNA origami biosensor that combined target-specific aptamers with nanopore detection [156]. Their system achieved quantitative measurement of C-reactive protein at concentrations as low as 3 nM in buffer and 9 nM in diluted plasma by distinguishing between occupied and unoccupied carriers through characteristic current signatures. Complementary research by Ding et al. systematically examined how aptamer modifications affect DNA origami translocation through solid-state nanopores, revealing that target binding and enzymatic regulation produce detectable changes in current signals [157].

The structural advantages of DNA origami carriers are particularly evident when compared to conventional flexible DNA carriers. Their inherent rigidity prevents carrier folding and knotting artefacts that often lead to false positives in nanopore measurements [127, 158, 159]. However, current implementations have primarily utilised static DNA origami designs. The field now stands to benefit from exploring dynamic, reconfigurable DNA origami carriers that could enable more sophisticated sensing capabilities through structural adaptability [160, 161].

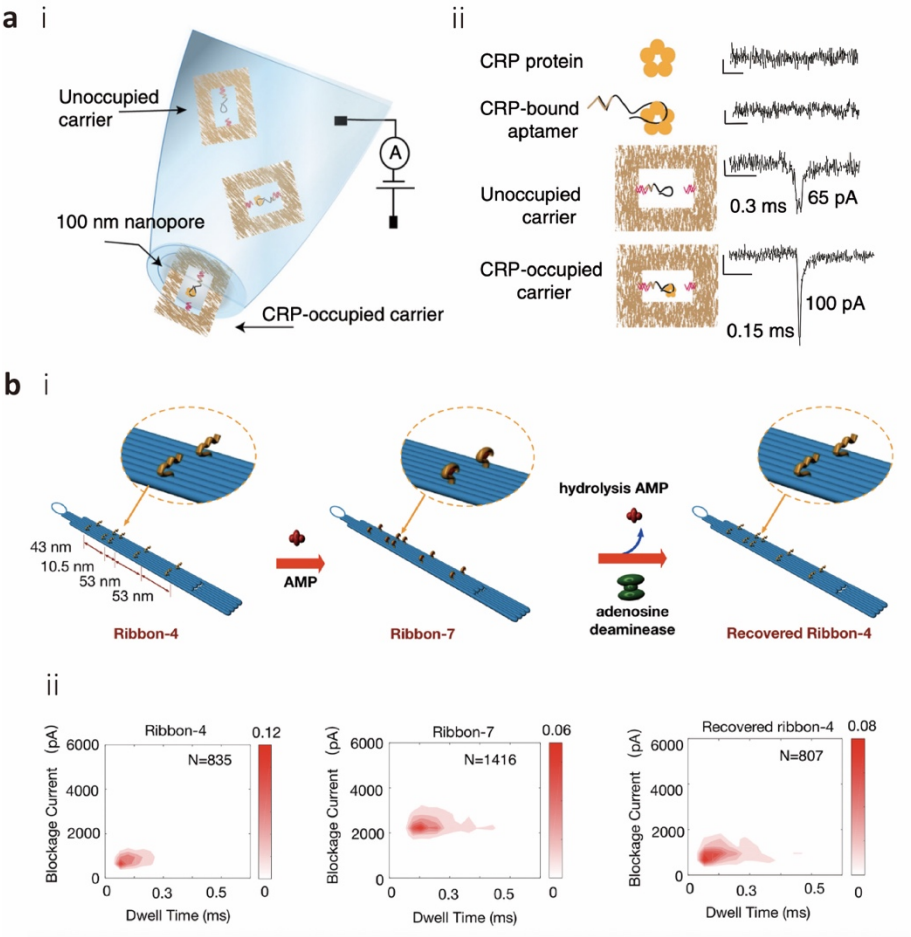


Figure 1.14 Examples of DNA origami molecular carriers for nanopore sensing. **a. i.** Schematic representation of the DNA nanostructure-based biosensing concept exploiting translocation through nanopipettes as the sensing mechanism. **ii.** Typical ion current signatures upon translocation of (C-reactive protein) CRP molecules, CRP–DNA aptamer complexes, unoccupied carriers and CRP-bound occupied carriers. The scale bars represent 20 pA and 1 ms, respectively. **b.** Enzymatic regulation on surface modification to influence the origami carrier translocation. **i.** Design of ribbon-4 with 10 aptamers on the surface. Addition of adenosine monophosphate (AMP)

to ribbon-4 forms ribbon-7. The addition of the enzyme adenosine deaminase (ADA) converts AMP to inosine monophosphate (IMP), which dissociates from the aptamers, and the ribbon-7 is recovered back to ribbon-4. **ii.** Scatter plots of translocation events using a 20 nm nanopore at 500 mV. Figure adapted and reprinted with permission from references 156 and 157.

1.6 Summary of Dissertation

This thesis focuses on developing single-molecule nanopore sensing platforms for selective detection of small biomarker miRNAs using DNA-based molecular carriers. The work pursued two primary goals: (1) creating a dsDNA carrier system that enables selective miRNA detection through streptavidin binding and (2) designing a reconfigurable DNA origami hinge whose configuration changes upon miRNA binding allow quantitative detection via nanopore signals. Both molecular carrier systems were successfully implemented not only in nanopipette-based platforms but also in solid-state nanopores fabricated using the CBD method.

Chapter 2 outlines the experimental methods, including nanopore fabrication and characterisation, translocation experiment setup, design and assembly of DNA-based molecular carriers, and data analysis approaches for signal processing and statistical evaluation.

Chapter 3 explores a nanopore-based miRNA detection method that employs a functionalised dsDNA carrier and a sandwich complex design. The engineered dsDNA carrier enables selective miRNA capture, with streptavidin probes boosting signal resolution. Carrier characterisation combined electrophoretic and nanopore analyses. Optimisation studies examined buffer conditions and compared direct versus carrier-mediated detection of miRNA-141-3p, later extended to multiplexed analysis of miRNA-7-5p and miRNA-382-5p. Refined incubation protocols improved binding efficiency, advancing nanopore-based miRNA detection for diagnostic applications.

Chapter 4 examines a reconfigurable DNA origami hinge system through an integrated analysis of its structural and dynamic properties. Bulk fluorescence assays with dual photophore quenching monitored hinge transitions, while TEM (transmission electron microscopy) and nanopore sensing characterised configuration-dependent dynamics. Voltage-controlled measurements revealed distinct translocation signatures for closed, extended, and open states, demonstrating conformation-specific nanopore interactions.

Chapter 5 develops a reconfigurable DNA origami hinge for nanopore-based detection of prostate cancer (pCa) biomarker miRNA-141-3p. The hinge undergoes programmable closed-to-extended transitions upon miRNA binding, producing distinct ionic current signatures. Results show nanomolar sensitivity and excellent specificity in distinguishing target miRNAs, establishing DNA nanostructure enhanced nanopore sensing for ultrasensitive biomarker detection.

Chapter 6 presents a cost-effective CBD method for fabricating solid-state nanopores that match nanopipette performance in dsDNA detection while enabling selective miRNA sensing via DNA molecular carriers and analysis of reconfigurable DNA origami hinges, demonstrating versatile capabilities for nanostructure characterisation and biosensing.

1.7 References

[1] Bartel, D. P. MicroRNAs: genomics, biogenesis, mechanism, and function. *Cell* **2004**, *116*, 281-297.

[2] Bartel, D. P. MicroRNAs: target recognition and regulatory functions. *Cell* **2009**, *136*, 215-233.

[3] John, B.;Enright, A. J.;Aravin, A.;Tuschl, T.;Sander, C.; Marks, D. S. Human MicroRNA targets. *PLoS Biol* **2004**, *2*, e363.

[4] Baek, D.;Villen, J.;Shin, C.;Camargo, F. D.;Gygi, S. P.; Bartel, D. P. The impact of microRNAs on protein output. *Nature* **2008**, *455*, 64-71.

[5] Ambros, V. The functions of animal microRNAs. *Nature* **2004**, *431*, 350-355.

[6] Parizi, P. K.;Yarahmadi, F.;Tabar, H. M.;Hosseini, Z.;Sarli, A.;Kia, N.;Tafazoli, A.; Esmaeili, S. A. MicroRNAs and target molecules in bladder cancer. *Med Oncol* **2020**, *37*, 118.

[7] Nikolac Perkovic, M.;Videtic Paska, A.;Konjevod, M.;Kouter, K.;Svob Strac, D.;Nedic Erjavec, G.; Pivac, N. Epigenetics of Alzheimer's Disease. *Biomolecules* **2021**, *11*.

[8] Rottiers, V.; Naar, A. M. MicroRNAs in metabolism and metabolic disorders. *Nat Rev Mol Cell Biol* **2012**, *13*, 239-250.

[9] Lee, C. T.;Risom, T.; Strauss, W. M. Evolutionary conservation of microRNA regulatory circuits: an examination of microRNA gene complexity and conserved microRNA-target interactions through metazoan phylogeny. *DNA Cell Biol* **2007**, *26*, 209-218.

[10] Roy, B.;Lee, E.;Li, T.; Rampersaud, M. Role of miRNAs in Neurodegeneration: From Disease Cause to Tools of Biomarker Discovery and Therapeutics. *Genes (Basel)* **2022**, *13*.

[11] Hayes, J.;Peruzzi, P. P.; Lawler, S. MicroRNAs in cancer: biomarkers, functions and therapy. *Trends Mol Med* **2014**, *20*, 460-469.

[12] Kramna, D.;Riedlova, P.; Jirik, V. MicroRNAs as a Potential Biomarker in the Diagnosis of Cardiovascular Diseases. *Medicina (Kaunas)* **2023**, *59*.

[13] Li, Z.; Rana, T. M. Therapeutic targeting of microRNAs: current status and future challenges. *Nat Rev Drug Discov* **2014**, *13*, 622-638.

[14] Christopher, A. F.;Kaur, R. P.;Kaur, G.;Kaur, A.;Gupta, V.; Bansal, P. MicroRNA therapeutics: Discovering novel targets and developing specific therapy. *Perspect Clin Res* **2016**, *7*, 68-74.

[15] Bader, A. G.;Brown, D.; Winkler, M. The promise of microRNA replacement therapy. *Cancer Res* **2010**, *70*, 7027-7030.

[16] Li, H.; Yang, B. B. Friend or foe: the role of microRNA in chemotherapy resistance. *Acta Pharmacol Sin* **2013**, *34*, 870-879.

[17] Cortez, M. A.;Anfossi, S.;Ramapriyan, R.;Menon, H.;Atalar, S. C.;Aliru, M.;Welsh, J.; Calin, G. A. Role of miRNAs in immune responses and immunotherapy in cancer. *Genes Chromosomes Cancer* **2019**, *58*, 244-253.

[18] Segal, M.; Slack, F. J. Challenges identifying efficacious miRNA therapeutics for cancer. *Expert Opin Drug Discov* **2020**, *15*, 987-992.

[19] Ye, J.;Xu, M.;Tian, X.;Cai, S.; Zeng, S. Research advances in the detection of miRNA. *J Pharm Anal* **2019**, *9*, 217-226.

[20] Chen, C.;Ridzon, D. A.;Broomer, A. J.;Zhou, Z.;Lee, D. H.;Nguyen, J. T.;Barbisin, M.;Xu, N. L.;Mahuvakar, V. R.;Andersen, M. R.;Lao, K. Q.;Livak, K. J.; Guegler, K. J. Real-time quantification of microRNAs by stem-loop RT-PCR. *Nucleic Acids Res* **2005**, *33*, e179.

[21] Fu, H. J.;Zhu, J.;Yang, M.;Zhang, Z. Y.;Tie, Y.;Jiang, H.;Sun, Z. X.; Zheng, X. F. A novel method to monitor the expression of microRNAs. *Mol Biotechnol* **2006**, *32*, 197-204.

[22] Roberts, T. C.;Coenen-Stass, A. M.;Betts, C. A.; Wood, M. J. Detection and quantification of extracellular microRNAs in murine biofluids. *Biol Proced Online* **2014**, *16*, 5.

[23] Sykes, P. J.;Neoh, S. H.;Brisco, M. J.;Hughes, E.;Condon, J.; Morley, A. A. Quantitation of targets for PCR by use of limiting dilution. *Biotechniques* **1992**, *13*, 444-449.

[24] Hudecova, I. Digital PCR analysis of circulating nucleic acids. *Clin Biochem* **2015**, *48*, 948-956.

[25] Benesova, S.;Kubista, M.; Valihrach, L. Small RNA-Sequencing: Approaches and Considerations for miRNA Analysis. *Diagnostics (Basel)* **2021**, *11*.

[26] Androvic, P.;Benesova, S.;Rohlova, E.;Kubista, M.; Valihrach, L. Small RNA-Sequencing for Analysis of Circulating miRNAs: Benchmark Study. *J Mol Diagn* **2022**, *24*, 386-394.

[27] Liu, C. G.;Calin, G. A.;Volinia, S.; Croce, C. M. MicroRNA expression profiling using microarrays. *Nat Protoc* **2008**, *3*, 563-578.

[28] Miska, E. A.;Alvarez-Saavedra, E.;Townsend, M.;Yoshii, A.;Sestan, N.;Rakic, P.;Constantine-Paton, M.; Horvitz, H. R. Microarray analysis of microRNA expression in the developing mammalian brain. *Genome Biol* **2004**, *5*, R68.

[29] Tavallaie, R.;McCarroll, J.;Le Grand, M.;Ariotti, N.;Schuhmann, W.;Bakker, E.;Tilley, R. D.;Hibbert, D. B.;Kavallaris, M.; Gooding, J. J. Nucleic acid hybridization on an electrically reconfigurable network of gold-coated magnetic nanoparticles enables microRNA detection in blood. *Nat Nanotechnol* **2018**, *13*, 1066-1071.

[30] Yuan, Y. H.;Wu, Y. D.;Chi, B. Z.;Wen, S. H.;Liang, R. P.; Qiu, J. D. Simultaneously electrochemical detection of microRNAs based on multifunctional magnetic nanoparticles probe coupling with hybridization chain reaction. *Biosens Bioelectron* **2017**, *97*, 325-331.

[31] Zhou, J.;Yang, Y.; Zhang, C. Y. Toward Biocompatible Semiconductor Quantum Dots: From Biosynthesis and Bioconjugation to Biomedical Application. *Chem Rev* **2015**, *115*, 11669-11717.

[32] Ali, A.;Zafar, H.;Zia, M.;Ul Haq, I.;Phull, A. R.;Ali, J. S.; Hussain, A. Synthesis, characterization, applications, and challenges of iron oxide nanoparticles. *Nanotechnol Sci Appl* **2016**, *9*, 49-67.

[33] Coutinho, C.; Somoza, A. MicroRNA sensors based on gold nanoparticles. *Anal Bioanal Chem* **2019**, *411*, 1807-1824.

[34] Ratre, P.;Nazeer, N.;Kumari, R.;Thareja, S.;Jain, B.;Tiwari, R.;Kamthan, A.;Srivastava, R. K.; Mishra, P. K. Carbon-Based Fluorescent Nano-Biosensors for the Detection of Cell-Free Circulating MicroRNAs. *Biosensors (Basel)* **2023**, *13*.

[35] Wang, J.;Wen, J.; Yan, H. Recent Applications of Carbon Nanomaterials for microRNA Electrochemical Sensing. *Chem Asian J* **2021**, *16*, 114-128.

[36] Gutierrez-Galvez, L.;Garcia-Mendiola, T.;Gutierrez-Sanchez, C.;Guerrero-Esteban, T.;Garcia-Diego, C.;Buendia, I.;Garcia-Bermejo, M. L.;Pariente, F.; Lorenzo, E. Carbon nanodot-based electrogenerated chemiluminescence biosensor for miRNA-21 detection. *Mikrochim Acta* **2021**, *188*, 398.

[37] Wanunu, M.;Dadosh, T.;Ray, V.;Jin, J.;McReynolds, L.; Drndic, M. Rapid electronic detection of probe-specific microRNAs using thin nanopore sensors. *Nat Nanotechnol* **2010**, *5*, 807-814.

[38] Wang, Y.;Zheng, D.;Tan, Q.;Wang, M. X.; Gu, L. Q. Nanopore-based detection of circulating microRNAs in lung cancer patients. *Nat Nanotechnol* **2011**, *6*, 668-674.

[39] Koch, C.;Reilly-O'Donnell, B.;Gutierrez, R.;Lucarelli, C.;Ng, F. S.;Gorelik, J.;Ivanov, A. P.; Edel, J. B. Nanopore sequencing of DNA-barcoded probes for highly multiplexed detection of microRNA, proteins and small biomarkers. *Nat Nanotechnol* **2023**, *18*, 1483-1491.

[40] Akkilic, N.;Geschwindner, S.; Hook, F. Single-molecule biosensors: Recent advances and applications. *Biosens Bioelectron* **2020**, *151*, 111944.

[41] Swierczewska, M.;Liu, G.;Lee, S.; Chen, X. High-sensitivity nanosensors for biomarker detection. *Chem Soc Rev* **2012**, *41*, 2641-2655.

[42] Chauhan, N.;Saxena, K.; Jain, U. Single molecule detection; from microscopy to sensors. *Int J Biol Macromol* **2022**, *209*, 1389-1401.

[43] Gooding, J. J.; Gaus, K. Single-Molecule Sensors: Challenges and Opportunities for Quantitative Analysis. *Angew Chem Int Ed Engl* **2016**, *55*, 11354-11366.

[44] Szalai, A. M.;Siarry, B.;Lukin, J.;Williamson, D. J.;Unsain, N.;Caceres, A.;Pilo-Pais, M.;Acuna, G.;Refojo, D.;Owen, D. M.;Simoncelli, S.; Stefani, F. D. Three-dimensional total-internal reflection fluorescence nanoscopy with nanometric axial resolution by photometric localization of single molecules. *Nat Commun* **2021**, *12*, 517.

[45] Ha, T.;Fei, J.;Schmid, S.;Lee, N. K.;Gonzalez, R. L.;Paul, S.; Yeou, S. Fluorescence resonance energy transfer at the single-molecule level. *Nature Reviews Methods Primers* **2024**, *4*, 21.

[46] Neuman, K. C.; Nagy, A. Single-molecule force spectroscopy: optical tweezers, magnetic tweezers and atomic force microscopy. *Nat Methods* **2008**, *5*, 491-505.

[47] Macchia, E.;Manoli, K.;Di Franco, C.;Scamarcio, G.; Torsi, L. New trends in single-molecule bioanalytical detection. *Anal Bioanal Chem* **2020**, *412*, 5005-5014.

[48] Wanunu, M. Nanopores: A journey towards DNA sequencing. *Phys Life Rev* **2012**, *9*, 125-158.

[49] Kodoyianni, V. Label-free analysis of biomolecular interactions using SPR imaging. *Biotechniques* **2011**, *50*, 32-40.

[50] Wang, J.;Zhu, Z.; Ma, H. Label-free real-time detection of DNA methylation based on quartz crystal microbalance measurement. *Anal Chem* **2013**, *85*, 2096-2101.

[51] Lin, M.;Song, P.;Zhou, G.;Zuo, X.;Aldalbahi, A.;Lou, X.;Shi, J.; Fan, C. Electrochemical detection of nucleic acids, proteins, small molecules and cells using a DNA-nanostructure-based universal biosensing platform. *Nat Protoc* **2016**, *11*, 1244-1263.

[52] Howorka, S.; Siwy, Z. Nanopore analytics: sensing of single molecules. *Chemical Society Reviews* **2009**, *38*, 2360-2384.

[53] Coulter, W. Means for counting particles suspended in a fluid. US Patent, 2656508, United States Pat. Off. Patentiert Am. 20 (1953) 1953.

[54] Hladky, S. B.; Haydon, D. A. Discreteness of Conductance Change in Bimolecular Lipid Membranes in the Presence of Certain Antibiotics. *Nature* **1970**, *225*, 451-453.

[55] Neher, E.; Sakmann, B. Single-channel currents recorded from membrane of denervated frog muscle fibres. *Nature* **1976**, *260*, 799-802.

[56] Bezrukov, S. M.;Vodyanoy, I.; Parsegian, V. A. Counting polymers moving through a single ion channel. *Nature* **1994**, *370*, 279-281.

[57] Kasianowicz, J. J.;Brandin, E.;Branton, D.; Deamer, D. W. Characterization of individual polynucleotide molecules using a membrane channel. *Proc Natl Acad Sci U S A* **1996**, *93*, 13770-13773.

[58] Wang, H. Y.;Ying, Y. L.;Li, Y.; Long, Y. T. Peering into biological nanopore: a practical technology to single-molecule analysis. *Chem Asian J* **2010**, *5*, 1952-1961.

[59] Ayub, M.;Stoddart, D.; Bayley, H. Nucleobase Recognition by Truncated alpha-Hemolysin Pores. *ACS Nano* **2015**, *9*, 7895-7903.

[60] Takeuchi, N.;Hiratani, M.; Kawano, R. Pattern Recognition of microRNA Expression in Body Fluids Using Nanopore Decoding at Subfemtomolar Concentrations. *JACS Au* **2022**, *2*, 1829-1838.

[61] Lee, D. H.;Oh, S.;Lim, K.;Lee, B.;Yi, G. S.;Kim, Y. R.;Kim, K. B.;Lee, C. K.;Chi, S. W.; Lee, M. K. Tertiary RNA Folding-Targeted Drug Screening Strategy Using a Protein Nanopore. *Anal Chem* **2021**, *93*, 2811-2819.

[62] Derrington, I. M.;Butler, T. Z.;Collins, M. D.;Manrao, E.;Pavlenok, M.;Niederweis, M.; Gundlach, J. H. Nanopore DNA sequencing with MspA. *Proc Natl Acad Sci U S A* **2010**, *107*, 16060-16065.

[63] Cao, C.;Ying, Y. L.;Hu, Z. L.;Liao, D. F.;Tian, H.; Long, Y. T. Discrimination of oligonucleotides of different lengths with a wild-type aerolysin nanopore. *Nat Nanotechnol* **2016**, *11*, 713-718.

[64] Kwak, D. K.;Kim, J. S.;Lee, M. K.;Ryu, K. S.; Chi, S. W. Probing the Neuraminidase Activity of Influenza Virus Using a Cytolysin A Protein Nanopore. *Anal Chem* **2020**, *92*, 14303-14308.

[65] Lucas, F. L. R.;Versloot, R. C. A.;Yakovlieva, L.;Walvoort, M. T. C.; Maglia, G. Protein identification by nanopore peptide profiling. *Nat Commun* **2021**, *12*, 5795.

[66] Venkatesan, B. M.; Bashir, R. Nanopore sensors for nucleic acid analysis. *Nat Nanotechnol* **2011**, *6*, 615-624.

[67] Storm, A. J.;Chen, J. H.;Ling, X. S.;Zandbergen, H. W.; Dekker, C. Fabrication of solid-state nanopores with single-nanometre precision. *Nat Mater* **2003**, *2*, 537-540.

[68] Talaga, D. S.; Li, J. Single-molecule protein unfolding in solid state nanopores. *J Am Chem Soc* **2009**, *131*, 9287-9297.

[69] Venkatesan, B. M.;Dorvel, B.;Yemenicioglu, S.;Watkins, N.;Petrov, I.; Bashir, R. Highly Sensitive, Mechanically Stable Nanopore Sensors for DNA Analysis. *Adv Mater* **2009**, *21*, 2771.

[70] Merchant, C. A.;Healy, K.;Wanunu, M.;Ray, V.;Peterman, N.;Bartel, J.;Fischbein, M. D.;Venta, K.;Luo, Z.;Johnson, A. T.; Drndic, M. DNA translocation through graphene nanopores. *Nano Lett* **2010**, *10*, 2915-2921.

[71] Cai, S.;Sze, J. Y. Y.;Ivanov, A. P.; Edel, J. B. Small molecule electro-optical binding assay using nanopores. *Nat Commun* **2019**, *10*, 1797.

[72] Parkin, W. M.; Drndic, M. Signal and Noise in FET-Nanopore Devices. *ACS Sens* **2018**, *3*, 313-319.

[73] Confederat, S.;Lee, S.;Vang, D.;Soulias, D.;Marcuccio, F.;Peace, T. I.;Edwards, M. A.;Strobbia, P.;Samanta, D.;Walti, C.; Actis, P. Next-Generation Nanopore Sensors Based on Conductive Pulse Sensing for Enhanced Detection of Nanoparticles. *Small* **2024**, *20*, e2305186.

[74] Chien, C. C.;Shekar, S.;Niedzwiecki, D. J.;Shepard, K. L.; Drndic, M. Single-Stranded DNA Translocation Recordings through Solid-State Nanopores on Glass Chips at 10 MHz Measurement Bandwidth. *ACS Nano* **2019**, *13*, 10545-10554.

[75] Rodriguez-Manzo, J. A.;Puster, M.;Nicolai, A.;Meunier, V.; Drndic, M. DNA Translocation in Nanometer Thick Silicon Nanopores. *ACS Nano* **2015**, *9*, 6555-6564.

[76] Xue, L.;Yamazaki, H.;Ren, R.;Wanunu, M.;Ivanov, A. P.; Edel, J. B. Solid-state nanopore sensors. *Nature Reviews Materials* **2020**, *5*, 931-951.

[77] Li, J.;Stein, D.;McMullan, C.;Branton, D.;Aziz, M. J.; Golovchenko, J. A. Ion-beam sculpting at nanometre length scales. *Nature* **2001**, *412*, 166-169.

[78] Wu, M.-Y.;Krapf, D.;Zandbergen, M.;Zandbergen, H.; Batson, P. E. Formation of nanopores in a SiN/SiO2 membrane with an electron beam. *Applied Physics Letters* **2005**, *87*.

[79] Kwok, H.;Briggs, K.; Tabard-Cossa, V. Nanopore fabrication by controlled dielectric breakdown. *PLoS One* **2014**, *9*, e92880.

[80] Rutkowska, A.;Freedman, K.;Skalkowska, J.;Kim, M. J.;Edel, J. B.; Albrecht, T. Electrodeposition and bipolar effects in metallized nanopores and their use in the detection of insulin. *Anal Chem* **2015**, *87*, 2337-2344.

[81] Choi, J.;Lee, C. C.; Park, S. Scalable fabrication of sub-10 nm polymer nanopores for DNA analysis. *Microsyst Nanoeng* **2019**, *5*, 12.

[82] Nam, S.;Choi, I.;Fu, C. C.;Kim, K.;Hong, S.;Choi, Y.;Zettl, A.; Lee, L. P. Graphene nanopore with a self-integrated optical antenna. *Nano Lett* **2014**, *14*, 5584-5589.

[83] Siwy, Z. S.;Powell, M. R.;Petrov, A.;Kalman, E.;Trautmann, C.; Eisenberg, R. S. Calcium-induced voltage gating in single conical nanopores. *Nano Lett* **2006**, *6*, 1729-1734.

[84] Stanley, J.; Pourmand, N. Nanopipettes—The past and the present. *APL Materials* **2020**, *8*.

[85] Morris, C. A.;Friedman, A. K.; Baker, L. A. Applications of nanopipettes in the analytical sciences. *Analyst* **2010**, *135*, 2190-2202.

[86] Wei, C.;Bard, A. J.; Feldberg, S. W. Current Rectification at Quartz Nanopipet Electrodes. *Analytical Chemistry* **1997**, *69*, 4627-4633.

[87] Bell, N. A.; Keyser, U. F. Digitally encoded DNA nanostructures for multiplexed, single-molecule protein sensing with nanopores. *Nat Nanotechnol* **2016**, *11*, 645-651.

[88] Han, C.;Hao, R.;Fan, Y.;Edwards, M. A.;Gao, H.; Zhang, B. Observing Transient Bipolar Electrochemical Coupling on Single Nanoparticles Translocating through a Nanopore. *Langmuir* **2019**, *35*, 7180-7190.

[89] Wang, X.;Wilkinson, M. D.;Lin, X.;Ren, R.;Willison, K. R.;Ivanov, A. P.;Baum, J.; Edel, J. B. Single-molecule nanopore sensing of actin dynamics and drug binding. *Chem Sci* **2019**, *11*, 970-979.

[90] Umehara, S.;Pourmand, N.;Webb, C. D.;Davis, R. W.;Yasuda, K.; Karhanek, M. Current rectification with poly-l-lysine-coated quartz nanopipettes. *Nano Lett* **2006**, *6*, 2486-2492.

[91] Ding, S.;Gao, C.; Gu, L. Q. Capturing single molecules of immunoglobulin and ricin with an aptamer-encoded glass nanopore. *Anal Chem* **2009**, *81*, 6649-6655.

[92] Vitol, E. A.;Orynbayeva, Z.;Bouchard, M. J.;Azizkhan-Clifford, J.;Friedman, G.; Gogotsi, Y. In situ intracellular spectroscopy with surface enhanced Raman spectroscopy (SERS)-enabled nanopipettes. *ACS Nano* **2009**, *3*, 3529-3536.

[93] Freedman, K. J.;Otto, L. M.;Ivanov, A. P.;Barik, A.;Oh, S. H.; Edel, J. B. Nanopore sensing at ultra-low concentrations using single-molecule dielectrophoretic trapping. *Nat Commun* **2016**, *7*, 10217.

[94] Miles, B. N.;Ivanov, A. P.;Wilson, K. A.;Dogan, F.;Japrung, D.; Edel, J. B. Single molecule sensing with solid-state nanopores: novel materials, methods, and applications. *Chem Soc Rev* **2013**, *42*, 15-28.

[95] Hall, J. E. Access resistance of a small circular pore. *J Gen Physiol* **1975**, *66*, 531-532.

[96] Vodyanoy, I.; Bezrukov, S. M. Sizing of an ion pore by access resistance measurements. *Biophys J* **1992**, *62*, 10-11.

[97] Edel, J. B.; Albrecht, T. *Engineered nanopores for bioanalytical applications*; William Andrew, 2013.

[98] Willmott, G. R.;Vogel, R.;Yu, S. S.;Groenewegen, L. G.;Roberts, G. S.;Kozak, D.;Anderson, W.; Trau, M. Use of tunable nanopore blockade rates to investigate colloidal dispersions. *J Phys Condens Matter* **2010**, *22*, 454116.

[99] Steinbock, L. J.;Lucas, A.;Otto, O.; Keyser, U. F. Voltage-driven transport of ions and DNA through nanocapillaries. *ELECTROPHORESIS* **2012**, *33*, 3480-3487.

[100] Lin, X.;Ivanov, A. P.; Edel, J. B. Selective single molecule nanopore sensing of proteins using DNA aptamer-functionalised gold nanoparticles. *Chem Sci* **2017**, *8*, 3905-3912.

[101] Ivanov, A. P.;Actis, P.;Jonsson, P.;Klenerman, D.;Korchev, Y.; Edel, J. B. On-demand delivery of single DNA molecules using nanopipets. *ACS Nano* **2015**, *9*, 3587-3595.

[102] Wei, R.;Gatterdam, V.;Wieneke, R.;Tampe, R.; Rant, U. Stochastic sensing of proteins with receptor-modified solid-state nanopores. *Nat Nanotechnol* **2012**, *7*, 257-263.

[103] Wang, Y.;Wang, Y.;Du, X.;Yan, S.;Zhang, P.;Chen, H. Y.; Huang, S. Electrode-free nanopore sensing by DiffusiOptoPhysiology. *Sci Adv* **2019**, *5*, eaar3309.

[104] Yusko, E. C.;Bruhn, B. R.;Eggenberger, O. M.;Houghtaling, J.;Rollings, R. C.;Walsh, N. C.;Nandivada, S.;Pindrus, M.;Hall, A. R.;Sept, D.;Li, J.;Kalonia, D. S.; Mayer, M. Real-time shape approximation and fingerprinting of single proteins using a nanopore. *Nature Nanotechnology* **2017**, *12*, 360-367.

[105] Bhattacharyya, B. Chapter 2 - Electrochemical Machining: Macro to Micro. In *Electrochemical Micromachining for Nanofabrication, MEMS and Nanotechnology*. B. Bhattacharyya, Ed.; William Andrew Publishing, 2015; pp 25-52.

[106] Stern, O. ZUR THEORIE DER ELEKTROLYTISCHEN DOPPELSCHICHT. *Zeitschrift für Elektrochemie und angewandte physikalische Chemie* **1924**, *30*, 508-516.

[107] Gonella, G.;Backus, E. H. G.;Nagata, Y.;Bonthuis, D. J.;Loche, P.;Schlaich, A.;Netz, R. R.;Kuhnle, A.;McCrum, I. T.;Koper, M. T. M.;Wolf, M.;Winter, B.;Meijer, G.;Campen, R. K.; Bonn, M. Water at charged interfaces. *Nat Rev Chem* **2021**, *5*, 466-485.

[108] Cevc, G. Membrane electrostatics. *Biochimica et Biophysica Acta (BBA) - Reviews on Biomembranes* **1990**, *1031*, 311-382.

[109] Singh, K. P.; Kumar, M. Effect of Nanochannel Diameter and Debye Length on Ion Current Rectification in a Fluidic Bipolar Diode. *The Journal of Physical Chemistry C* **2011**, *115*, 22917-22924.

[110] Experton, J.;Wu, X.; Martin, C. R. From Ion Current to Electroosmotic Flow Rectification in Asymmetric Nanopore Membranes. *Nanomaterials (Basel)* **2017**, *7*.

[111] Hall, A. R.;van Dorp, S.;Lemay, S. G.; Dekker, C. Electrophoretic force on a protein-coated DNA molecule in a solid-state nanopore. *Nano Lett* **2009**, *9*, 4441-4445.

[112] Smeets, R. M.;Keyser, U. F.;Krapf, D.;Wu, M. Y.;Dekker, N. H.; Dekker, C. Salt dependence of ion transport and DNA translocation through solid-state nanopores. *Nano Lett* **2006**, *6*, 89-95.

[113] Zanjani, M. B.;Engelke, R. E.;Lukes, J. R.;Meunier, V.; Drndic, M. Up and down translocation events and electric double-layer formation inside solid-state nanopores. *Phys Rev E Stat Nonlin Soft Matter Phys* **2015**, *92*, 022715.

[114] He, Y.;Gillespie, D.;Boda, D.;Vlassiouk, I.;Eisenberg, R. S.; Siwy, Z. S. Tuning transport properties of nanofluidic devices with local charge inversion. *J Am Chem Soc* **2009**, *131*, 5194-5202.

[115] Firnkes, M.;Pedone, D.;Knezevic, J.;Doblinger, M.; Rant, U. Electrically facilitated translocations of proteins through silicon nitride nanopores: conjoint and competitive action of diffusion, electrophoresis, and electroosmosis. *Nano Lett* **2010**, *10*, 2162-2167.

[116] Schoch, R. B.;Han, J.; Renaud, P. Transport phenomena in nanofluidics. *Reviews of Modern Physics* **2008**, *80*, 839-883.

[117] Chen, K.;Bell, N. A. W.;Kong, J.;Tian, Y.; Keyser, U. F. Direction- and Salt-Dependent Ionic Current Signatures for DNA Sensing with Asymmetric Nanopores. *Biophys J* **2017**, *112*, 674-682.

[118] Kowalczyk, S. W.;Wells, D. B.;Aksimentiev, A.; Dekker, C. Slowing down DNA translocation through a nanopore in lithium chloride. *Nano Lett* **2012**, *12*, 1038-1044.

[119] Wang, V.;Ermann, N.; Keyser, U. F. Current Enhancement in Solid-State Nanopores Depends on Three-Dimensional DNA Structure. *Nano Lett* **2019**, *19*, 5661-5666.

[120] Wanunu, M.; Meller, A. Chemically modified solid-state nanopores. *Nano Lett* **2007**, *7*, 1580-1585.

[121] Hall, A. R.;Scott, A.;Rotem, D.;Mehta, K. K.;Bayley, H.; Dekker, C. Hybrid pore formation by directed insertion of alpha-haemolysin into solid-state nanopores. *Nat Nanotechnol* **2010**, *5*, 874-877.

[122] Yusko, E. C.;Prangkio, P.;Sept, D.;Rollings, R. C.;Li, J.; Mayer, M. Single-particle characterization of Abeta oligomers in solution. *ACS Nano* **2012**, *6*, 5909-5919.

[123] Mussi, V.;Fanzio, P.;Repetto, L.;Firpo, G.;Stigliani, S.;Tonini, G. P.; Valbusa, U. "DNA-Dressed NAnopore" for complementary sequence detection. *Biosensors and Bioelectronics* **2011**, *29*, 125-131.

[124] Kowalczyk, S. W.;Kapinos, L.;Blosser, T. R.;Magalhaes, T.;van Nies, P.;Lim, R. Y.; Dekker, C. Single-molecule transport across an individual biomimetic nuclear pore complex. *Nat Nanotechnol* **2011**, *6*, 433-438.

[125] Iqbal, S. M.;Akin, D.; Bashir, R. Solid-state nanopore channels with DNA selectivity. *Nat Nanotechnol* **2007**, *2*, 243-248.

[126] Yusko, E. C.;Johnson, J. M.;Majd, S.;Prangkio, P.;Rollings, R. C.;Li, J.;Yang, J.; Mayer, M. Controlling protein translocation through nanopores with bio-inspired fluid walls. *Nat Nanotechnol* **2011**, *6*, 253-260.

[127] Sze, J. Y. Y.;Ivanov, A. P.;Cass, A. E. G.; Edel, J. B. Single molecule multiplexed nanopore protein screening in human serum using aptamer modified DNA carriers. *Nat Commun* **2017**, *8*, 1552.

[128] Plesa, C.;Ruitenberg, J. W.;Witteveen, M. J.; Dekker, C. Detection of Individual Proteins Bound along DNA Using Solid-State Nanopores. *Nano Lett* **2015**, *15*, 3153-3158.

[129] Bell, N. A.; Keyser, U. F. Specific protein detection using designed DNA carriers and nanopores. *J Am Chem Soc* **2015**, *137*, 2035-2041.

[130] Cai, S.;Ren, R.;He, J.;Wang, X.;Zhang, Z.;Luo, Z.;Tan, W.;Korchev, Y.;Edel, J. B.; Ivanov, A. P. Selective Single-Molecule Nanopore Detection of mpox A29 Protein Directly in Biofluids. *Nano Lett* **2023**, *23*, 11438-11446.

[131] Liu, Y.;Wang, X.;Campolo, G.;Teng, X.;Ying, L.;Edel, J. B.; Ivanov, A. P. Single-Molecule Detection of alpha-Synuclein Oligomers in Parkinson's Disease Patients Using Nanopores. *ACS Nano* **2023**, *17*, 22999-23009.

[132] Ren, R.;Cai, S.;Fang, X.;Wang, X.;Zhang, Z.;Damiani, M.;Hudlerova, C.;Rosa, A.;Hope, J.;Cook, N. J.;Gorelkin, P.;Erofeev, A.;Novak, P.;Badhan, A.;Crone, M.;Freemont, P.;Taylor, G. P.;Tang, L.;Edwards, C.;Shevchuk, A.;Cherepanov, P.;Luo, Z.;Tan, W.;Korchev, Y.;Ivanov, A. P.; Edel, J. B. Multiplexed detection of viral antigen and RNA using nanopore sensing and encoded molecular probes. *Nat Commun* **2023**, *14*, 7362.

[133] Ren, R.;Sun, M.;Goel, P.;Cai, S.;Kotov, N. A.;Kuang, H.;Xu, C.;Ivanov, A. P.; Edel, J. B. Single-Molecule Binding Assay Using Nanopores and Dimeric NP Conjugates. *Adv Mater* **2021**, *33*, e2103067.

[134] Rothemund, P. W. Folding DNA to create nanoscale shapes and patterns. *Nature* **2006**, *440*, 297-302.

[135] Seeman, N. C.; Sleiman, H. F. DNA nanotechnology. *Nature Reviews Materials* **2017**, *3*, 17068.

[136] Dey, S.;Fan, C.;Gothelf, K. V.;Li, J.;Lin, C.;Liu, L.;Liu, N.;Nijenhuis, M. A. D.;Saccà, B.;Simmel, F. C.;Yan, H.; Zhan, P. DNA origami. *Nature Reviews Methods Primers* **2021**, *1*, 13.

[137] Johnson, J. A.;Dehankar, A.;Winter, J. O.; Castro, C. E. Reciprocal Control of Hierarchical DNA Origami-Nanoparticle Assemblies. *Nano Lett* **2019**, *19*, 8469-8475.

[138] Kuzyk, A.;Schreiber, R.;Zhang, H.;Govorov, A. O.;Liedl, T.; Liu, N. Reconfigurable 3D plasmonic metamolecules. *Nat Mater* **2014**, *13*, 862-866.

[139] He, Z.;Shi, K.;Li, J.; Chao, J. Self-assembly of DNA origami for nanofabrication, biosensing, drug delivery, and computational storage. *iScience* **2023**, *26*, 106638.

[140] Chandrasekaran, A. R.;Anderson, N.;Kizer, M.;Halvorsen, K.; Wang, X. Beyond the Fold: Emerging Biological Applications of DNA Origami. *Chembiochem* **2016**, *17*, 1081-1089.

[141] Nguyen, L.;Dass, M.;Ober, M. F.;Besteiro, L. V.;Wang, Z. M.;Nickel, B.;Govorov, A. O.;Liedl, T.; Heuer-Jungemann, A. Chiral Assembly of Gold-Silver Core-Shell Plasmonic Nanorods on DNA Origami with Strong Optical Activity. *ACS Nano* **2020**, *14*, 7454-7461.

[142] Wang, J.;Yue, L.;Li, Z.;Zhang, J.;Tian, H.; Willner, I. Active generation of nanoholes in DNA origami scaffolds for programmed catalysis in nanocavities. *Nat Commun* **2019**, *10*, 4963.

[143] Zhou, L.;Marras, A. E.;Su, H. J.; Castro, C. E. DNA origami compliant nanostructures with tunable mechanical properties. *ACS Nano* **2014**, *8*, 27-34.

[144] Kuzuya, A.;Sakai, Y.;Yamazaki, T.;Xu, Y.; Komiyama, M. Nanomechanical DNA origami 'single-molecule beacons' directly imaged by atomic force microscopy. *Nat Commun* **2011**, *2*, 449.

[145] Steinhauer, C.;Jungmann, R.;Sobey, T. L.;Simmel, F. C.; Tinnefeld, P. DNA origami as a nanoscopic ruler for super-resolution microscopy. *Angew Chem Int Ed Engl* **2009**, *48*, 8870-8873.

[146] Wei, R.;Martin, T. G.;Rant, U.; Dietz, H. DNA origami gatekeepers for solid-state nanopores. *Angew Chem Int Ed Engl* **2012**, *51*, 4864-4867.

[147] Hernandez-Ainsa, S.;Bell, N. A.;Thacker, V. V.;Gopfrich, K.;Misiunas, K.;Fuentes-Perez, M. E.;Moreno-Herrero, F.; Keyser, U. F. DNA origami nanopores for controlling DNA translocation. *ACS Nano* **2013**, *7*, 6024-6030.

[148] Joty, K.;Ghimire, M. L.;Kahn, J. S.;Lee, S.;Alexandrakis, G.; Kim, M. J. DNA Origami Incorporated into Solid-State Nanopores Enables Enhanced Sensitivity for Precise Analysis of Protein Translocations. *Anal Chem* **2024**, *96*, 17496-17505.

[149] Bell, N. A.;Engst, C. R.;Ablay, M.;Divitini, G.;Ducati, C.;Liedl, T.; Keyser, U. F. DNA origami nanopores. *Nano Lett* **2012**, *12*, 512-517.

[150] Gopfrich, K.;Li, C. Y.;Ricci, M.;Bhamidimarri, S. P.;Yoo, J.;Gyenes, B.;Ohmann, A.;Winterhalter, M.;Aksimentiev, A.; Keyser, U. F. Large-Conductance Transmembrane Porin Made from DNA Origami. *ACS Nano* **2016**, *10*, 8207-8214.

[151] Langecker, M.;Arnaut, V.;Martin, T. G.;List, J.;Renner, S.;Mayer, M.;Dietz, H.; Simmel, F. C. Synthetic lipid membrane channels formed by designed DNA nanostructures. *Science* **2012**, *338*, 932-936.

[152] Burns, J. R.;Gopfrich, K.;Wood, J. W.;Thacker, V. V.;Stulz, E.;Keyser, U. F.; Howorka, S. Lipid-bilayer-spanning DNA nanopores with a bifunctional porphyrin anchor. *Angew Chem Int Ed Engl* **2013**, *52*, 12069-12072.

[153] Burns, J. R.;Stulz, E.; Howorka, S. Self-assembled DNA nanopores that span lipid bilayers. *Nano Lett* **2013**, *13*, 2351-2356.

[154] Yang, J.;Wang, J.;Liu, X.;Chen, Y.;Liang, Y.;Wang, Q.;Jiang, S.; Zhang, C. Translocation of Proteins through Solid-State Nanopores Using DNA Polyhedral Carriers. *Small* **2023**, *19*, e2303715.

[155] Ketterer, P.;Ananth, A. N.;Laman Trip, D. S.;Mishra, A.;Bertosin, E.;Ganji, M.;van der Torre, J.;Onck, P.;Dietz, H.; Dekker, C. DNA origami scaffold for studying intrinsically disordered proteins of the nuclear pore complex. *Nat Commun* **2018**, *9*, 902.

[156] Raveendran, M.;Lee, A. J.;Sharma, R.;Walti, C.; Actis, P. Rational design of DNA nanostructures for single molecule biosensing. *Nat Commun* **2020**, *11*, 4384.

[157] Ding, T.;Yang, J.;Wang, J.;Pan, V.;Lu, Z.;Ke, Y.; Zhang, C. Shaped DNA origami carrier nanopore translocation influenced by aptamer based surface modification. *Biosens Bioelectron* **2022**, *195*, 113658.

[158] Plesa, C.;Verschueren, D.;Pud, S.;van der Torre, J.;Ruitenberg, J. W.;Witteveen, M. J.;Jonsson, M. P.;Grosberg, A. Y.;Rabin, Y.; Dekker, C. Direct observation of DNA knots using a solid-state nanopore. *Nat Nanotechnol* **2016**, *11*, 1093-1097.

[159] Kumar Sharma, R.;Agrawal, I.;Dai, L.;Doyle, P. S.; Garaj, S. Complex DNA knots detected with a nanopore sensor. *Nat Commun* **2019**, *10*, 4473.

[160] Yang, J.;Zhao, N.;Liang, Y.;Lu, Z.; Zhang, C. Structure-flexible DNA origami translocation through a solid-state nanopore. *RSC Adv* **2021**, *11*, 23471-23476.

[161] Zhu, J.;Tivony, R.;Boskovic, F.;Pereira-Dias, J.;Sandler, S. E.;Baker, S.; Keyser, U. F. Multiplexed Nanopore-Based Nucleic Acid Sensing and Bacterial Identification Using DNA Dumbbell Nanoswitches. *J Am Chem Soc* **2023**, *145*, 12115-12123.

Chapter 2 Methodology

Synopsis

This chapter provides a comprehensive overview of the research methodology. It begins with the fabrication and characterisation of nanopores, detailing the materials and processes involved. Next, it discusses nanopore translocation experiments, including the experimental setup and conditions used to study molecule dynamics. The chapter also describes the fabrication of DNA-based molecular carriers, focusing on their design principles and assembly methods. Finally, it outlines the data analysis techniques, such as signal processing and statistical methods, employed to interpret the experimental results.

Chapter 2 Methodology.....77

2.1 Nanopore Fabrication and Characterisation.....79

2.1.1 Nanopipette.....79

2.1.1.1 Nanopipette Fabrication.....79

2.1.1.2 Nanopipette Characterisation.....81

2.1.3 CBD Nanopore.....83

2.2 Nanopore Translocation Experiment.....86

2.2.1 Ag/AgCl Electrode.....86

2.2.2 Buffer Solution.....87

2.2.3 Translocation Setup and Ionic Current Measurement.....88

2.3 DNA-based Carrier Preparation.....90

2.3.1 dsDNA Carrier.....90

2.3.2 DNA Origami Hinge.....92

2.4 Data Analysis.....93

2.4.1 Binding Analysis.....99

2.4.1.1 Fractional Subpeak Position Threshold.....100

2.4.1.2 Peak Current Threshold.....101

2.5 References.....101

2.1 Nanopore Fabrication and Characterisation

2.1.1 Nanopipette

2.1.1.1 Nanopipette Fabrication

The nanopores used in the translocation experiments in Chapters 3, 4, and 5 were nanopipettes. These nanopipettes were fabricated from quartz capillaries (QF100-50-7.5, Sutter Instrument, USA) as the precursor material, with an outer diameter of 1.00 mm, an inner diameter of 0.50 mm, and an overall length of 7.5 cm. Quartz capillaries were selected as they are the strongest among the common formulations. The inner surface of the capillaries was annealed using a filament to facilitate easier liquid injection and to prevent microbubble formation.

The nanopipettes were fabricated using the laser-assisted pulling method. Before pulling, quartz capillaries were cleaned in a plasma cleaner (Harrick Plasma) for at least 30 minutes to remove surface contaminants thoroughly. The laser-based pipette puller (P-2000, Sutter Instrument, USA) was switched on 20 minutes beforehand. The cleaned capillaries were then gently placed into the puller, and the nanopipettes were pulled by applying the two-line pulling protocol, as shown in **Figure 2.1**. Only one capillary can be loaded into the puller at a time. The capillary was first heated with a CO_2 laser source and gently pulled to form a sandglass-shaped area in the middle. It was then further heated and pulled to produce two nanopipettes. A nano-scaled pore was formed at the tip of each nanopipette.

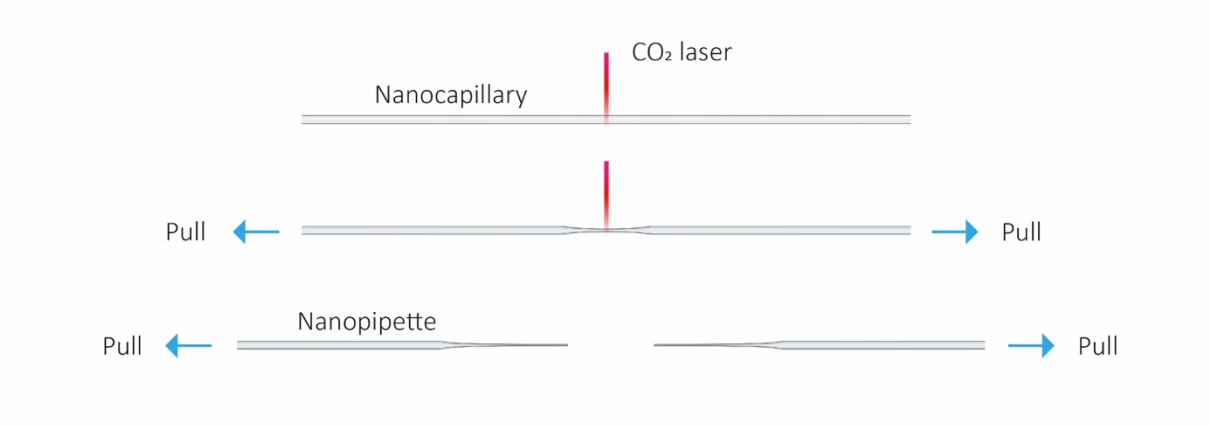


Figure 2.1 Schematic of the fabrication of nanopipettes from capillaries using laser assisted pulling method by two-line protocol.

The geometry of the nanopore, including its diameter, length, and shape, depends on the specific protocol used. In this study, two-line protocols were employed to produce nanopipettes with pore diameters as small as tens of nanometres. Two different pulling protocols were utilised, and their parameters are listed in **Table 2.1**. The **HEAT** parameter affects the tip size and length; higher heat generally results in longer and finer tips. The **FIL** (filament) parameter determines the scanning pattern of the laser beam. The **VEL** (velocity) parameter indicates the speed during the weak pull and determines the point at which the heat is turned off. In our study, the filament and velocity parameters were fixed and less critical. The **DEL** (delay) parameter represents the timing between the hard pull and the heat being turned off. A longer delay typically results in cooler glass, leading to shorter tips. The **PUL** (pull or hard pull) parameter refers to the strength applied to pull the capillaries, with greater strength generally producing smaller tips.

Table 2.1 Parameters for two-line protocols used for nanopipette fabrication.

Protocol	Line	HEAT	FIL	VEL	DEL	PUL	Pore Diameter (nm)
1	1	825	4	30	130	80	15

	2	850	3	20	127	185	
2	1	800	4	30	160	90	22
	2	825	3	20	135	180	

In our experiments, Protocol 1 yielded nanopipettes with finer and longer tips compared to Protocol 2. These nanopipettes were subsequently used in nanopore studies involving different types of biomolecules. It is noteworthy that the effectiveness of the same protocol can vary significantly across different pullers, and environmental factors such as humidity and temperature also influence the fabrication process. The reproducibility of the pulling time can serve as a straightforward criterion for assessing the consistency of nanopipettes.

2.1.1.2 Nanopipette Characterisation

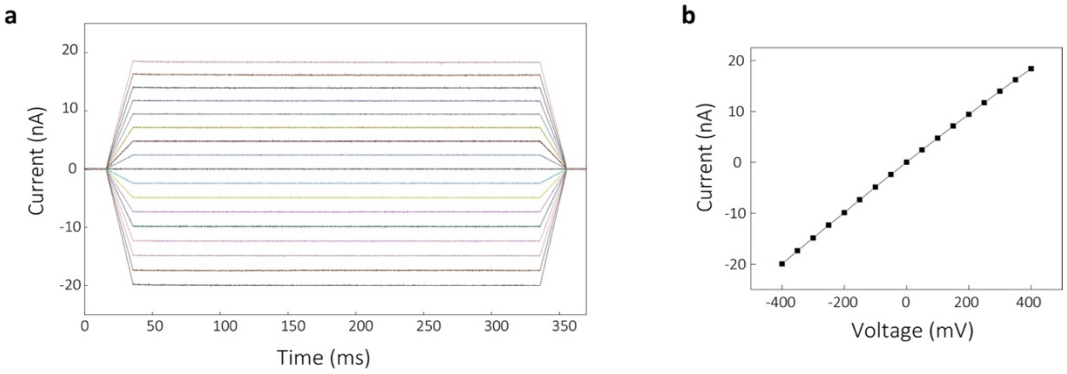


Figure 2.2 I-V characterisation of a nanopipette. **a.** I-t measurement of the nanopipette under the voltage of ±400 mV in 1M KCl buffer solution. **b.** I-V curve of the nanopipette.

Nanopipettes were characterised using both electrochemical and optical methods. Electrochemical characterisation was conducted by measuring current-voltage (I-V) curves using an AxoPatch 700B Multiclamp amplifier (Molecular Devices, US) and a Digidata 1550B digitizer (Molecular Devices, US). The I-V measurements were performed in the buffer solution employed for subsequent molecular translocation experiments. **Figure 2.1** illustrates a representative I-V characterisation of a nanopipette fabricated using Protocol 2 in a buffer solution containing 1M KCl, 12.5 mM $MgCl_2$, 10 mM Tris, 1 mM EDTA, pH 8. Voltages

ranging from +400 mV to -400 mV were applied in 50 mV increments, and the ionic current was measured for 300 ms at each voltage. The average currents obtained at each voltage were plotted to generate the I-V curve.

The I-V curve exhibits a linear region (±100 mV) that adheres to Ohm's law. This ohmic region can be utilised to calculate the conductance of the nanopore, which is directly related to the nanopore geometry, as described by **Equation 2.1**:

$$G = \frac{1}{R} = \frac{\Delta I}{\Delta V} \qquad 2.1$$

where G is conductance of the nanopore, R is the resistance of the nanopore, ΔI denotes the current variation within the ohmic region, and ΔV represents the voltage variation across the ohmic region.

By approximating the nanopipette as truncated hollow cone, the conductance calculated from the I-V measurements can be used to estimate the nanopore size based on **Equation 2.2** [1]:

$$1/G = \frac{1}{\sigma\pi r_i \tan\beta} + R_{\text{access}} \approx \frac{1}{\sigma\pi r_i \tan\beta} + \frac{1}{4\sigma r_i} \qquad 2.2$$

where G is the conductance of the nanopore, σ is the conductivity of the solution, r_i is the inner radius of the nanopipette, and β is the inner half-cone angle of nanopipette.

Optical characterisation of the nanopipettes was conducted using scanning electron microscopy (SEM) (Leo Gemini 1525, Carl Zeiss AG, Germany). Prior to imaging, the nanopipettes were sputter-coated with a 5 nm layer of chromium to enhance conductivity. The precise geometry and size of the nanopore were determined from high-resolution SEM images. The SEM characterisation of nanopipettes fabricated using Protocol 1 (**Figure 2.3**) and Protocol 2 (**Figure 2.4**) was performed by Dr Xiaoyi Wang of Imperial College London [2, 3].

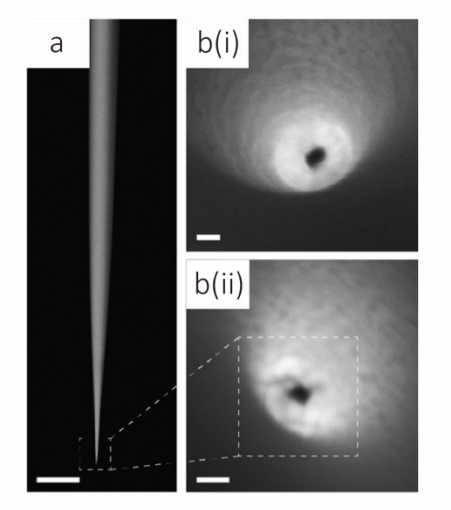


Figure 2.3 a. SEM image of the side view of a typical nanopipette fabricated by Protocol 1. (scale bar: 10 um) **b.** SEM image of the cross-section of the nanopipette. (scale bar: (i) 20 nm, (ii) 20 nm). The diameter of nanopipettes measured by SEM is 15 ± 3 nm (n = 5). Figure adapted and reprinted with permission from reference 2.

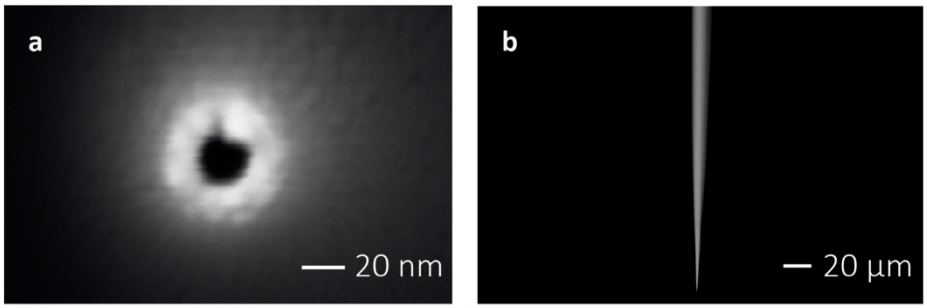


Figure 2.4 a. SEM image of the top view of a typical nanopipette fabricated by Protocol 2. **b.** SEM image of the side view of the nanopipette. The diameter of nanopipettes measured by SEM is 22 ± 3 nm (n = 5). Figure adapted and reprinted with permission from reference 3.

2.1.3 CBD Nanopore

CBD nanopores were utilised in **Chapter 6**, where a nanopore was drilled into a SiN_x membrane/chip using the CBD technique. The SiNx chips used in this study were prepared by Prof. Joshua Edel (Imperial College London), Dr Aleksandar Ivanov (Imperial College London), and Dr Binoy Paulose Nadappuram (University of Strathclyde) at Oak Ridge National

Laboratory, USA. The schematic of the SiN_x chip structure is shown in **Figure 2.5**. A SiN_x membrane (20 nm thick) was deposited on a multilayer of Si (360 µm) and SiO_2 (513 nm). The exposed area of the SiN_x membrane serves as a window for subsequent CBD drilling. The Si layer prevents charge transfer from the electrolyte to uncovered SiN_x layer, which increases the leakage current during the drilling process. The additional SiO_2 layers is used to eliminate device capacitance and contributes to noise reduction [4, 5].

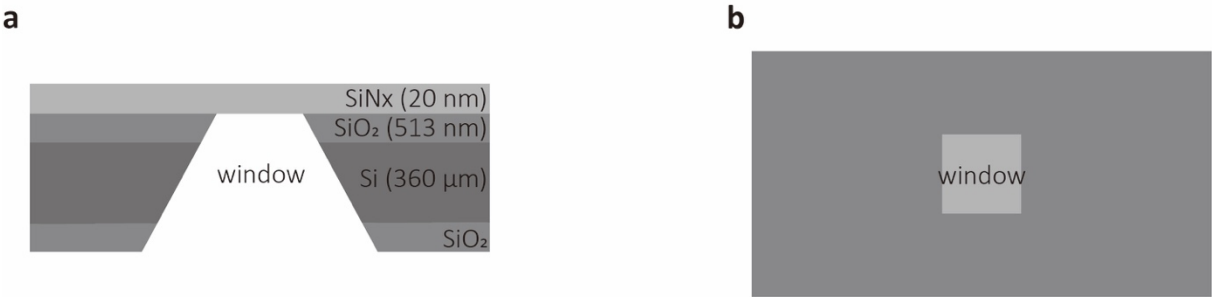


Figure 2.5 Schematic representation of the SiN_x chip structure. **a.** Lateral view of the multilayered chip. **b.** Vertical view of the chip, showing a thinner window exposed at the centre of the chip.

The refractive index of the chips has variation from batch to batch but typically ranges from 2.15 to 2.2, as measured by ellipsometry. The refractive index can be used to estimate the stoichiometry of the chip, as described in **Equation 2.3** [6]:

$$Si{:}N = \frac{3n + 3n_{\infty} - 6n_{3/4}}{4n_{\infty} - 4n} \qquad 2.3$$

where n_{∞} is the refractive index of pure Si (n_{∞} = 3.86), $n_{3/4}$ is the refractive index of Si_3N_4 ($n_{3/4}$ = 1.99), and n represents the measured refractive index of the SiN_x chip. The stoichiometry parameter x of our chips was calculated to range from 0.89 to 0.94.

A cleansing step was performed to remove contaminants from the chip surface prior to the CBD process. Chips were treated with hot piranha solution for 15 min if they had not been used for an extended period. Otherwise, they were cleaned using UV-ozone treatment, with each side exposed for 15 min. Next, the chip was carefully transferred into a Teflon fluidic cell (Nanopore

Solution Ltd., UK) using carbon-coated PEEK tip tweezers (Agar Scientific, UK). Both chambers of the fluidic cell were filled with a buffer solution containing 1 M KCl, 10 mM Tris, 1EDTA, pH 8. The cell was connected via Ag/AgCl electrodes to a Keithley 2450 Source Meter (Keithley Instruments, USA), which provided the voltage bias and measured the current. A Python-based protocol developed by Dr Jasper Fried (University of New South Wales) was utilised to control and monitor the CBD process. For the CBD process, a voltage ramp was applied, generating an electric field within the range of 0.6–1.6 V/nm across the membrane. A current threshold was set in advance; when the breakdown occurred, the leakage current increased dramatically and reached the threshold value, triggering an automatic stop to the process once the pore was formed. I-V measurements within the range of ±400 mV were performed before and after the CBD process to verify pore formation.

A subsequent pore expansion process was performed to enlarge the pore to the desired size, as a sub-2 nm pore is typically formed during the CBD process. The electrolyte in the chambers was replaced with a solution containing 3.6 M LiCl, 10 mM Tris, 1 mM EDTA, pH 8. Voltage pulse cycles were applied to the pore, and a current threshold at ±100 mV was set in advance to ensure the pore expanded to the required size. Positive and negative voltages were applied alternately, with each voltage pulse lasting 0.5 seconds. A current check step at ±100 mV, lasting 0.2 seconds, followed each voltage pulse. The pore size can be estimated based on **Equation 2.4** [7]:

$$G = \sigma \left[\frac{4l}{\pi d^2} + \frac{1}{l} \right]^{-1} \qquad 2.4$$

where G is the conductance, σ represents the conductivity of the electrolyte, l and d denote the length and diameter of the pore, respectively. It is noteworthy that this equation is based on the theoretical assumption of a cylindric and symmetric pore geometry.

After pore formation and expansion, the electrolyte in the chambers was rinsed and replaced with deionised water for subsequent translocation experiments.

2.2 Nanopore Translocation Experiment

2.2.1 Ag/AgCl Electrode

Ag/AgCl electrodes were utilised in all electrochemical experiments in this study. These electrodes offer significant advantages, including ease of fabrication, chemical stability, superior electrical conductivity, and non-polarizable properties [8]. Ag wires (Goodfellow Cambridge, UK) with diameters of 0.125 mm and 0.25 mm were used to fabricate Ag/AgCl electrodes through electrochemical deposition. The 0.125 mm wires were employed for nanopore translocation experiments, while the 0.25 mm wires were used in the CBD process. Ag/AgCl wires were chosen due to their suitability for nano-scale electrochemical experiments, as their size is appropriate, and they exhibit negligible polarisation under microcurrent conditions [9].

The electrochemical deposition was performed using a CHI 760 C potentiostat (CH Instruments). The experimental setup is illustrated in **Figure 2.6**. Ag wires were connected to the potentiostat and partially immersed in a 1 M KCl solution. A bias of 2 V was applied for at least 2 minutes. The Ag wire at the anode was coated with a charcoal-coloured Ag/AgCl layer, while H_2 bubbles were observed on the Ag wire at the cathode during the bias applied. Ag/AgCl electrodes were rinsed with deionised water after the deposition process and after each nanopore translocation experiment if they were awaiting reuse.

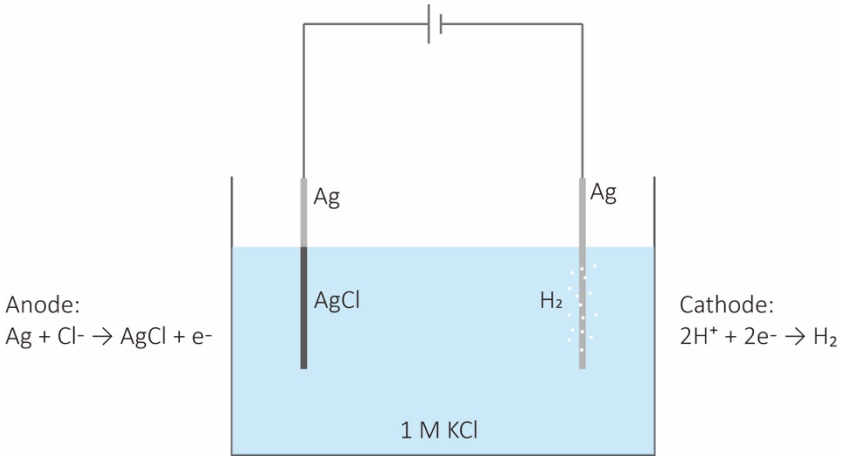


Figure 2.6 The setup of Ag/AgCl electrode preparation.

2.2.2 Buffer Solution

Nanopore translocation experiments require different buffer solutions, depending on the analyte species and nanopore geometry. The buffer solutions used in this study primarily contained KCl (Sigma-Aldrich), LiCl (Sigma-Aldrich), Tris-EDTA buffer (Sigma-Aldrich), $MgCl_2$ (Sigma-Aldrich), and nuclease-free water (Sigma-Aldrich). Before the translocation, binding and CBD experiments, the buffer solutions were filtered using a 0.2 μm syringe filter (VWR International). The pH and conductivity σ of the buffer solutions were measured using a pH/ion/conductivity meter (Mettler-Toledo, UK). More detailed information about the buffer solutions is provided in **Table 2.2**:

Table 2.2 Buffer solutions.

Buffer Name	Ingredients	Chapter
Translocation 1	2 M LiCl, 5 mM $MgCl_2$, 10 mM Tris, 1 mM EDTA, pH = 8	3, 6
Translocation 2	1.5 M LiCl, 5 mM $MgCl_2$, 10 mM Tris, 1 mM EDTA, pH = 8	3
Translocation 3	1M KCl, 12.5 mM $MgCl_2$, 10 mM Tris, 1 mM EDTA, pH = 8	4, 5, 6
Translocation 4	1 M KCl, 5 mM $MgCl_2$, 10 mM Tris, 1 mM EDTA, pH = 8	6
Binding 1	5 mM Mg Cl_2, 10 mM Tris, 1 mM EDTA, pH = 8	3, 6
Binding 2	12.5 mM $MgCl_2$, 5 mM Tris, 0.5 mM EDTA, pH = 8	4, 5

CBD 1	1M KCl, 10 mM Tris, 1 mM EDTA, pH = 8, σ = 10.8 S/m	6
CBD 2	3.6 M LiCl, 10 mM Tris, 1 mM 1 mM EDTA, pH = 8, σ = 15.9 S/m	6

2.2.3 Translocation Setup and Ionic Current Measurement

The setup for the nanopore translocation experiments consists of an amplifier, which serves as the voltage supplier for the nanopore sensing platform and is connected to external ionic current recording software. (**Figure 2.7**). Two amplifiers were used in this research. An AxoPatch 700B Multiclamp amplifier (Molecular Devices, US) with a Digidata 1550B digitizer (Molecular Devices, US) was utilised for all nanopore I-V characterisation experiments and translocation experiments in **Chapter 6**. A Chimera VC100 amplifier (Chimera Instruments, UK) was employed for translocation experiments in Chapters 3, 4, and 5, as high-bandwidth measurements were required. The amplifiers were connected to additional devices to enhance signal processing and transmission. For example, a pre-amplifier headstage was connected to the AxoPatch Multiclamp amplifier to interface with the electrodes and measure currents below the nA level, and a DAQ device was used for data acquisition. Data filtration and recording were performed using a Clampex software (Molecular Devices, US) for the AxoPatch Multiclamp amplifier and a MATLAB-based graphical user interface (Chimera Instruments, UK) for the Chimera VC100 amplifier.

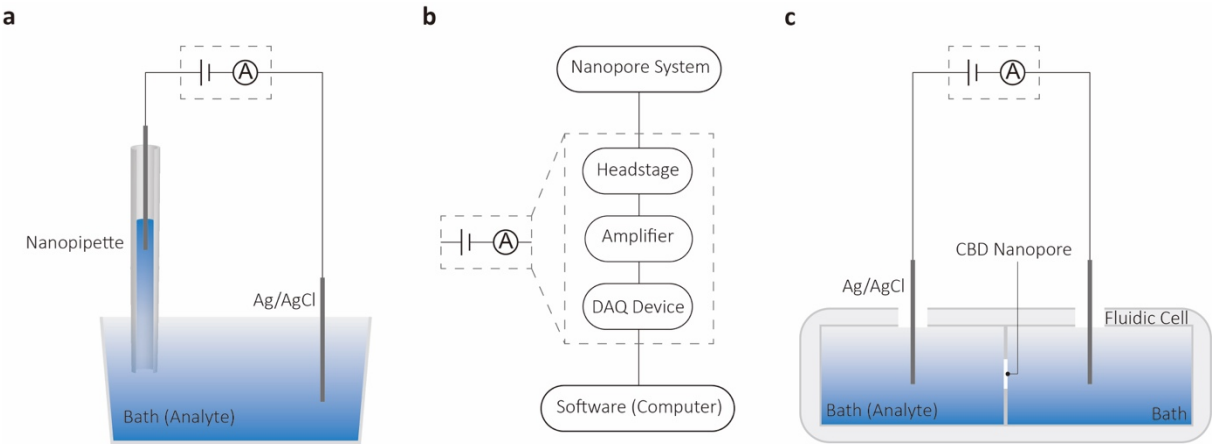


Figure 2.7 Schematic illustration of the nanopore translocation setup and ionic current measurement. **a.** Nanopipette translocation setup. **b.** Devices used in ionic current measurement. **c.** CBD nanopore translocation setup.

Analytes were introduced into the cis side (outside the nanopipette) and translocated through the nanopore to the trans side (inside the nanopipette) by applying a positive bias. This configuration was used for both nanopipette and CBD nanopore translocation experiments in this study.

For nanopipette translocation, the translocation buffer was loaded into the nanopipette using a Microfil needle (MF34G, World Precision Instruments, UK). Bubbles and microbubbles inside the nanopipette were removed by gently vibrating the pipette with tweezers or by reducing air pressure with a syringe. The bath, typically the lid of an Eppendorf tube, was filled with a translocation buffer containing analytes. One Ag/AgCl electrode was inserted into the buffer inside the nanopipette using tweezers, while the other was immersed in the bath solution. The Ag/AgCl electrodes were connected to the headstage to complete the current circuit.

For CBD nanopore translocation, pure translocation buffer was added to the cis chamber of the fluidic cell, while the trans chamber was filled with a translocation buffer containing analytes. Bubbles and microbubbles were eliminated by carefully pipetting the fluidic cell with a 200 µL pipette (Eppendorf Research). Ag/AgCl electrodes were immersed into both chambers and connected to the headstage.

2.3 DNA-based Carrier Preparation

2.3.1 dsDNA Carrier

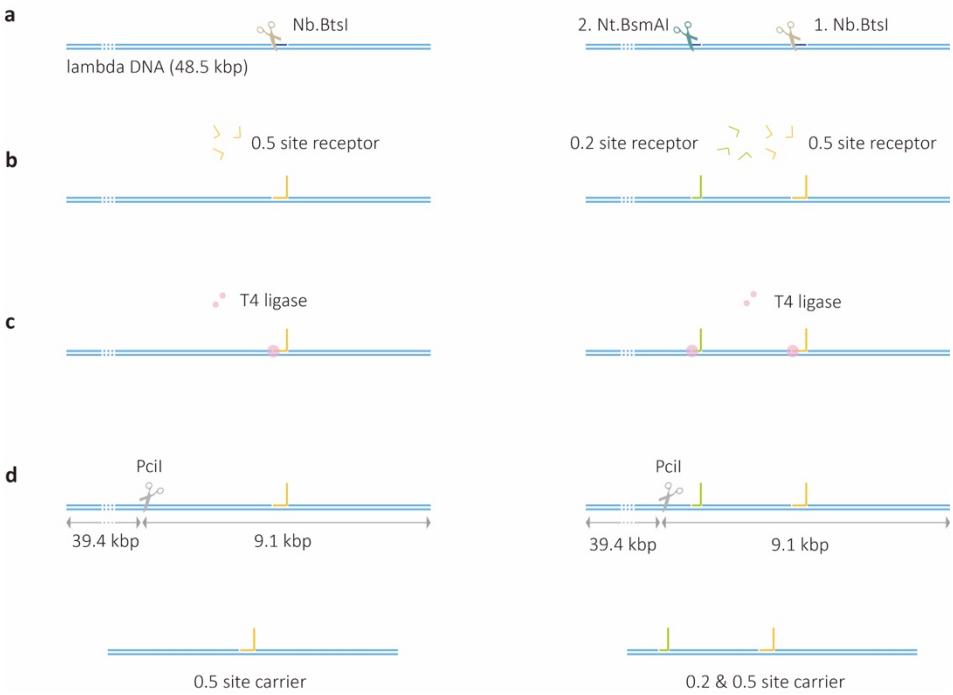


Figure 2.8 Schematic illustration of the 9.1 kbp dsDNA carrier. **a.** Nicking step to create single-stranded regions, the 0.5 site by Nb.BtsI and the 0.2 site by Nt.BsmAI. **b.** Hybridisation step of the receptor sequences with the single-stranded regions. **c.** T4 ligase step. **d.** Digestion step to excise the 9.1 kbp carrier from the lambda DNA.

A 9.1 kbp dsDNA molecular carrier was utilised in **Chapter 3**. The preparation of the 9.1 kbp dsDNA carrier was adapted from a strategy previously reported by our group [2], lambda DNA was used as the starting material and was sequentially treated with enzymes and functionalised with receptor sequences.

Figure 2.8 illustrates the preparation procedure of the 9.1 kbp dsDNA molecular carrier. First, 25 µL of lambda DNA (500 µg/mL, New England Biolabs) was mixed with 6.4 µL of Nb.BtsI (10

units/μL, New England Biolabs), 10 μL of 10× rCutSmart buffer (New England Biolabs), and additional nuclease-free water (Sigma-Aldrich) to achieve a total volume of 100 μL. The mixture was incubated at 37 °C for 60 min and then inactivated at 80 °C for 20 min, exposing a 45-base single-stranded region at the 0.5 site. To create an additional 32-base single-stranded region at the 0.2 site, 6.4 μL of Nt.BsmAI (10 units/μL, New England Biolabs) was added, and the mixture was incubated at 37 °C for 60 min, followed by inactivation at 80 °C for 20 min. 1 μL of receptor sequences (20 μM, 100x excess) was added to the mixture to displace and hybridize to the nicking sites using a hybridisation protocol: heating to 95 °C for 5 min, quenching to 15 °C at a rate of 1 °C/min, and holding at 4 °C. The receptor sequences (Integrated DNA Technologies, IDT) were ordered in tubes which is purified by standard desalting. 7.2 μL of T4 DNA ligase (400 units/μL, New England Biolabs) and 12 μL of T4 ligation buffer (New England Biolabs) were added to the mixture and incubated at 22 °C for 2 hours and inactivated at 65 °C for 15 min in the next ligation step. Finally, the product was mixed with 3.2 μL of PciI (10 units/ μL) and incubated at 37 °C for 1 hour and inactivated at 80 °C for 20 min to digest and excise the 9.1 kbp carrier from the lambda DNA. A TC-3000 thermal cycler (TECHNE) was employed for the above reactions.

The separation of the 9.1 kbp dsDNA from the DNA fragments was performed using gel electrophoresis. The reaction product was mixed with 40 μL of gel loading dye (Purple, 6×, New England Biolabs) and nuclease-free water (Sigma-Aldrich) to achieve a total volume of 240 μL. The prepared sample was loaded onto a 0.7% (w/v) agarose gel in 1× TBE buffer (Sigma-Aldrich). Gel electrophoresis was conducted at 5 V/cm for 100 min. The gel was then stained with 1× SYBR Safe (SYBR Safe DNA Gel Stain, Thermo Fisher) in 1× TBE buffer for at least 2 hours in the dark. The 9.1 kbp dsDNA carrier band was excised using a gel imaging LED light box (Biotium Inc.) and collected in an Eppendorf tube. The extraction of the carrier was performed using a gel extraction kit (T1020L, Monarch DNA Gel Extraction Kit, New England Biolabs). The concentration and purity of the 9.1 kbp dsDNA carrier were determined using a Nanodrop 2000c device (Thermo Scientific) by measuring UV-Vis absorbance from 220 nm to 350 nm. DNA purity was assessed using the A260/A280 and A260/A230 ratios, with expected values for pure DNA ranging from 1.80 to 2.00 for A260/A280 and from 2.00 to 2.20 for

A260/A230. The 9.1 kbp dsDNA carrier products were stored at -20 °C for subsequent experiments.

2.3.2 DNA Origami Hinge

A DNA origami hinge molecular carrier was used in Chapters 4 and 5. The DNA origami hinge sample was provided by our collaborator, Dr Joshua Johnson (Imperial College London), a former postdoctoral researcher in the Di Michele group. The three-dimensional DNA origami hinge nanostructure was designed using an open-source origami design software called caDNAno. The scaffold routing of the hinge is illustrated in **Figure 2.9**.

The preparation of the hinge is as follows: hinge staples were ordered in plates (Integrated DNA Technologies, IDT), purified by standard desalting and suspended in 10 mM Tris, 0.1 mM EDTA buffer. Fluorescently labelled oligos and latching overhangs (Integrated DNA Technologies, IDT) were ordered in tubes with HPLC purification. Hinges were self-assembled in folding reactions composed of 20 nM scaffold (8064 bp, Tilibit Nanosystems), 100 nM staples, 18 mM $MgCl_2$, 10 mM Tris, 1 mM EDTA buffer. The folding reactions were annealed from 65 °C to 25 °C over 16 hours and then cooled to 12 °C in a C1000 Touch Thermal Cycler (Bio-Rad Laboratories). Hinges folded in the extended state included 500 nM of each extender strand, while hinges folded in the closed state typically included 1.5 μM of each closer strands (3x excess for each closer overhang pair).

Hinges used in bulk fluorescence characterisation were purified via polyethylene glycol (PEG) precipitation. After annealing, a standard volume of 500 μL of hinge folding reaction was mixed in equal volumes with a solution of 15% (w%) 8000 kDa PEG (PEG8000, Sigma-Aldrich) with 500 mM NaCl. The mixture was briefly vortexed and centrifuged at 16000x *g* for at least 25 minutes. The supernatant was discarded, and the remaining pellet was resuspended in 5 mM Tris, 0.5 mM EDTA buffer with 12.5 mM $MgCl_2$. Hinges for nanopipette experiments were purified via gel electrophoresis. Hinge folding reactions were mixed with gel loading dye and

run through a 2% (w%) agarose gel typically at 80 V for 45 minutes. The leading band in the gel was excised and transferred to a Freeze 'N Squeeze™ DNA Gel Extraction Spin Column (Bio-Rad Laboratories) which was then centrifuged at 10000x *g* for 10 minutes. The concentration of hinge in the resulting effluent was quantified using a Nanodrop One (Thermo Scientific) and was typically 1-2 nM. For all nanopipette experiments, it was assumed that gel-purified hinges were at approximately 1.5 nM. After PEG or gel purification, the quality of the hinges was verified by imaging with an FEI Tecnai G2 spirit transmission electron microscopy (TEM) using either 2% (w%) uranyl formate or uranyl acetate stained formvar TEM grids.

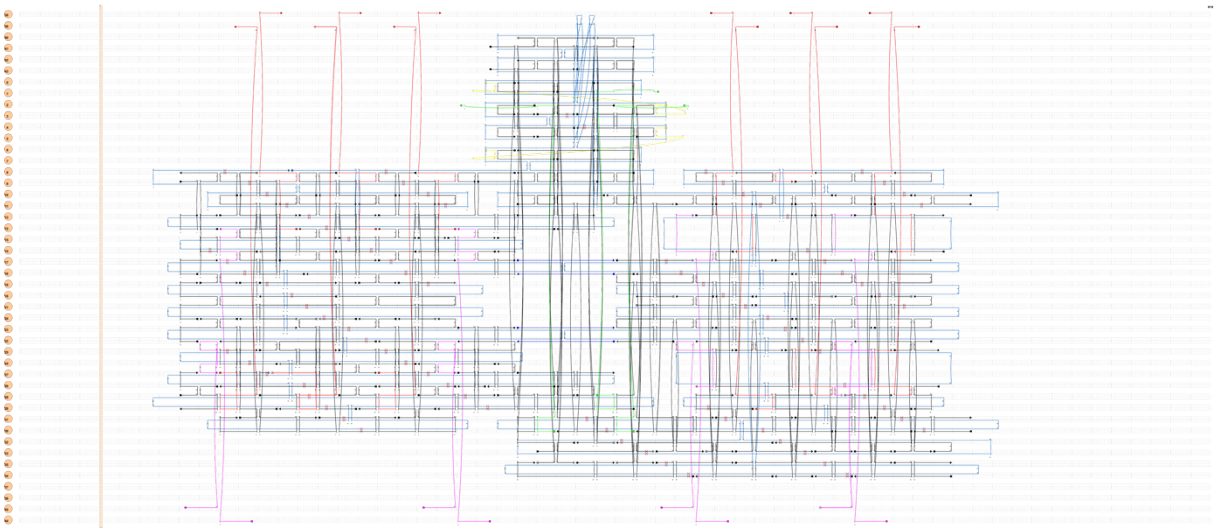


Figure 2.9 The caDNAno scaffold routing of the DNA origami hinge.

2.4 Data Analysis

Nanopore translocation data were processed using a custom MATLAB script named 'The Nanopore App,' developed by Prof. Joshua Edel (Imperial College London). Below, the procedure for data analysis using this MATLAB-based script is demonstrated with data collected from the nanopipette translocation of the 500 pM 9.1 kbp dsDNA carrier in a 2 M LiCl translocation buffer under 300 mV.

Step 1: Data loading and refiltering (**Figure 2.10**). Nanopore translocation data recorded in Axon Binary File format (abf.) by the AxoPatch Multiclamp amplifier with a pClamp 10.5 software or in Log File format (log.) by the Chimera amplifier were directly loaded into the app. Multiple files could be loaded simultaneously by selecting them from the same folder. However, loading multiple files with excessively large sizes may cause the software to stop or crash. A recorded trace was displayed after the data was loaded. An appropriate refiltering or resampling operation was then applied to the original trace to improve the signal-to-noise ratio for analysis. This step was necessary because the data were recorded at a high sampling rate to ensure data integrity and filtered using a relatively high low-pass Bessel filter to avoid over-filtering. For instance, the demonstration data were recorded at 4.16 MHz using the Chimera amplifier, and a 20 kHz low-pass filter was applied during the refiltering operation in the app.

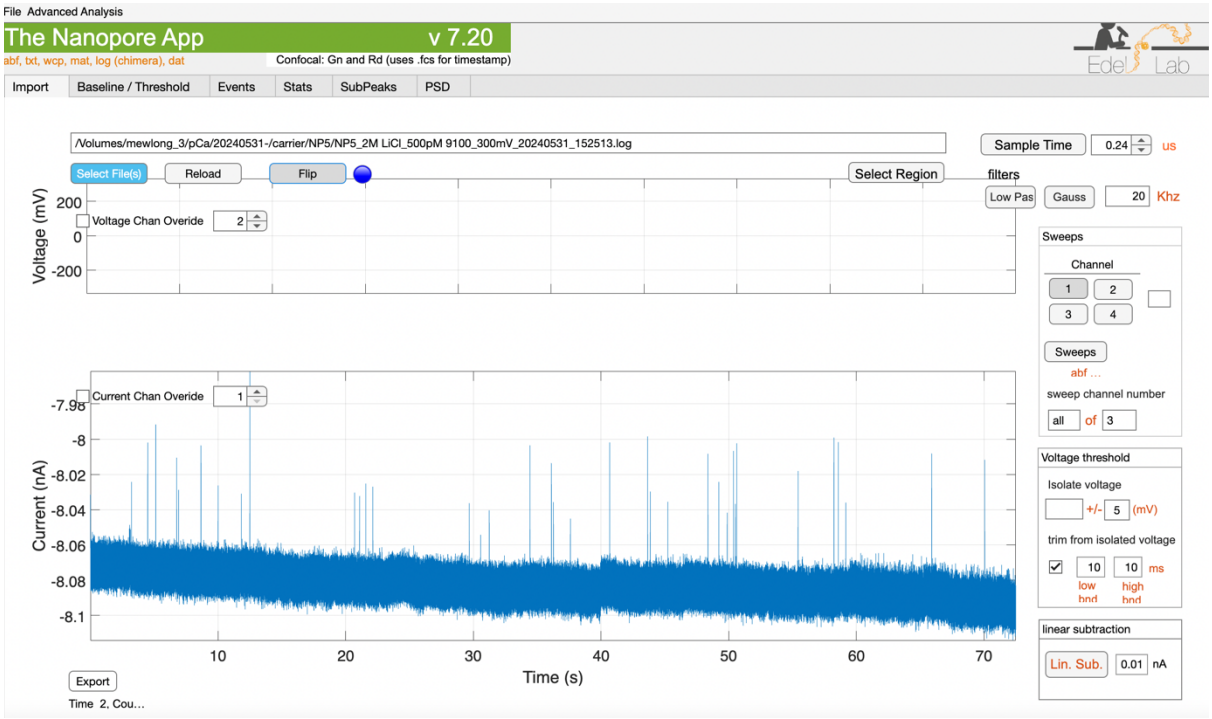


Figure 2.10 Data loading and refiltering in 'The Nanopore App'.

Step 2: Baseline tracking and threshold defining (**Figure 2.11**). The baseline of the trace was tracked using polynomial fitting to eliminate trace fluctuations and improve event classification. The parameters 'Step,' 'Poly-1,' and 'Poly-2' were adjusted to optimize the baseline fitting. 'Step'

represents the sampling rate used for baseline tracking, while 'Poly-1' and 'Poly-2' are the coefficients in the polynomial fitting. A higher 'Step' value means more sample points are used in the polynomial fitting, but this increases processing time. Decreasing 'Poly-1' and increasing 'Poly-2' are suitable for baseline tracking of a fluctuating trace. Balancing these parameters is essential for successful baseline tracking. The tracked baseline was displayed as a red line on the trace, and the trace was then corrected using an asymmetric least square smoothing algorithm.

An open-pore current histogram was generated and fitted using a Poisson distribution function, displayed as a red curve. Two thresholds, 'std' and 'SO,' were defined and used for subsequent peak identification. These thresholds were represented as a black line and a green line on the corrected trace figure, respectively. Current signals above the 'std' threshold were identified as events, while the 'SO' threshold was used set the cutoff to determine the start and end points of an event. In this example, 'SO' was set to the default value of 1.8 times the square of standard deviation above the mean open-pore current, and 'std' was adjusted to 9 times the standard deviation above the mean to avoid detecting noise.

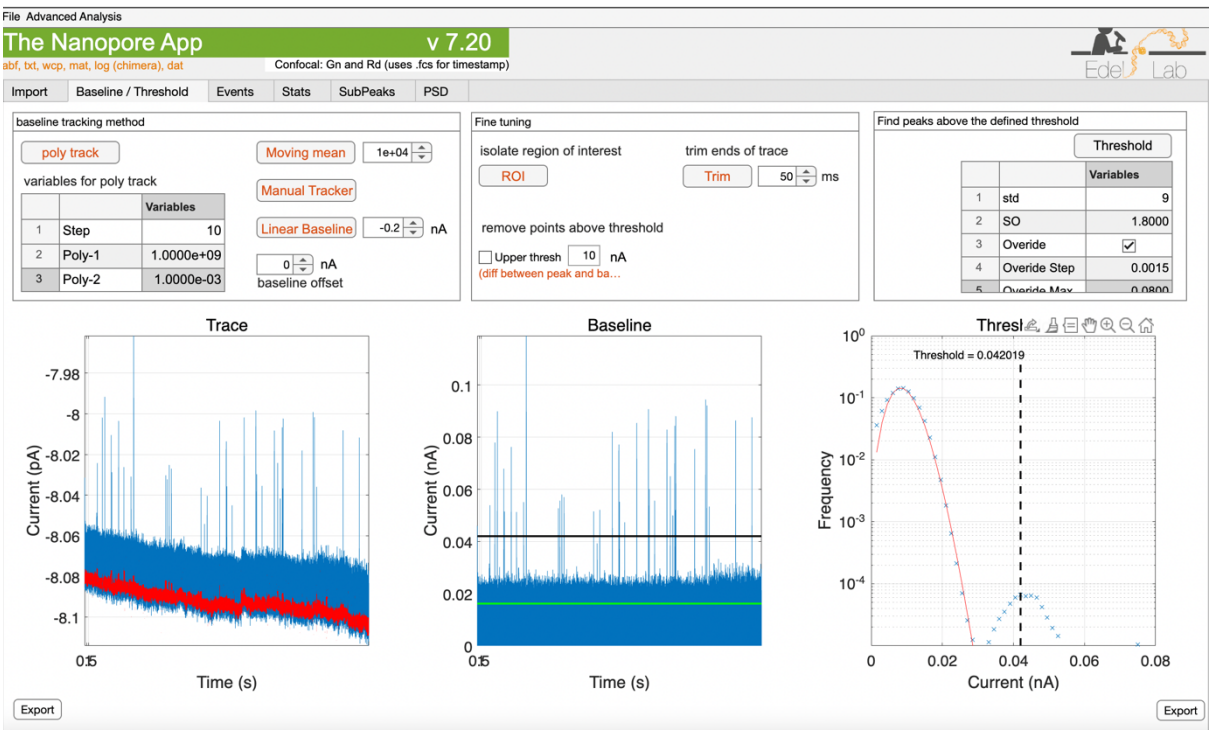


Figure 2.11 Baseline tracking and threshold defining in 'The Nanopore App'.



Figure 2.12 Peak finding in 'The Nanopore App'.

Step 3: Peak finding (**Figure 2.12**). Current peaks above the previously defined 'std' threshold were selected and identified as events. An additional 'thresholds' segment could be used to quickly select events of interest. Selected events were then refined using the CUSUM (cumulative sum) algorithm by adjusting specific parameters. The CUSUM fit was displayed as a dashed red line on the events. Parameters were adjusted to optimize event refinement. 'Approx delta' represents the detection level for a shift in the process mean. 'Sigma' is related to the noise level. 'Max levels' determines the maximum peak current levels. 'Min bin' defines the step size of the temporal axis. '+/- bin' is associated with the width of the selected time scale. 'Min dl' refers to the step size of the current axis. This algorithm is designed to detect current shifts between changepoints of segments with stationarity. Another algorithm, named ADEPT, could also be applied for event refinement. ADEPT is more suitable for short dwell-time events, such as sharp triangular-shaped nanoparticle translocation events. It is worth noting that the choice of algorithm is highly dependent on the specific data. In this study, only the CUSUM algorithm was employed.

Current level, translocation time, peak amplitude, peak area, and subpeak information were obtained and listed alongside each event. Events were manually checked, and poorly refined events or false positives were removed. The information from the processed events was then exported to the MATLAB workspace. Further data analysis and visualisation were performed using OriginPro and GraphPad Prism.

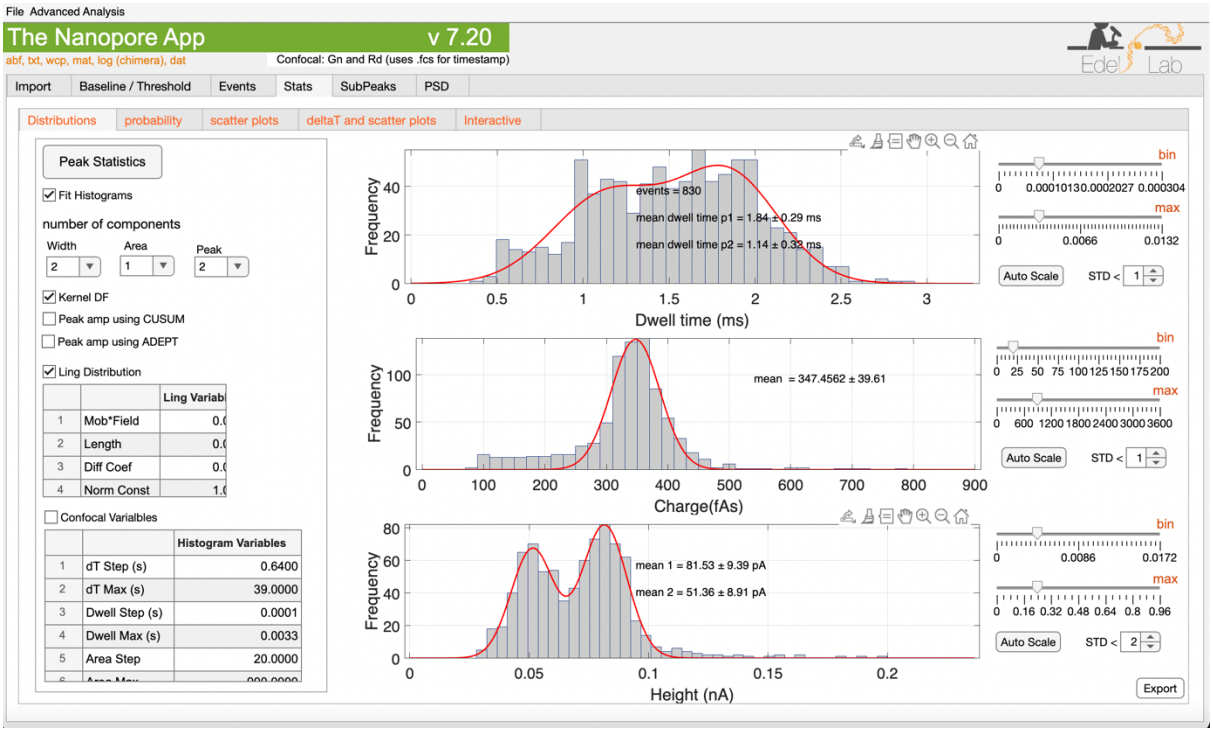


Figure 2.13 Peak statistics in 'The Nanopore App'.

Step 4: Peak Statistics (**Figure 2.13**). Processed data could be further statistically analysed using the app. In this step, statistics such as dwell time, peak current, and charge were processed and visualised in the form of histograms and scatterplots. The distribution of events was discerned from the plots as a preliminary observation. The distribution can be fitted using parametric probability distribution functions, such as Gaussian, lognormal (Ling), exponential and others. The mean and standard deviation values can subsequently be determined.

The frequency of the translocation, also known as capture rate, can also be determined in the app. The capture rate can be approximately estimated by counting the number of occurrences over a sufficiently long time period, and is expressed as:

$$r = \frac{N}{T} \tag{2.5}$$

where r represents the capture rate, N denotes the number of events occurring within the time T. If the time interval ΔT is extremely short, the probability of detecting an event within ΔT can be expressed as $r\Delta T$. Consequently, the probability of no event occurring in ΔT is given by $1 - r\Delta T$. When the total observation period is divided into n intervals of ΔT such that $T = n\Delta T$, the probability of no events occurring within this period can be determined using the following equation:

$$P(T) \approx (1 - r\Delta T)^n \tag{2.6}$$

If the time is sufficiently long**, Equation 2.6** can be rewritten to:

$$P(T) \approx \lim_{n\to\infty}(1 - r\Delta T)^n = e^{-rt} \tag{2.7}$$

The probability $P_1(t)$ of observing an interval l of time length t between consecutive events is given by:

$$P_1(t)\,dt = P(T)r\,dt \tag{2.8}$$

Equation 2.7 and **Equation 2.8** can be combined and expressed as:

$$P_1(t) = re^{-rt} \tag{2.9}$$

The time intervals between events were automatically calculated by the app and plotted. By fitting the data using **Equation 2.9**, the capture rate was determined.

Step 5: Subpeak Statistics (**Figure 2.14**). Subpeak analysis was performed for nanopore translocation data relevant to the 9.1 kbp carrier. Events refined by the CUSUM algorithm were further analysed in this step. Information related to subpeaks, such as the number of subpeaks, subpeak location, subpeak width, and subpeak amplitude, was obtained. Additionally, thresholds were used to isolate events of interest. For example, subpeak amplitude and subpeak width were used to filter out folded dsDNA events, ensuring that only true positive events were displayed. A fractional peak location threshold was applied to isolate positive events at specific sites on the dsDNA carrier.

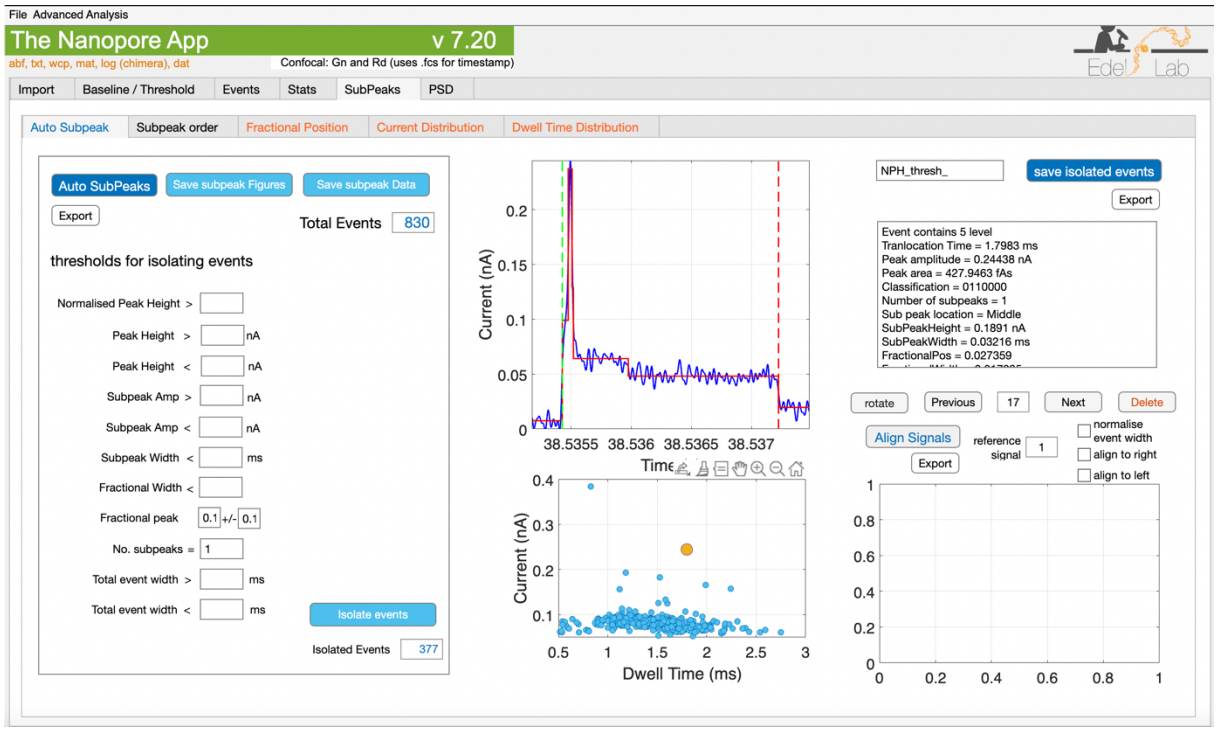


Figure 2.14 Subpeak Analysis in 'The Nanopore App'.

2.4.1 Binding Analysis

Binding (Positive) Analysis was systematically performed to assess the binding efficiency and conduct further quantitative analysis aimed at investigating the sensitivity and selectivity of our nanopore sensing platform. This analysis was based on event data extracted from the peak and subpeak statistics steps within 'The Nanopore App' data processing framework, reducing human error by relying on numerical-based data processing. Specifically, for the dsDNA carrier-based nanopore sensing platform described in **Chapter 3** and **Chapter 6**, the fractional subpeak position was adopted as the primary criterion for identifying positive events, providing a reliable method for distinguishing binding events. In contrast, for the DNA origami hinge carrier-based nanopore sensing platform discussed in **Chapter 4**, **Chapter 5**, and **Chapter 6**, the peak current or peak amplitude served as the defining criteria for detecting positive events, offering a distinct approach for event recognition in this system.

2.4.1.1 Fractional Subpeak Position Threshold

For the detection of miRNA-141-3p, the threshold for the normalised subpeak position was defined as 0.5 ± 0.2. This value closely aligns with the expected location of the miRNA-141-3p binding site, which was designed to correspond to a fractional position of 0.5, based on the molecular carrier sequence. Subpeak amplitude was not utilized for event discrimination due to the similarity in amplitude between folded DNA and streptavidin-bound events. The occurrence of DNA knots during translocation is rare, and therefore, all miRNA-bound events could be effectively isolated using the normalized peak position. To ensure accurate event counting, all folded events were manually cross-verified, as partial folding may cause a slight shift in the fractional position.

For the multiplexed detection of miRNA-7-5p and miRNA-382-5p, the thresholds for the normalized subpeak position were defined as 0.2 ± 0.1/0.8 ± 0.1 and 0.5 ± 0.2, respectively. The first threshold was chosen based on the fact that miRNA-7-5p binds to a fractional position of 0.2, near the end of the molecular carrier, with instances observed where both ends of the carrier entered the nanopore. The second threshold value closely corresponds to the expected binding

site of miRNA-382-5p, which was designed to align with a fractional position of 0.5. Notably, these threshold ranges for the two miRNAs do not overlap, effectively preventing crosstalk between their binding secondary peaks. Moreover, the likelihood of both miRNAs exhibiting secondary peaks simultaneously in a single event is minimal. To ensure accurate event counting, all folded events were manually cross-verified, as partial folding can result in slight shifts in the fractional position.

2.4.1.2 Peak Current Threshold

A sample-specific peak current threshold was implemented for the identification of positive events in the nanopore detection of miRNA-141-3p using the DNA origami hinge carrier. This threshold was chosen due to the distinct peak current differences between the closed hinge and the extended (reconfigured) hinge states. The rationale behind selecting this specific threshold value is detailed in **Chapter 5**. By setting this threshold, we are able to effectively identify positive events, even at low miRNA concentrations, while minimising standard errors. Furthermore, this approach helps reduce interference caused by hinges in the intermediate state, ensuring more accurate and reliable event detection.

2.5 References

[1] Perry, D.;Momotenko, D.;Lazenby, R. A.;Kang, M.; Unwin, P. R. Characterization of Nanopipettes. *Anal Chem* **2016**, *88*, 5523-5530.

[2] Ren, R.;Cai, S.;Fang, X.;Wang, X.;Zhang, Z.;Damiani, M.;Hudlerova, C.;Rosa, A.;Hope, J.;Cook, N. J.;Gorelkin, P.;Erofeev, A.;Novak, P.;Badhan, A.;Crone, M.;Freemont, P.;Taylor, G. P.;Tang, L.;Edwards, C.;Shevchuk, A.;Cherepanov, P.;Luo, Z.;Tan, W.;Korchev, Y.;Ivanov, A. P.; Edel, J. B. Multiplexed detection of viral antigen and RNA using nanopore sensing and encoded molecular probes. *Nat Commun* **2023**, *14*, 7362.

[3] Liu, Y.;Wang, X.;Campolo, G.;Teng, X.;Ying, L.;Edel, J. B.; Ivanov, A. P. Single-Molecule Detection of alpha-Synuclein Oligomers in Parkinson's Disease Patients Using Nanopores. *ACS Nano* **2023**, *17*, 22999-23009.

[4] Chien, C. C.;Shekar, S.;Niedzwiecki, D. J.;Shepard, K. L.; Drndic, M. Single-Stranded DNA Translocation Recordings through Solid-State Nanopores on Glass Chips at 10 MHz Measurement Bandwidth. *ACS Nano* **2019**, *13*, 10545-10554.

[5] Rosenstein, J. K.;Wanunu, M.;Merchant, C. A.;Drndic, M.; Shepard, K. L. Integrated nanopore sensing platform with sub-microsecond temporal resolution. *Nat Methods* **2012**, *9*, 487-492.

[6] Gilboa, T.;Zvuloni, E.;Zrehen, A.;Squires, A. H.; Meller, A. Automated, Ultra-Fast Laser-Drilling of Nanometer Scale Pores and Nanopore Arrays in Aqueous Solutions. *Advanced Functional Materials* **2019**, *30*.

[7] Kowalczyk, S. W.;Grosberg, A. Y.;Rabin, Y.; Dekker, C. Modeling the conductance and DNA blockade of solid-state nanopores. *Nanotechnology* **2011**, *22*, 315101.

[8] Wanunu, M. Nanopores: A journey towards DNA sequencing. *Phys Life Rev* **2012**, *9*, 125-158.

[9] Bentley, C. L.;Perry, D.; Unwin, P. R. Stability and Placement of Ag/AgCl Quasi-Reference Counter Electrodes in Confined Electrochemical Cells. *Anal Chem* **2018**, *90*, 7700-7707.

Chapter 3 Nanopore Detection of miRNA with dsDNA Carrier

Synopsis

This chapter explores a nanopore-based miRNA detection strategy utilising a functionalised dsDNA carrier and a sandwich complex approach. A dsDNA carrier was designed and functionalised to facilitate selective miRNA binding, with a streptavidin probe incorporated to enhance detection signals. The dsDNA carrier was characterised through electrophoretic and nanopore-based analyses. To optimise detection performance, various translocation buffer conditions were evaluated, and the detection of miRNA-141-3p was investigated both directly and in the presence of a dsDNA carrier. The study also extends to multiplexed detection of miRNA-7-5p and miRNA-382-5p, demonstrating the adaptability of this approach for detecting multiple targets. Additionally, miRNA incubation conditions were refined to enhance the binding ratio. These advances lay the groundwork for nanopore-based miRNA detection, with potential applications in biomedical diagnostics.

Chapter 3 Nanopore Detection of miRNA with dsDNA Carrier..... 103

3.1 Introduction 105

3.2 Methods 107

3.2.1 dsDNA Carrier Preparation 107

3.2.2 DNA Carrier–miRNA–Streptavidin Probe Complex Preparation 109

3.3 Results and Discussion 110

3.3.1 Nanopipette Characterisation 110

3.3.2 dsDNA Carrier Characterisation 111

3.3.2.1 Gel Electrophoresis 111

3.3.2.2 Nanopore Study of dsDNA Carrier 112

3.3.3 Detection of miRNA with dsDNA Carrier 113

3.3.3.1 Direct Detection of miRNA-141 114

3.3.3.2 Translocation Buffer Selection 114

3.3.3.3 Detection of miRNA-141 with dsDNA Carrier 116

3.3.3.4 Multiplexed Detection of miRNA-7 and miRNA-382 with dsDNA Carrier 118

3.3.3.5 miRNA Binding Optimisation 120

3.4 Conclusion 122

3.5 References 122

3.1 Introduction

miRNAs are a class of small, non-coding RNAs, typically averaging 22 nucleotides in length, that regulate gene expression at the post-transcriptional level [1, 2]. They play a critical role in organisms for several reasons: (1) miRNAs regulate protein expression by binding to mRNAs in a complementary manner, leading to mRNA degradation or translational repression [3, 4]; (2) miRNAs are closely associated with various diseases, including cancer, neurodegenerative disorders, and metabolic diseases such as diabetes, and are regarded as potential biomarkers and therapeutic targets [5-7]; and (3) miRNAs are evolutionarily conserved and play a crucial role in various biological processes [8, 9].

miRNAs have been widely applied in clinical research, with one of the most promising applications being their use for early diagnosis and prognostic assessment of cancer, cardiovascular diseases, and [10-12]. This is because miRNAs can be released from cells into bodily fluids and remain stable in biological environments such as blood, urine, and tissues. Commonly used miRNA quantification methods, including RT-qPCR [13, 14], northern blot [15, 16], microarray [17], and high-throughput small RNA sequencing [18], often require laborious sample pretreatment procedures, involve tedious data processing steps, or lack sufficient sensitivity.

Single-molecule detection techniques offer significant potential for improving diagnostics, especially when applied directly to patient-derived samples [19, 20]. Among these methods, nanopore sensing is particularly notable for its high-precision detection and characterisation of individual biomolecules [21, 22]. This technique enables real-time, single-molecule analysis, providing single-molecule level insights that are beyond the reach of conventional bulk sensing approaches. However, its application in early-stage diagnostics remains challenging due to the need for exceptionally high sensitivity, selectivity, and compatibility with complex biological fluids [23, 24]. Achieving a sufficient SNR requires the nanopore size to closely match that of the target biomolecule, posing a particular challenge for small biomolecules such as miRNAs

and small proteins, which often generate low SNR signals [23], making detection difficult. Additionally, nanopore sensing inherently lacks selectivity in biological fluids, which contain multiple biomolecules of similar size, shape, and charge, further complicating specific target identification. Therefore, improving both sensitivity and selectivity is crucial to fully unlocking the diagnostic potential of nanopore technology.

A promising strategy to address these challenges is the use of molecular carriers [23, 25]. These carriers bind to target biomolecules, ensuring that their passage through the nanopore produces distinct ionic current signals that can be differentiated from those of the carriers alone [26, 27]. This approach offers several key advantages. First, molecular carriers regulate translocation speed, improving signal resolution by aligning the movement of the target with that of the carrier. Second, they enhance the capture rate of target molecules—particularly DNA, due to its linear and elongated structure—thereby increasing sensitivity. Finally, molecular carriers offer versatility, as their receptor components can be readily modified to accommodate diverse applications.

To date, various linear DNA molecular carriers, in combination with nanopore sensing platforms, have been developed for detecting protein and nucleic acid biomarkers [28-30]. Typically, DNA carriers are functionalised with a receptor that specifically binds to the target biomarker. The presence of a bound biomarker is indicated by a subpeak superimposed on the DNA signal. In some studies, multiple receptors have been anchored at different sites on DNA carriers to enable multiplexed sensing [26, 31]. More recently, the sandwich structure concept, inspired by enzyme-linked immunosorbent assay (ELISA), has been adapted to molecular carriers for detecting small-sized biomarkers [32, 33]. In these studies, an extra reporter probe can bind to the target biomarker, further enhancing the subpeak signal during nanopore translocation.

In this chapter, a 9.1 kbp dsDNA derived from lambda DNA was utilised as a molecular carrier (**Figure 3.1**). A nicked 0.2 site and a 0.5 site (with the dsDNA carrier represented as 0–1) were functionalised with ssDNA receptor sequences for the selective binding of target miRNAs. To enhance the subpeak signal, a streptavidin (~52.8 KDa) probe was employed as a reporter. The

successful formation of the sandwich-structured DNA carrier–miRNA–streptavidin probe complex resulted in a distinct subpeak superimposed on the DNA signal. Additionally, multiplexed miRNA sensing was achieved by functionalizing the 0.2 and 0.5 sites with different ssDNA receptor sequences.

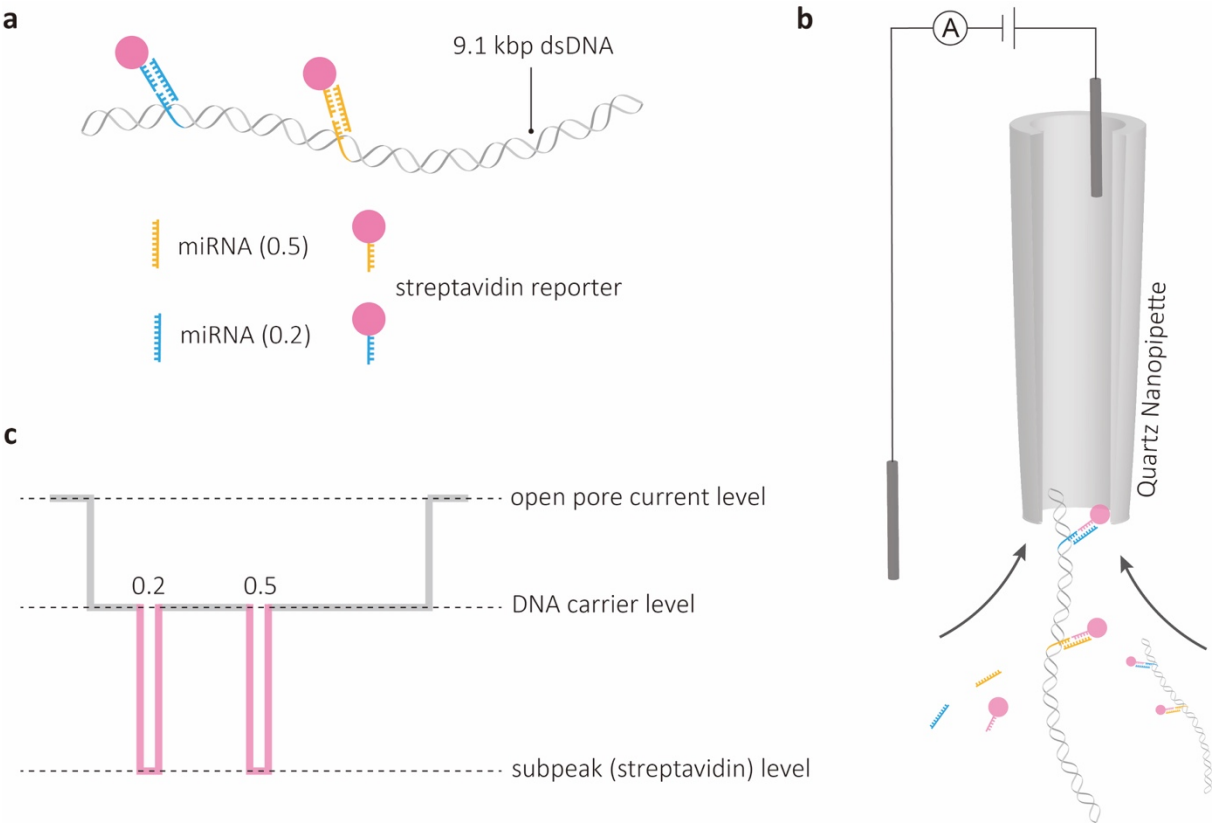


Figure 3.1 Design and nanopore sensing of miRNAs using a 9.1 kbp dsDNA carrier. **a.** The 9.1 kbp dsDNA carrier (0-1) enables the formation of a DNA carrier–miRNA–streptavidin probe sandwich structure. The 0.2 and 0.5 sites can be used to detect different miRNAs. **b.** Schematic of the nanopore sensing platform. **c.** Representative nanopore translocation event of the miRNA-bound dsDNA carrier.

3.2 Methods

3.2.1 dsDNA Carrier Preparation

The detailed method for preparing the 9.1 kbp dsDNA carrier is described in **Chapter 2**. PciI was used to excise the 9.1 kbp dsDNA carrier from the 48.5 kbp lambda DNA. Two types of nicking endonucleases were employed: Nb.BtsI, which creates a 48-base single-stranded region at the 0.5 site on the dsDNA carrier, and Nt.BsmAI, which generates a 32-base single-stranded region at the 0.2 site. The DNA sequences of the action sites for the enzymes mentioned above are shown in **Figure 3.2**.

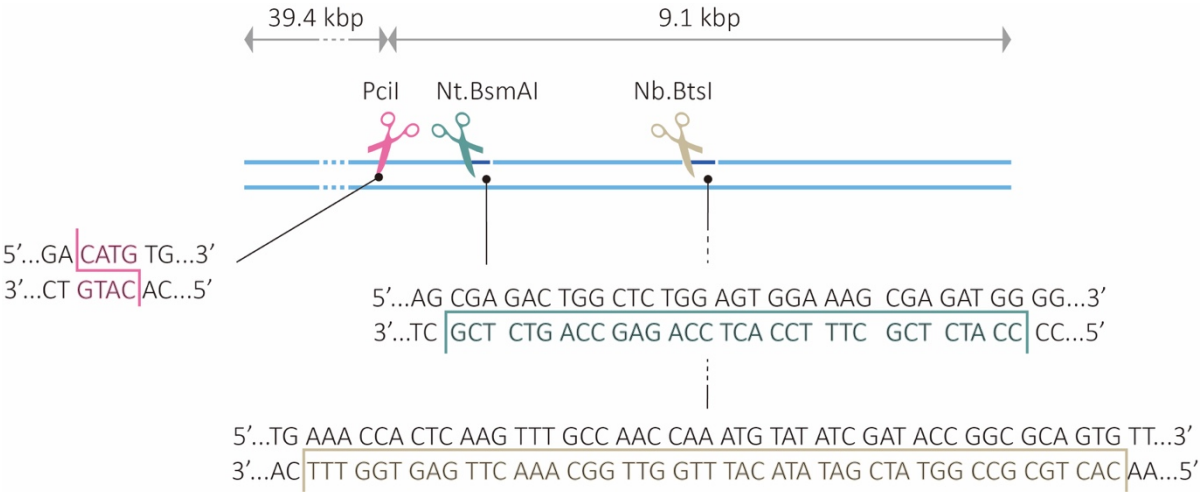


Figure 3.2 Enzymes used for 9.1 kbp dsDNA carrier preparation.

The ssDNA receptor sequences were partially complementary to the nicked single-stranded region and partially complementary to half of the target miRNA sequence. Additionally, the streptavidin probe consists of a streptavidin-conjugated biotinylated ssDNA sequence, which is complementary to the other half of the target miRNA sequence. Thus, hybridisation between the receptor-functionalised dsDNA, the target miRNA, and the streptavidin probe results in the formation of a sandwich structure. The DNA sequences used in this chapter are shown in **Figure 3.3**. The receptor sequences were phosphorylated at the 5' terminus to serve as substrates for DNA ligase, which seals the gap between adjacent residues at a single-stranded break on a double-stranded substrate.

The phosphorylated receptor sequences and biotinylated ssDNA sequences (Integrated DNA Technologies, IDT) were ordered in tubes which is purified by standard desalting. The

concentration of these sequences was determined using a Nanodrop 2000c device (Thermo Scientific) by measuring UV-Vis absorbance from 220 nm to 350 nm. The sequences were then diluted to 200 µM with nuclease-free water (Sigma-Aldrich) and stored at -20 °C until use.



Figure 3.3 Sequences used for detection of miRNAs. **a.** Schematic representations of 0.5 site 9.1 kbp dsDNA carrier used for detection of miRNA-141-3p. **b.** Schematic representation of 0.2 and 0.5 sites 9.1 kbp dsDNA carrier used for multiplexed detection of miRNA-7-5p and miRNA-382-5p.

3.2.2 DNA Carrier–miRNA–Streptavidin Probe Complex Preparation

For the detection of miRNAs, the 9.1 kbp dsDNA carrier at a concentration of 5 nM was incubated with miRNAs (at variable concentrations), 100 nM of each streptavidin reporter sequence and 500 nM of streptavidin (1 mg/mL, New England Biolabs) at 37 °C for 20 hours.

The incubated samples were then diluted with a buffer containing 2 M LiCl or 1.5 M LiCl, 5 mM $MgCl_2$, 10 mM Tris, and 1 mM EDTA (pH = 8) to achieve a final carrier concentration of 500 pM for subsequent nanopore translocation experiments.

An alternative method involving a ligase step was also employed. The 9.1 kbp dsDNA carrier at a concentration of 5 nM was incubated with miRNAs (at variable concentrations) and 100 nM of each streptavidin reporter sequence at 37 °C for 2 hours. T4 RNA ligase 1 (10,000 units/mL, New England Biolabs) at a volumetric ratio of 1:20 and T4 RNA ligase reaction buffer (10x, New England Biolabs) at a volumetric ratio of 1: 10 were added to the samples, which were kept on ice during the addition. The samples were then incubated at 37 °C for 15 min and inactivated at 65 °C for 15 min. A QIAquick Gel Extraction Kit (QIAGEN N.V.) was utilised for clean-up and extracting DNA carrier and DNA carrier-miRNA complex. The concentration of the carrier in the extracted samples was determined using a Nanodrop 2000c device (Thermo Scientific). Then above samples were then incubated at a carrier concentration of 2 nM with 200 nM of streptavidin at 37 °C for 2 hours. The samples were then diluted with a buffer containing 1.5 M LiCl, 5 mM $MgCl_2$, 10 mM Tris, and 1 mM EDTA (pH = 8) to achieve a final carrier concentration of 500 pM for subsequent nanopore translocation experiments.

3.3 Results and Discussion

3.3.1 Nanopipette Characterisation

The nanopores used in this chapter were nanopipettes fabricated using Protocol 1 (**Table 2.1**). The SEM image of the nanopipette is shown in **Figure 2.3**. A conical-shaped nanopore was formed at the tip of the nanopipette, with a diameter calculated to be 15 ± 3 nm based on measurements from five nanopipettes.

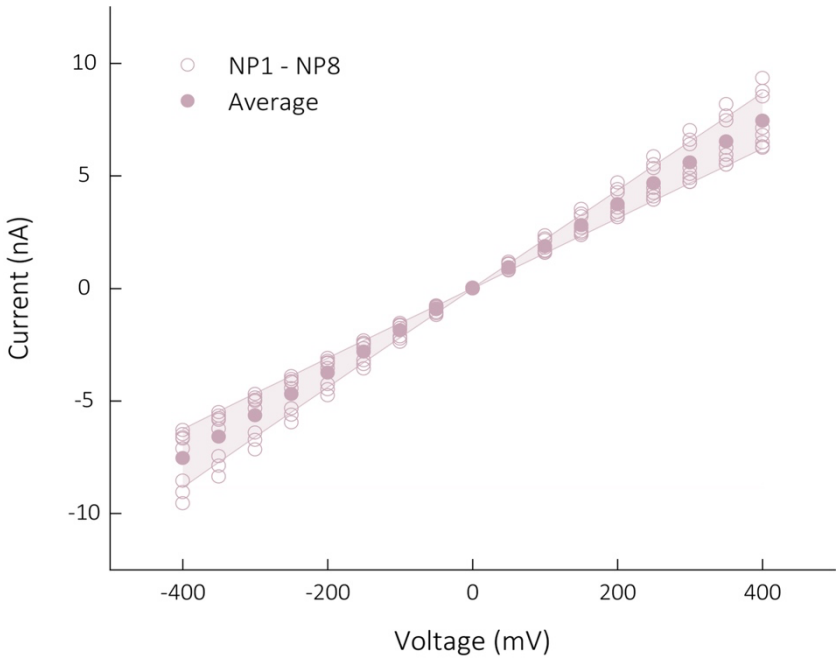


Figure 3.4 I-V characterisation of the nanopipettes fabricated using Protocol 1. The measurements were performed in 2 M LiCl, 5 mM $MgCl_2$, 10 mM Tris, 1 mM EDTA, pH = 8. The conductance of the quartz nanopore was 18.7 ± 3.1 nS (n = 8), calculated from the ohmic region (± 100 mV). The error band represents one standard deviation.

Electrochemical characterisation was conducted using I-V measurements (**Figure 3.4**). This process involved applying a voltage range of −400 mV to +400 mV in 50 mV increments across the nanopipette while it was immersed in a buffer solution containing 2 M LiCl, 5 mM $MgCl_2$, and 10 mM Tris 1 mM EDTA (pH = 8). The conductance of the quartz nanopipettes was determined to be G = 18.7 ± 3.1 nS using **Equation 2.1**, based on measurements from eight different nanopipettes.

3.3.2 dsDNA Carrier Characterisation

3.3.2.1 Gel Electrophoresis

Gel electrophoresis characterisation was performed after all hybridisation and enzyme reaction steps (**Figure 3.5**). Lane 1 was loaded with the reaction product, while lane 2 was loaded with a

1 kbp extended DNA ladder for reference to estimate the length of the DNA fragments and identify the target 9.1 kbp dsDNA carrier. Three DNA fragments were observed, corresponding to three distinct bands in the gel electrophoresis. The lagging band and the 9.1 kbp band were DNA fragments digested by PciI. However, an additional band with a length of approximately 5 kbp was observed, corresponding to a DNA fragment generated by two nicking sites on opposite strands of the lambda DNA.

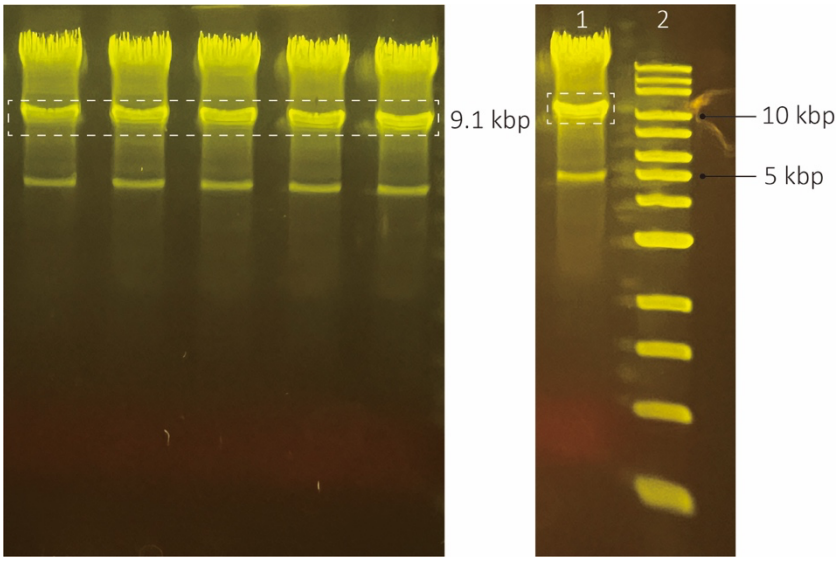


Figure 3.5 Gel electrophoresis of the 9.1 kbp dsDNA carrier after all enzyme and hybridisation reactions (lane 1: reaction product; lane 2: 1 kbp extended DNA ladder).

3.3.2.2 Nanopore Study of dsDNA Carrier

Nanopore translocation experiments were conducted to study the 9.1 kbp dsDNA carrier (**Figure 3.6**). A translocation buffer containing 2 M LiCl, 5 mM MgCl2, 10 mM Tris, and 1 mM EDTA (pH 8) was used, and 500 pM of the dsDNA carrier was introduced into the bath. With a 300 mV bias applied, dsDNA carriers were translocated through the nanopore, resulting in ionic current blockades. The translocation events of the dsDNA carrier exhibited a steady platform shape. Additionally, events with a secondary platform were observed, indicating that the DNA folded while translocating through the nanopore.

Quantitative analysis was performed to further characterize the translocation behaviour of the dsDNA carrier. Two populations of translocation events were identified, with mean dwell times of 958 ± 225 μs and 1420 ± 157 μs and peak currents of 62 ± 7 pA and 95 ± 10 pA, respectively. This is attributed to the folded DNA exhibiting a faster translocation speed and a secondary peak current level. The amplitude of the current blockade is proportional to the hydrodynamic cross-section of the DNA molecule, while the dwell time is proportional to the DNA length [34, 35]. The mean charge equivalent value was calculated to be 301 ± 31 fAs, further confirming the two distinct translocation behaviours of the dsDNA carrier. The folding ratio of the 9.1 kbp dsDNA was calculated to be 62.4 ± 4.8% (n = 3).

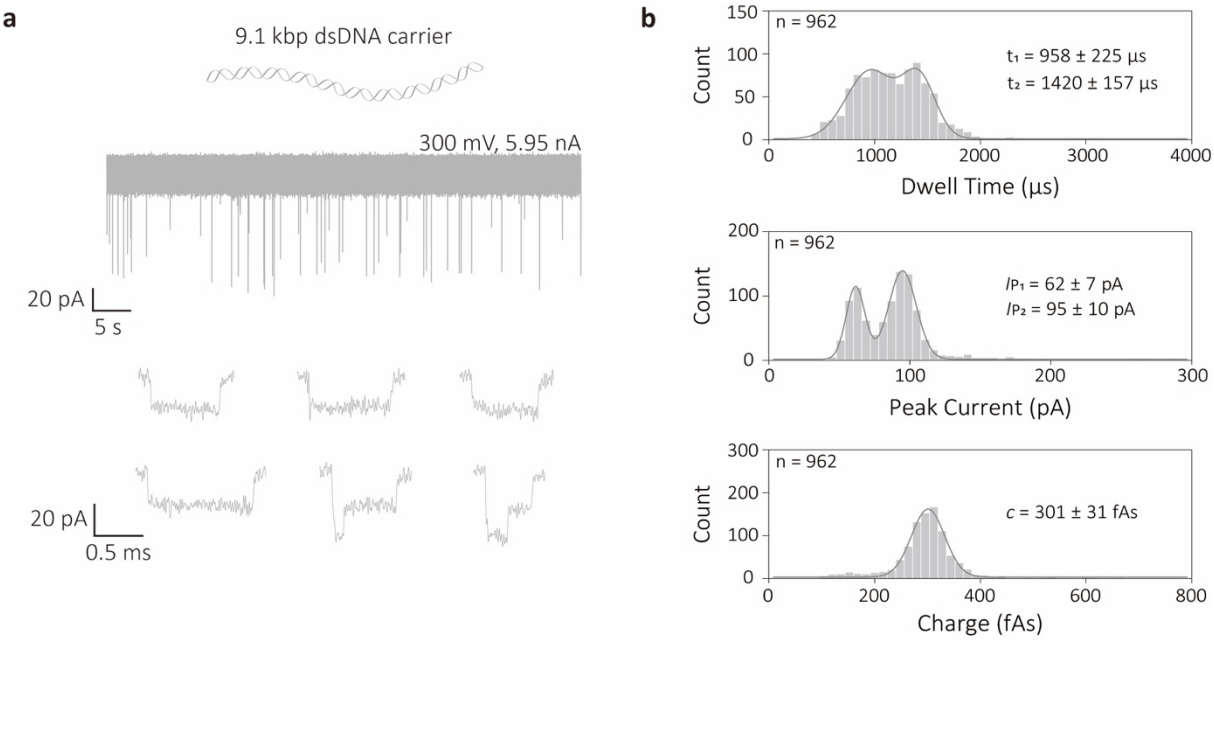


Figure 3.6 Nanopore translocation study of 9.1 kbp dsDNA carrier. **a.** Current-time trace and typical events. Experiments were performed in 2 M LiCl, 5 mM $MgCl_2$, 10 mM Tris, 1 mM EDTA, pH = 8, and at a voltage bias of 300 mV. **b.** Dwell time and peak current statistics.

3.3.3 Detection of miRNA with dsDNA Carrier

3.3.3.1 Direct Detection of miRNA-141

miR-141-3p, a member of the miR-200 family, has been extensively studied in the context of cancer, inflammation, and metabolic diseases. It holds significant potential for early cancer diagnosis, as serum miR-141-3p serves as a biomarker for PCa and colorectal cancer (CRC) [36, 37]. Furthermore, miR-141-3p has demonstrated utility in both the diagnosis and treatment of cancer.

A control nanopore translocation experiment was conducted to directly detect miRNA (**Figure 3.7**). The translocation buffer consisted of 2 M LiCl, 5 mM $MgCl_2$, 10 mM Tris, and 1 mM EDTA (pH 8). miRNA-141-3p at a concentration of 50 nM was introduced into the bath. A 300 mV voltage was applied, but no translocation events were observed during the experiment. This result highlights the challenge of detecting small biomolecules using nanopipettes due to their size disparity.

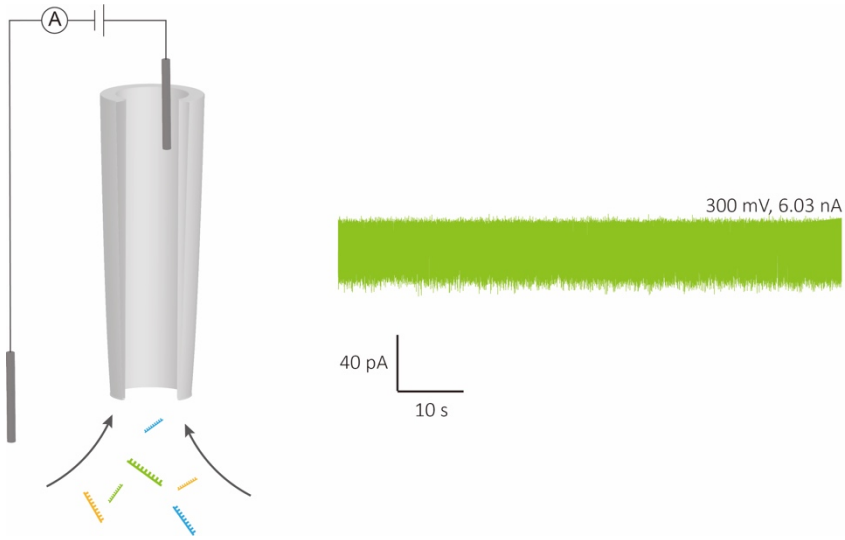


Figure 3.7 Nanopore sensing of miRNA-141-3p (500 pM). Experiments were performed in 2 M LiCl, 5 mM $MgCl_2$, 10 mM Tris, 1 mM EDTA, pH = 8, and at a voltage bias of 300 mV.

3.3.3.2 Translocation Buffer Selection

In nanopore translocation experiments, three key parameters require careful consideration: translocation time, peak current, and capture rate. Sufficient dwell time ensures adequate temporal resolution for signal analysis, while peak current similarly affects signal clarity. The capture rate determines whether a statistically significant number of events can be detected within a given timeframe for reliable quantitative analysis. Achieving successful nanopore translocation depends on the appropriate selection of the translocation buffer to meet these requirements.

Translocation buffers containing 2 M or 1.5 M LiCl, 5 mM $MgCl_2$, 10 mM Tris, and 1 mM EDTA (pH 8) were selected for nanopore detection of miRNA-141-3p using the dsDNA carrier. LiCl was chosen because DNA translocation time in LiCl is significantly longer than in KCl or NaCl, which is attributed to the strong binding of Li^+ to DNA, resulting in a reduced net force and lower translocation velocity, as observed in simulations [38]. $MgCl_2$ was included for its stabilizing effect on DNA structure.

Figure 3.8 presents the comparative translocation results obtained in 2 M and 1.5 M LiCl buffer solutions. While both conditions enabled effective detection, the 2 M LiCl demonstrated marginally better performance, showing a longer mean dwell time (1.42 ± 0.28 ms vs. 1.28 ± 0.17 ms) and a greater mean current blockade amplitude (68.3 ± 6.9 pA vs. 53.8 ± 4.9 pA). This is attributed to the increased number of bound ions at higher salt concentrations. Notably, both conditions permitted clear identification of miRNA-streptavidin complex subpeaks. The mean capture rates were calculated to be 0.17 ± 0.02 s^{-1} for 2 M LiCl and 0.35 ± 0.11 s^{-1} for 1.5 M LiCl. This result aligns with previous studies, which have shown that the capture rate is inversely correlated with translocation time in DNA nanopore detection [38, 39].

1.5 M LiCl translocation buffer was chosen for further nanopore detection of miRNA with dsDNA carrier, as this concentration provides an optimal balance between effective signal processing and sufficient capture rate.

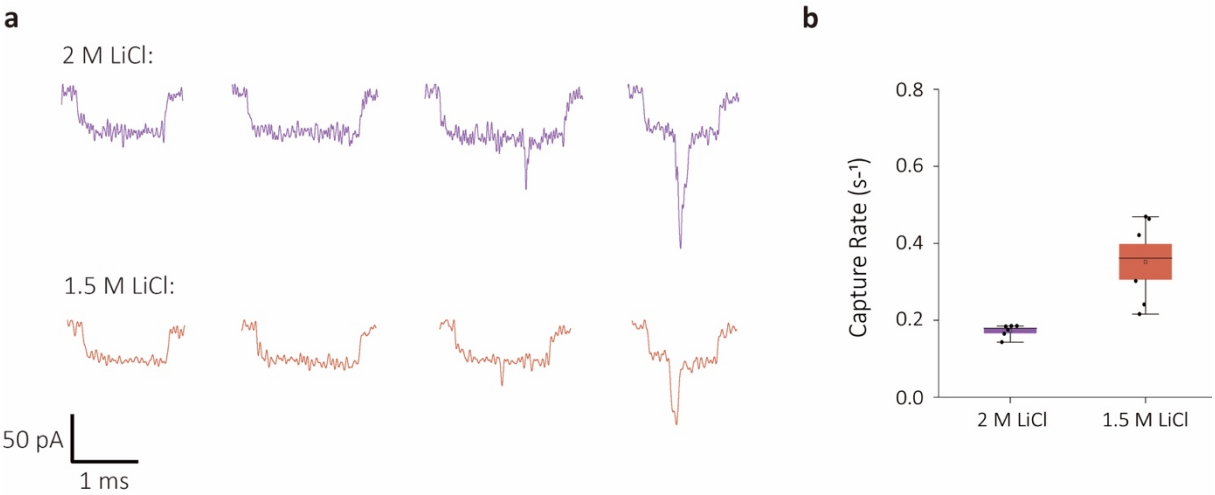


Figure 3.8 Experiments showing the nanopore detection of miRNA-141-3p using the dsDNA carrier in 2 M and 1.5 M LiCl buffer solutions. **a.** Example translocation events for unbound dsDNA carrier and miRNA-141-3p bound dsDNA carrier. **b.** Box plot showing the capture rate for nanopore detection in 2 M and 1.5 M LiCl. The black central line represents the median, the bottom and top edges mark the one standard error, and the whiskers represent 1.5× interquartile range (IQR). The measurements were performed with six independent nanopores.

3.3.3.3 Detection of miRNA-141 with dsDNA Carrier

To investigate the feasibility of applying the sandwich complex to nanopore sensing of miRNA with dsDNA carrier, nanopore experiments were conducted (**Figure 3.9**). The 9.1 kbp dsDNA carrier was incubated with miRNA-141-3p, reporter sequence, and streptavidin for 20 hours before detection. Example events are shown in **Figure 3.9a**, where the subpeaks of bound miRNA-streptavidin (green) are superimposed at the middle of the dsDNA event (grey), corresponding to the 0.5 binding site of the dsDNA carrier. In addition, it is worth noting that some events exhibit both subpeaks and signal peaks from DNA folding, which represents the most significant limitation of using dsDNA carriers for nanopore detection of target molecules [26, 28]. However, these DNA folding signal peaks do not affect subpeak discrimination because folding only occurs at the dsDNA carrier ends. Subpeaks from bound miRNA-streptavidin remain clearly recognizable even when substantial folding occurs (e.g., when half or more of the dsDNA is folded).

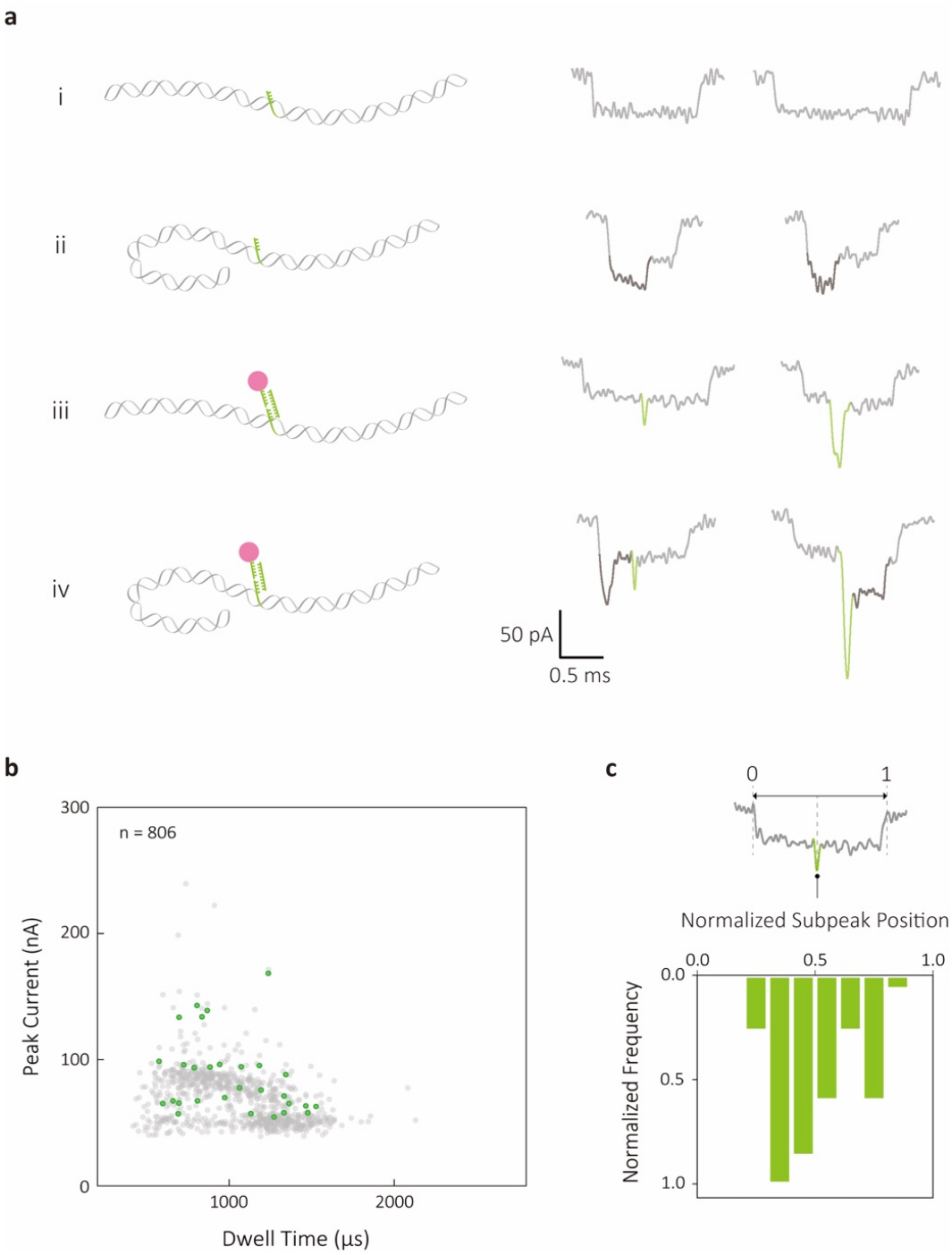


Figure 3.9 Nanopore detection of miRNA-141-3p using dsDNA carrier–miRNA–streptavidin complex strategy. **a.** example events for: (i) receptor sequence modified 9.1 kbp dsDNA carrier, (ii) partially folded dsDNA carrier, (iii) dsDNA carrier–miRNA–streptavidin complex, and (iv) partially folded dsDNA carrier–miRNA–streptavidin complex. **b.** The scatter plot of peak current and dwell time for the translocation events of the dsDNA carrier (500 pM), reporter sequence (10 nM), and streptavidin (50 nM) in the presence of miRNA-141-3p (50 nM). Events with a bound complex subpeak are highlighted in green. **c.** Statistics of normalised subpeak position.

Subpeak analysis was performed to reveal information of both the miRNA-streptavidin subpeaks and DNA folding signals, including subpeak width, subpeak amplitude, and fractional position. The DNA folding signals showed widely dispersed subpeak widths, indicating high variability, with some values overlapping those of bound miRNA-streptavidin subpeaks. Unlike larger proteins or protein aggregates [28], the streptavidin reporter produces subpeaks with relatively small amplitudes that are difficult to distinguish from DNA folding signals based solely on amplitude. This observation is also reflected in the peak amplitudes of the event. As shown in **Figure 3.9b**, the peak amplitude distributions of miRNA-streptavidin bound dsDNA carriers were indistinguishable from those of unbound dsDNA carriers.

The fractional position of subpeaks proved to be the most reliable criterion for identifying bound miRNA-streptavidin complexes. In the time dimension, the start and end of dsDNA translocation events were normalised to 0 and 1, respectively, with the 'normalised subpeak position' defined as the fractional location at which subpeaks occur. The distribution of normalised subpeak positions for miRNA-streptavidin-bound events is shown in **Figure 3.9c**. The mean normalised subpeak position was 0.49 ± 0.15, matching the expected 0.5 binding site position of the miRNA-141 receptor sequence on the 9.1 kbp dsDNA carrier.

3.3.3.4 Multiplexed Detection of miRNA-7 and miRNA-382 with dsDNA Carrier

Acute kidney injury (AKI) represents a frequent and serious complication in cardiac patients, typically resulting in worse clinical outcomes, extended hospitalisations, and elevated mortality rates [40, 41]. This condition develops through combined hemodynamic, inflammatory, and nephrotoxic mechanisms that impair renal perfusion and function [42]. Therefore, preventing AKI in cardiac patients represents a critical clinical need. This prevention can be facilitated through early prediction enabled by detecting relevant biomarkers in patient samples. Two miRNA biomarkers - miR-7-5p and miR-382-5p - were identified as candidate predictors of AKI in cardiac patients by Dr Sharad Kholia (Imperial College London).

The two nicked binding sites (0.2 and 0.5) on the 9.1 kbp dsDNA carrier enable multiplexed detection of miR-7-5p and miR-382-5p. The 0.2 site was functionalised with a receptor sequence partially complementary to miR-7-5p, while the 0.5 site was designed for miR-382-5p, with corresponding reporter sequences for each miRNA.

Nanopore translocation experiments were conducted to evaluate the feasibility of multiplexed miRNA detection using the sandwich complex approach with dsDNA carriers (**Figure 3.10**). The 9.1 kbp dsDNA carrier was co-incubated with both target miRNAs (miRNA-7-5p and miRNA-382-5p), their corresponding reporter sequences, and streptavidin for 20 hours prior to detection. Representative events in **Figure 3.10a** show: Orange subpeaks from bound streptavidin-miRNA-382-5p at mid-carrier positions (0.5 site); Blue subpeaks from bound streptavidin-miRNA-7-5p near carrier termini (0.2 site); Events containing both subpeak types, confirming simultaneous detection. All subpeak positions matched their respective programmed binding sites on the dsDNA carrier.

Subpeak analysis enabled discrimination of miRNA-streptavidin-bound dsDNA carrier events. The fractional subpeak positions were used as identification criteria: 0.5 ± 0.2 for bound streptavidin-miRNA-382-5p (0.5 site); 0.2 ± 0.1 and 0.8 ± 0.1 for bound streptavidin-miRNA-7-5p (0.2 site) [32, 33]. The distribution of normalised subpeak positions for miRNA-streptavidin-bound events is shown in **Figure 3.10b**. The mean normalised subpeak positions for bound streptavidin-miRNA-382-5p and bound streptavidin-miRNA-7-5p were 0.47 ± 0.12, 0.17 ± 0.06/0.79 ± 0.10, respectively, matching their expected 0.5 and 0.2 binding site positions on the 9.1 kbp dsDNA carrier.

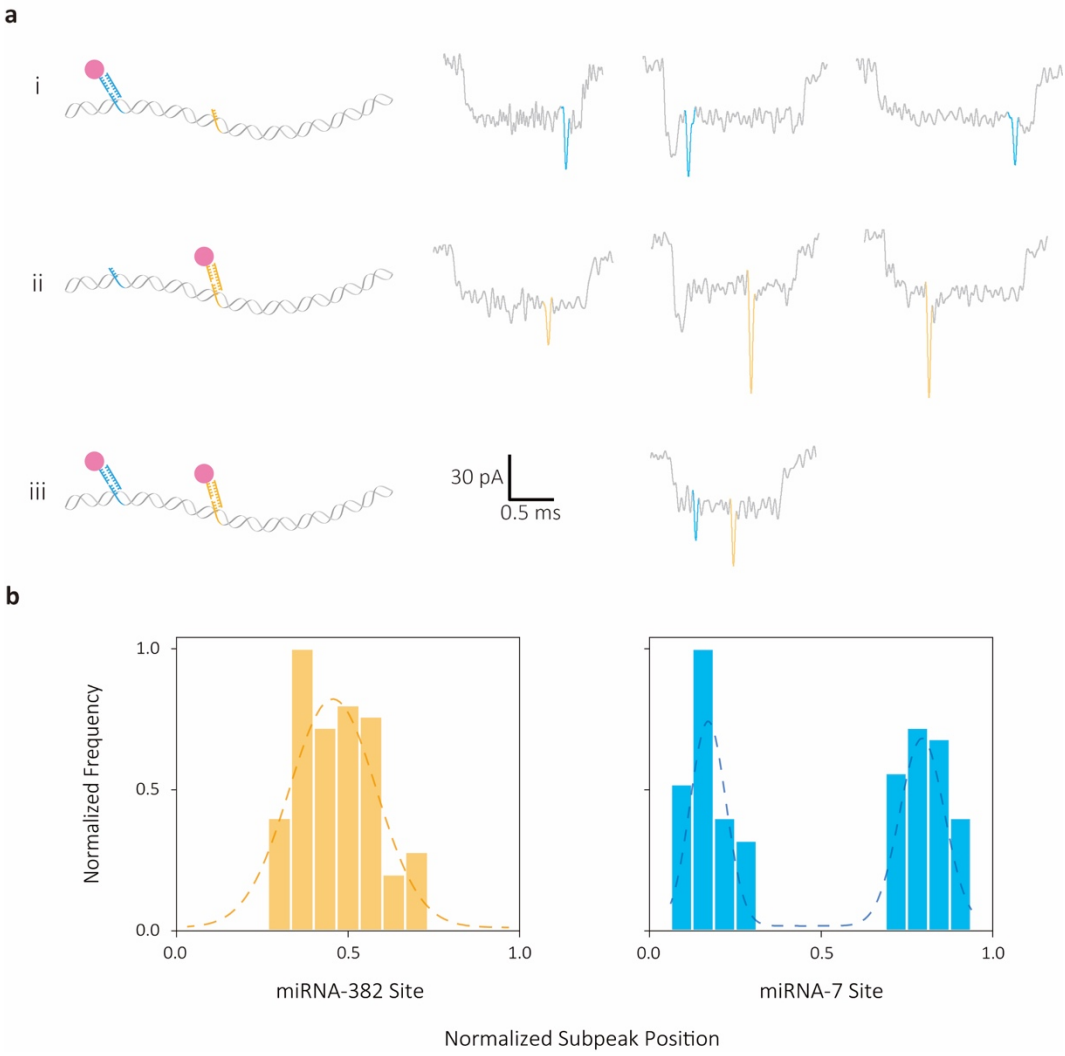


Figure 3.10 Nanopore multiplexed detection of miRNA-7-5p and miRNA-382-5p using dsDNA carrier–miRNA–streptavidin complex strategy. **a.** example events for: (i) streptavidin-miRNA-7-5p bound 9.1 kbp dsDNA carrier, (ii) streptavidin-miRNA-382-5p bound 9.1 kbp dsDNA carrier, (iii) streptavidin-miRNA-7-5p and streptavidin-miRNA-382-5p bound 9.1 kbp dsDNA carrier. **b.** Statistics of normalised subpeak position for bound streptavidin-miRNA-382-5p and bound streptavidin-miRNA-7-5p subpeaks.

3.3.3.5 miRNA Binding Optimisation

The binding ratio was observed to be 3.35 ± 0.43% for miRNA-141-3p, 6.30 ± 0.36% and 3.75 ± 1.03% for miRNA-7-5p and miRNA-382-5p, respectively. The binding ratio at the 0.5 site was lower than at the 0.2 site, consistent with results from previously published work. However, the binding ratios for these miRNAs were smaller than those for viral RNA fragments [32]. This

can be attributed to the fact that viral RNA fragments have much longer sequences than miRNAs, resulting in longer hybridisation regions with both receptor and reporter sequences and higher melting temperatures.

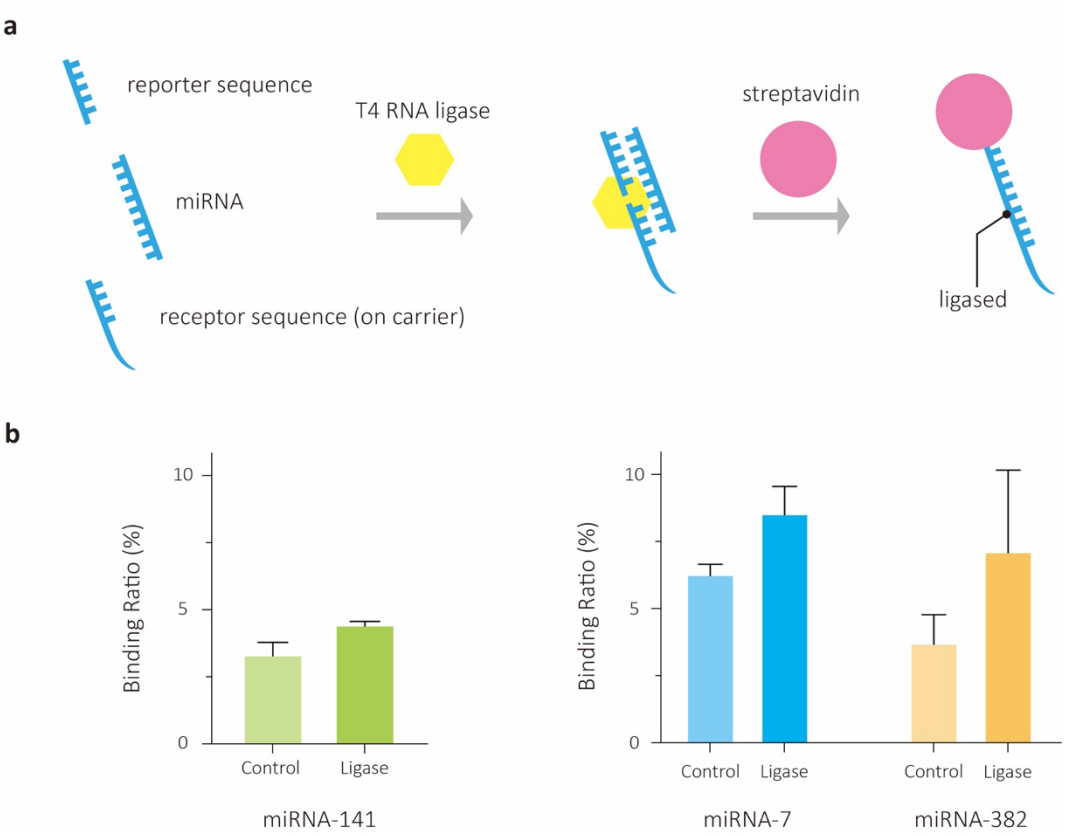


Figure 3.11 Enhancement of miRNA binding to the 9.1 kbp dsDNA carrier using T4 RNA ligase. **a.** Two-step T4 RNA ligase incubation approach for nanopore detection of miRNA with dsDNA carrier. The receptor sequence and reporter sequence can be ligated by T4 RNA ligase. **b.** Comparison of miRNA binding ratios with versus without the T4 RNA ligase incubation approach.

To enhance miRNA binding ratios, a two-step T4 RNA ligase incubation approach was employed (**Figure 3.11**). T4 RNA ligase catalyses 3'-5' phosphodiester bond formation between the 3'-OH and 5'-P groups of RNA molecules. In this approach, T4 RNA ligase ligates receptor and reporter sequences while both are bound to target miRNA. The ligated receptor sequence subsequently connects to streptavidin. As indicated in **Figure 3.11b**, the binding ratio was

observed to be increased to 4.46 ± 0.10% for miRNA-141-3p, 8.58 ± 0.98% and 7.16 ± 3.01% for miRNA-7-5p and miRNA-382-5p, respectively.

3.4 Conclusion

In this chapter, we explored the application of a dsDNA-based molecular carrier system for the nanopore detection of miRNAs, leveraging a sandwich complex approach. The 9.1 kbp dsDNA carrier was functionalised with specific receptor sequences to facilitate selective miRNA binding, with streptavidin probes serving as reporters to enhance signal resolution. Through systematic characterisation and optimisation, we demonstrated the feasibility of this approach for both single-target and multiplexed miRNA detection. Our findings confirm that the molecular carrier strategy effectively overcomes challenges related to low signal-to-noise ratios, thereby advancing the utility of nanopore sensing for miRNA analysis.

The experimental results further highlight key factors influencing detection performance, including the composition of the translocation buffer, the efficiency of dsDNA carrier binding, and the interpretation of nanopore signals. By optimizing binding conditions with a T4 RNA ligase-based strategy, we achieved notable improvements in miRNA capture efficiency. Additionally, the successful detection of miRNA-141-3p, miRNA-7-5p, and miRNA-382-5p underscores the potential of this method for clinical applications, such as the discovery of early disease biomarkers.

3.5 References

[1] Bartel, D. P. MicroRNAs: genomics, biogenesis, mechanism, and function. *Cell* **2004**, *116*, 281-297.

[2] Bartel, D. P. MicroRNAs: target recognition and regulatory functions. *Cell* **2009**, *136*, 215-233.

[3] Ambros, V. The functions of animal microRNAs. *Nature* **2004**, *431*, 350-355.

[4] Huang, A.;Zheng, H.;Wu, Z.;Chen, M.; Huang, Y. Circular RNA-protein interactions: functions, mechanisms, and identification. *Theranostics* **2020**, *10*, 3503-3517.

[5] Kai, K.;Dittmar, R. L.; Sen, S. Secretory microRNAs as biomarkers of cancer. *Semin Cell Dev Biol* **2018**, *78*, 22-36.

[6] Vishnoi, A.; Rani, S. miRNA Biogenesis and Regulation of Diseases: An Updated Overview. *Methods Mol Biol* **2023**, *2595*, 1-12.

[7] Paul, S.;Bravo Vazquez, L. A.;Perez Uribe, S.;Roxana Reyes-Perez, P.; Sharma, A. Current Status of microRNA-Based Therapeutic Approaches in Neurodegenerative Disorders. *Cells* **2020**, *9*.

[8] Kristensen, L. S.;Andersen, M. S.;Stagsted, L. V. W.;Ebbesen, K. K.;Hansen, T. B.; Kjems, J. The biogenesis, biology and characterization of circular RNAs. *Nat Rev Genet* **2019**, *20*, 675-691.

[9] Jeck, W. R.; Sharpless, N. E. Detecting and characterizing circular RNAs. *Nat Biotechnol* **2014**, *32*, 453-461.

[10] Grasso, M.;Piscopo, P.;Confaloni, A.; Denti, M. A. Circulating miRNAs as biomarkers for neurodegenerative disorders. *Molecules* **2014**, *19*, 6891-6910.

[11] Mitchell, P. S.;Parkin, R. K.;Kroh, E. M.;Fritz, B. R.;Wyman, S. K.;Pogosova-Agadjanyan, E. L.;Peterson, A.;Noteboom, J.;O'Briant, K. C.;Allen, A.;Lin, D. W.;Urban, N.;Drescher, C. W.;Knudsen, B. S.;Stirewalt, D. L.;Gentleman, R.;Vessella, R. L.;Nelson, P. S.;Martin, D. B.; Tewari, M. Circulating microRNAs as stable blood-based markers for cancer detection. *Proc Natl Acad Sci U S A* **2008**, *105*, 10513-10518.

[12] Zhou, S. S.;Jin, J. P.;Wang, J. Q.;Zhang, Z. G.;Freedman, J. H.;Zheng, Y.; Cai, L. miRNAS in cardiovascular diseases: potential biomarkers, therapeutic targets and challenges. *Acta Pharmacol Sin* **2018**, *39*, 1073-1084.

[13] Redshaw, N.;Wilkes, T.;Whale, A.;Cowen, S.;Huggett, J.; Foy, C. A. A comparison of miRNA isolation and RT-qPCR technologies and their effects on quantification accuracy and repeatability. *Biotechniques* **2013**, *54*, 155-164.

[14] Mestdagh, P.;Feys, T.;Bernard, N.;Guenther, S.;Chen, C.;Speleman, F.; Vandesompele, J. High-throughput stem-loop RT-qPCR miRNA expression profiling using minute amounts of input RNA. *Nucleic Acids Res* **2008**, *36*, e143.

[15] Pall, G. S.; Hamilton, A. J. Improved northern blot method for enhanced detection of small RNA. *Nat Protoc* **2008**, *3*, 1077-1084.

[16] Varallyay, E.;Burgyan, J.; Havelda, Z. MicroRNA detection by northern blotting using locked nucleic acid probes. *Nat Protoc* **2008**, *3*, 190-196.

[17] Lodes, M. J.;Caraballo, M.;Suciu, D.;Munro, S.;Kumar, A.; Anderson, B. Detection of cancer with serum miRNAs on an oligonucleotide microarray. *PLoS One* **2009**, *4*, e6229.

[18] Martens-Uzunova, E. S.;Jalava, S. E.;Dits, N. F.;van Leenders, G. J.;Moller, S.;Trapman, J.;Bangma, C. H.;Litman, T.;Visakorpi, T.; Jenster, G. Diagnostic and prognostic signatures from the small non-coding RNA transcriptome in prostate cancer. *Oncogene* **2012**, *31*, 978-991.

[19] Ye, J.;Xu, M.;Tian, X.;Cai, S.; Zeng, S. Research advances in the detection of miRNA. *J Pharm Anal* **2019**, *9*, 217-226.

[20] Akkilic, N.;Geschwindner, S.; Hook, F. Single-molecule biosensors: Recent advances and applications. *Biosens Bioelectron* **2020**, *151*, 111944.

[21] Wanunu, M. Nanopores: A journey towards DNA sequencing. *Phys Life Rev* **2012**, *9*, 125-158.

[22] Miles, B. N.;Ivanov, A. P.;Wilson, K. A.;Dogan, F.;Japrung, D.; Edel, J. B. Single molecule sensing with solid-state nanopores: novel materials, methods, and applications. *Chem Soc Rev* **2013**, *42*, 15-28.

[23] Xue, L.;Yamazaki, H.;Ren, R.;Wanunu, M.;Ivanov, A. P.; Edel, J. B. Solid-state nanopore sensors. *Nature Reviews Materials* **2020**, *5*, 931-951.

[24] Howorka, S.; Siwy, Z. Nanopore analytics: sensing of single molecules. *Chem Soc Rev* **2009**, *38*, 2360-2384.

[25] Liu, L.; Wu, H. C. DNA-Based Nanopore Sensing. *Angew Chem Int Ed Engl* **2016**, *55*, 15216-15222.

[26] Sze, J. Y. Y.;Ivanov, A. P.;Cass, A. E. G.; Edel, J. B. Single molecule multiplexed nanopore protein screening in human serum using aptamer modified DNA carriers. *Nat Commun* **2017**, *8*, 1552.

[27] Yang, W.;Restrepo-Perez, L.;Bengtson, M.;Heerema, S. J.;Birnie, A.;van der Torre, J.; Dekker, C. Detection of CRISPR-dCas9 on DNA with Solid-State Nanopores. *Nano Lett* **2018**, *18*, 6469-6474.

[28] Liu, Y.;Wang, X.;Campolo, G.;Teng, X.;Ying, L.;Edel, J. B.; Ivanov, A. P. Single-Molecule Detection of alpha-Synuclein Oligomers in Parkinson's Disease Patients Using Nanopores. *ACS Nano* **2023**, *17*, 22999-23009.

[29] Bell, N. A.; Keyser, U. F. Specific protein detection using designed DNA carriers and nanopores. *J Am Chem Soc* **2015**, *137*, 2035-2041.

[30] Cai, S.;Pataillot-Meakin, T.;Shibakawa, A.;Ren, R.;Bevan, C. L.;Ladame, S.;Ivanov, A. P.; Edel, J. B. Single-molecule amplification-free multiplexed detection of circulating microRNA cancer biomarkers from serum. *Nat Commun* **2021**, *12*, 3515.

[31] Kong, J.;Zhu, J.;Chen, K.; Keyser, U. F. Specific Biosensing Using DNA Aptamers and Nanopores. *Advanced Functional Materials* **2018**, *29*.

[32] Ren, R.;Cai, S.;Fang, X.;Wang, X.;Zhang, Z.;Damiani, M.;Hudlerova, C.;Rosa, A.;Hope, J.;Cook, N. J.;Gorelkin, P.;Erofeev, A.;Novak, P.;Badhan, A.;Crone, M.;Freemont, P.;Taylor, G. P.;Tang, L.;Edwards, C.;Shevchuk, A.;Cherepanov, P.;Luo, Z.;Tan, W.;Korchev, Y.;Ivanov, A. P.; Edel, J. B. Multiplexed detection of viral antigen and RNA using nanopore sensing and encoded molecular probes. *Nat Commun* **2023**, *14*, 7362.

[33] Cai, S.;Ren, R.;He, J.;Wang, X.;Zhang, Z.;Luo, Z.;Tan, W.;Korchev, Y.;Edel, J. B.; Ivanov, A. P. Selective Single-Molecule Nanopore Detection of mpox A29 Protein Directly in Biofluids. *Nano Lett* **2023**, *23*, 11438-11446.

[34] Li, J.;Gershow, M.;Stein, D.;Brandin, E.; Golovchenko, J. A. DNA molecules and configurations in a solid-state nanopore microscope. *Nat Mater* **2003**, *2*, 611-615.

[35] Chen, P.;Gu, J.;Brandin, E.;Kim, Y. R.;Wang, Q.; Branton, D. Probing Single DNA Molecule Transport Using Fabricated Nanopores. *Nano Lett* **2004**, *4*, 2293-2298.

[36] Cheng, H.;Zhang, L.;Cogdell, D. E.;Zheng, H.;Schetter, A. J.;Nykter, M.;Harris, C. C.;Chen, K.;Hamilton, S. R.; Zhang, W. Circulating plasma MiR-141 is a novel biomarker for metastatic colon cancer and predicts poor prognosis. *PLoS One* **2011**, *6*, e17745.

[37] Porzycki, P.;Ciszkowicz, E.;Semik, M.; Tyrka, M. Combination of three miRNA (miR-141, miR-21, and miR-375) as potential diagnostic tool for prostate cancer recognition. *Int Urol Nephrol* **2018**, *50*, 1619-1626.

[38] Kowalczyk, S. W.;Wells, D. B.;Aksimentiev, A.; Dekker, C. Slowing down DNA translocation through a nanopore in lithium chloride. *Nano Lett* **2012**, *12*, 1038-1044.

[39] Wanunu, M.;Morrison, W.;Rabin, Y.;Grosberg, A. Y.; Meller, A. Electrostatic focusing of unlabelled DNA into nanoscale pores using a salt gradient. *Nat Nanotechnol* **2010**, *5*, 160-165.

[40] Vives, M.;Hernandez, A.;Parramon, F.;Estanyol, N.;Pardina, B.;Munoz, A.;Alvarez, P.; Hernandez, C. Acute kidney injury after cardiac surgery: prevalence, impact and management challenges. *Int J Nephrol Renovasc Dis* **2019**, *12*, 153-166.

[41] Karkouti, K.;Wijeysundera, D. N.;Yau, T. M.;Callum, J. L.;Cheng, D. C.;Crowther, M.;Dupuis, J. Y.;Fremes, S. E.;Kent, B.;Laflamme, C.;Lamy, A.;Legare, J. F.;Mazer, C. D.;McCluskey, S. A.;Rubens, F. D.;Sawchuk, C.; Beattie, W. S. Acute kidney injury after cardiac surgery: focus on modifiable risk factors. *Circulation* **2009**, *119*, 495-502.

[42] Basile, D. P.;Anderson, M. D.; Sutton, T. A. Pathophysiology of acute kidney injury. *Compr Physiol* **2012**, *2*, 1303-1353.

Chapter 4 Reconfigurable DNA Origami Nanostructure and Nanopore Characterisation

Synopsis

This chapter presents investigation of a DNA origami hinge mechanism, encompassing structural design, dynamic behaviour, and single-molecule characterisation. The study utilised bulk fluorescence assays and a dual photophore quenching pair to quantify hinge conformation transitions, complemented by TEM and nanopore sensing to probe configuration-dependent molecular dynamics. Through nanopore sensing and systematic voltage-dependent measurements, we identify and characterize distinct translocation signatures for closed, extended, and open hinge configurations, revealing conformation-specific nanopore interactions.

Chapter 4 Reconfigurable DNA Origami Nanostructure and Nanopore Characterisation

4.1 Introduction 128

4.2 Methods 130

4.2.1 DNA Origami Hinge Preparation 130

4.2.2 Bulk Fluorescence Characterisation 131

4.3 Results and Discussion 131

4.3.1 DNA Origami Hinge 131

4.3.1.1 Hinge Mechanism 131

4.3.1.2 Bulk Fluorescence Assays 133

4.3.1.3 TEM Analysis 135

4.3.2 Nanopore Characterisation of DNA Origami Hinge 136

4.3.2.1 Nanopipette Characterisation 136

4.3.2.2 Closed Hinge vs Extended Hinge 138

4.2.3.3 Voltage Dependant 140

4.2.3.4 Open Hinge 144

4.4 Conclusion 145

4.5 References 146

4.1 Introduction

DNA origami, a groundbreaking self-assembly technique introduced by Rothemund in 2006, has revolutionised the field of DNA nanotechnology [1, 2]. This approach utilises a long, single-stranded viral DNA scaffold that is folded into precise nanoscale structures through the programmable hybridisation of hundreds of short staple strands, governed by Watson-Crick base pairing [3-5]. The entire assembly process occurs in a single reaction, enabling the robust and high-yield fabrication of complex two- and three-dimensional nanostructures with sub-nanometre precision. A key advantage of DNA origami lies in its exceptional structural programmability, which extends beyond static shapes to include dynamic reconfigurability through controlled strand displacement and hybridisation [6-8]. This capability, combined with the ability to position functional moieties precisely, has established DNA origami as a versatile platform for engineering responsive nano-systems with tailored mechanical and chemical properties.

The unique attributes of DNA origami have enabled transformative applications across multiple disciplines. In biomedicine, it has been employed for ultrasensitive biosensing, spatially controlled drug delivery, and high-specificity molecular diagnostics [9, 10]. Materials science has leveraged DNA origami to construct functional nanomaterials with programmable optical, catalytic, and mechanical behaviours [11-13]. Additionally, this technology has become indispensable in single-molecule studies, where its nanometre-precise patterning capabilities have enhanced techniques such as super-resolution microscopy and single-molecule force spectroscopy [14, 15]. By providing unprecedented control over molecular organisation and interactions, DNA origami continues to open new frontiers in both fundamental biological research and the development of advanced nanodevices.

DNA origami has emerged as a powerful component in hybrid nanopore systems, enabling novel approaches to molecular sensing and nanoscale manipulation [16]. Current research has established two principal methodologies for incorporating DNA origami structures into these

systems. The first approach utilizes precisely positioned DNA origami nanostructures within solid-state nanopores, where they function as modular sensing elements capable of regulating molecular transport and enhancing recognition specificity [17, 18]. The second method involves the stable incorporation of DNA origami into lipid bilayers through strategic hydrophobic modifications, facilitating their seamless integration with biological membrane environments [19, 20]. These complementary strategies offer distinct advantages in terms of structural integrity, system tunability, and platform compatibility, enabling tailored applications across various experimental configurations.

Recent advances have significantly expanded the utility of DNA origami-enhanced nanopore systems for molecule detection [21, 22]. The technology's programmability has been particularly valuable in nanopore sensing applications, where DNA origami structures serve as highly customizable platforms for the selective identification of target biomolecules with exceptional sensitivity. Furthermore, DNA origami-based molecular carriers have demonstrated precise control over translocation dynamics, enabling selective nanopore sensing through engineered interaction mechanisms [23]. While these developments have established the foundation for DNA origami-nanopore integration, current implementations have predominantly utilised static configurations [24, 25]. The field now stands to benefit from further exploration of dynamic DNA origami systems, which could unlock new capabilities in adaptive sensing and real-time molecular manipulation within nanopore environments [26, 27].

In this chapter, we investigate the structural dynamics of a DNA origami hinge and further characterize its behaviour using nanopore sensing (**Figure 4.1**). The hinge is designed to transition between a compact, closed state and an elongated, extended state, facilitated by precise strand design and structural flexibility. These distinct conformations produce characteristic current blockade patterns during nanopore translocation, enabling real-time observation of conformational changes at single-molecule resolution. Our analysis reveals key dynamic properties, including transition kinetics and state stability under different conditions. These findings demonstrate nanopore sensing as an effective tool for studying DNA

nanostructure dynamics, while providing design insights for developing functional nanodevices, such as electrochemical biosensors.

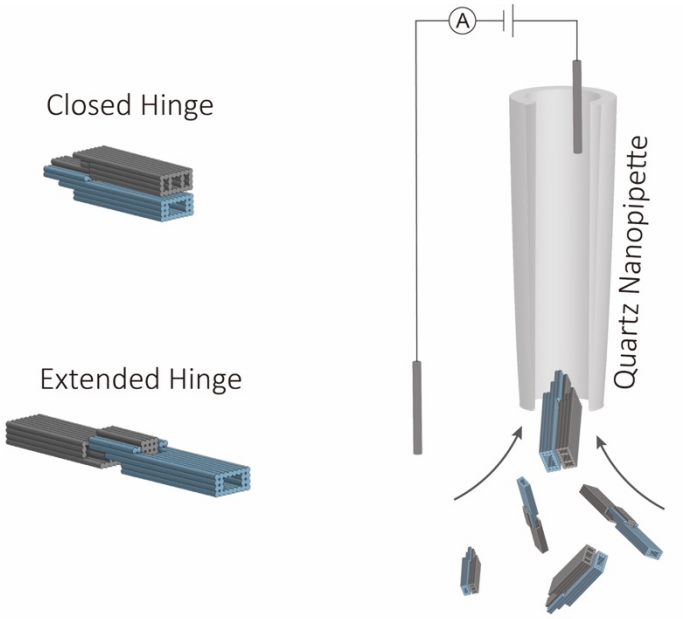


Figure 4.1 Design and nanopore sensing of DNA origami hinge.

4.2 Methods

4.2.1 DNA Origami Hinge Preparation

DNA hinge assembly and purification were performed by Dr Joshua Johnson (Imperial College London). The details are described in **Chapter 2**. Hinges utilised in bulk fluorescence characterisation were purified via PEG precipitation, a well-established method for rapid separation of DNA origami from excess staple strands [28, 29]. Hinges for nanopore translocation experiments were purified via gel electrophoresis, as DNA origami must remain monomolecular while avoiding aggregation.

4.2.2 Bulk Fluorescence Characterisation

Samples for bulk fluorescence characterisation were prepared using an Opentrons OT-2 pipetting robot to minimise human error in experiments monitoring more than 12 samples. PEG purified hinges were incubated at 45°C for ~15 minutes prior to use. The robot was programmed to make multiples of 12 wells, each with 40 µL of 5 nM hinges with 25 nM extender strands, 250nM closer displacer strands in a buffer containing 1 M KCl, 12.5 mM MgCl2, 5 mM Tris and 0.5 mM EDTA. The plate was then quickly transferred to a plate reader (ClarioStar Plus), and the fluorescence of each well was monitored once every 45 seconds with orbital shaking at 300 rpm between each read.

4.3 Results and Discussion

4.3.1 DNA Origami Hinge

4.3.1.1 Hinge Mechanism

Our DNA origami hinge mechanism is designed with a pair of flexible joints that connect two structurally rigid yet adaptable arms, enabling controlled rotational movement (**Figure 4.2**). This flexibility allows the arms to pivot across a broad angular range of 0 to 300 degrees, facilitating dynamic transitions between conformations. At specific angles—particularly 0 and 180 degrees—the arms adopt distinct configurations: a compact closed state (vertical alignment) and an extended state (lateral alignment). These represent the hinge's extreme positional states, providing precise mechanical control at the nanoscale. In terms of dimensions, the hinge shows significant variation between closed and extended states. In the closed state, it measures approximately 60 nm (length) × 16 nm (width) × 18 nm (height), while the extended state measures 100 nm × 16 nm × 8 nm. Notably, the cross-sectional area nearly halves during the transition, reflecting substantial geometric reconfiguration. To verify structural fidelity, we

performed TEM imaging with negative staining. The images clearly confirmed the expected morphological differences between the two configurations, validating the successful assembly and function of the hinge.

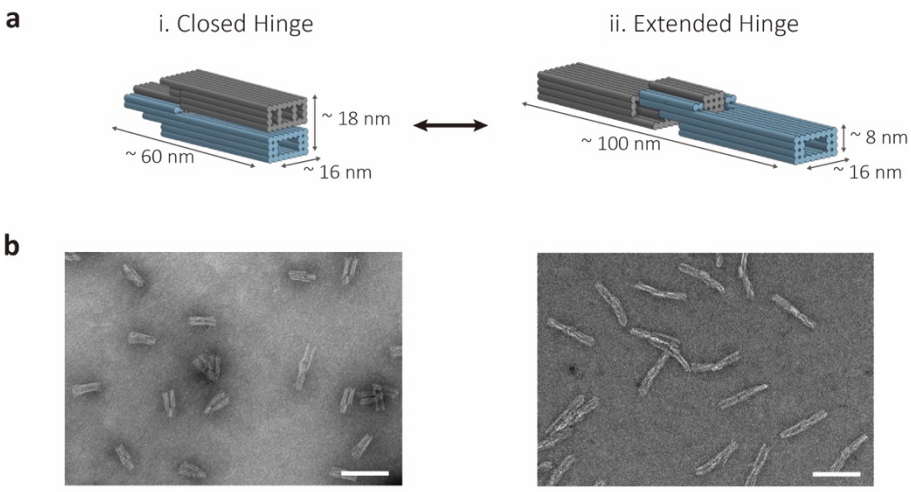


Figure 4.2 Design of the reconfigurable DNA origami hinge. **a.** Schematic illustration of the DNA hinge reconfiguration. The cross-sectional area of the closed hinge being approximately twice that of the extended hinge. **b.** TEM images of the closed and extended hinge (scale bar: 100 nm).

The detailed origami structure design is shown in **Figure 4.3**. Each joint consists of a pair of scaffold crossovers with two unpaired bases, intentionally limited to create a partial bias towards the extended state. Additionally, each hinge arm features a pair of large single-strand scaffold loops, which can be secured into the extended state through bridging by specific staples (extender strands). Along the interior face of each arm, a set of up to six overhangs is arranged. A closer helper strand can bridge these overhangs to lock the hinge into the closed state. Notably, each closer helper strand possesses a 6-base toehold, enabling a toehold-mediated strand displacement reaction triggered by closer displacer strands for releasing the hinge into an unconfined state.

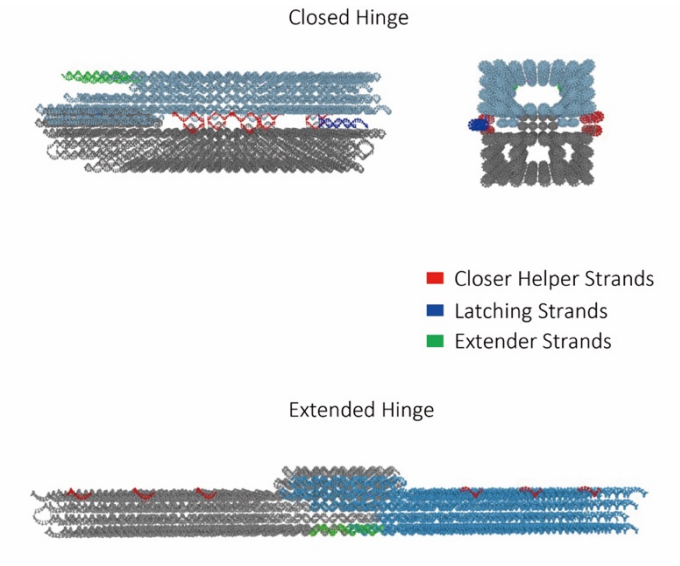


Figure 4.3 Schematic illustration of DNA origami closed hinge and extended hinge, showing the positions of the closer helper strands, latching strands, and extender strands.

4.3.1.2 Bulk Fluorescence Assays

To characterize the hinge transition, we incorporated Alexa488- and Atto550-labelled oligos on the bottom arm, positioned on opposite sides of the rotation axis, with a quencher attached to the top arm (**Figure 4.4**). In the closed state, the quencher is proximal to Atto550, while in the extended state, it swings adjacent to Alexa488. This dual fluorophore and quencher system effectively mitigates experimental artefacts during characterisation. Due to the hinge's natural bias towards the extended state, maintaining it in the closed state was optimised by incorporating closer helper strands during folding. Transitioning the hinge from a closed to an extended state was achieved by adding an excess of closer displacer and extender strands.

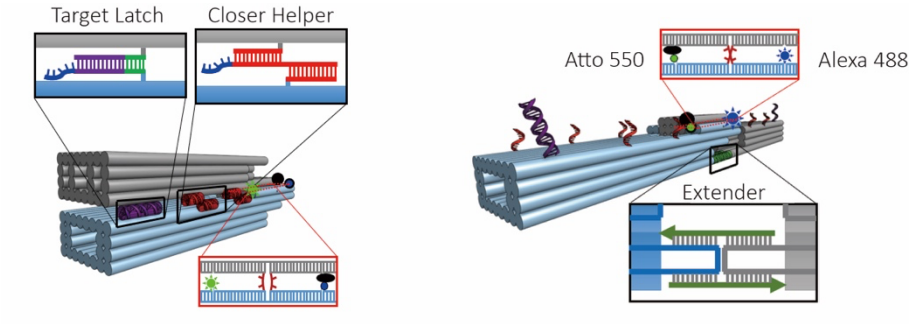


Figure 4.4 Design of the DNA origami hinge. The hinge in a closed configuration, with the top and bottom arms linked by six closer helper strands. A pair of fluorophores (Alexa488 and Atto550) are positioned on the bottom arm, with a quencher on the top arm, which suppresses Alexa488 fluorescence in the closed state. The extender strands lock the hinge in an extended configuration to ensure irreversible reconfiguration. The quencher is now closer to the Atto550.

Bulk fluorescence assays were performed by Dr Joshua Johnson (Imperial College London) to characterize the hinge reconfiguration kinetics (**Figure 4.5**) (Also in **Chapter 5**). Closer helper and extender strands were introduced to initiate the transition from the closed to extended configuration. The process was monitored through fluorescence intensity changes in Alexa488/Atto550 fluorophore pairs, where increasing Alexa488 signal accompanied by Atto550 quenching confirmed successful hinge reconfiguration.

To minimize artifacts, a fluorescence ratio (Alexa488/Atto550 intensity) was used to more accurately track the reconfiguration trend. As the hinge transitions from the closed conformation to the extended conformation, the fluorescence ratio exhibits a two-phase increase: an initial rapid rise followed by a slower increase until reaching a stable plateau.

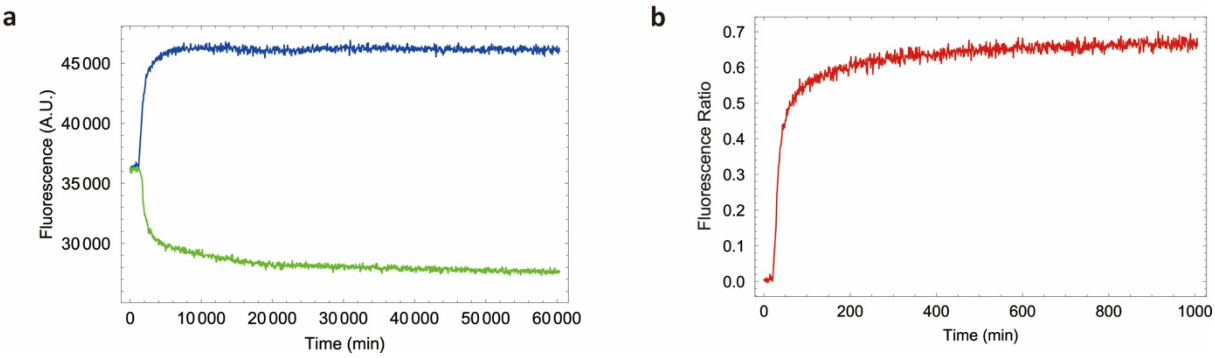


Figure 4.5 a. Kinetics of hinge reconfiguration of closed hinge using displacer strand and a mixture of displacer and extender strands compared with hinge folded in the closed, open, and extended states. **b.** Endpoint of fluorescence ratio.

4.3.1.3 TEM Analysis

TEM characterisation of hinge reconfiguration kinetics was performed by Dr Joshua Johnson (Imperial College London) at single-molecule resolution (**Figure 4.6**) (Also in **Chapter 5**). Closed hinge samples were incubated with a 5-fold molar excess of closer displacer and extender strands for varying durations (0, 0.25, 0.5, 1, 4, and 24 hours). Quantitative analysis of the resulting conformations revealed populations of closed, extended, and open hinge configurations, with their relative fractions calculated for each time point. To ensure accurate quantification, we excluded aggregated structures, overlapping molecules and poorly stained molecules.

The temporal analysis demonstrated successful reconfiguration, as evidenced by the increasing proportion of extended hinges with longer incubation times. However, a persistent subpopulation of hinges maintained open configurations throughout the process, suggesting they were at a transient intermediate state (open hinge configuration) during reconfiguration.

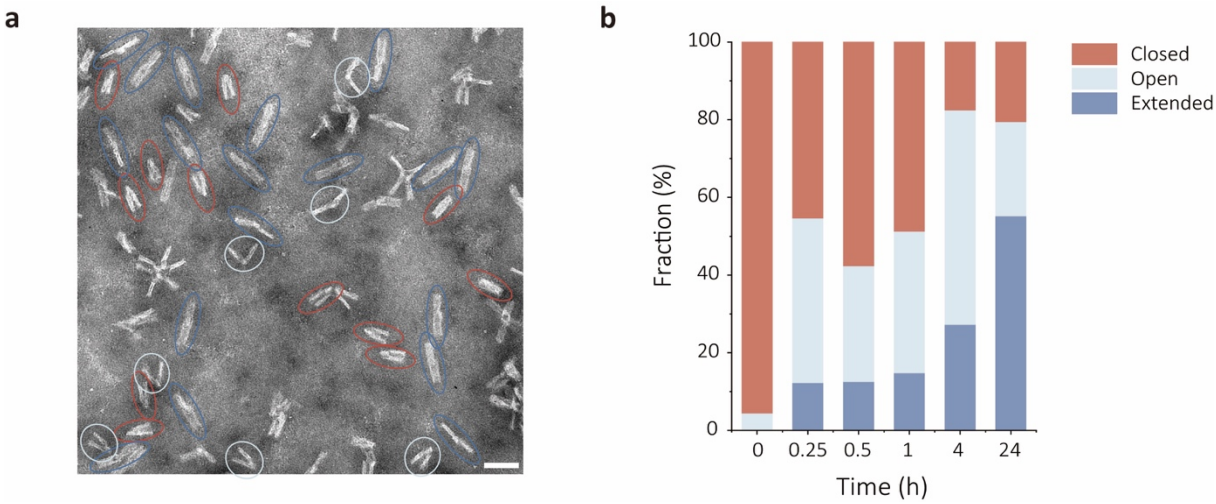


Figure 4.6 a. Representative TEM image of closed hinge after 4 hours incubation with 5-fold excess of closer displacer and extender strands (scale bar: 100 nm). Only structures which were clearly identifiable in the closed, open, or extended states were counted while aggregates, overlapping structures, or structures with unclear stain were not included. **b.** Fraction of hinge in closed, open, or extended states counted on TEM images after various incubation times.

4.3.2 Nanopore Characterisation of DNA Origami Hinge

4.3.2.1 Nanopipette Characterisation

The nanopores used in this chapter and next chapter were nanopipettes fabricated using Protocol 2 (**Table 2.1**). The SEM image of the nanopipette is shown in **Figure 2.4**. A conical-shaped nanopore was formed at the tip of the nanopipette, with a diameter calculated to be 22 ± 3 nm based on measurements from five nanopipettes.

Electrochemical characterisation was conducted using I-V measurements (**Figure 4.7**). This process involved applying a voltage range of −400 mV to +400 mV in 50 mV increments across the nanopipette while it was immersed in a buffer solution containing 1 M KCl, 12.5 mM $MgCl_2$, and 10 mM Tris 1 mM EDTA (pH = 8). The conductance of the quartz nanopipettes was

determined to be G = 36.8 ± 3.1 nS using **Equation 2.1**, based on measurements from 20 different nanopipettes.

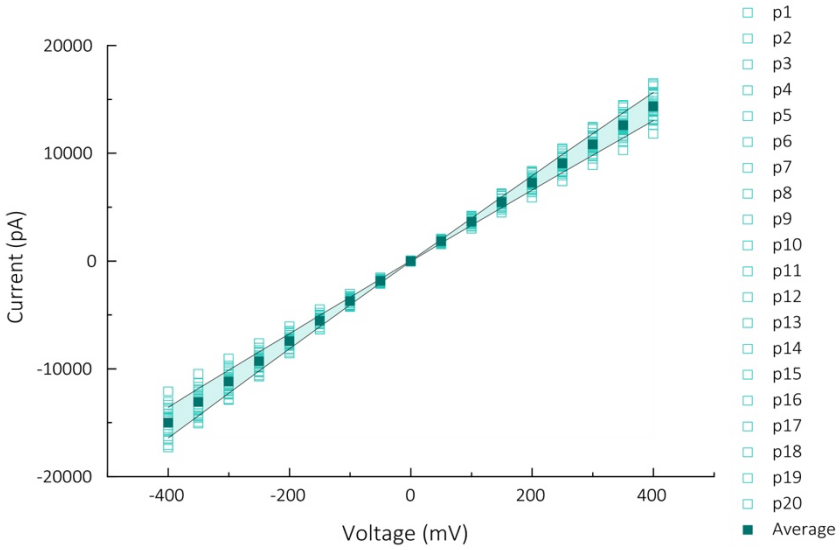


Figure 4.7 I-V characterisation of the nanopipettes fabricated using Protocol 2. The measurements were performed in 1 M KCl, 12.5 mM $MgCl_2$, 10 mM Tris, 1 mM EDTA, pH = 8. The conductance of the quartz nanopore was 36.8 ± 3.1 nS (n = 20), calculated from the ohmic region (± 100 mV). The error band represents one standard deviation.

4.3.2.2 Closed Hinge vs Extended Hinge

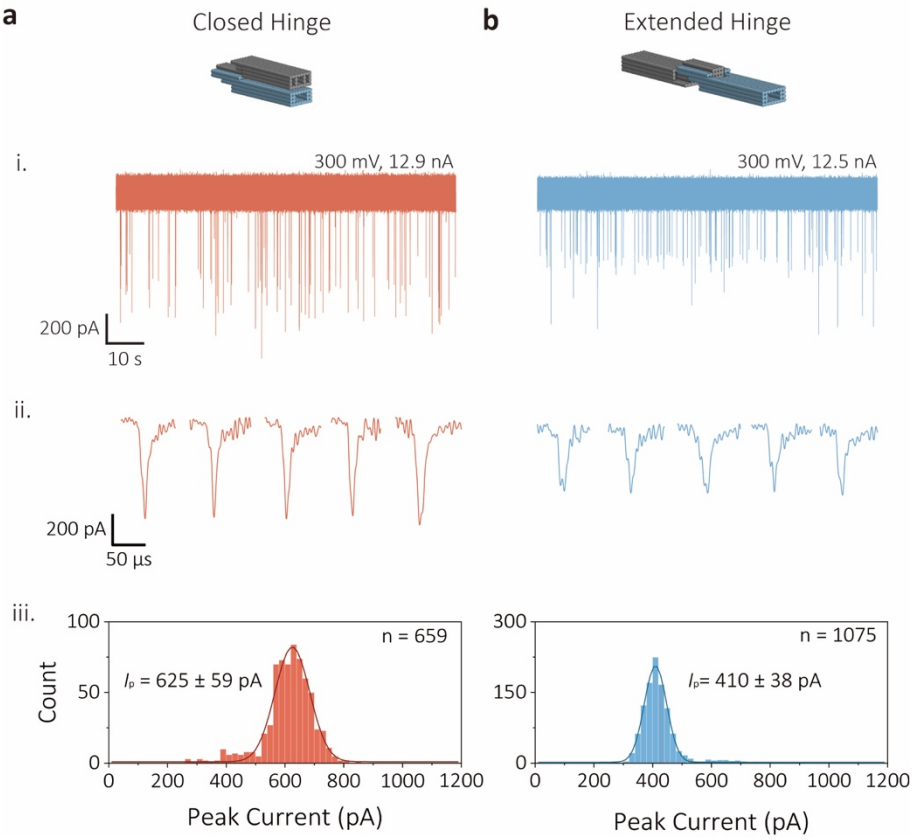


Figure 4.8 Nanopore detection of closed and extended DNA origami hinges. **a.** Ionic current analysis of the closed hinge (300 pM): i. Representative current-time trace. ii. Example translocation events. iii. Peak current distribution. **b.** Corresponding data for the extended hinge (300 pM), measured under identical conditions. All experiments were conducted using the same nanopipette in a buffer containing 1 M KCl, 12.5 mM $MgCl_2$, 10 mM Tris, and 1 mM EDTA (pH 8) at a voltage bias of 300 mV.

Nanopore sensing offers substantial throughput advantages over TEM imaging, enabling the rapid characterisation of hundreds to thousands of biomolecules within brief experimental timescales. This technique's operation in aqueous environments renders it particularly suitable for analysing dynamic DNA nanostructures. We proposed that incorporating our hinge mechanism with nanopore sensing could expand its functional capabilities. To evaluate this hypothesis, we performed nanopore translocation experiments to investigate potential differences in ionic current signatures between closed and extended hinge conformations. The

experimental setup employed a 1 M KCl buffer filling both the nanopipette interior and exterior reservoir, with hinge molecules suspended in the external electrolyte bath. Due to the uniform negative surface charge of the hinge structures, the application of a positive voltage bias enabled electrophoretic-driven translocation from the bath through the nanopore into the pipette interior.

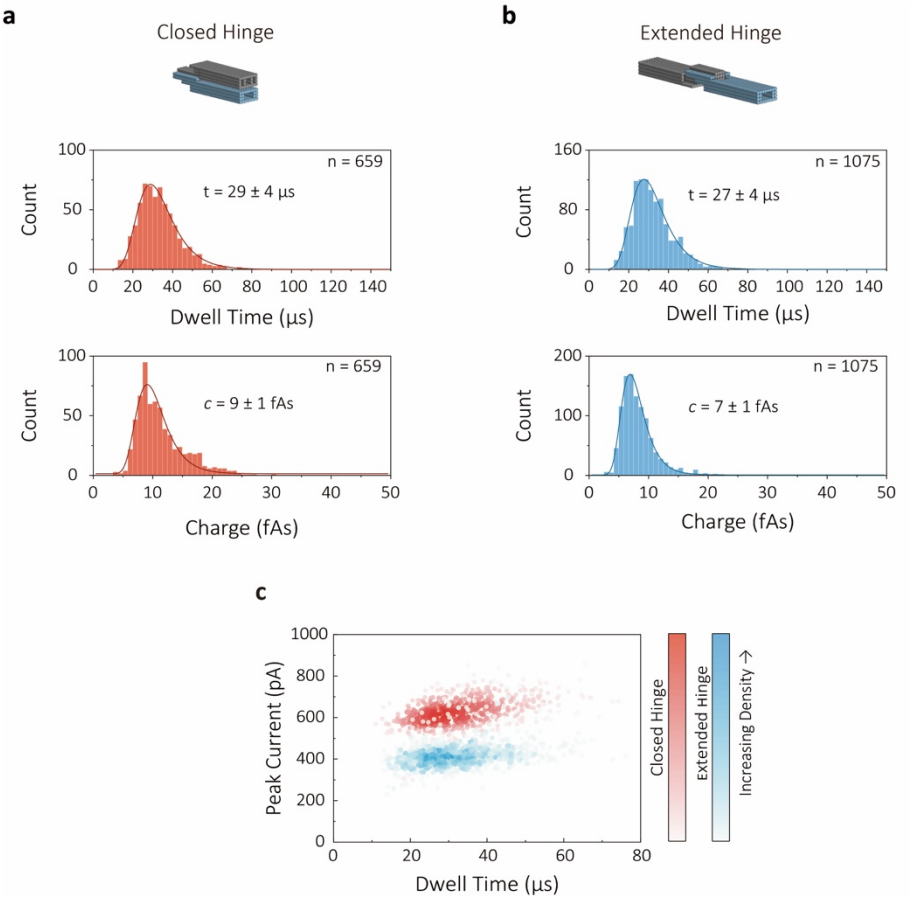


Figure 4.9 Nanopore detection of closed and extended DNA origami hinges. Dwell time and charge statistics for translocation of **a.** closed hinge (300 pM) and **b.** extended hinge (300 pM). **c.** Scatter plot of peak current vs dwell time for closed and extended hinges, illustrating distinct event distributions.

Figure 4.8 displays representative time-current traces and characteristic ionic current events from translocation experiments comparing closed and extended hinge configurations (300 pM). The analysis identified frequent current blockades, each representing the passage of either hinge conformation through the nanopore. These blockade events arise because in high-salt buffer conditions, the volume-excluded ions from the translocating hinge structure significantly

outnumber its accompanying counterions [30, 31]. Both hinge states produced similarly shaped single-peak events, preventing reliable conformation discrimination based solely on event morphology. However, closed hinge translocations consistently generated larger current deviations (625 ± 59 pA mean peak current) compared to extended hinge events (410 ± 38 pA). This difference reflects the greater cross-sectional area of closed configurations, which temporarily displace more ions during translocation, thereby creating stronger current perturbations.

Additional analysis, detailed in **Figure 4.9**, showed that the mean dwell time for closed hinge and extended hinge events was 29 ± 4 μs and 27 ± 4 μs, respectively, while the mean charge was 9 ± 1 fAs and 7 ± 1 fAs, respectively. Notably, the peak current of closed hinge translocation events was approximately 200 pA higher than that of extended hinge events. This substantial difference in peak current between the two types of hinge events is illustrated in the scatter plot. Theoretically, extended and closed hinges should exhibit different dwell times due to their varying lengths [32]. However, our DNA origami hinge is relatively short compared to the nanopore length, resulting in an exceptionally brief translocation time. This makes it challenging to accurately resolve the duration of the event, even with a high-bandwidth amplifier.

4.2.3.3 Voltage Dependant

We systematically investigated the translocation behaviour of both closed and extended hinge states across a range of applied voltages (150–350 mV). The data revealed a pronounced voltage dependence, with translocation event frequency increasing substantially at higher potentials (**Figure 4.10** and **Figure 4.12**). To quantify these effects, we analysed three key parameters—dwell time, peak current amplitude, and blockade charge—with comparative distributions for both conformational states presented in **Figure 4.11** and **Figure 4.13**. As the voltage increased, we observed a notable rise in peak current and a corresponding decrease in dwell time for both hinge states. However, the reduction in dwell time for the extended hinge was less pronounced

than for the closed hinge. Notably, the charge remained largely unchanged across varying voltage.

Peak current analysis revealed conformation-dependent signatures. Extended hinge events showed a narrow distribution centred around the mean value, contrasting with the broader dispersion observed for closed hinge configurations (**Figure 4.14**). Although dwell times showed minimal voltage-dependent variation between states, closed hinges exhibited significantly greater charge distribution width (**Figure 4.15**). The marked separation in peak current distributions enables reliable differentiation of hinge states without requiring additional parameters.

For subsequent translocation experiments, 300 mV was chosen as the optimal applied potential, satisfying two critical criteria: (1) maximizing the peak current differential between closed and extended hinge configurations, and (2) generating an ideal event frequency for robust statistical analysis. This voltage selection enabled clear discrimination of conformational states while maintaining sufficient data throughput for quantitative comparisons.

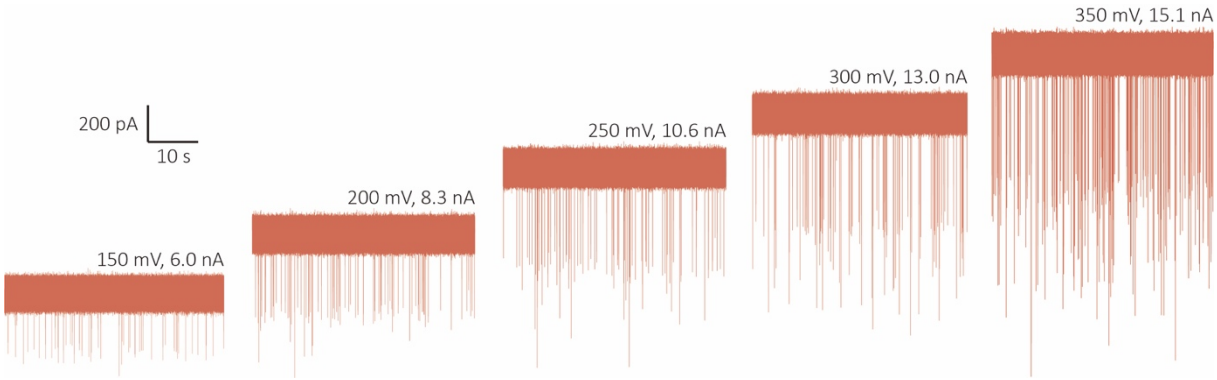


Figure 4.10 Voltage dependant current-time traces for translocation of closed hinge (300 pM) at voltage ranging from 150 mV to 350 mV in 1 M KCl, 12.5 mM $MgCl_2$, 10 mM Tris, 1 mM EDTA, pH = 8.

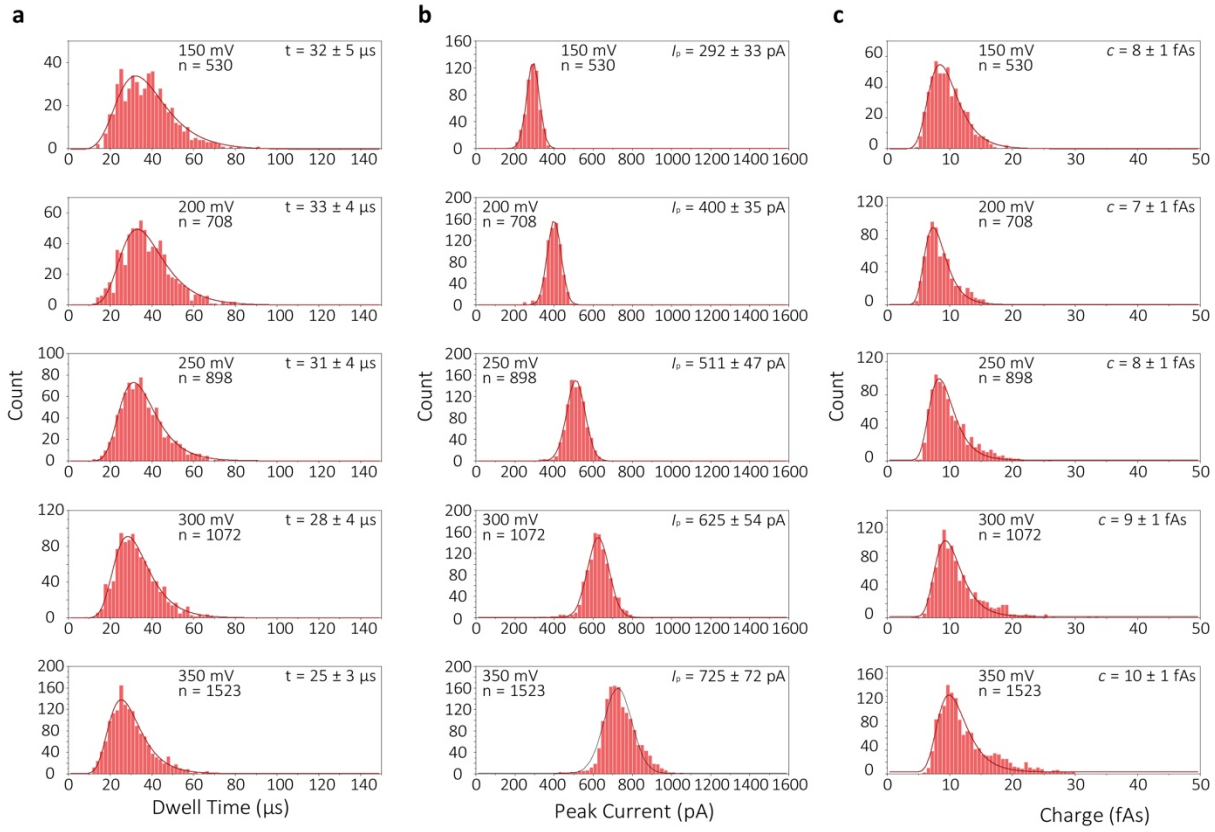


Figure 4.11 Volatge dependant **a.** dwell time, **b.** peak current and **c.** charge statistics for translocation of closed hinge (300 pM) at voltage ranging from 150 mV to 350 mV in 1 M KCl, 12.5 mM $MgCl_2$, 10 mM Tris, 1 mM EDTA, pH = 8.

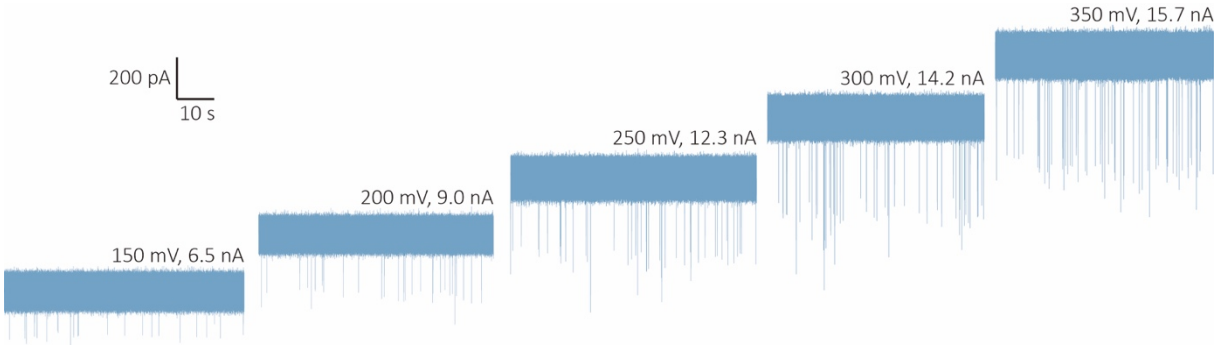


Figure 4.12 Volatge dependant current-time traces for translocation of extended hinge (300 pM) at voltage ranging from 150 mV to 350 mV in 1 M KCl, 12.5 mM $MgCl_2$, 10 mM Tris, 1 mM EDTA, pH = 8.

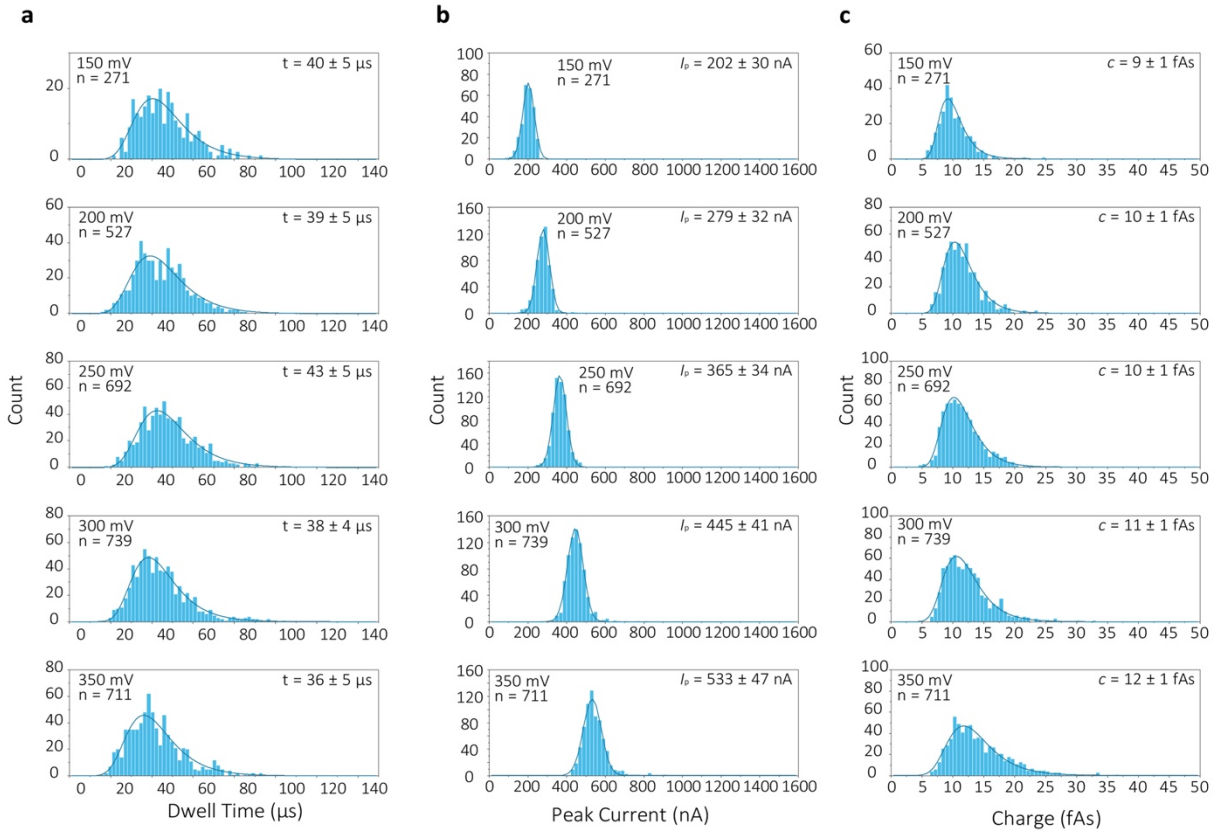


Figure 4.13 Volatge dependant **a.** dwell time, **b.** peak current and **c.** charge statistics for translocation of extened hinge (300 pM) at voltage ranging from 150 mV to 350 mV in 1 M KCl, 12.5 mM $MgCl_2$, 10 mM Tris, 1 mM EDTA, pH = 8.

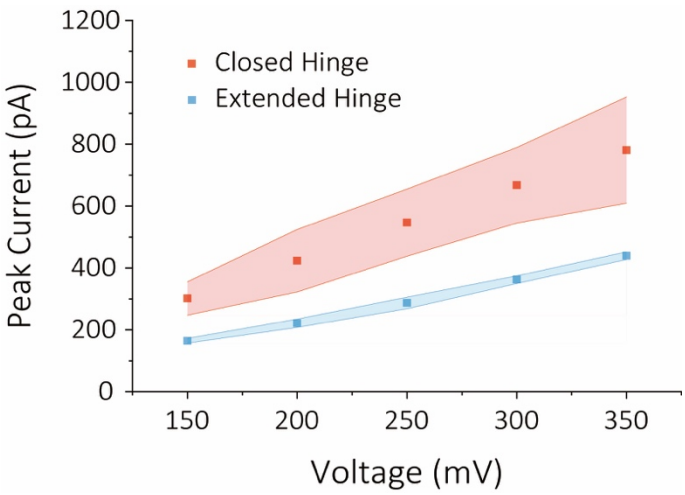


Figure 4.14 Voltage-dependent peak current characteristics for both hinge states. Shaded error bands represent one standard deviation from three independent experiments.

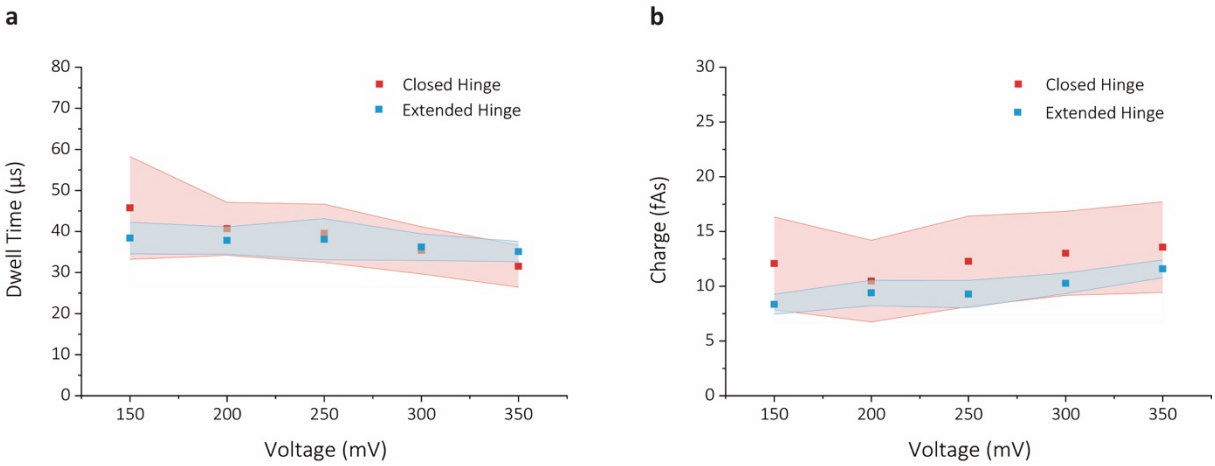


Figure 4.15 Voltage-dependant **a.** dwell time and **b.** charge for closed hinge and extended hinge. The error bands represent one standard deviation of three independent repeats.

4.2.3.4 Open Hinge

Nanopore analysis of open hinge (300 pM) translocations revealed two distinct event populations characterised by different peak current amplitudes (**Figure 4.16**). These populations exhibited mean peak currents of 416 ± 41 pA and 585 ± 89 pA, respectively. The predominant event type (69 ± 21% of total events, n = 3) showed current amplitudes matching

those of extended hinge configurations. The secondary population displayed currents approaching, but consistently below closed hinge reference values. We propose that these discrete states arise from nanopore-induced geometric constraints that force the open hinge to adopt either a quasi-extended or a quasi-closed conformation during translocation.

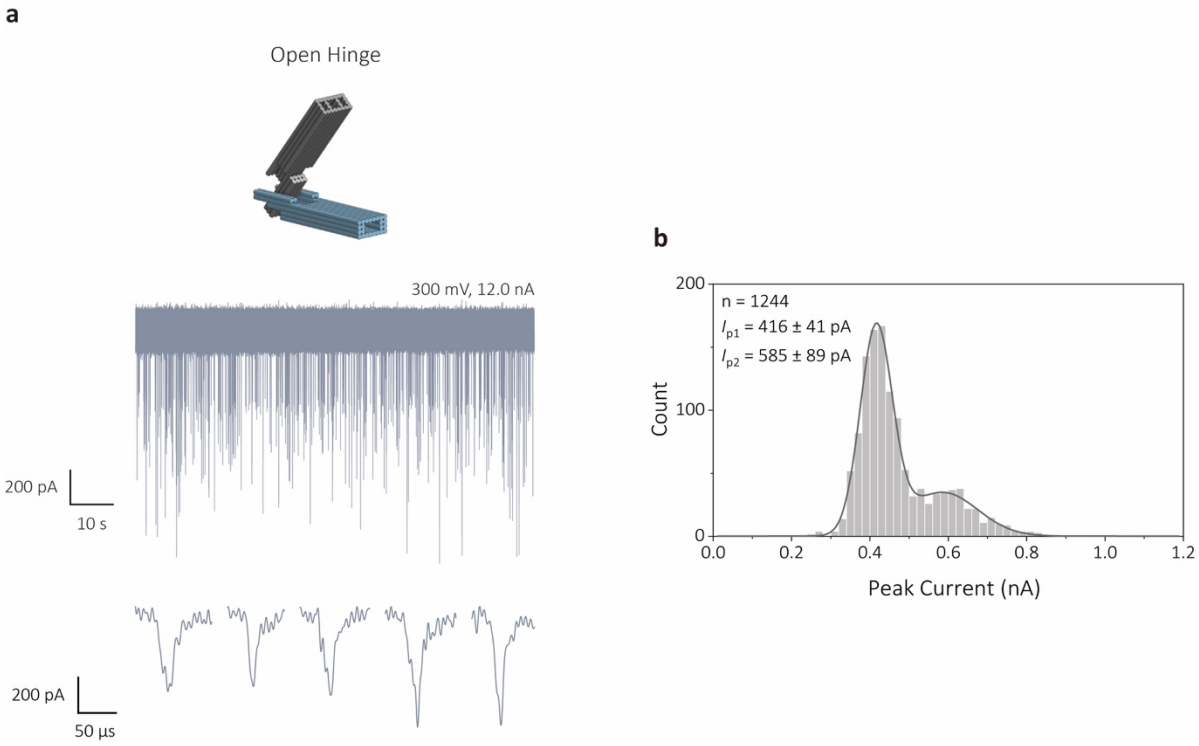


Figure 4.16 a. Current-time trace, typical events and **b.** peak current statistics for translocation of open hinge (300 pM). Experiments were performed with the same nanopipette (for closed and extended hinges) in 1 M KCl, 12.5 mM $MgCl_2$, 10 mM Tris, 1 mM EDTA, pH = 8, and at a voltage bias of 300 mV.

A small but consistent subpopulation of events (7.4 ± 1.4%) exhibited reduced peak currents within the closed hinge range (**Figure 4.8**). We propose that these events correspond to the translocation of open hinges, suggesting that some closed hinges failed to maintain their structural integrity, which was also indicated in TEM images (**Figure 4.6**).

4.4 Conclusion

This chapter introduces a dynamic DNA origami hinge mechanism capable of controlled reconfiguration between closed and extended states through strand displacement. TEM imaging verified successful hinge assembly, while bulk fluorescence assays employing a dual fluorophore-quencher pair confirmed the conformational transitions.

Single-molecule nanopore characterisation revealed distinct translocation signatures for each hinge configuration, with the open state exhibiting unique dynamic behaviour. These findings establish nanopore sensing as a powerful tool for real-time observation of nanostructure reconfiguration.

Building on this configurational discrimination capability, we propose applying this strategy to overcome current limitations in miRNA detection. The rapid translocation of small miRNAs typically produces undetectable signals, but our DNA origami hinge-based approach may enable their selective sensing at single-molecule level, as developed in the following chapter.

4.5 References

[1] Rothemund, P. W. Folding DNA to create nanoscale shapes and patterns. *Nature* **2006**, *440*, 297-302.

[2] Seeman, N. C.; Sleiman, H. F. DNA nanotechnology. *Nature Reviews Materials* **2017**, *3*.

[3] Castro, C. E.;Kilchherr, F.;Kim, D. N.;Shiao, E. L.;Wauer, T.;Wortmann, P.;Bathe, M.; Dietz, H. A primer to scaffolded DNA origami. *Nat Methods* **2011**, *8*, 221-229.

[4] Hong, F.;Zhang, F.;Liu, Y.; Yan, H. DNA Origami: Scaffolds for Creating Higher Order Structures. *Chem Rev* **2017**, *117*, 12584-12640.

[5] Wagenbauer, K. F.;Engelhardt, F. A. S.;Stahl, E.;Hechtl, V. K.;Stommer, P.;Seebacher, F.;Meregalli, L.;Ketterer, P.;Gerling, T.; Dietz, H. How We Make DNA Origami. *Chembiochem* **2017**, *18*, 1873-1885.

[6] Marras, A. E.;Zhou, L.;Su, H. J.; Castro, C. E. Programmable motion of DNA origami mechanisms. *Proc Natl Acad Sci U S A* **2015**, *112*, 713-718.

[7] Johnson, J. A.;Dehankar, A.;Winter, J. O.; Castro, C. E. Reciprocal Control of Hierarchical DNA Origami-Nanoparticle Assemblies. *Nano Lett* **2019**, *19*, 8469-8475.

[8] Kuzyk, A.;Schreiber, R.;Zhang, H.;Govorov, A. O.;Liedl, T.; Liu, N. Reconfigurable 3D plasmonic metamolecules. *Nat Mater* **2014**, *13*, 862-866.

[9] He, Z.;Shi, K.;Li, J.; Chao, J. Self-assembly of DNA origami for nanofabrication, biosensing, drug delivery, and computational storage. *iScience* **2023**, *26*, 106638.

[10] Chandrasekaran, A. R.;Anderson, N.;Kizer, M.;Halvorsen, K.; Wang, X. Beyond the Fold: Emerging Biological Applications of DNA Origami. *Chembiochem* **2016**, *17*, 1081-1089.

[11] Nguyen, L.;Dass, M.;Ober, M. F.;Besteiro, L. V.;Wang, Z. M.;Nickel, B.;Govorov, A. O.;Liedl, T.; Heuer-Jungemann, A. Chiral Assembly of Gold-Silver Core-Shell Plasmonic Nanorods on DNA Origami with Strong Optical Activity. *ACS Nano* **2020**, *14*, 7454-7461.

[12] Wang, J.;Yue, L.;Li, Z.;Zhang, J.;Tian, H.; Willner, I. Active generation of nanoholes in DNA origami scaffolds for programmed catalysis in nanocavities. *Nat Commun* **2019**, *10*, 4963.

[13] Zhou, L.;Marras, A. E.;Su, H. J.; Castro, C. E. DNA origami compliant nanostructures with tunable mechanical properties. *ACS Nano* **2014**, *8*, 27-34.

[14] Kuzuya, A.;Sakai, Y.;Yamazaki, T.;Xu, Y.; Komiyama, M. Nanomechanical DNA origami 'single-molecule beacons' directly imaged by atomic force microscopy. *Nat Commun* **2011**, *2*, 449.

[15] Steinhauer, C.;Jungmann, R.;Sobey, T. L.;Simmel, F. C.; Tinnefeld, P. DNA origami as a nanoscopic ruler for super-resolution microscopy. *Angew Chem Int Ed Engl* **2009**, *48*, 8870-8873.

[16] Hernandez-Ainsa, S.; Keyser, U. F. DNA origami nanopores: developments, challenges and perspectives. *Nanoscale* **2014**, *6*, 14121-14132.

[17] Bell, N. A.;Engst, C. R.;Ablay, M.;Divitini, G.;Ducati, C.;Liedl, T.; Keyser, U. F. DNA origami nanopores. *Nano Lett* **2012**, *12*, 512-517.

[18] Hernandez-Ainsa, S.;Bell, N. A.;Thacker, V. V.;Gopfrich, K.;Misiunas, K.;Fuentes-Perez, M. E.;Moreno-Herrero, F.; Keyser, U. F. DNA origami nanopores for controlling DNA translocation. *ACS Nano* **2013**, *7*, 6024-6030.

[19] Burns, J. R.;Stulz, E.; Howorka, S. Self-assembled DNA nanopores that span lipid bilayers. *Nano Lett* **2013**, *13*, 2351-2356.

[20] Langecker, M.;Arnaut, V.;Martin, T. G.;List, J.;Renner, S.;Mayer, M.;Dietz, H.; Simmel, F. C. Synthetic lipid membrane channels formed by designed DNA nanostructures. *Science* **2012**, *338*, 932-936.

[21] Ding, T.;Yang, J.;Pan, V.;Zhao, N.;Lu, Z.;Ke, Y.; Zhang, C. DNA nanotechnology assisted nanopore-based analysis. *Nucleic Acids Res* **2020**, *48*, 2791-2806.

[22] Joty, K.;Ghimire, M. L.;Kahn, J. S.;Lee, S.;Alexandrakis, G.; Kim, M. J. DNA Origami Incorporated into Solid-State Nanopores Enables Enhanced Sensitivity for Precise Analysis of Protein Translocations. *Anal Chem* **2024**, *96*, 17496-17505.

[23] Raveendran, M.;Lee, A. J.;Sharma, R.;Walti, C.; Actis, P. Rational design of DNA nanostructures for single molecule biosensing. *Nat Commun* **2020**, *11*, 4384.

[24] Wang, J.;Zhu, J.;Li, Y.;Gui, C.;Zhu, B.;Zhu, Z.; Chen, D. Rational design of a 3D DNA origami cube as an ideal signal carrier for glass nanopore-based biosensors. *Anal Chim Acta* **2025**, *1343*, 343660.

[25] Ding, T.;Yang, J.;Wang, J.;Pan, V.;Lu, Z.;Ke, Y.; Zhang, C. Shaped DNA origami carrier nanopore translocation influenced by aptamer based surface modification. *Biosens Bioelectron* **2022**, *195*, 113658.

[26] Zhu, J.;Tivony, R.;Boskovic, F.;Pereira-Dias, J.;Sandler, S. E.;Baker, S.; Keyser, U. F. Multiplexed Nanopore-Based Nucleic Acid Sensing and Bacterial Identification Using DNA Dumbbell Nanoswitches. *J Am Chem Soc* **2023**, *145*, 12115-12123.

[27] Yang, J.;Zhao, N.;Liang, Y.;Lu, Z.; Zhang, C. Structure-flexible DNA origami translocation through a solid-state nanopore. *RSC Adv* **2021**, *11*, 23471-23476.

[28] Stahl, E.;Martin, T. G.;Praetorius, F.; Dietz, H. Facile and scalable preparation of pure and dense DNA origami solutions. *Angew Chem Int Ed Engl* **2014**, *53*, 12735-12740.

[29] Bellot, G.;McClintock, M. A.;Chou, J. J.; Shih, W. M. DNA nanotubes for NMR structure determination of membrane proteins. *Nat Protoc* **2013**, *8*, 755-770.

[30] Smeets, R. M.;Keyser, U. F.;Krapf, D.;Wu, M. Y.;Dekker, N. H.; Dekker, C. Salt dependence of ion transport and DNA translocation through solid-state nanopores. *Nano Lett* **2006**, *6*, 89-95.

[31] Wang, V.;Ermann, N.; Keyser, U. F. Current Enhancement in Solid-State Nanopores Depends on Three-Dimensional DNA Structure. *Nano Lett* **2019**, *19*, 5661-5666.

[32] Fologea, D.;Uplinger, J.;Thomas, B.;McNabb, D. S.; Li, J. Slowing DNA translocation in a solid-state nanopore. *Nano Lett* **2005**, *5*, 1734-1737.

Chapter 5 Nanopore Detection of miRNA with Reconfigurable DNA Origami Carrier

Synopsis

This chapter presents the development of a reconfigurable DNA origami hinge serving as a molecular carrier for nanopore detection of PCa-associated miRNA-141-3p. The hinge mechanism exhibits programmable conformational switching from closed to extended states upon target miRNA binding, generating characteristic ionic current signatures during nanopore translocation. Experimental results demonstrate nanomolar-level detection sensitivity and exceptional sequence specificity in discriminating miRNA-141-3p from similar sequences. These advances establish DNA nanostructure-enhanced nanopore sensing as a promising platform for ultrasensitive biomarker analysis in complex biological media.

Chapter 5 Nanopore Detection of miRNA with Reconfigurable DNA Origami Carrier..... 149

5.1 Introduction 151

5.2 Methods 153

5.2.1 Kinetic Assays 153

5.2.2 Hinge-miRNA Binding Preparation 154

5.2.3 Sigmoidal Trend Fitting 154

5.3 Results and Discussion 155

5.3.1 DNA Origami Hinge Carrier 155

5.3.1.1 Hinge Mechanism and miRNA Binding 155

5.3.1.2 Kinetic Assays 157

5.3.1.3 TEM Analysis 160

5.3.2 DNA Origami Hinge Carrier for Nanopore Detection of miRNA 161

5.3.2.1 Direct Detection of miRNA-141 161

5.3.2.2 Nanopore Study of Binding Dynamic Mechanism 162

5.3.2.3 Nanopore Study of Binding Mechanism 167

5.3.2.4 Detection in Human Serum 168

5.3.2.5 Dual Detection of miRNA-141 and miRNA-375 171

5.4 Conclusion 173

5.5 References 174

5.1 Introduction

Early disease diagnosis enables timely therapeutic intervention and improved clinical outcomes by identifying pathologies during their most treatable stages. Contemporary biosensing platforms achieve this through sensitive detection of disease biomarkers, including proteins, nucleic acids, and metabolites [1-3]. Modern biosensor architectures employ diverse detection modalities such as optical, electrochemical, SPR, and microstructured systems, enabling rapid biomarker quantification [4-8]. Nanotechnology-enhanced biosensors now permit real-time, point-of-care diagnostics with minimal sample requirements [9, 10].

Nanopore sensing has emerged as a particularly promising biosensing platform [11-13]. Conventional solid-state nanopore systems improve selectivity through surface modifications with biomolecular receptors, which enhance target transport kinetics while reducing nonspecific interactions [14-16]. However, these approaches suffer from uncontrolled receptor placement and limited sensitivity for small biomolecules [17]. An alternative strategy employs molecular carriers that bind targets prior to translocation [18, 19]. These carrier-target complexes generate distinctive current signatures, offering advantages over surface modification through precise receptor positioning and reduced size dependence. Various carrier systems including nanoparticles and linear DNA constructs have enabled direct detection in clinical samples, with some achieving multiplexed analysis [18, 20-22].

Among the most promising strategies for building molecular carriers is that of DNA origami, which allows the fabrication of monodisperse nanostructures with precisely controlled morphology and mechanical properties [23-27]. The DNA origami technique enables the production of monodisperse nanostructures with precisely controlled morphology and mechanical characteristics, which can be decorated with ligands at precise locations [28-31]. Constructing molecular carriers with DNA origami may bring substantial advantages compared to simpler carriers constructed from flexible strands. For instance, the rigidity of DNA origami helps avoid false positive signals produced by folding or knotting of the carrier

configurations producing false-positive signals, enhancing the accuracy and reliability of nanopore-based detection techniques [18, 32, 33]. Despite these successes, the full potential of DNA origami molecular carriers remains to be explored. Most studies have focused on predominantly static DNA origami carriers, while few have harnessed the potential of reconfigurable DNA origami [34, 35].

This chapter provides further investigation of the DNA origami hinge mechanism initially presented in **Chapter 4**, specifically designed to improve nanopore-based detection of small biomolecules (**Figure 5.1**). We focus on miRNAs as target analytes due to their significance as disease biomarkers [36, 37]. In addition, the challenges associated with achieving sufficiently selective and specific detection with nanopore sensing, target miRNA needs to be discriminated from the other numerous species of miRNAs and structurally similar molecules present in complex biofluidic environments. By adjusting to the hinge mechanism, the closed hinge configuration can be disrupted via toehold-mediated strand displacement [38, 39], enabling the hinge to relax into its extended state upon binding to the target miRNA. These distinct structural states produce characteristic translocation events during nanopore sensing, allowing for straightforward identification of the target strand. Our findings demonstrate that this sensing strategy enables the detection of low-concentration miRNA in human serum with excellent selectivity, effectively distinguishing similar miRNA sequences. Notably, this approach eliminates the need for laborious sample preparation, which would be required in conventional detection methods [40].

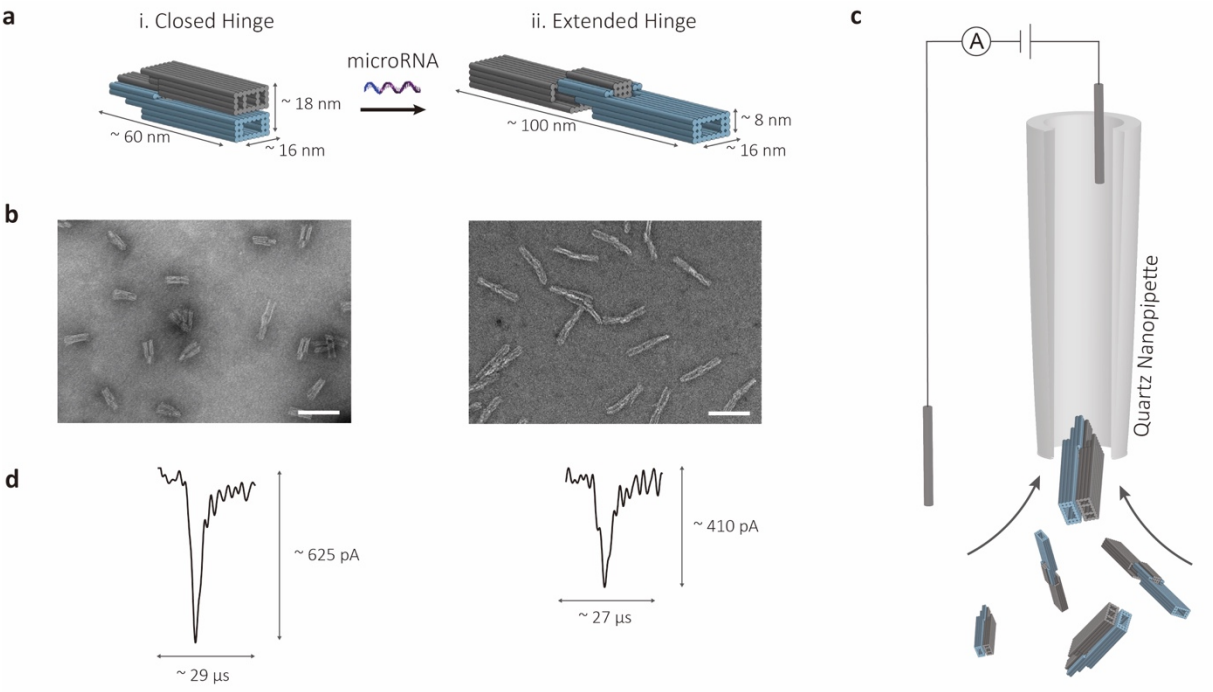


Figure 5.1 Design and nanopore sensing of the reconfigurable DNA origami hinge. **a.** Schematic illustration of the DNA hinge reconfiguration. Upon binding to miRNA, the hinge transitions from a closed to an extended state, with the cross-sectional area of the closed hinge being approximately twice that of the extended hinge. **b.** TEM images of the closed and extended hinge (scale bar: 100 nm). **c.** Schematic of the nanopore sensing platform. The nanopipette is filled with 1 M KCl Tris-EDTA buffer, with DNA hinges initially placed outside. Under an applied positive voltage, electrophoretic force drives the hinges from the outer to the inner chamber of the nanopipette. **d.** Representative nanopore translocation events of closed and extended hinges, showing distinct differences in peak current.

5.2 Methods

5.2.1 Kinetic Assays

Samples for kinetics assays were prepared using an Opentrons OT-2 pipetting robot to minimise human error in experiments monitoring more than 12 samples. PEG purified hinges were incubated at 45°C for ~15 minutes prior to use. The robot was programmed to make

multiples of 12 wells, each with 40 µL of 5 nM hinges with 25 nM extender strands, 250nM closer displacer strands, and 0, 0.2, 0.5, 1, 2, 5, 10, 20, 50, 100, 200, or 500 nM target strand in a buffer containing 1 M KCl, 12.5 mM $MgCl_2$, 5 mM Tris and 0.5 mM EDTA. A stop was included before adding the final solution of the target strand to allow the plate to be transferred to a plate reader (ClarioStar Plus) and scanned for ~10 minutes or until a stable baseline fluorescence was observed in all wells. Then, the plate was transferred back into the pipetting robot to add and mix the solution containing the extender, closer displacer, and target strands. The plate was then quickly transferred back to the plate reader, and the fluorescence of each well was monitored once every 45 seconds for 12 hours with orbital shaking at 300 rpm between each read.

5.2.2 Hinge-miRNA Binding Preparation

For the detection of miRNAs, the closed hinge at a concentration of 1 nM was incubated with miRNAs (at variable concentrations of 0, 1, 10, 100, 1000 nM), at 20 °C for 8 hours. For Kinetic study, the closed hinge at a concentration of 1 nM was incubated with miRNAs at a concentration of 1000 nM, at 20 °C for 0, 2, 4, 8, 16 hours. The incubated samples were then diluted with a buffer containing 1 M KCl, 12.5 mM $MgCl_2$, 10 mM Tris, and 1 mM EDTA (pH = 8) to achieve a final carrier concentration of 200 pM for subsequent nanopore translocation experiments

5.2.3 Sigmoidal Trend Fitting

A logistic function was employed to fit the sigmoidal binding dynamics curve [41]:

$$y = \frac{A_1 - A_2}{1 + \left(\frac{x}{x_0}\right)^p} + A_2 \qquad 5.1$$

where A_1 and A_2 represent the initial and final values of the binding ratio, respectively, while x_o denotes the inflection point (centre) of the curve, corresponding to the time at which the response is half-maximal (half-life), p is the power value. The parameter p defines the curve's steepness, reflecting the cooperativity of the binding process.

The half-life of the binding can be expressed by the following equation [20, 42]:

$$t_{1/2} = \frac{\ln 2}{k_{on} \times [A]} \quad 5.2$$

where $t_{1/2}$ represents the half-life of the binding process, k_{on} is the association rate constant, and $[A]$ denotes the concentration of the closed hinge carrier.

A Hill function was employed to fit the sigmoidal binding curve [43, 44]:

$$y = A_1 + (A_2 - A_1) \cdot \frac{x^n}{k^n + x^n} \quad 5.3$$

where A_1 and A_2 represent the initial and final values of the binding ratio, respectively, k is the Michaelis constant, and n denotes the number of cooperative binding sites. k^n denotes the inflection point (centre) of the curve, corresponding to the concentration at which the response is half-maximal (dissociation constant K_d).

5.3 Results and Discussion

5.3.1 DNA Origami Hinge Carrier

5.3.1.1 Hinge Mechanism and miRNA Binding

To improve the sequence specificity of the DNA origami hinges—particularly for targets such as specific miRNAs—we introduced a design modification in which one pair of closer overhangs was replaced with a set of "latching overhangs" that are engineered to bind directly to each other (**Figure 5.2**). These latching overhangs establish a singular connection between the hinge arms when the closer helper strands are removed, effectively locking the hinge in a closed conformation. The latching strand on the bottom arm features a 6-nucleotide toehold that is part of a domain complementary to the target sequence. In addition, the latching region includes 5 supplementary base pairs that are not displaced by the target, serving to stabilize the closed configuration.

Although maintaining the hinge in a closed conformation results in a high entropic penalty, the added base pairing within the latching region provides sufficient reinforcement to keep the hinge closed in the absence of the target. Importantly, this reinforcement is intentionally limited, such that it does not prevent the hinge from opening once the target strand is fully hybridised. Upon the introduction of closer displacer strands and extender strands, the hinge becomes primed to respond to target recognition.

In this configuration, the hinge behaves analogously to a molecular mousetrap—remaining closed under stabilizing interactions until a specific target is detected. Binding of the target strand to the toehold domain initiates a strand displacement reaction, which overcomes the stabilizing base pairs and triggers a conformational change, allowing the hinge to open. This mechanism enables sensitive and specific detection of biomolecular targets, integrating structural control with sequence-selective responsiveness.

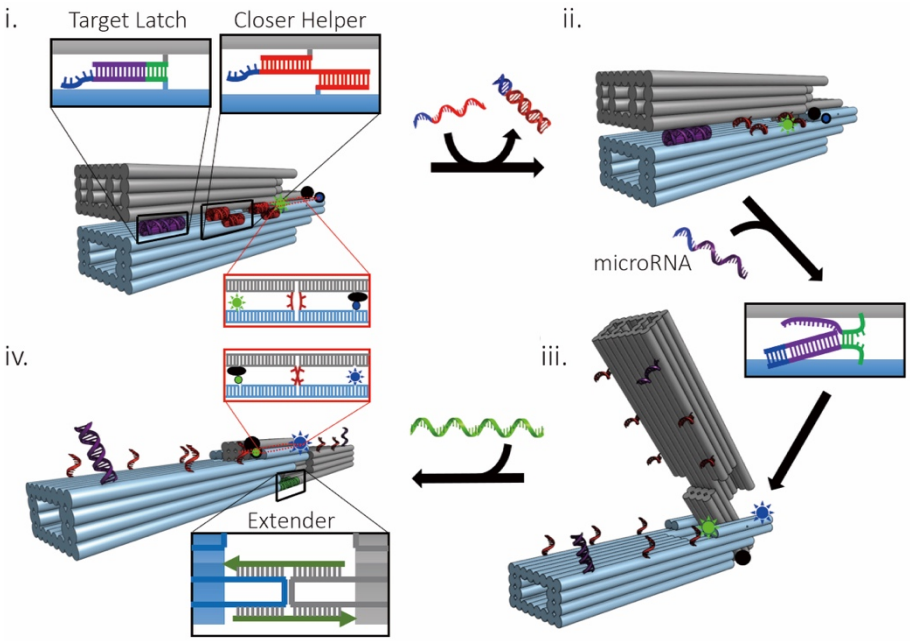


Figure 5.2 Schematic of the triggered hinge reconfiguration process: i. The hinge is initially folded in a closed configuration, with the top and bottom arms linked by a target latch and five closer helper strands. A pair of fluorophores (Alexa488 and Atto550) are positioned on the bottom arm, with a quencher on the top arm, which suppresses Alexa488 fluorescence in the closed state. ii. The hinge is primed for target detection after closer helper strands are removed via toehold-mediated strand displacement. iii. The target strand displaces the top arm latching strand, allowing the hinge to relax into an open configuration. The quencher moves away from the Alexa488. iv. The extender strands lock the hinge in an extended configuration to ensure irreversible reconfiguration. The quencher is now closer to the Atto550. This design allows for the anti-correlation signals from the two fluorophores, facilitating the readout of the hinge state.

5.3.1.2 Kinetic Assays

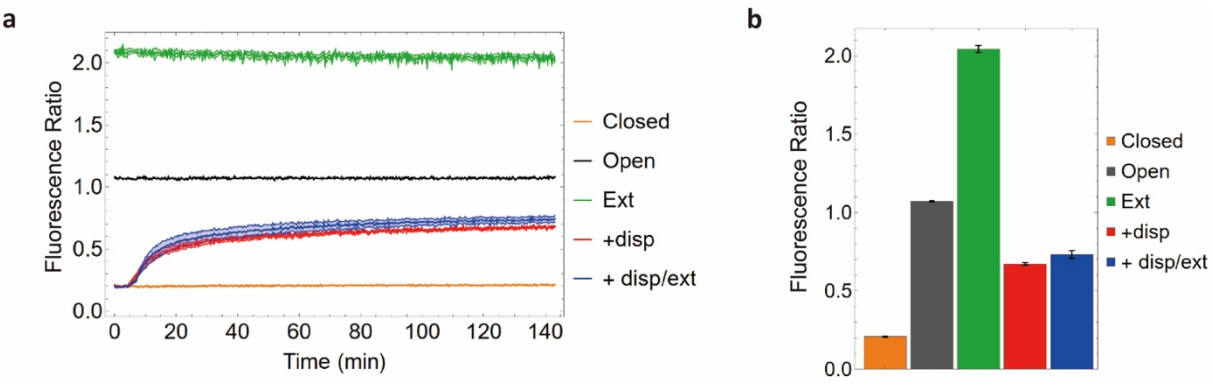


Figure 5.3 a. Example raw Fluorescence data for Alexa488 and Atto550 dyes collected after adding 500nM of miRNA-375-3p_DNA to closed hinge with a miRNA-375-3p latching strand. **b.** Ratio of raw data (with -1 offset) helps eliminate sample variation and artifacts.

As described in **Chapter 4**, the conformational transition of the hinge was effectively monitored using a dual fluorophore–quencher system. During the transition from the closed to the extended state, an increase in Alexa488 fluorescence is observed, while Atto550 fluorescence decreases proportionally. This inverse fluorescence relationship serves as a robust and sensitive indicator of the hinge's dynamic behaviour, enabling precise tracking of structural changes.

We investigated the kinetics of the hinge opening process triggered by DNA analogues of miRNA-141-3p and miRNA-375-3p, referred to as miRNA-141-3p_DNA and miRNA-375-3p_DNA, respectively. These miRNAs have been identified in previous studies as valuable biomarkers for PCa, highlighting their potential relevance for early detection and disease monitoring [45, 46]. These studies were conducted across a range of concentrations to evaluate the concentration-dependent response and binding efficiency of each target analogue.

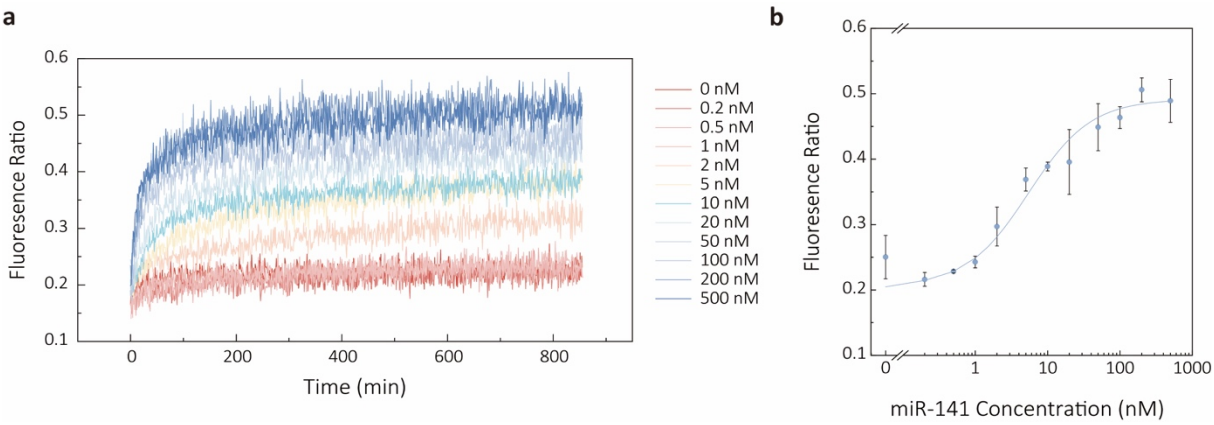


Figure 5.4 a. Fluorescence response against different miRNA-141-3p_DNA concentrations over time for closed hinge with a miRNA-141-3p latching strand. **b.** Endpoint fluorescence ratio as a function of miRNA-141-3p_DNA concentration, fitted using a Hill equation, yielding a dissociation constant (K_d) of 5.5 ± 0.3 nM. Error bars indicate one standard deviation from 3 independent experimental repeats.

We detected fluorescence changes in both the Alexa488 and Atto550 channels, which were expected to exhibit anti-correlated behaviour (**Figure 5.3**). To track the hinge opening transition, we computed the ratio between the two fluorescence signals, adopting a ratiometric approach that effectively minimised artifacts arising from sample-to-sample variability. The resulting fluorescence-ratio traces showed a gradual increase over time, eventually plateauing at levels that correlated with the concentration of the target strands (**Figure 5.4a.** and **Figure 5.5a.**). By interpreting the plateau fluorescence ratios as analogous to binding ratios, we constructed a pseudo-binding curve describing the interaction between the hinge and target strands (**Figure 5.4a.** and **Figure 5.5b.**). The hinge engineered to detect miRNA-141-3p_DNA exhibited a stronger binding affinity compared to the hinge designed for miRNA-375-3p_DNA, as reflected by their respective dissociation constants (K_d), which were determined to be 5.5 ± 0.3 nM and 45.6 ± 0.5 nM. However, no clear correlation was observed between the rate of change of the fluorescence ratio and the concentration of the target strands.

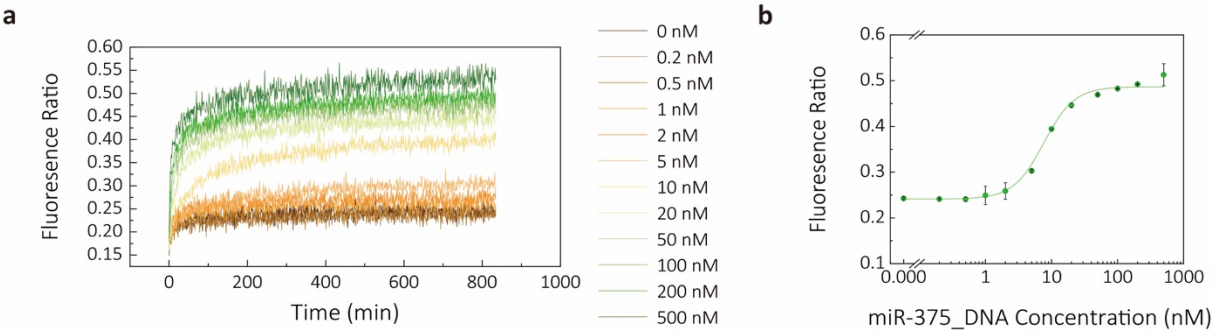


Figure 5.5 a. Fluorescence response against different miR-375-3p_DNA concentrations over time for closed hinge with a miR-375-3p latching strand. **b.** Endpoint of fluorescence ratio against miR-375-3p_DNA concentration. The data were fitted with a Hill equation, the dissociation constant (K_d) was determined to be 45.6 ± 0.5 nM. The error bars represent one standard deviation of independent experimental repeats.

5.3.1.3 TEM Analysis

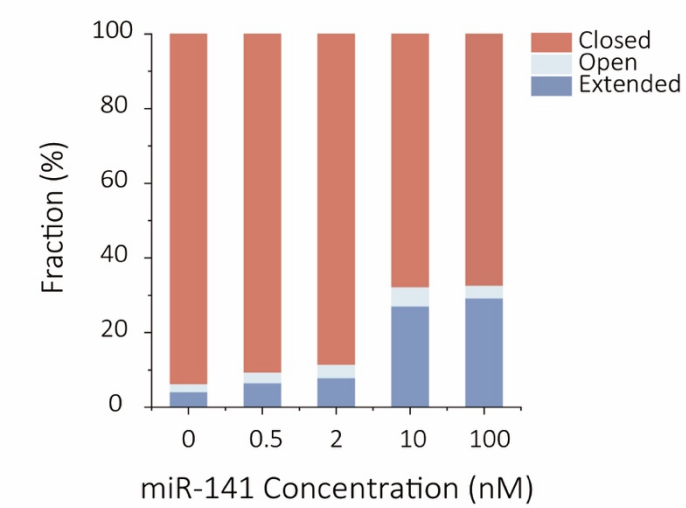


Figure 5.6 TEM-based quantification of hinge state distribution across different miRNA-141-3p_DNA concentrations.

To further investigate hinge behaviour upon target strand binding, we employed TEM imaging to directly visualize individual hinge conformations (**Figure 5.6** and **Figure 5.7**). In agreement with fluorescence-based measurements, the proportion of hinges undergoing structural reconfiguration increased with rising concentrations of the target strands. In addition to clearly

defined closed and extended states, we identified a subset of hinges in an intermediate conformation, characterised by arm angles ranging from 0° to 180°. We hypothesize that these intermediate structures represent hinges that partially opened upon target binding but did not complete the transition to the fully extended state, likely due to incomplete guidance from the extender strands. This intermediate state was particularly prominent at higher concentrations of target strands and was especially noticeable in hinges designed to detect miRNA-375-3p_DNA (**Figure 5.7a.**). Based on TEM observations, we classified hinge conformations into three distinct states: closed, extended, and open.

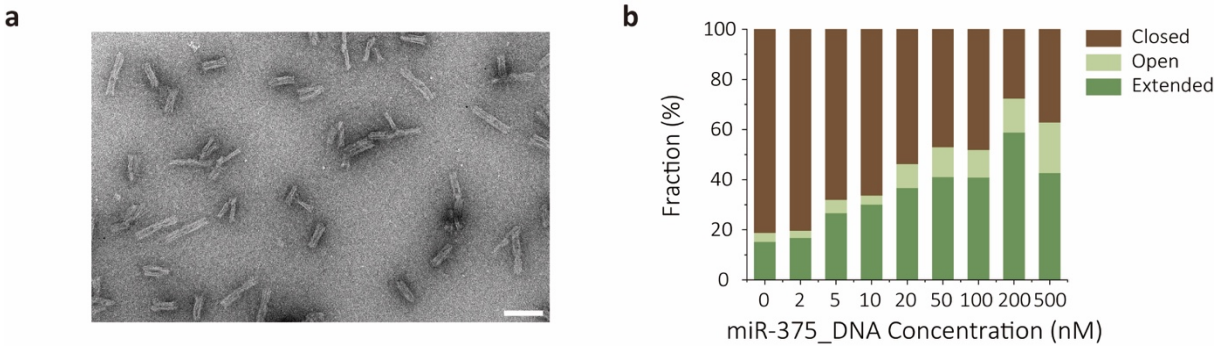


Figure 5.7 a. Example of TEM image of hinge imaged after adding 500 nM of miR-375-3p_DNA to closed hinge with a miR-375 latching strand and allowing to incubate for 24 hours (scale bar: 100 nm). **b.** Fraction of hinge in closed, open, or extended states counted on TEM images after 24 h incubating with various miR-375-3p_DNA concentrations.

5.3.2 DNA Origami Hinge Carrier for Nanopore Detection of miRNA

5.3.2.1 Direct Detection of miRNA-141

A control nanopore translocation experiment was conducted to directly detect miRNA-141-3p (**Figure 5.8**). The translocation buffer consisted of 1 M KCl, 12.5 mM $MgCl_2$, 10 mM Tris, and 1 mM EDTA (pH 8). miRNA-141-3p at a concentration of 200 nM was introduced into the bath. A 300 mV voltage was applied, but no translocation events were observed during the

experiment. This result highlights the challenge of detecting small biomolecules using nanopipettes due to their size disparity.

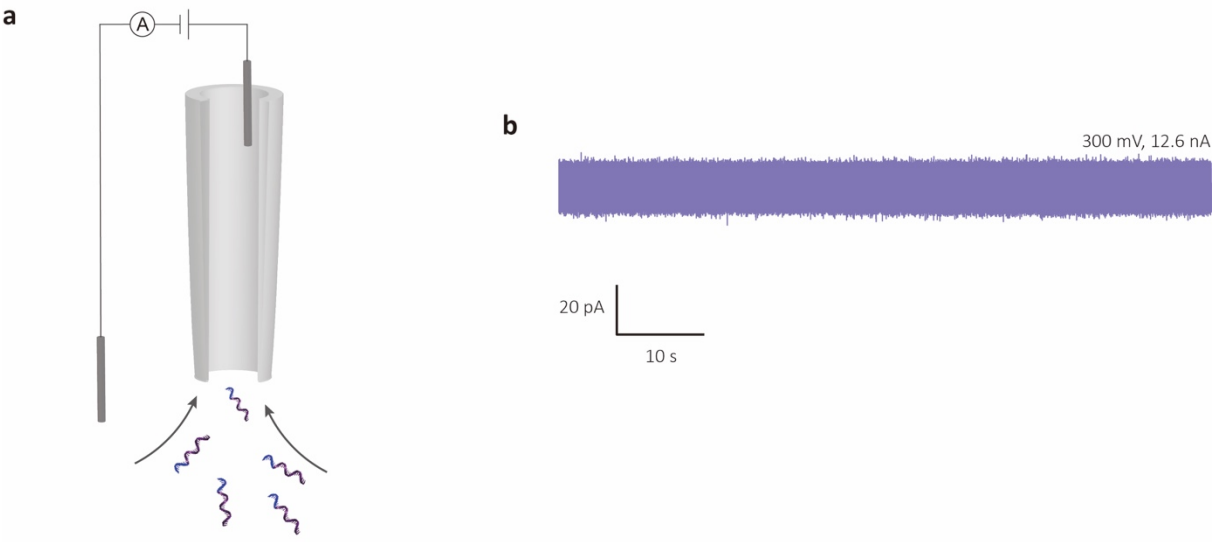


Figure 5.8 Nanopore sensing of miR-141-3p (200 nM). The translocation experiment was performed in 1 M KCl, 12.5 mM $MgCl_2$, 10 mM Tris, 1 mM EDTA, pH = 8, and at a volatge bias of 300 mV.

5.3.2.2 Nanopore Study of Binding Dynamic Mechanism

Our experiments demonstrated that target strands can successfully bind to the closed hinge, triggering a conformational transition to the extended state. This structural reconfiguration provides a dependable readout of target strand presence, establishing a direct link between molecular recognition and mechanical response. Furthermore, it enables the application of nanopore sensing to investigate hinge dynamics and monitor binding interactions with high sensitivity.

To investigate the binding kinetics, we incubated miRNA-141-3p with closed hinges for up to 16 hours, using the same nanopipette across multiple time points to maintain measurement consistency. Despite the low concentration of gel-purified hinges, our nanopipettes consistently detected the presence of miRNA-141-3p across independent samples (N = 5). Histograms of peak currents at various incubation durations are shown in **Figure 5.9a.**, revealing two clearly

distinguishable distributions. The lower peak current corresponds to hinges that successfully bound miRNA-141-3p and underwent structural reconfiguration, while the higher distribution reflects unbound closed hinges. Notably, an increasing trend in the proportion of reconfigured hinges, marked by lower peak currents, was observed over time, with the most significant change occurring within the first four hours of incubation.

To quantify binding, we determined the fraction of hinges by analysing the peak current histograms. Several methods were tested, including Gaussian fitting and threshold-based classification (**Figure 5.10** and **Figure 5.11**). Ultimately, the binding ratio was defined as the mean plus one standard deviation of the reconfigured hinge distribution, serving as a sample-specific threshold (**Figure 5.9b.**). This adaptive approach minimised errors associated with the use of uniform thresholds.

The binding ratio over time exhibited a sigmoidal trend (**Figure 5.9c.**), which was fitted using a logistic function, yielding a half-life of 1.27 ± 0.05 hours for miRNA-141-3p binding. From this, we determined an association rate constant K_{on} of 606 $M^{-1} \cdot s^{-1}$. After eight hours—exceeding five half-lives—over 97% of the hinges had reconfigured, marking the near-completion of the binding process.

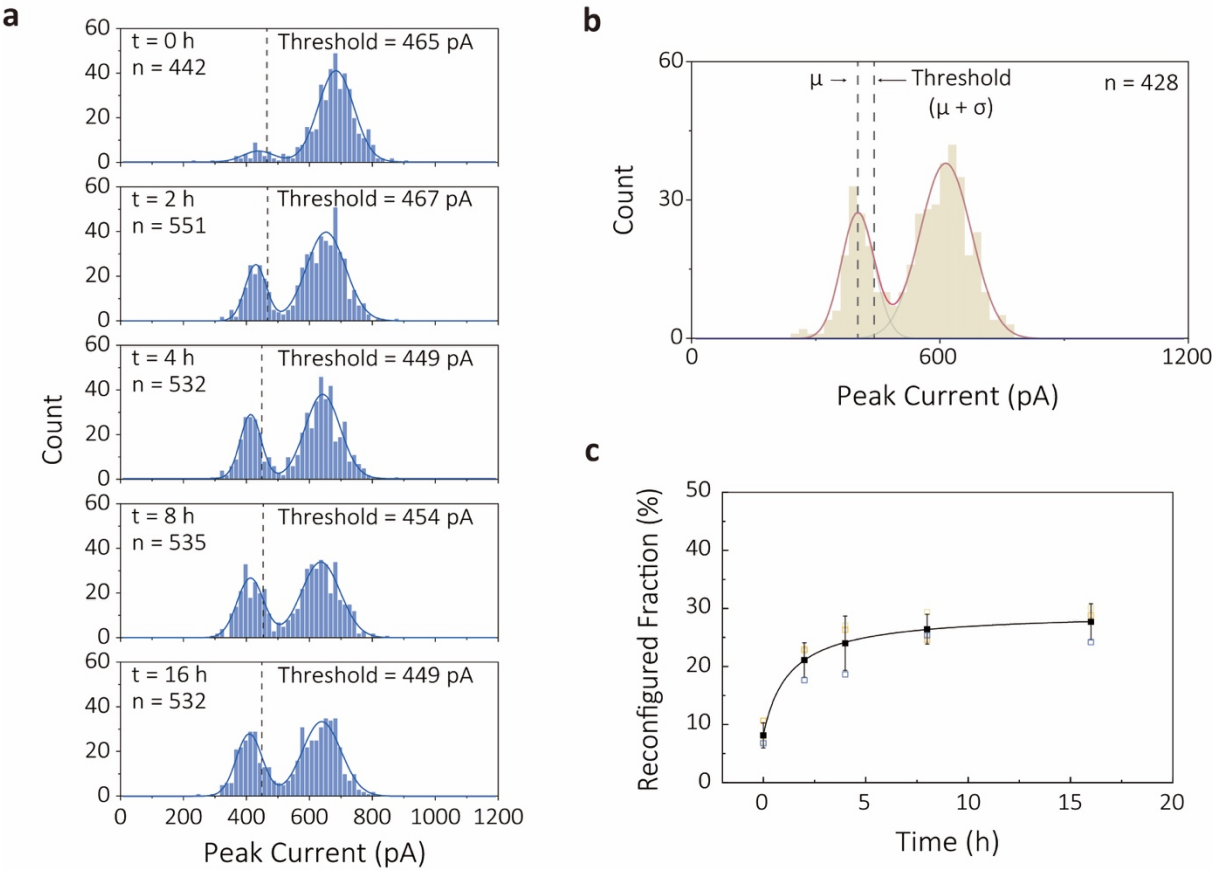


Figure 5.9 Study of the binding dynamics between the DNA origami hinge with miRNA-141-3p studied via nanopore sensing. **a.** Peak current distribution of initially closed hinge (1 nM) after incubation with miRNA-141-3p (1 μM) for varying durations (0–16 h). Incubated samples (N = 5) were diluted to a final hinge concentration of 200 pM and a final miRNA-141-3p concentration of 200 nM before translocation experiments. Histograms were fitted using a Gaussian function. **b.** Schematic illustration of the threshold definition. The mean (μ) and standard deviation (σ) were derived from Gaussian fitting, with 84.1% of reconfigured hinge events included within the mean +1σ threshold. **c.** Reconfigured fraction as a function of incubation time, fitted with a logistic equation. The half-life ($t_1/_2$) and association rate constant (K_{on}) were determined to be 1.27 ± 0.05 h and 606 $M^{-1}{\cdot}s^{-1}$. Error bars represent one standard deviation from 3 independent experiments.

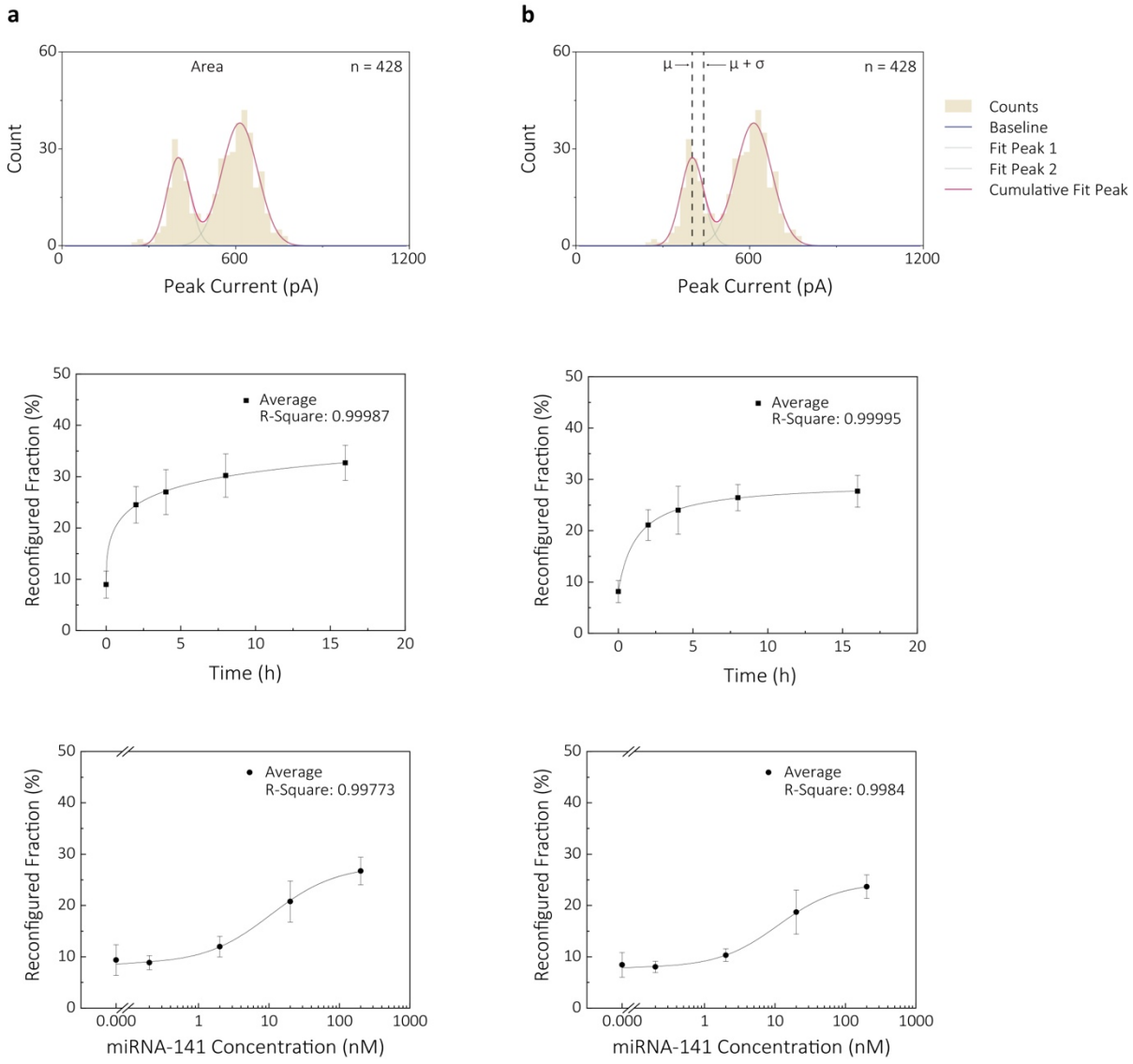


Figure 5.10 Methods of defining the binding ratio or reconfigured fraction. **a.** The reconfigured fraction is calculated as the proportion of the area covered by reconfigured events to the total area encompassed by all events. **b.** The reconfigured fraction is determined by dividing the count of reconfigured events by the total number of events. Reconfigured events are identified using a threshold: events with peak current below the mean + 1 sigma (μ + σ) value of the distribution of reconfigured events are considered as reconfigured. Binding ratios, fitted binding dynamic curve and fitted binding dynamic curve corresponding to different defining method. The error bars represent one standard deviation of independent experimental repeats. R-square represents coefficient of determination.

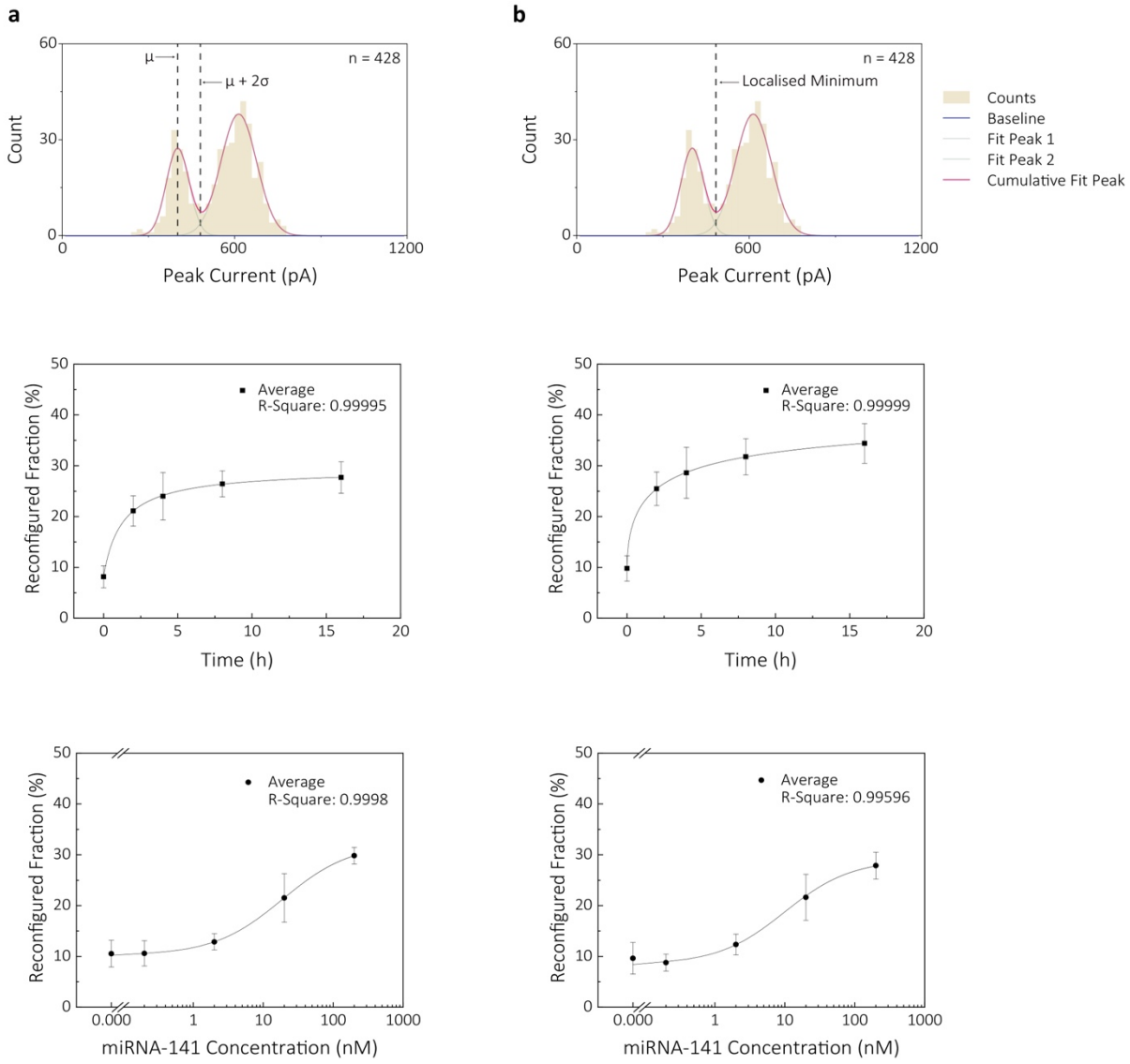


Figure 5.11 Methods of defining the binding ratio or reconfigured fraction. The reconfigured fraction is determined by dividing the count of reconfigured events by the total number of events. **a.** Reconfigured events are identified using a threshold: events with peak current below the mean + 2 sigma (μ + 2σ) value of the distribution of reconfigured events are considered as reconfigured. **b.** Reconfigured events are identified using a threshold: events with peak current below the localised minimum value between the distribution of reconfigured events and the distribution of closed hinge events are considered as reconfigured. Binding ratios, fitted binding dynamic curve and fitted binding dynamic curve corresponding to different defining method. The error bars represent one standard deviation of independent experimental repeats. R-square represents coefficient of determination.

5.3.2.3 Nanopore Study of Binding Mechanism

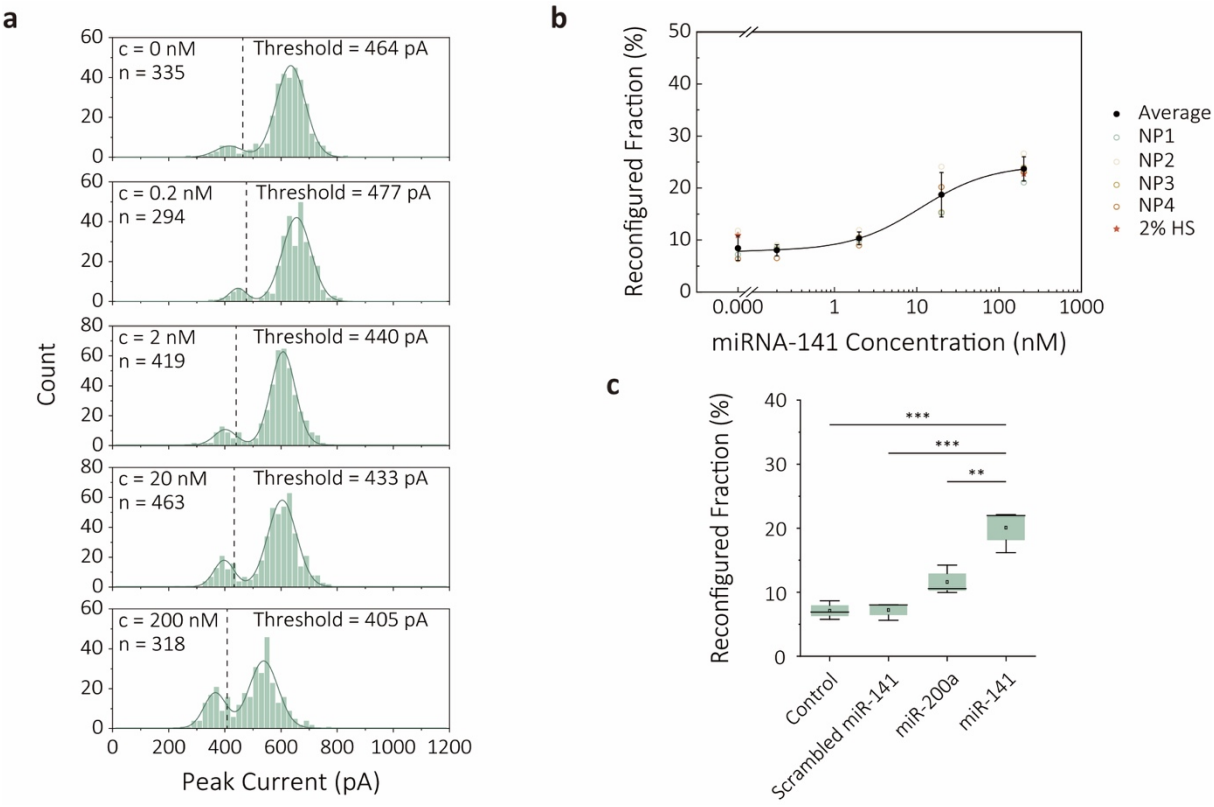


Figure 5.12 Nanopore analysis of the binding between the closed hinge and miRNA-141-3p. **a.** Peak current distribution for the closed hinge (1 nM) after incubation with varying concentrations of miRNA-141-3p (0–1 μM) for 8 h. Incubated samples were diluted to a final hinge concentration of 200 pM and final miRNA-141-3p concentrations of 0, 200 pM, 2 nM, 20 nM, and 200 nM for translocation experiments. Histograms were fitted using a Gaussian function to determine the fraction of open and closed hinges. **b.** Fraction of reconfigured hinges as a function of miRNA-141-3p concentration, fitted with a Hill equation. The dissociation constant (K_d) was determined to be 11.6 ± 0.4 nM. Error bars represent one standard deviation from four independent experimental repeats (excluding 2% human serum data points). **c.** Fraction of reconfigured hinges for blank control, scrambled miRNA-141-3p, miRNA-200a-3p, and miRNA-141-3p (final concentration: 200 nM). The black central line indicates the median, the lower and upper edges mark one standard error, and whiskers represent 1.5× the interquartile range (IQR). Statistical significance was assessed using one-way analysis of variance (**P < 0.01, ***P < 0.001). Experiments were performed using 3 independent nanopores.

To elucidate the binding mechanism between the hinge and miRNA-141-3p, we performed nanopore translocation experiments across a range of target concentrations. Closed hinges at a constant concentration were incubated with varying amounts of miRNA-141-3p (0–200 nM) for eight hours prior to detection. As shown in the peak current histograms (**Figure 5.12a.**), an increased fraction of reconfigured hinges was observed above nanomolar concentrations. For each sample, thresholds were extracted via histogram fitting, and the corresponding reconfiguration ratios were calculated and plotted in **Figure 5.12b.**, ranging from 8.42 ± 2.38% at 0 nM to 23.67 ± 2.32% at 200 nM. Fitting the binding curve with a Hill function yielded a dissociation constant (K_d) of 11.6 ± 0.4 nM. This value slightly deviates from those obtained via fluorescence assays, likely due to the use of DNA analogues in the latter. Notably, lower detection thresholds were observed at 2 nM, 20 nM, and 200 nM, which may reflect an increased population of open hinge conformations at higher target concentrations, influencing their translocation behaviours.

To evaluate the selectivity of the hinge toward its target strand, we performed mismatch discrimination experiments, as illustrated in **Figure 5.12c.**. We tested three sequences—miRNA-141-3p, miRNA-200a-3p, and a scrambled version of miRNA-141-3p—ensuring that all strands had identical lengths. Importantly, miRNA-141-3p and miRNA-200a-3p differed by only two nucleotides located at or near the 3' end, enabling an assessment of the hinge's ability to distinguish closely related sequences.

Our results showed that mismatched sequences triggered minimal hinge reconfiguration. Even at a high concentration of 200 nM, miRNA-200a-3p induced only a partial opening of the hinge, yielding a reconfigured ratio of 11.59 ± 2.32%. This was markedly lower than the 20.09 ± 3.39% observed for miRNA-141-3p under identical conditions, highlighting the high selectivity of our nanopore-based sensing strategy in distinguishing closely related sequences.

5.3.2.4 Detection in Human Serum

To extend our detection strategy beyond buffer conditions, we investigated its performance in biological samples, motivated by the relevance of miRNA-141-3p as a PCa biomarker [47, 48]. Given that our nanopore measurements required high-salt conditions, serum samples were diluted with electrolyte buffer to achieve a final KCl concentration of 1 M, using volumetric dilution ratios ranging from 20% to 2% (**Figure 5.13**). At higher serum contents, we observed significant ion current fluctuations and, in some instances, irreversible nanopore blockage—likely due to the abundance of biomolecules in serum. To maintain stable current traces and obtain sufficient translocation events, we selected a 2% serum dilution as the optimal condition for subsequent experiments.

We subsequently compared nanopore sensing results from human serum samples spiked with 200 nM miRNA-141-3p to those from blank controls. The reconfigured ratios obtained under these conditions were consistent with measurements in pure electrolyte, yielding values of 10.95% for the 0 nM control and 22.77% for the 200 nM sample (**Figure 5.14**). This consistency highlights the method's robustness and applicability in complex biological matrices.

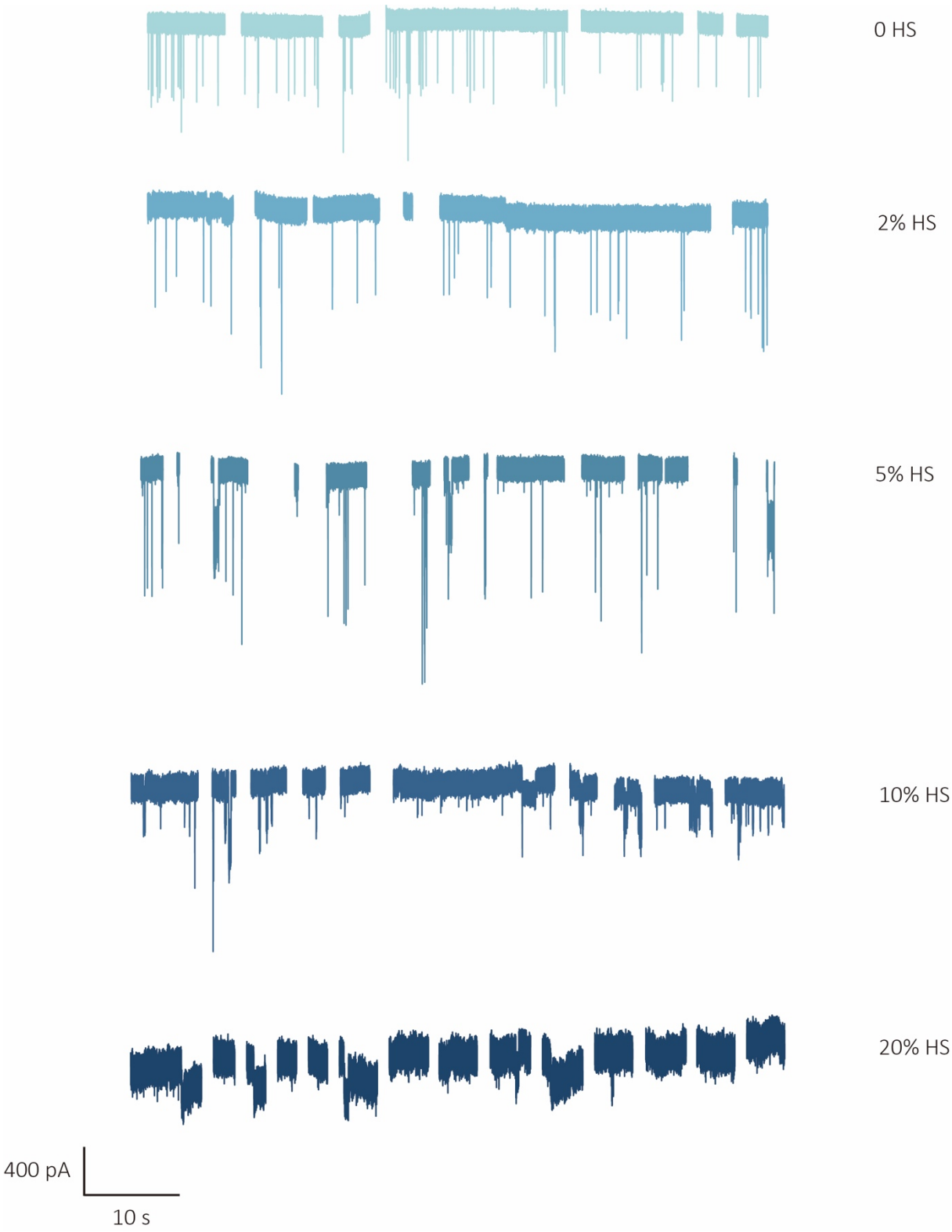


Figure 5.13 Nanopore sensing of closed hinge (200 pM) with human serum at 300 mV. Current-time traces for a range dilution of human serum from 2% to 20% and blank control. Human serum was diluted in 1 M KCl, 12.5 mM $MgCl_2$, 10 mM Tris, 1 mM EDTA, pH = 8 according to the multiplicity and was placed in the bath outside the nanopipette.

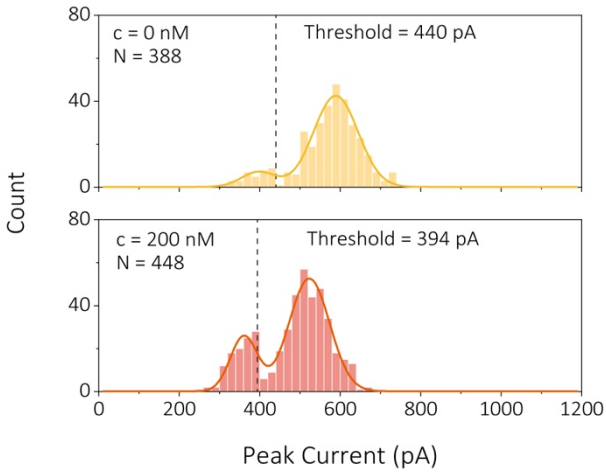


Figure 5.14 Peak current statistics for closed hinge (1 nM) incubated with 1000 nM miRNA-141-3p and blank control for 8 hours. Incubated samples were diluted with 2% human serum in 1 M KCl, 12.5 mM $MgCl_2$, 10 mM Tris, 1 mM EDTA, pH = 8 at the final hinge concentration at 200 pM and the final miRNA-141-3p concentration at 200 nM for translocation experiments.

5.3.2.5 Dual Detection of miRNA-141 and miRNA-375

To enable dual detection of miRNA-141-3p and miRNA-375-3p, we introduced a design modification in which two pairs of closer overhangs were replaced with distinct latching overhangs—one specific to miRNA-141-3p and the other to miRNA-375-3p (**Figure 5.15a.**). These latching overhangs formed dual connections between the hinge arms following the removal of the closer helper strands, thereby locking the hinge into a closed conformation. Upon the addition of closer displacer strands and extender strands, the hinge was reconfigured to respond specifically to the simultaneous recognition of both target miRNAs.

To characterize hinge reconfiguration upon dual miRNA binding, we employed complementary fluorescence assays and TEM quantification (**Figure 5.15b.**). Fluorescence analysis revealed significantly enhanced hinge reconfiguration when both target miRNAs were present concurrently, compared to single miRNA or control conditions. However, TEM-based

population counts showed no statistically significant differences between experimental groups. Furthermore, both analytical approaches exhibited non-negligible false positives.

The reconfiguration ratios remained statistically indistinguishable among control samples (1.57 ± 0.10%), miRNA-141-3p only (2.46 ± 1.72%), and miRNA-375-3p only conditions (3.58 ± 0.82%). Strikingly, co-incubation with both miRNAs triggered a significant increase in reconfiguration efficiency (14.84 ± 2.69%), demonstrating synergistic activation of the hinge mechanism.

This series of experiments demonstrates that the reconfigurable hinge mechanism, when employed as a molecular carrier in nanopore platforms, achieves superior sensitivity for dual miRNA detection compared to traditional techniques.

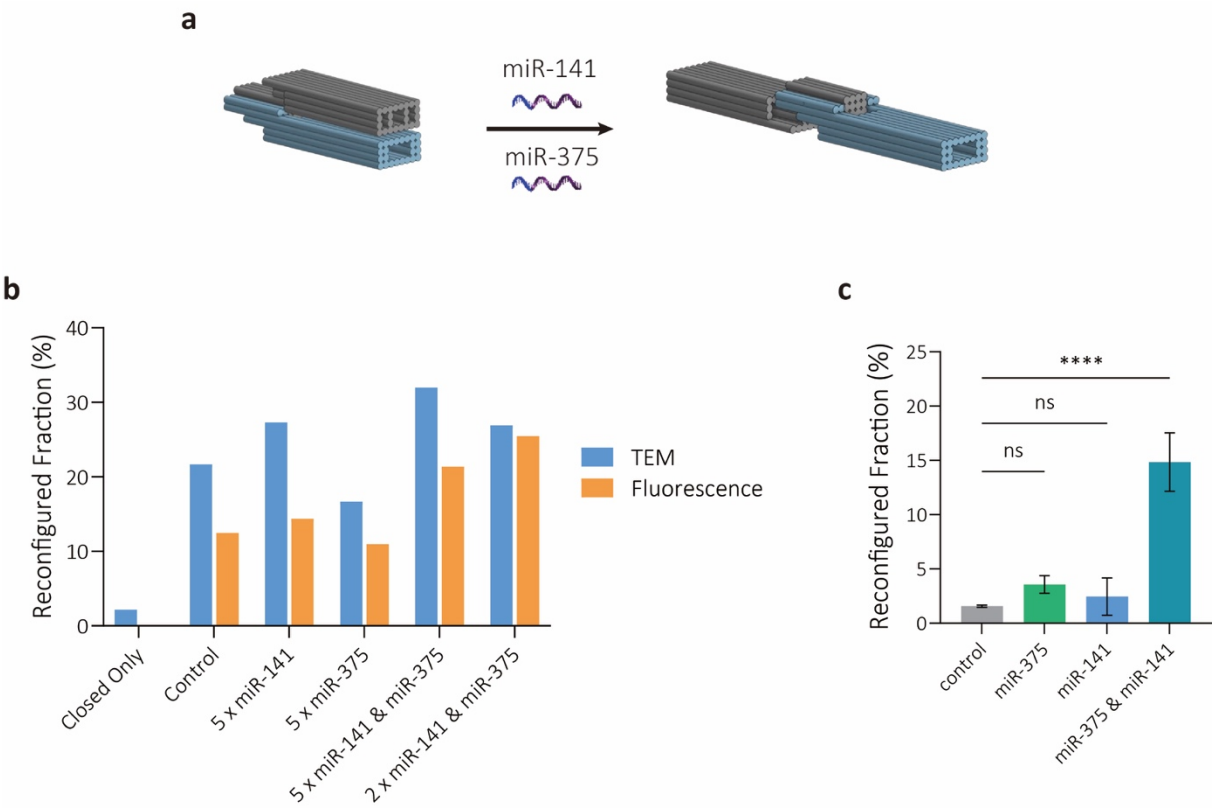


Figure 5.15 Hinge reconfiguration of closed hinge with dual latching strands. **a.** Closed hinge with one miRNA-141-3p latching strand and one miRNA-375-3p latching strand for miRNA dual sensing. **b.** TEM counting and fluorescence bulk measurement for miRNA dual sensing. **c.** Nanopore sensing for miRNA dual sensing. The error

bars represent one standard deviation of three independent experimental repeats. Statistical significance was tested by one-way analysis of variance. (****P < 0.0001; ns, not siganificant)

5.4 Conclusion

In this chapter, we present a reconfigurable DNA hinge as a nanopore-based platform for detecting small biomolecules, such as miRNA, utilising binding-induced conformational changes for real-time analysis. Nanopore sensing reliably differentiated between closed and extended hinge configurations, enabling quantitative detection of miRNA-141-3p across a range of concentrations and within human serum, with high sensitivity and selectivity. Furthermore, the method allowed simultaneous detection of miRNA-141-3p and miRNA-375-3p, outperforming traditional techniques such as TEM counting and fluorescence assays in terms of sensitivity.

Compared to traditional linear DNA carriers, our DNA nanostructure provides a mechanically rigid framework, minimizing false positives caused by structural twisting or deformation and addressing charge distribution challenges commonly associated with uniform carriers. In contrast to previous nanopore studies that focused on static DNA nanostructures, our approach demonstrates the potential of nanopores for probing dynamic structural changes in DNA-based nanostructures. Notably, the electrolyte conditions necessary for nanopore sensing do not disrupt hinge reconfiguration, ensuring compatibility between structural responsiveness and detection requirements.

Our platform represents a promising approach for small-molecule sensing, with potential for further optimisation toward protein detection and multiplexed biomarker analysis. These advancements lay the groundwork for broader applications in disease diagnostics, enhancing the versatility and clinical relevance of nanopore-based biosensing technologies.

5.5 References

[1] Luo, X.; Davis, J. J. Electrical biosensors and the label free detection of protein disease biomarkers. *Chem Soc Rev* **2013**, *42*, 5944-5962.

[2] Islam, M. N.;Masud, M. K.;Haque, M. H.;Hossain, M. S. A.;Yamauchi, Y.;Nguyen, N.-T.; Shiddiky, M. J. A. RNA Biomarkers: Diagnostic and Prognostic Potentials and Recent Developments of Electrochemical Biosensors. *Small Methods* **2017**, *1*, 1700131.

[3] Farzin, L.;Shamsipur, M.;Samandari, L.; Sheibani, S. Advances in the design of nanomaterial-based electrochemical affinity and enzymatic biosensors for metabolic biomarkers: A review. *Mikrochim Acta* **2018**, *185*, 276.

[4] Belushkin, A.;Yesilkoy, F.; Altug, H. Nanoparticle-Enhanced Plasmonic Biosensor for Digital Biomarker Detection in a Microarray. *ACS Nano* **2018**, *12*, 4453-4461.

[5] Li, Z.;Wang, Y.;Wang, J.;Tang, Z.;Pounds, J. G.; Lin, Y. Rapid and sensitive detection of protein biomarker using a portable fluorescence biosensor based on quantum dots and a lateral flow test strip. *Anal Chem* **2010**, *82*, 7008-7014.

[6] Chiorcea-Paquim, A. M. Advances in Electrochemical Biosensor Technologies for the Detection of Nucleic Acid Breast Cancer Biomarkers. *Sensors (Basel)* **2023**, *23*.

[7] Haes, A. J.;Chang, L.;Klein, W. L.; Van Duyne, R. P. Detection of a biomarker for Alzheimer's disease from synthetic and clinical samples using a nanoscale optical biosensor. *J Am Chem Soc* **2005**, *127*, 2264-2271.

[8] Jayanthi, V.;Das, A. B.; Saxena, U. Recent advances in biosensor development for the detection of cancer biomarkers. *Biosens Bioelectron* **2017**, *91*, 15-23.

[9] Swierczewska, M.;Liu, G.;Lee, S.; Chen, X. High-sensitivity nanosensors for biomarker detection. *Chem Soc Rev* **2012**, *41*, 2641-2655.

[10] Kim, S. J.;Choi, S. J.;Jang, J. S.;Cho, H. J.; Kim, I. D. Innovative Nanosensor for Disease Diagnosis. *Acc Chem Res* **2017**, *50*, 1587-1596.

[11] Howorka, S.; Siwy, Z. Nanopore analytics: sensing of single molecules. *Chem Soc Rev* **2009**, *38*, 2360-2384.

[12] Chen, X.;Zhou, S.;Wang, Y.;Zheng, L.;Guan, S.;Wang, D.;Wang, L.; Guan, X. Nanopore Single-molecule Analysis of Biomarkers: Providing Possible Clues to Disease Diagnosis. *Trends Analyt Chem* **2023**, *162*.

[13] Wanunu, M. Nanopores: A journey towards DNA sequencing. *Phys Life Rev* **2012**, *9*, 125-158.

[14] Yusko, E. C.;Johnson, J. M.;Majd, S.;Prangkio, P.;Rollings, R. C.;Li, J.;Yang, J.; Mayer, M. Controlling protein translocation through nanopores with bio-inspired fluid walls. *Nat Nanotechnol* **2011**, *6*, 253-260.

[15] Kowalczyk, S. W.;Kapinos, L.;Blosser, T. R.;Magalhaes, T.;van Nies, P.;Lim, R. Y.; Dekker, C. Single-molecule transport across an individual biomimetic nuclear pore complex. *Nat Nanotechnol* **2011**, *6*, 433-438.

[16] Wei, R.;Gatterdam, V.;Wieneke, R.;Tampe, R.; Rant, U. Stochastic sensing of proteins with receptor-modified solid-state nanopores. *Nat Nanotechnol* **2012**, *7*, 257-263.

[17] Xue, L.;Yamazaki, H.;Ren, R.;Wanunu, M.;Ivanov, A. P.; Edel, J. B. Solid-state nanopore sensors. *Nature Reviews Materials* **2020**, *5*, 931-951.

[18] Sze, J. Y. Y.;Ivanov, A. P.;Cass, A. E. G.; Edel, J. B. Single molecule multiplexed nanopore protein screening in human serum using aptamer modified DNA carriers. *Nat Commun* **2017**, *8*, 1552.

[19] Liu, Y.;Wang, X.;Campolo, G.;Teng, X.;Ying, L.;Edel, J. B.; Ivanov, A. P. Single-Molecule Detection of alpha-Synuclein Oligomers in Parkinson's Disease Patients Using Nanopores. *ACS Nano* **2023**, *17*, 22999-23009.

[20] Cai, S.;Pataillot-Meakin, T.;Shibakawa, A.;Ren, R.;Bevan, C. L.;Ladame, S.;Ivanov, A. P.; Edel, J. B. Single-molecule amplification-free multiplexed detection of circulating microRNA cancer biomarkers from serum. *Nat Commun* **2021**, *12*, 3515.

[21] Ren, R.;Cai, S.;Fang, X.;Wang, X.;Zhang, Z.;Damiani, M.;Hudlerova, C.;Rosa, A.;Hope, J.;Cook, N. J.;Gorelkin, P.;Erofeev, A.;Novak, P.;Badhan, A.;Crone, M.;Freemont, P.;Taylor, G. P.;Tang, L.;Edwards, C.;Shevchuk, A.;Cherepanov, P.;Luo, Z.;Tan, W.;Korchev, Y.;Ivanov, A. P.; Edel, J. B. Multiplexed detection of viral antigen and RNA using nanopore sensing and encoded molecular probes. *Nat Commun* **2023**, *14*, 7362.

[22] Ren, R.;Sun, M.;Goel, P.;Cai, S.;Kotov, N. A.;Kuang, H.;Xu, C.;Ivanov, A. P.; Edel, J. B. Single-Molecule Binding Assay Using Nanopores and Dimeric NP Conjugates. *Adv Mater* **2021**, *33*, e2103067.

[23] Raveendran, M.;Lee, A. J.;Sharma, R.;Walti, C.; Actis, P. Rational design of DNA nanostructures for single molecule biosensing. *Nat Commun* **2020**, *11*, 4384.

[24] Ding, T.;Yang, J.;Wang, J.;Pan, V.;Lu, Z.;Ke, Y.; Zhang, C. Shaped DNA origami carrier nanopore translocation influenced by aptamer based surface modification. *Biosens Bioelectron* **2022**, *195*, 113658.

[25] Wen, C.;Bertosin, E.;Shi, X.;Dekker, C.; Schmid, S. Orientation-Locked DNA Origami for Stable Trapping of Small Proteins in the Nanopore Electro-Osmotic Trap. *Nano Lett* **2023**, *23*, 788-794.

[26] Bell, N. A.;Engst, C. R.;Ablay, M.;Divitini, G.;Ducati, C.;Liedl, T.; Keyser, U. F. DNA origami nanopores. *Nano Lett* **2012**, *12*, 512-517.

[27] Burns, J. R.;Gopfrich, K.;Wood, J. W.;Thacker, V. V.;Stulz, E.;Keyser, U. F.; Howorka, S. Lipid-bilayer-spanning DNA nanopores with a bifunctional porphyrin anchor. *Angew Chem Int Ed Engl* **2013**, *52*, 12069-12072.

[28] Rothemund, P. W. Folding DNA to create nanoscale shapes and patterns. *Nature* **2006**, *440*, 297-302.

[29] Castro, C. E.;Kilchherr, F.;Kim, D. N.;Shiao, E. L.;Wauer, T.;Wortmann, P.;Bathe, M.; Dietz, H. A primer to scaffolded DNA origami. *Nat Methods* **2011**, *8*, 221-229.

[30] Hong, F.;Zhang, F.;Liu, Y.; Yan, H. DNA Origami: Scaffolds for Creating Higher Order Structures. *Chem Rev* **2017**, *117*, 12584-12640.

[31] Wagenbauer, K. F.;Engelhardt, F. A. S.;Stahl, E.;Hechtl, V. K.;Stommer, P.;Seebacher, F.;Meregalli, L.;Ketterer, P.;Gerling, T.; Dietz, H. How We Make DNA Origami. *Chembiochem* **2017**, *18*, 1873-1885.

[32] Plesa, C.;Verschueren, D.;Pud, S.;van der Torre, J.;Ruitenberg, J. W.;Witteveen, M. J.;Jonsson, M. P.;Grosberg, A. Y.;Rabin, Y.; Dekker, C. Direct observation of DNA knots using a solid-state nanopore. *Nat Nanotechnol* **2016**, *11*, 1093-1097.

[33] Kumar Sharma, R.;Agrawal, I.;Dai, L.;Doyle, P. S.; Garaj, S. Complex DNA knots detected with a nanopore sensor. *Nat Commun* **2019**, *10*, 4473.

[34] Yang, J.;Zhao, N.;Liang, Y.;Lu, Z.; Zhang, C. Structure-flexible DNA origami translocation through a solid-state nanopore. *RSC Adv* **2021**, *11*, 23471-23476.

[35] Zhu, J.;Tivony, R.;Boskovic, F.;Pereira-Dias, J.;Sandler, S. E.;Baker, S.; Keyser, U. F. Multiplexed Nanopore-Based Nucleic Acid Sensing and Bacterial Identification Using DNA Dumbbell Nanoswitches. *J Am Chem Soc* **2023**, *145*, 12115-12123.

[36] Chen, X.;Ba, Y.;Ma, L.;Cai, X.;Yin, Y.;Wang, K.;Guo, J.;Zhang, Y.;Chen, J.;Guo, X.;Li, Q.;Li, X.;Wang, W.;Zhang, Y.;Wang, J.;Jiang, X.;Xiang, Y.;Xu, C.;Zheng, P.;Zhang, J.;Li, R.;Zhang, H.;Shang, X.;Gong, T.;Ning, G.;Wang, J.;Zen, K.;Zhang, J.; Zhang, C. Y. Characterization of microRNAs in serum: a novel class of biomarkers for diagnosis of cancer and other diseases. *Cell Res* **2008**, *18*, 997-1006.

[37] Wang, J.;Chen, J.; Sen, S. MicroRNA as Biomarkers and Diagnostics. *J Cell Physiol* **2016**, *231*, 25-30.

[38] Yurke, B.;Turberfield, A. J.;Mills, A. P., Jr.;Simmel, F. C.; Neumann, J. L. A DNA-fuelled molecular machine made of DNA. *Nature* **2000**, *406*, 605-608.

[39] Simmel, F. C.;Yurke, B.; Singh, H. R. Principles and Applications of Nucleic Acid Strand Displacement Reactions. *Chem Rev* **2019**, *119*, 6326-6369.

[40] Pritchard, C. C.;Cheng, H. H.; Tewari, M. MicroRNA profiling: approaches and considerations. *Nat Rev Genet* **2012**, *13*, 358-369.

[41] Focke, W. W.;van der Westhuizen, I.;Musee, N.; Loots, M. T. Kinetic interpretation of log-logistic dose-time response curves. *Sci Rep* **2017**, *7*, 2234.

[42] Jarmoskaite, I.;AlSadhan, I.;Vaidyanathan, P. P.; Herschlag, D. How to measure and evaluate binding affinities. *eLife* **2020**, *9*, e57264.

[43] Gesztelyi, R.;Zsuga, J.;Kemeny-Beke, A.;Varga, B. A.;Juhász, B.; Tósaki, Á. The Hill equation and the origin of quantitative pharmacology. *Archive for History of Exact Sciences* **2012**, *66*, 427-438.

[44] Gesztelyi, R.;Zsuga, J.;Kemeny-Beke, A.;Varga, B.;Juhasz, B.; Tosaki, A. The Hill equation and the origin of quantitative pharmacology. *Archive for History of Exact Sciences* **2012**, *66*, 427-438.

[45] Bryant, R. J.;Pawlowski, T.;Catto, J. W.;Marsden, G.;Vessella, R. L.;Rhees, B.;Kuslich, C.;Visakorpi, T.; Hamdy, F. C. Changes in circulating microRNA levels associated with prostate cancer. *Br J Cancer* **2012**, *106*, 768-774.

[46] Bergez-Hernandez, F.;Arambula-Meraz, E.;Alvarez-Arrazola, M.;Irigoyen-Arredondo, M.;Luque-Ortega, F.;Martinez-Camberos, A.;Cedano-Prieto, D.;Contreras-Gutierrez, J.;Martinez-Valenzuela, C.; Garcia-Magallanes, N. Expression Analysis of miRNAs and Their Potential Role as Biomarkers for Prostate Cancer Detection. *Am J Mens Health* **2022**, *16*, 15579883221120989.

[47] Porzycki, P.;Ciszkowicz, E.;Semik, M.; Tyrka, M. Combination of three miRNA (miR-141, miR-21, and miR-375) as potential diagnostic tool for prostate cancer recognition. *Int Urol Nephrol* **2018**, *50*, 1619-1626.

[48] Kosaka, N.;Iguchi, H.; Ochiya, T. Circulating microRNA in body fluid: a new potential biomarker for cancer diagnosis and prognosis. *Cancer Sci* **2010**, *101*, 2087-2092.

Chapter 6 CBD Nanopore and Detection

Synopsis

This chapter introduces a cost-effective and efficient CBD-based method for fabricating single solid-state nanopores with tuneable diameters suited for various analytes. The resulting nanopores demonstrated comparable performance to nanopipettes in dsDNA translocation experiments and effectively enabled the use of DNA-based molecular carriers for selective miRNA detection. Additionally, these nanopores supported the sensing of dynamic DNA origami hinges, underscoring their versatility for real-time analysis of reconfigurable nanostructures.

Chapter 6 CBD Nanopore and Detection 177

6.1 Introduction 179

6.2 Methods 181

6.2.1 CBD Pore Formation 181

6.2.2 Pore Expansion 182

6.3 Results and Discussion 183

6.3.1 CBD Nanopore Fabrication 183

6.3.2 Detection with CBD Nanopore 185

6.3.2.1 Detection of dsDNA 185

6.3.2.2 Detection of miRNA with dsDNA Carrier 187

6.3.2.3 Detection of DNA Origami Hinge 188

6.4 Conclusion 190

6.5 References 190

6.1 Introduction

Solid-state nanopores are nanoscale openings fabricated in thin membranes made of materials like SiN_x, SiO_2, or graphene [1-3]. When an electric field is applied across the membrane, charged biomolecules such as nucleic acids or proteins are driven through the nanopore [4-6]. This temporarily disrupts the ionic current and creates detectable signals. This principle allows for single-molecule analysis with high temporal resolution, making solid-state nanopores a powerful tool for biomolecular sensing [7, 8].

Compared to biological nanopores, solid-state versions offer several key advantages. Their manufacturing process enables precise control over pore size and membrane thickness, which allows analysis of various different analytes [2, 9]. They demonstrate strong mechanical durability and chemical stability, making them suitable for use in demanding conditions, including high salt concentrations or extreme pH levels [10, 11]. Additionally, their surfaces can be chemically and biomimetically modified to improve molecular recognition or reduce nonspecific background signals [12-15]. The solid membrane material also enables easier integration with electronic, optical components and microfluidic systems, supporting the development of scalable, high-throughput, and reusable sensing platforms [10, 16, 17].

CBD is an innovative approach for generating nanopores in solid-state membranes, including SiN_x [18-23]. Unlike conventional fabrication techniques, which require sophisticated instrumentation such as focused ion or electron beams or transmission electron microscopy, CBD operates by applying a progressively increasing electric field across an insulating membrane [19, 24]. A sudden current spike signals the formation of a nanopore, eliminating dependence on complex nanofabrication equipment.

A major advantage of CBD is its simplicity and versatility. The nanopore diameter can be precisely controlled by modulating the applied voltage, breakdown time, or subsequent processing steps, ensuring adaptability for diverse molecular detection applications.

Furthermore, CBD enables spatially selective pore formation through electric field focusing, making it compatible with integrated chip-based platforms. Due to its cost-effectiveness, potential for high-throughput production, and ease of automation, CBD presents a promising alternative to traditional nanopore fabrication methods, particularly for scalable biosensing applications [25-27].

This chapter details the implementation of CBD technique for creating single solid-state nanopores in SiN_x membranes (**Figure 6.1**). Unlike conventional lithographic techniques, this electrical fabrication strategy enables rapid and reproducible pore formation while eliminating dependence on specialised nanofabrication tools. The final pore diameter can be tuned within a broad range, from a few nanometres up to several tens of nanometres, depending on the dimensions of the target molecules to be analysed. Our CBD fabricated nanopores have demonstrated versatility beyond the detection of standard dsDNA. In particular, we utilised dsDNA not only as an analyte but also as a molecular carrier to deliver specific target molecules through the nanopore for sensing purposes. This approach expands the functional application of solid-state nanopores to more complex molecular systems. Moreover, these nanopores successfully enabled the detection of dynamic DNA origami hinges, highlighting the system's compatibility with reconfigurable nanostructures.

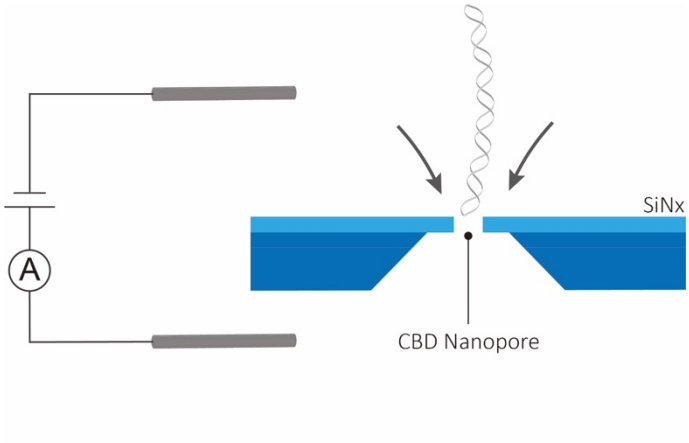


Figure 6.1 Schematic for detection of DNA molecule using CBD solid-state nanopore. The SiN_x membrane with a single nanopore is positioned between two chambers of electrolyte solution.

6.2 Methods

For comprehensive methodological details regarding the CBD procedure employed in this investigation, readers are directed to **Chapter 2**, which provides a complete experimental protocol.

6.2.1 CBD Pore Formation

Nanopore fabrication begins by applying an electric field near the membrane's dielectric strength limit (**Figure 6.2**). This can be implemented through multiple electrical approaches: fixed potential, gradually increasing voltage, pulsed fields, steady current, or photonic excitation [20, 21, 28-31]. The imposed field induces a tunnelling current, enabled by random formation of charge-trapping centres in the dielectric material [32, 33]. Progressive accumulation of these localised defects, combined with possible thermal effects from resistive heating, leads to the development of conductive channels [34, 35]. When these defects interconnect to form a complete pathway, an abrupt current surge occurs, culminating in an uncontrolled breakdown process that generates a nanopore.

The fundamental physics governing charge trap formation remains actively studied, with hypothesised mechanisms involving the generation of electron-hole pairs and avalanche ionisation [36]. For reliable pore fabrication, computer-controlled setups prove essential. These automated platforms continuously track conduction current and immediately disable the applied field upon pore formation, minimizing structural over-etching while maintaining consistent results.

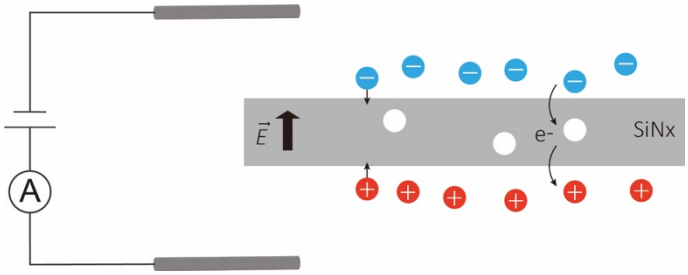


Figure 6.2 Schematic representation of a SiN_x membrane during nanopore fabrication via CBD.

6.2.2 Pore Expansion

Following initial nanopore formation via CBD, the pore diameter can be precisely adjusted by applying a sequence of voltage pulses. Critical to this process is maintaining the pulse peak voltage below the dielectric breakdown threshold to prevent the unintended creation of additional pores [7, 19]. This enlargement mechanism is believed to operate differently from the initial breakdown event, although the exact details remain actively under investigation.

A leading hypothesis proposes that pore widening primarily results from electrochemical reactions at the pore walls [37]. Ionic flow under the applied electric field gradually removes material from the membrane surface through an etching or dissolution process. While not yet fully understood, this mechanism fundamentally differs from the rapid, defect-driven initial breakdown and provides a practical means for post-fabrication nanopore size refinement.

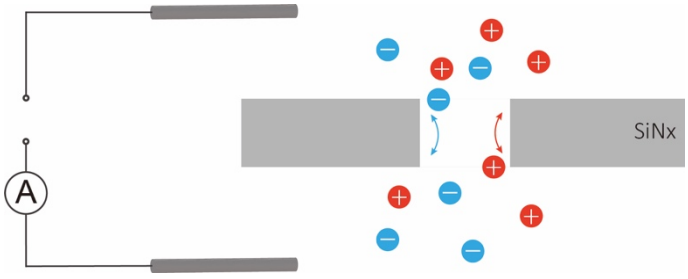


Figure 6.3 Schematic representation of a SiN_x membrane during expansion, with a voltage pulse applied in high salt.

6.3 Results and Discussion

6.3.1 CBD Nanopore Fabrication

Individual nanopores are generated directly in solution on thin insulating solid-state membranes. In our setup, a SiN_x membrane (suspended on a Si/SiO_2 substrate) serves as the core structure (**Figure 2.5**). This membrane is integrated into a fluidic cell, which divides two chambers filled with 1 M KCl aqueous electrolyte (**Figure 2.7c.**). The integration of the membrane into the fluidic cell greatly streamlines the transition to sensing experiments by eliminating the need for further membrane manipulation.

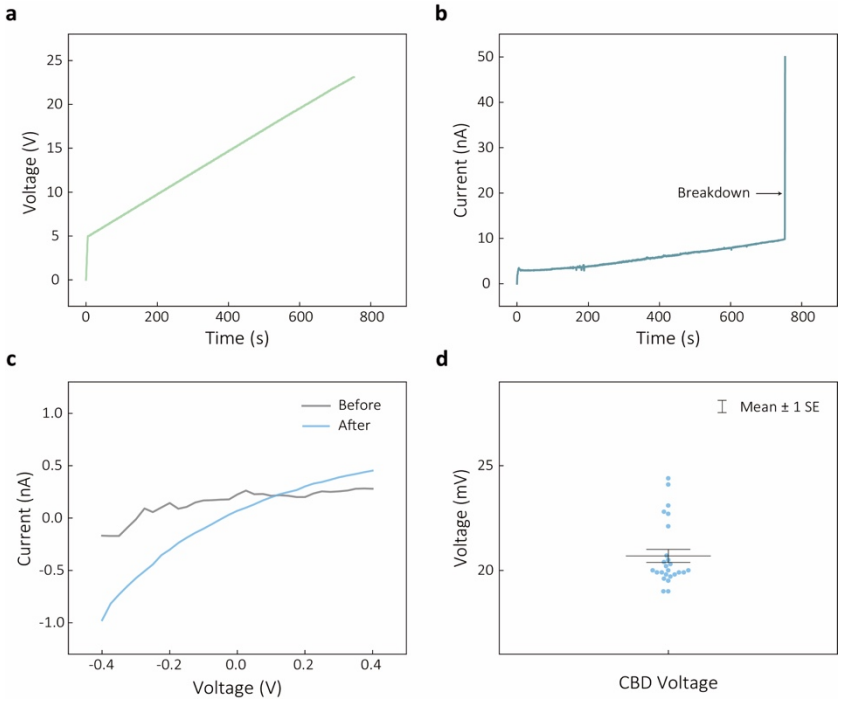


Figure 6.4 CBD nanopore fabrication of a SiN_x membrane. **a.** Voltage-time plot of the CBD process. The voltage profile consisted of two sequential phases: An initial linear ramp from 0 V to 5 V at 1 V/s, a subsequent slower ramp from 5 V to the breakdown threshold (or 30 V maximum) at 0.025 V/s. **b.** Current-time plot of the CBD process. A termination threshold was set at 50 nA. **c.** I-V measurements before and after CBD process under the voltage of ±400 mV. **d.** Breakdown voltages of SiN_x membranes. The measurements were performed in 1 M KCl, 10 mM Tris, 1 mM EDTA, pH = 8.

A single nanopore was fabricated by applying ramped voltage across the SiN_x membrane (**Figure 6.4**). The voltage application followed a two-phase ramping strategy: an initial fast ramp increased the voltage linearly from 0 V to 5 V at a rate of 1 V/s, followed by a slower ramp that progressed up to a maximum of 30 V at 0.025 V/s. A current threshold of 50 nA was set to monitor for leakage current, which served as an indicator of nanopore formation. Once this threshold was reached, the system automatically halted the voltage application. The appearance of a detectable leakage current (current surge) signified the dielectric breakdown of the membrane, and the corresponding voltage at which this event occurred was recorded as the breakdown voltage. Statistical analysis of the breakdown process across multiple membranes (n = 25) yielded an average breakdown voltage of 20.69 V with a standard deviation of ±1.54 V for this batch of SiN_x membranes.

I-V measurements were conducted both prior to and following the CBD process to confirm successful pore formation as well as characterize the resulting nanopore. The post-fabrication I-V curve exhibited I-V characteristic; the pore diameter was calculated to be 1.95 nm from the ohmic region (±100 mV) using **Equation 2.4**.

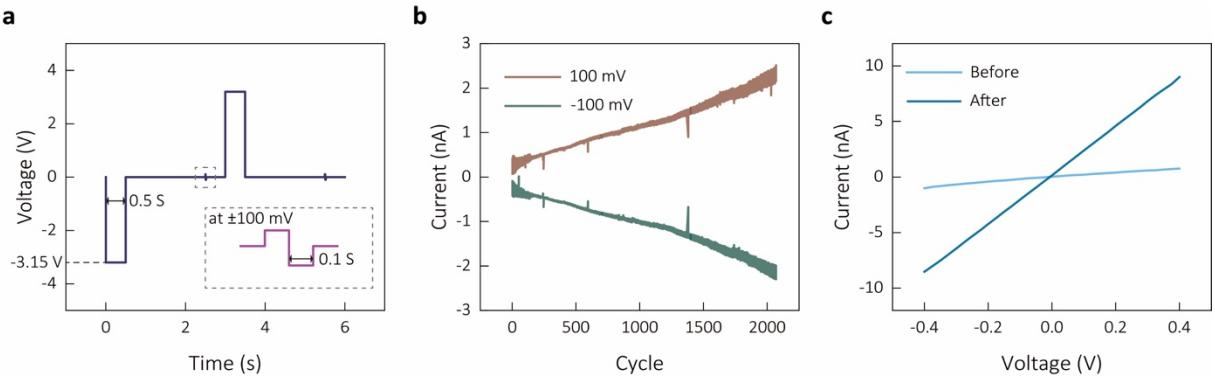


Figure 6.5 Expansion of a CBD nanopore. **a.** Voltage-time plot of one voltage pulse cycle in the expansion process. Each processing cycle consisted of: Application of 0.5 s pulses at 1/3 of the breakdown voltage, subsequent current measurement at ±100 mV for 0.2 s following each pulse. **b.** Currents measured at ±100 mV. A termination threshold was set at 2.5 nA. **c.** I-V measurements before and after expansion process under the voltage of ±400 mV. The measurements were performed in 3.6 M LiCl, 10 mM Tris, 1 mM EDTA, pH = 8.

To achieve the optimal pore size for sensing applications, we performed an expansion process (**Figure 6.5**). A 3.6 M LiCl solution was introduced into both chambers to replace the initial electrolyte, as prior research has shown that higher ionic conductivity enhances the efficiency of nanopore enlargement [37]. To facilitate pore enlargement, a series of voltage pulse cycles were applied across the nanopore. Each cycle consisted of two 0.5s voltage pulses at ±1/3 of the previously determined breakdown voltage, followed by a 0.2s current measurements at ±100 mV after each pulse. This step enabled real-time monitoring of changes in nanopore conductance throughout the enlargement process. A predefined current threshold of 2.5 nA was set to automatically terminate the voltage pulse cycles once the nanopore reached the desired conductance level. This threshold corresponds to an estimated pore diameter of approximately 7 nm, ensuring consistency with the target size for subsequent sensing experiments.

I-V measurements were performed both before and after the pore expansion process to confirm that the nanopore reached the desired size. The diameter of the expanded nanopore was determined to be 6.67 nm from the ohmic region (±100 mV), calculated using **Equation 2.4**.

6.3.2 Detection with CBD Nanopore

6.3.2.1 Detection of dsDNA

To characterize the sensing performance of our CBD-fabricated nanopores, we conducted dsDNA translocation experiments using 10 kbp fragments as model analytes (**Figure 6.6**). Five nanopores with diameters of approximately 7 nm were employed, as determined by I-V measurements analysed using **Equation 2.4** under the cylindrical symmetry approximation.

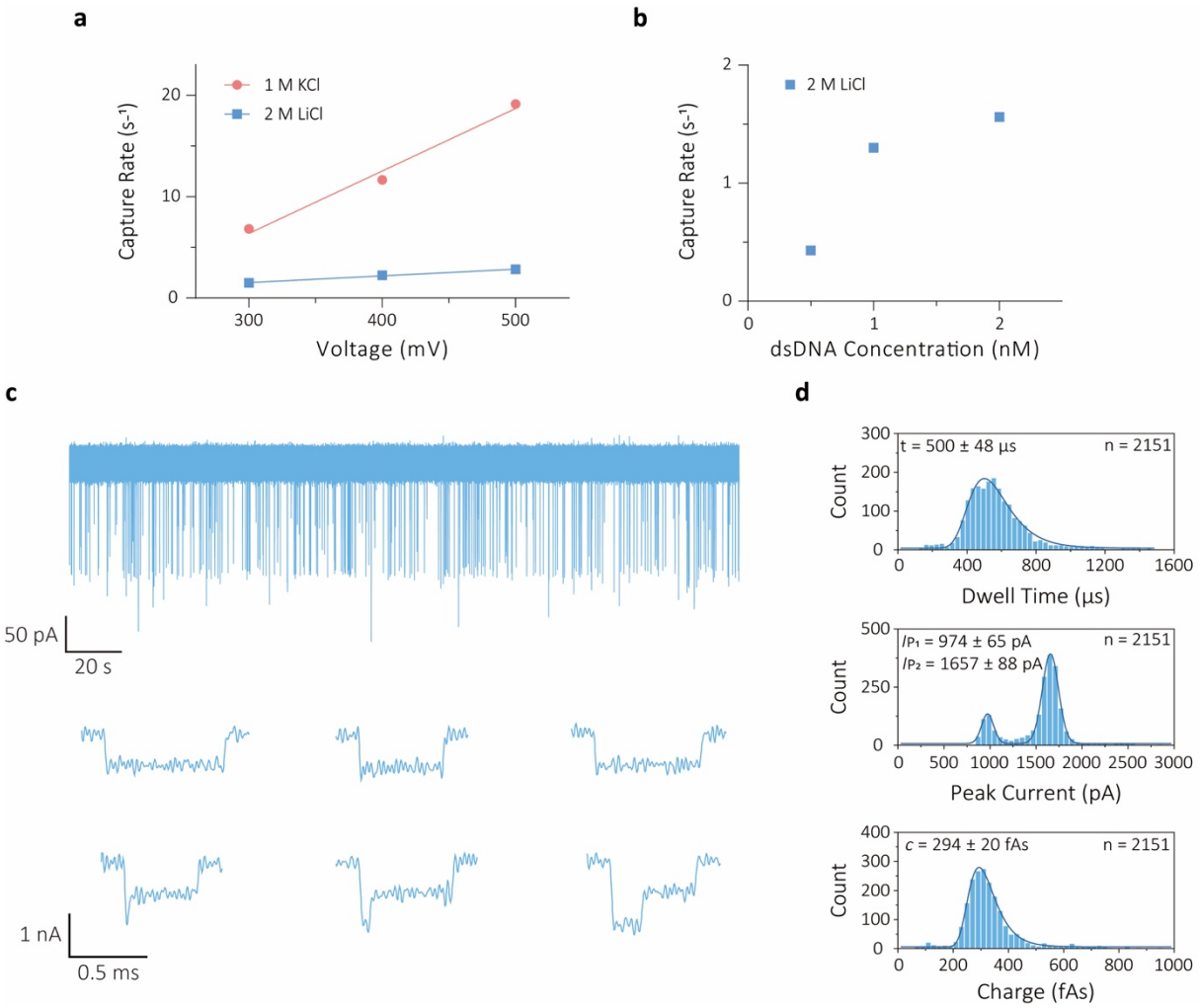


Figure 6.6 Detection of 10 kbp dsDNA using CBD-fabricated nanopores. **a.** Voltage dependant of capture rate for detection of 2 nM 10 kbps dsDNA in 1 M KCl buffer (1 M KCl, 5 mM $MgCl_2$, 10 mM Tris and 1 mM EDTA, pH 8) and 2 M LiCl buffer (2 M LiCl, 5 mM $MgCl_2$, 10 mM Tris and 1 mM EDTA, pH 8). **b.** Concentration dependant of capture rate for detection in 2 M LiCl buffer at a volatge bias of 300 mV. **c.** Current-time trace, typical events and **d.** peak current statistics for detection of 2 nM 10 kbps dsDNA in 2M LiCl buffer at a volatge bias of 300 mV.

Translocation buffers containing 1 M KCl or 2 M LiCl, 5 mM $MgCl_2$, 10 mM Tris, and 1 mM EDTA (pH 8) were used for dsDNA detection with CBD nanopores. A linear voltage dependence of the capture rate was observed in both buffers, consistent with previous reports [38, 39]. This agrees with the barrier-free capture process of dsDNA in large solid-state nanopores [40]. The capture rate in 1 M KCl was much higher than in 2 M LiCl buffer, matching published results [41]. This occurs because the DNA capture rate is inversely proportional to the translocation time, and very short translocation events were observed in 1 M KCl buffer

[41]. Given the critical importance of dwell time in translocation analysis, we selected 2 M LiCl buffer for all subsequent dsDNA translocation experiments.

We investigated the effect of DNA concentration on capture rate and observed a concentration-dependent increase that followed a nonlinear relationship. This nonlinear behaviour is consistent with previously reported results obtained at relatively high voltage biases [42]. The observed trend can be explained by the positive correlation between applied voltage and both barrier-limited and diffusion-limited capture rates. Specifically, higher applied voltages lead to expansion of the effective capture region while simultaneously reducing the energy barrier for molecular entry into the nanopore [43].

Analysis of 10 kbp dsDNA translocations in 2 M LiCl buffer showed a mean dwell time of 500 ± 48 μs and mean charge of 294 ± 20 fAs. The peak current histogram displayed two populations corresponding to unfolded (964 ± 65 pA) and folded (1657 ± 88 pA) conformations, indicating structural variability during translocation.

6.3.2.2 Detection of miRNA with dsDNA Carrier

To evaluate the miRNA sensing capability, we utilised a 7 nm CBD-fabricated nanopore with the 9.1 kbp dsDNA carrier system described in **Chapter 3** (**Figure 6.7**). The translocation experiments employed an optimised buffer system (2 M LiCl, 5 mM $MgCl_2$, 10 mM Tris, and 1 mM EDTA, pH 8) based on its demonstrated performance for 10 kbp dsDNA detection. All analyte components, including the 9.1 kbp dsDNA carrier, reporter sequences, streptavidin, and miRNA-141-3p, their concentrations were corresponding to twice the concentrations used in nanopipette experiments, as 1 nM was previously shown to yield optimal capture rates for 10 kbp dsDNA fragments.

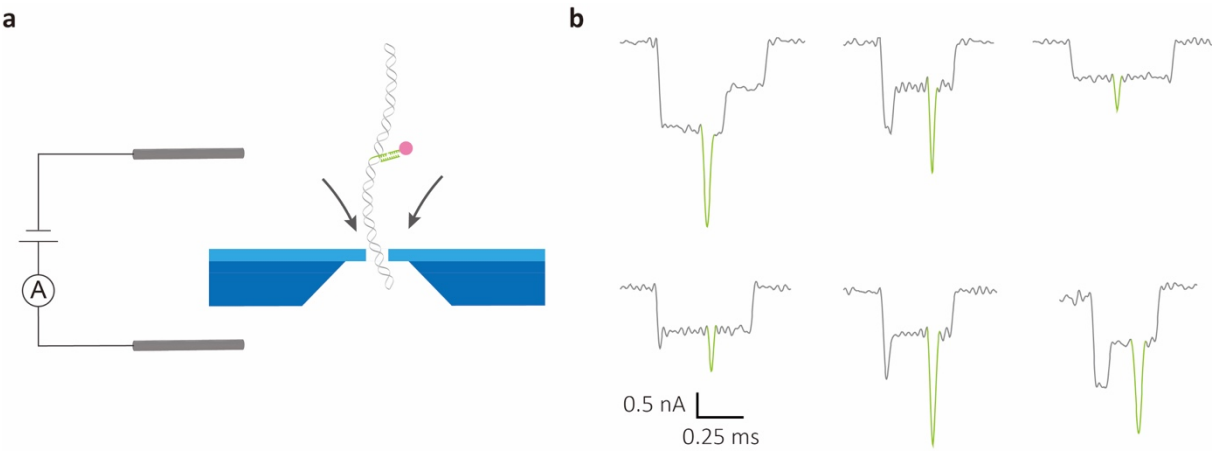


Figure 6.7 CBD nanopore sensing of miRNA using a 9.1 kbp dsDNA carrier. **a.** Schematic of the CBD nanopore sensing platform. **b.** Example translocation events for dsDNA carrier–miRNA–streptavidin complex (dsDNA carrier :1 nM, reporter sequence: 20 nM, streptavidin: 100 nM, and in the presence of miRNA-141-3p: 100 nM). All experiments were conducted using a 7 nm nanopore in a buffer containing 2 M LiCl, 5 mM $MgCl_2$, 10 mM Tris, and 1 mM EDTA (pH 8) at a voltage bias of 300 mV.

Consistent with nanopipette translocation results, the CBD nanopore translocation event of dsDNA carrier–miRNA–streptavidin complexes displayed a characteristic subpeak at 0.5 fractional peak position, superimposed on the primary dsDNA carrier signal. Quantitative analysis of these subpeaks yielded a miRNA-141-3p binding fraction of 3.16%, in excellent agreement with the nanopipette derived value of 3.35 ± 0.43%.

6.3.2.3 Detection of DNA Origami Hinge

To extend the detection capabilities of CBD-fabricated nanopores to dynamic nanostructures, we employed a 28 nm diameter pore for characterizing the DNA origami hinge mechanism detailed in **Chapter 4** and **Chapter 5** (**Figure 6.8**). The 28 nm pore diameter was specifically chosen to match the dimensional requirements of the DNA origami hinge structure.

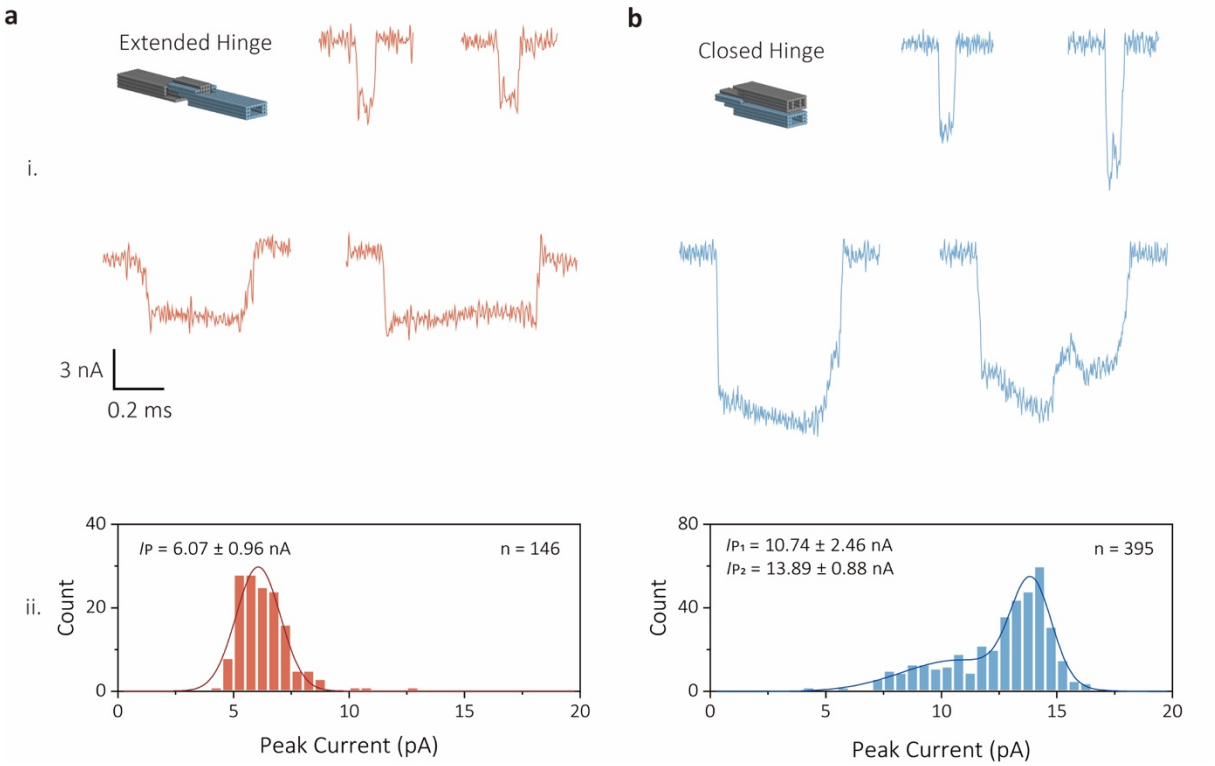


Figure 6.8 CBD nanopore detection of closed and extended DNA origami hinges. **a.** Ionic current analysis of the closed hinge (500 pM): i. Example translocation events. ii. Peak current distribution. **b.** Corresponding data for the extended hinge (500 pM), measured under identical conditions. All experiments were conducted using a 28 nm nanopore in a buffer containing 1 M KCl, 12.5 mM $MgCl_2$, 10 mM Tris, and 1 mM EDTA (pH 8) at a voltage bias of 300 mV.

Similar to the results obtained from nanopipette translocation, hinges at the closed and extended configurations can be distinguished based on the peak current of the translocation events. Quantitative analysis revealed that the mean peak current for closed hinge events was 6.07 ± 0.69 nA, whereas for extended hinge events, it was 10.74 ± 2.46 nA/13.89 ± 0.88 nA. The peak current histogram for closed hinge events revealed two distinct populations corresponding to different translocation behaviours: rapid translocation and prolonged translocation. While these event types exhibited distinguishable peak currents for closed hinges, they showed no such differentiation for extended hinges. This observation suggests the effective pore diameter more closely approximates the hinge dimensions than the theoretically estimated 28 nm value. The prolonged translocation events likely indicate transient interactions or temporary steric hindrance occurring at the nanopore entrance before successful translocation.

6.4 Conclusion

This chapter introduces the use of the CBD method for fabricating single solid-state nanopores in SiNx membranes, offering a fast, low-cost, and equipment-independent alternative to traditional nanofabrication techniques. The pore size can be precisely tuned to match the dimensions of target molecules, ranging from a few to several tens of nanometres. In performance assessments, CBD-fabricated nanopores exhibited comparable sensing capability to nanopipette-based platforms in dsDNA translocation experiments. Beyond standard DNA sensing, these nanopores effectively supported a DNA-based molecular carrier system for detecting small biomolecules such as miRNAs. Furthermore, the platform enabled real-time detection of dynamic DNA origami hinges, demonstrating its adaptability for probing reconfigurable nanostructures and expanding the functional scope of solid-state nanopore sensing.

6.5 References

[1] Wanunu, M.;Dadosh, T.;Ray, V.;Jin, J.;McReynolds, L.; Drndic, M. Rapid electronic detection of probe-specific microRNAs using thin nanopore sensors. *Nat Nanotechnol* **2010**, *5*, 807-814.

[2] Storm, A. J.;Chen, J. H.;Ling, X. S.;Zandbergen, H. W.; Dekker, C. Fabrication of solid-state nanopores with single-nanometre precision. *Nat Mater* **2003**, *2*, 537-540.

[3] Merchant, C. A.;Healy, K.;Wanunu, M.;Ray, V.;Peterman, N.;Bartel, J.;Fischbein, M. D.;Venta, K.;Luo, Z.;Johnson, A. T.; Drndic, M. DNA translocation through graphene nanopores. *Nano Lett* **2010**, *10*, 2915-2921.

[4] Xue, L.;Yamazaki, H.;Ren, R.;Wanunu, M.;Ivanov, A. P.; Edel, J. B. Solid-state nanopore sensors. *Nature Reviews Materials* **2020**, *5*, 931-951.

[5] Miles, B. N.;Ivanov, A. P.;Wilson, K. A.;Dogan, F.;Japrung, D.; Edel, J. B. Single molecule sensing with solid-state nanopores: novel materials, methods, and applications. *Chem Soc Rev* **2013**, *42*, 15-28.

[6] Wanunu, M. Nanopores: A journey towards DNA sequencing. *Phys Life Rev* **2012**, *9*, 125-158.

[7] Yanagi, I.;Akahori, R.; Takeda, K. I. Stable fabrication of a large nanopore by controlled dielectric breakdown in a high-pH solution for the detection of various-sized molecules. *Sci Rep* **2019**, *9*, 13143.

[8] Zhao, X.;Ma, R.;Hu, Y.;Chen, X.;Dou, R.;Liu, K.;Cui, C.;Liu, H.;Li, Q.;Pan, D.;Shan, X.;Wang, L.;Fan, C.; Lu, X. Translocation of tetrahedral DNA nanostructures through a solid-state nanopore. *Nanoscale* **2019**, *11*, 6263-6269.

[9] Venkatesan, B. M.;Dorvel, B.;Yemenicioglu, S.;Watkins, N.;Petrov, I.; Bashir, R. Highly Sensitive, Mechanically Stable Nanopore Sensors for DNA Analysis. *Adv Mater* **2009**, *21*, 2771.

[10] Howorka, S.; Siwy, Z. Nanopore analytics: sensing of single molecules. *Chem Soc Rev* **2009**, *38*, 2360-2384.

[11] Venkatesan, B. M.; Bashir, R. Nanopore sensors for nucleic acid analysis. *Nat Nanotechnol* **2011**, *6*, 615-624.

[12] Wanunu, M.; Meller, A. Chemically modified solid-state nanopores. *Nano Lett* **2007**, *7*, 1580-1585.

[13] Gyurcsányi, R. E. Chemically-modified nanopores for sensing. *TrAC Trends in Analytical Chemistry* **2008**, *27*, 627-639.

[14] Yusko, E. C.;Johnson, J. M.;Majd, S.;Prangkio, P.;Rollings, R. C.;Li, J.;Yang, J.; Mayer, M. Controlling protein translocation through nanopores with bio-inspired fluid walls. *Nat Nanotechnol* **2011**, *6*, 253-260.

[15] Wei, R.;Gatterdam, V.;Wieneke, R.;Tampe, R.; Rant, U. Stochastic sensing of proteins with receptor-modified solid-state nanopores. *Nat Nanotechnol* **2012**, *7*, 257-263.

[16] Nam, S. W.;Rooks, M. J.;Kim, K. B.; Rossnagel, S. M. Ionic field effect transistors with sub-10 nm multiple nanopores. *Nano Lett* **2009**, *9*, 2044-2048.

[17] McNally, B.;Singer, A.;Yu, Z.;Sun, Y.;Weng, Z.; Meller, A. Optical recognition of converted DNA nucleotides for single-molecule DNA sequencing using nanopore arrays. *Nano Lett* **2010**, *10*, 2237-2244.

[18] Kwok, H.;Briggs, K.; Tabard-Cossa, V. Nanopore fabrication by controlled dielectric breakdown. *PLoS One* **2014**, *9*, e92880.

[19] Waugh, M.;Briggs, K.;Gunn, D.;Gibeault, M.;King, S.;Ingram, Q.;Jimenez, A. M.;Berryman, S.;Lomovtsev, D.;Andrzejewski, L.; Tabard-Cossa, V. Solid-state nanopore fabrication by automated controlled breakdown. *Nat Protoc* **2020**, *15*, 122-143.

[20] Yanagi, I.;Akahori, R.;Hatano, T.; Takeda, K. Fabricating nanopores with diameters of sub-1 nm to 3 nm using multilevel pulse-voltage injection. *Sci Rep* **2014**, *4*, 5000.

[21] Arcadia, C. E.;Reyes, C. C.; Rosenstein, J. K. In Situ Nanopore Fabrication and Single-Molecule Sensing with Microscale Liquid Contacts. *ACS Nano* **2017**, *11*, 4907-4915.

[22] Bandara, Y.;Karawdeniya, B. I.;Hagan, J. T.;Chevalier, R. B.; Dwyer, J. R. Chemically Functionalizing Controlled Dielectric Breakdown Silicon Nitride Nanopores by Direct Photohydrosilylation. *ACS Appl Mater Interfaces* **2019**, *11*, 30411-30420.

[23] Zhang, Y.;Miyahara, Y.;Derriche, N.;Yang, W.;Yazda, K.;Capaldi, X.;Liu, Z.;Grutter, P.; Reisner, W. Nanopore Formation via Tip-Controlled Local Breakdown Using an Atomic Force Microscope. *Small Methods* **2019**, *3*, 1900147.

[24] Fried, J. P.;Swett, J. L.;Nadappuram, B. P.;Mol, J. A.;Edel, J. B.;Ivanov, A. P.; Yates, J. R. In situ solid-state nanopore fabrication. *Chem Soc Rev* **2021**, *50*, 4974-4992.

[25] Lin, Y.;Ying, Y. L.;Shi, X.;Liu, S. C.; Long, Y. T. Direct sensing of cancer biomarkers in clinical samples with a designed nanopore. *Chem Commun (Camb)* **2017**, *53*, 11564-11567.

[26] Roelen, Z.; Tabard-Cossa, V. Synthesis of length-tunable DNA carriers for nanopore sensing. *PLoS One* **2023**, *18*, e0290559.

[27] Elliott, B.;Charron, M.;Pezacki, J.;McConnell, E.; Tabard-Cossa, V. Solid-state nanopore counting of amplicons from recombinase polymerase isothermal amplification. *Sensors & Diagnostics* **2024**, *3*, 1733-1742.

[28] Feng, J.;Liu, K.;Graf, M.;Lihter, M.;Bulushev, R. D.;Dumcenco, D.;Alexander, D. T.;Krasnozhon, D.;Vuletic, T.;Kis, A.; Radenovic, A. Electrochemical Reaction in Single Layer MoS2: Nanopores Opened Atom by Atom. *Nano Lett* **2015**, *15*, 3431-3438.

[29] Kuan, A. T.;Lu, B.;Xie, P.;Szalay, T.; Golovchenko, J. A. Electrical pulse fabrication of graphene nanopores in electrolyte solution. *Appl Phys Lett* **2015**, *106*, 203109.

[30] Plesa, C.;van Loo, N.;Ketterer, P.;Dietz, H.; Dekker, C. Velocity of DNA during translocation through a solid-state nanopore. *Nano Lett* **2015**, *15*, 732-737.

[31] Ying, C.;Houghtaling, J.;Eggenberger, O. M.;Guha, A.;Nirmalraj, P.;Awasthi, S.;Tian, J.; Mayer, M. Formation of Single Nanopores with Diameters of 20-50 nm in Silicon Nitride Membranes Using Laser-Assisted Controlled Breakdown. *ACS Nano* **2018**, *12*, 11458-11470.

[32] Stathis, J. H. Percolation models for gate oxide breakdown. *Journal of Applied Physics* **1999**, *86*, 5757-5766.

[33] DiMaria, D. J. Explanation for the oxide thickness dependence of breakdown characteristics of metal-oxide-semiconductor structures. *Microelectronic Engineering* **1997**, *36*, 317-320.

[34] Lombardo, S.;Stathis, J. H.;Linder, B. P.;Pey, K. L.;Palumbo, F.; Tung, C. H. Dielectric breakdown mechanisms in gate oxides. *Journal of Applied Physics* **2005**, *98*.

[35] Lombardo, S.;La Magna, A.;Spinella, C.;Gerardi, C.; Crupi, F. Degradation and hard breakdown transient of thin gate oxides in metal–SiO2–Si capacitors: Dependence on oxide thickness. *Journal of Applied Physics* **1999**, *86*, 6382-6391.

[36] DiMaria, D. J.;Cartier, E.; Arnold, D. Impact ionization, trap creation, degradation, and breakdown in silicon dioxide films on silicon. *Journal of Applied Physics* **1993**, *73*, 3367-3384.

[37] Leung, C.;Briggs, K.;Laberge, M. P.;Peng, S.;Waugh, M.; Tabard-Cossa, V. Mechanisms of solid-state nanopore enlargement under electrical stress. *Nanotechnology* **2020**, *31*, 44LT01.

[38] Chen, P.;Gu, J.;Brandin, E.;Kim, Y. R.;Wang, Q.; Branton, D. Probing Single DNA Molecule Transport Using Fabricated Nanopores. *Nano Lett* **2004**, *4*, 2293-2298.

[39] Gershow, M.; Golovchenko, J. A. Recapturing and trapping single molecules with a solid-state nanopore. *Nat Nanotechnol* **2007**, *2*, 775-779.

[40] Wanunu, M.;Morrison, W.;Rabin, Y.;Grosberg, A. Y.; Meller, A. Electrostatic focusing of unlabelled DNA into nanoscale pores using a salt gradient. *Nat Nanotechnol* **2010**, *5*, 160-165.

[41] Kowalczyk, S. W.;Wells, D. B.;Aksimentiev, A.; Dekker, C. Slowing down DNA translocation through a nanopore in lithium chloride. *Nano Lett* **2012**, *12*, 1038-1044.

[42] Zhang, Y.;Zhao, J.;Kan, Y.;Ji, R.;Pan, J.;Huang, W.;Xu, Z.;Si, W.; Sha, J. Concentration effects on capture rate and translocation configuration of nanopore-based DNA detection. *Electrophoresis* **2020**, *41*, 1523-1528.

[43] Grosberg, A. Y.; Rabin, Y. DNA capture into a nanopore: interplay of diffusion and electrohydrodynamics. *J Chem Phys* **2010**, *133*, 165102.

Chapter 7 Conclusion and Future Work

Synopsis

This chapter concludes the PhD research by summarising the key objectives and major findings. It highlights the overall contributions of the work and discusses future directions, including possible enhancements to device design and sensing strategies for broader applications.

Chapter 7 Conclusion and Future Work 193

7.1 Aims 195

7.2 Achievements 195

7.3 Future Works 197

7.3.1 Protein Biomarker Detection 197

7.3.2 Multiplexed Biomarker Detection 199

7.3.3 Multi-nanopore Sensing 200

7.4 Conclusion 202

7.5 References 202

7.1 Aims

The most clinically valuable application of miRNAs lies in their role as biomarkers for disease diagnosis, prognosis monitoring, and therapeutic response evaluation. However, current bulk miRNA quantification methods face significant limitations in both sensitivity and specificity, particularly for low-abundance targets in complex biological samples. These technical constraints currently hinder the full clinical translation of miRNA biomarkers. The central aim of this thesis is to realize precise detection of small-molecule biomarkers, particularly miRNAs, through nanopore sensing technology. This research directly confronts three fundamental challenges currently limiting the field: first, the development of effective strategies to detect small biomolecules by overcoming the characteristically poor SNR inherent to nanopore-based detection systems; second, the improvement of target specificity to reliably distinguish particular miRNA sequences amidst the diverse mixture of biomolecules present in complex biological fluids; and third, the enhancement of detection sensitivity to enable accurate identification of biomarkers present at physiologically relevant low concentrations.

7.2 Achievements

This research established two DNA-based molecular carrier systems for the selective detection of miRNA using nanopore sensing. A streptavidin-assisted dsDNA carrier enabled specific target recognition, while a reconfigurable DNA origami hinge allowed miRNA-responsive signal detection. Both strategies were effectively applied across nanopipette and CBD-fabricated solid-state nanopore platforms.

Chapter 2 outlined the key methodologies employed in this study. It detailed the fabrication and characterisation of solid-state nanopores, followed by the setup and execution of nanopore translocation experiments to investigate molecular dynamics. The design and assembly of DNA-based molecular carriers were also described, highlighting their role in target-specific

detection. Lastly, the chapter introduced the data analysis techniques used to interpret translocation signals, ensuring robust and reliable extraction of meaningful results.

Chapter 3 demonstrated the application of a dsDNA-based molecular carrier system for nanopore detection of miRNAs using a sandwich complex approach. A 9.1 kbp dsDNA carrier was functionalised with target-specific receptor sequences and streptavidin reporters to enhance signal resolution. Through systematic optimisation, including a T4 RNA ligase-based binding strategy and translocation buffer adjustments, we achieved effective single and multiplexed miRNA detection with improved SNR.

Chapter 4 presents a dynamic DNA origami hinge capable of switching between closed and extended states via strand displacement. TEM imaging and fluorescence assays confirmed successful assembly and conformational changes. Single-molecule nanopore sensing distinguished between hinge states through distinct translocation signatures. Overall, the results highlight nanopore sensing as a powerful method for real-time monitoring of nanostructure reconfiguration.

Chapter 5 introduces a reconfigurable DNA hinge as a nanopore-based sensing platform for miRNA detection, where conformational changes upon target binding enable real-time analysis. Nanopore measurements effectively distinguished hinge states, enabling sensitive and selective quantification of miRNA-141-3p in buffer and serum, as well as dual detection of miRNA-141-3p and miRNA-375-3p with superior sensitivity to TEM and fluorescence methods. The rigid hinge structure reduced false positives common in linear DNA carriers and proved compatible with nanopore sensing, highlighting the platform's potential for probing dynamic DNA nanostructures without compromising detection performance.

Chapter 6 presents the CBD method as a rapid, low-cost approach for fabricating single solid-state nanopores in SiN_x membranes, with tuneable pore sizes suited for various target molecules. CBD nanopores showed sensing performance on par with nanopipettes in dsDNA translocation and effectively supported DNA-based molecular carriers for miRNA detection.

Additionally, they enabled real-time analysis of dynamic DNA origami hinges, showcasing the platform's versatility for detecting both static and reconfigurable nanostructures.

7.3 Future Works

This research has established two effective DNA-based molecular carrier systems for the selective detection of miRNA using nanopore technology. Building on these developments, future studies could explore several important extensions to further advance the field.

First, the carrier systems could be adapted for the detection of protein biomarkers. This would require modifying the carrier designs to accommodate the varying sizes, complex structures, and charge distributions of proteins while maintaining specific binding and detectable translocation signals. Second, developing multiplexed detection capabilities would be valuable. Creating carriers with orthogonal recognition elements or distinctive signal patterns could enable the simultaneous identification of multiple biomarkers in clinical samples, providing more comprehensive diagnostic information. Third, implementing multi-nanopore arrays could enhance throughput and reliability. Parallel analysis across multiple pores would improve statistical power, temporal resolution, and robustness for potential point-of-care applications.

7.3.1 Protein Biomarker Detection

Protein biomarkers serve as essential indicators for disease diagnosis and monitoring through their direct participation in physiological and pathological processes [1]. Their disease-associated alterations in expression, conformation, or localisation render them particularly valuable for clinical applications, including early disease detection, pathological classification, evaluation of treatment response, and prediction of outcome [2]. The compatibility of numerous clinically significant protein biomarkers with non-invasive detection in biological fluids, such as blood and urine, further enhances their practical utility. Building upon the DNA-

based molecular carrier systems developed in this study, subsequent investigations will focus on adapting these platforms for selective and stable protein recognition (**Figure 7.1**).

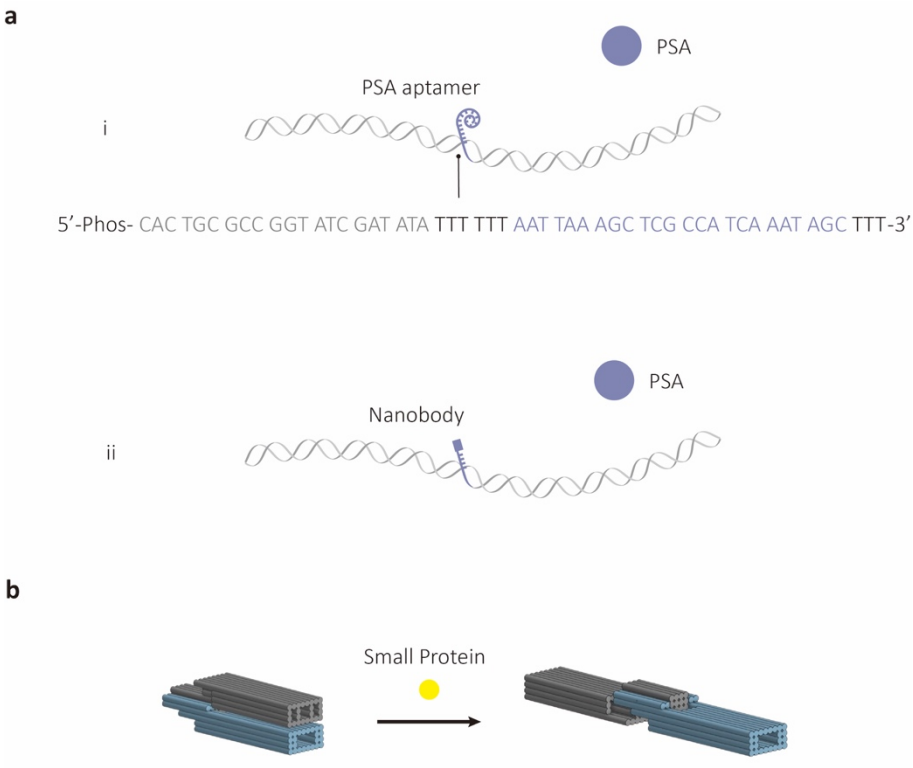


Figure 7.1 Schematic design of DNA-based molecular carriers for nanopore detection of protein biomarker. **a. i.** Aptamer sequence integrated 9.1 kbp dsDNA carrier for PSA detection. **ii.** Nanobody integrated 9.1 kbp dsDNA carrier for PSA detection. **b.** Hinge reconfiguration of closed hinge with aptamer sequence integrated latching strand for small protein detection.

Prostate-specific antigen (PSA), a widely used biomarker for prostate cancer (PCa), has served as a cornerstone in clinical diagnostics for several decades and is still considered among the most promising indicators for the disease [3]. Given the current study's focus on miRNA biomarkers related to PCa, PSA was chosen as a representative protein to evaluate the platform's adaptability for protein detection.

Similar to miRNA detection, we can integrate the dsDNA molecular carrier with receptor sequences to selectively bind target proteins. It should be noted that PSA has a slightly smaller molecular size than streptavidin [4]. Consequently, we expect to observe corresponding

subpeaks in the translocation signals of the dsDNA molecular carrier. Previous studies have addressed this approach by modifying dsDNA with aptamer sequences that bind specific target proteins with high affinity and specificity [5, 6]. Therefore, we can functionalize the dsDNA carrier with PSA-specific aptamers to adopt this strategy [7]. Additionally, recent studies have developed miniature nanobodies (~ 15 kDa, 4 nm long and 2.5 nm wide) that maintain the high binding specificity and strong affinity of conventional immunoglobulin G (IgG, 150 kDa) antibodies while being significantly smaller [8]. Compared to aptamers, nanobodies demonstrate greater tolerance to high-salt conditions. Thus, incorporating nanobodies into dsDNA carriers could further enhance the robustness and versatility of our sensing platform.

For protein biomarkers that are small in size and difficult to detect directly, the reconfigurable DNA origami hinge introduced in this study can serve as an effective molecular carrier. By integrating specific binding elements, such as aptamers, into the hinge structure, target protein binding can induce a conformational change. This structural transition generates a distinguishable signal in nanopore sensing, enabling indirect recognition and signal amplification for sensitive detection.

7.3.2 Multiplexed Biomarker Detection

The 9.1 kbp dsDNA developed in this thesis functions as an effective molecular carrier for multiplexed detection of multiple miRNA targets via nanopore sensing. Extending this capability, future studies could investigate simultaneous detection of diverse biomarker classes in complex biofluids. For example, integrating both miRNA-141-3p and PSA detection in a unified assay could enable more comprehensive PCa diagnostics, potentially enhancing early detection and disease monitoring.

The current reconfigurable DNA origami hinge carrier can only detect a single target, as each hinge is designed to respond to one specific analyte through its structural transformation. While

some experiments have shown dual miRNA detection, this does not represent true multiplexing capability.

To realize genuine multiplexed detection, future designs should incorporate hinge structures of different sizes, each tailored to a distinct target (**Figure 7.2**). For example, a second hinge (Hinge 2) could be engineered with a height roughly one-quarter that of the original (Hinge 1). This would yield four detectable conformations—closed and open states for each hinge—with cross-sectional areas differing by at least an integer-fold. These distinct geometries should produce separable translocation signals, enabling simultaneous detection of two targets in a single assay.

Expanding beyond two analytes will require developing more sophisticated hinge architectures with additional resolvable configurations.

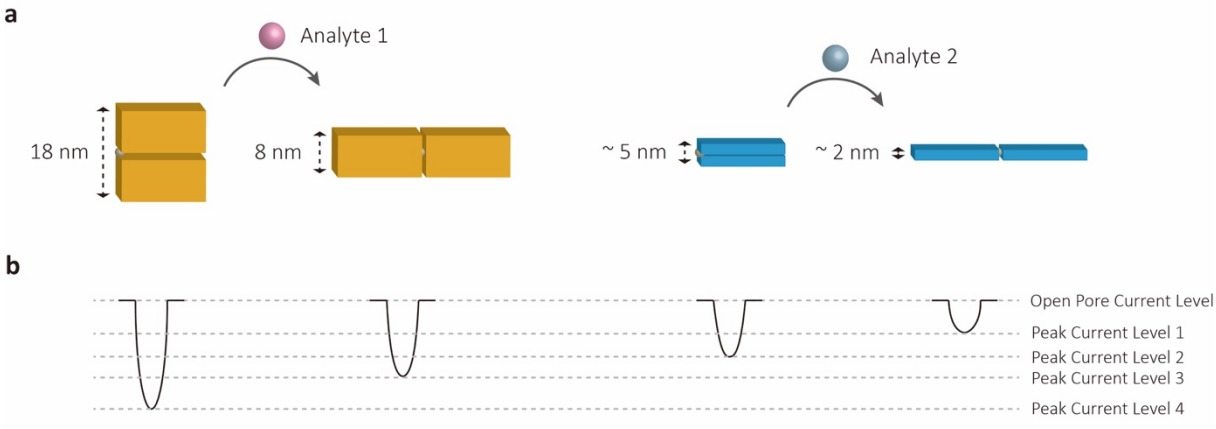


Figure 7.2 Schematic design of multi-scale reconfigurable DNA origami hinge molecular carriers for multiplexed nanopore detection. **a.** Hinge structures with fixed height parameters (Hinge 1: 18 nm closed state to 8 nm extended state; Hinge 2: 5 nm closed state to 2 nm extended state). **b.** Translocation events for multiplexed detection while maintaining target-responsive conformational changes.

7.3.3 Multi-nanopore Sensing

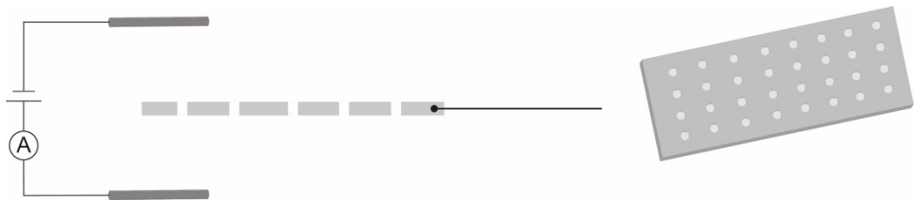


Figure 7.3 Schematic design of multi-nanopore sensing.

In this study, both nanopipettes and CBD-fabricated nanopores used for sensing belong to the solid-state nanopore category, with measurements performed through individual nanopores. Current research on solid-state nanopores predominantly focuses on single-pore configurations.

In contrast, biological nanopores have seen faster development. A prime example is the commercial MinION chip (Oxford Nanopore Technologies), which incorporates a dense array of biological nanopores enabling massively parallel sequencing [9]. This design significantly increases data throughput and sequencing speed while improving coverage and adaptability for complex samples across various applications [10, 11].

Future developments could adapt strategies from protein nanopores by organizing solid-state nanopores into integrated arrays on a single membrane, enabling parallel multi-pore sensing (**Figure 7.3**) [12]. This architecture would enhance data throughput and permit concurrent detection of multiple analytes in a single experiment. Each pore in the array could be independently monitored and controlled, offering greater experimental flexibility and improved result reliability.

Unlike protein nanopores, solid-state nanopores allow easier pore size adjustment to accommodate different target molecules, enhancing both detection accuracy and sensitivity. When combined with the DNA-based molecular carrier systems developed in this work, such solid-state nanopore arrays could evolve into practical platforms for multiplexed analysis in clinical diagnostics and biological research.

7.4 Conclusion

Nanopore-based sensing platform was developed for selective detection of small biomarkers, particularly miRNAs, using two DNA-based molecular carrier systems: a streptavidin-assisted dsDNA carrier functionalised with target-specific receptors, and a reconfigurable DNA origami hinge. These carrier designs overcome key nanopore sensing challenges including low signal-to-noise ratios, insufficient specificity in complex biofluids, and sensitivity limitations. Both systems were successfully implemented across nanopipette and solid-state nanopore platforms, demonstrating robust performance for single or multiplexed miRNA detection, as well as real-time monitoring of dynamic nanostructure reconfiguration.

While achieving successful miRNA detection, this work also provides a foundation for extending nanopore sensing to broader diagnostic applications. Future development will focus on adapting these carriers for protein biomarker detection via aptamer/nanobody integration, creating scalable multiplexing strategies using size-varied DNA hinge architectures, and developing solid-state nanopore arrays for parallelised sensing. Together, these advancements will significantly improve the sensitivity, specificity, and clinical utility of nanopore biosensing technologies.

7.5 References

[1] Rifai, N.;Gillette, M. A.; Carr, S. A. Protein biomarker discovery and validation: the long and uncertain path to clinical utility. *Nat Biotechnol* **2006**, *24*, 971-983.

[2] Etzioni, R.;Urban, N.;Ramsey, S.;McIntosh, M.;Schwartz, S.;Reid, B.;Radich, J.;Anderson, G.; Hartwell, L. The case for early detection. *Nature Reviews Cancer* **2003**, *3*, 243-252.

[3] Catalona, W. J.;Smith, D. S.; Ornstein, D. K. Prostate Cancer Detection in Men With Serum PSA Concentrations of 2.6 to 4.0 ng/mL and Benign Prostate Examination: Enhancement of Specificity With Free PSA Measurements. *JAMA* **1997**, *277*, 1452-1455.

[4] Varadi, M.;Bertoni, D.;Magana, P.;Paramval, U.;Pidruchna, I.;Radhakrishnan, M.;Tsenkov, M.;Nair, S.;Mirdita, M.;Yeo, J.;Kovalevskiy, O.;Tunyasuvunakool, K.;Laydon, A.;Zidek, A.;Tomlinson, H.;Hariharan, D.;Abrahamson, J.;Green, T.;Jumper, J.;Birney, E.;Steinegger,

M.;Hassabis, D.; Velankar, S. AlphaFold Protein Structure Database in 2024: providing structure coverage for over 214 million protein sequences. *Nucleic Acids Res* **2024**, *52*, D368-D375.

[5] Sze, J. Y. Y.;Ivanov, A. P.;Cass, A. E. G.; Edel, J. B. Single molecule multiplexed nanopore protein screening in human serum using aptamer modified DNA carriers. *Nat Commun* **2017**, *8*, 1552.

[6] Liu, Y.;Wang, X.;Campolo, G.;Teng, X.;Ying, L.;Edel, J. B.; Ivanov, A. P. Single-Molecule Detection of alpha-Synuclein Oligomers in Parkinson's Disease Patients Using Nanopores. *ACS Nano* **2023**, *17*, 22999-23009.

[7] Savory, N.;Abe, K.;Sode, K.; Ikebukuro, K. Selection of DNA aptamer against prostate specific antigen using a genetic algorithm and application to sensing. *Biosens Bioelectron* **2010**, *26*, 1386-1391.

[8] Salvador, J. P.;Vilaplana, L.; Marco, M. P. Nanobody: outstanding features for diagnostic and therapeutic applications. *Anal Bioanal Chem* **2019**, *411*, 1703-1713.

[9] Jain, M.;Olsen, H. E.;Paten, B.; Akeson, M. The Oxford Nanopore MinION: delivery of nanopore sequencing to the genomics community. *Genome Biol* **2016**, *17*, 239.

[10] Koch, C.;Reilly-O'Donnell, B.;Gutierrez, R.;Lucarelli, C.;Ng, F. S.;Gorelik, J.;Ivanov, A. P.; Edel, J. B. Nanopore sequencing of DNA-barcoded probes for highly multiplexed detection of microRNA, proteins and small biomarkers. *Nat Nanotechnol* **2023**, *18*, 1483-1491.

[11] Motone, K.;Kontogiorgos-Heintz, D.;Wee, J.;Kurihara, K.;Yang, S.;Roote, G.;Fox, O. E.;Fang, Y.;Queen, M.;Tolhurst, M.;Cardozo, N.;Jain, M.; Nivala, J. Multi-pass, single-molecule nanopore reading of long protein strands. *Nature* **2024**, *633*, 662-669.

[12] Fried, J. P.;Swett, J. L.;Nadappuram, B. P.;Fedosyuk, A.;Gee, A.;Dyck, O. E.;Yates, J. R.;Ivanov, A. P.;Edel, J. B.; Mol, J. A. Localised solid-state nanopore fabrication via controlled breakdown using on-chip electrodes. *Nano Research* **2022**, *15*, 9881-9889.

Appendices

Appendix 1 Copyright Permission

Figure Number	Source	Copyright Holder	Permission	License Number	Approval Number
1.2	*Biol Proced Online* **2014**, *16*, 5	Springer Nature	Open Access (under CC- BY)	N/A	N/A
1.3	*Chemical Society Reviews* **2009**, *38*, 2360-2384	Royal Society of Chemistry	Granted	1601646-1	1
1.4	*Chem Asian J* **2010**, *5*, 1952-1961.	John Wiley and Sons	Granted	6013700700120	2
1.5	*Nature Reviews Materials* **2020**, *5*, 931-951	Springer Nature	Granted	6013831089053	3
1.6	*Analyst* **2010**, *135*, 2190-2202.	Royal Society of Chemistry	Granted	1601857-1	4
1.7	*Chem Soc Rev* **2013**, *42*, 15-28	Royal Society of Chemistry	Granted	1602007-1	5
1.8	*Nat Rev Chem* **2021**, *5*, 466-485	Springer Nature	Granted	6014471475885	6
1.9	*Nano Lett* **2019**, *19*, 5661-5666	American Chemical Society	Granted	N/A	7
1.10a.	*Nat Nanotechnol* **2012**, *7*, 257-263	Springer Nature	Granted	6015910940223	8
1.10b.	*Nat Nanotechnol* **2007**, *2*, 243-248	Springer Nature	Granted	6015901117656	9

1.11a.	*ACS Nano* **2023**, *17*, 22999-23009	American Chemical Society	Open Access (under CC- BY)	N/A	N/A
1.11b.	*Adv Mater* **2021**, *33*, e2103067	John Wiley and Sons	Open Access (under CC- BY)	N/A	N/A
1.11c.	*Nat Commun* **2023**, *14*, 7362	Springer Nature	Open Access (under CC- BY)	N/A	N/A
1.12a.	*Nature Reviews Methods Primers* **2021**, *1*, 13	Springer Nature	Granted	6017210901775	10
1.12b.	*iScience* **2023**, *26*, 106638	Elsevier	Open Access (under CC- BY)	N/A	N/A
1.13a.	*Nano Lett* **2012**, *12*, 512-517	American Chemical Society	Granted	N/A	11
1.13b.	*Nano Lett* **2013**, *13*, 2351-2356	American Chemical Society	Granted	N/A	12
1.14a.	*Nat Commun* **2020**, *11*, 4384	Springer Nature	Open Access (under CC- BY)	N/A	N/A
1.14b.	*Biosens Bioelectron* **2022**, *195*, 113658	Elsevier	Open Access (under CC- BY)	N/A	N/A
2.3	*Nat Commun* **2023**, 14, 7362	Springer Nature	Open Access (under CC- BY)	N/A	N/A
2.4	*ACS Nano* **2023**, 17, 22999-23009	American Chemical Society	Open Access (under CC- BY)	N/A	N/A

Approve 1

CCC Marketplace

This is a License Agreement between Liquan Long ("User") and Copyright Clearance Center, Inc. ("CCC") on behalf of the Rightsholder identified in the order details below. The license consists of the order details, the Marketplace Permissions General Terms and Conditions below, and any Rightsholder Terms and Conditions which are included below.

All payments must be made in full to CCC in accordance with the Marketplace Permissions General Terms and Conditions below.

Order Date	21-Apr-2025	Type of Use	Republish in a thesis/ dissertation
Order License ID	1601646-1		
ISSN	0306-0012	Publisher	ROYAL SOCIETY OF CHEMISTRY, ETC.]
		Portion	Image/photo/illustration

LICENSED CONTENT

Publication Title	Chemical Society reviews	Rightsholder	Royal Society of Chemistry
Article Title	Nanopore analytics: sensing of single molecules.	Publication Type	Journal
		Start Page	2360
Author / Editor	CHEMICAL SOCIETY (GREAT BRITAIN)	Issue	8
		Volume	38
Date	01/01/1972		
Language	English		
Country	United Kingdom of Great Britain and Northern Ireland		

REQUEST DETAILS

Portion Type	Image/photo/illustration	Distribution	Worldwide
Number of Images / Photos / Illustrations	1	Translation	Original language of publication
Format (select all that apply)	Print, Electronic	Copies for the Disabled?	No
		Minor Editing Privileges?	Yes
Who Will Republish the Content?	Academic institution	Incidental Promotional Use?	No
Duration of Use	Life of current edition	Currency	GBP
Lifetime Unit Quantity	Up to 499		
Rights Requested	Main product, any product related to main product, and other compilations/ derivative products		

NEW WORK DETAILS

Title	Selective Nanopore Sensing of miRNA with DNA-based Carrier	Institution Name	Imperial College London
		Expected Presentation Date	2025-06-01

Instructor Name	Dr Aleksandar Ivanov

ADDITIONAL DETAILS

Order Reference Number	N/A	The Requesting Person / Organization to Appear on the License	Liquan Long

REQUESTED CONTENT DETAILS

Title, Description or Numeric Reference of the Portion(s)	Fig. 1	Title of the Article / Chapter the Portion Is From	Nanopore analytics: sensing of single molecules.
Editor of Portion(s)	Howorka, Stefan; Siwy, Zuzanna	Author of Portion(s)	Howorka, Stefan; Siwy, Zuzanna
Volume / Edition	38	Issue, if Republishing an Article From a Serial	8
Page or Page Range of Portion	2360	Publication Date of Portion	2009-08-01

Approve 2

JOHN WILEY AND SONS LICENSE TERMS AND CONDITIONS

Apr 21, 2025

This Agreement between Liquan Long ("You") and John Wiley and Sons ("John Wiley and Sons") consists of your license details and the terms and conditions provided by John Wiley and Sons and Copyright Clearance Center.

License Number	6013700700120
License date	Apr 21, 2025
Licensed Content Publisher	John Wiley and Sons
Licensed Content Publication	Chemistry - An Asian Journal
Licensed Content Title	Peering into Biological Nanopore: A Practical Technology to Single-Molecule Analysis
Licensed Content Author	Yi-Tao Long, Yang Li, Yi-Lun Ying, et al
Licensed Content Date	Jul 28, 2010
Licensed Content Volume	5
Licensed Content Issue	9
Licensed Content Pages	10
Type of Use	Dissertation/Thesis
Requestor type	University/Academic
Format	Print and electronic
Portion	Figure/table
Number of figures/tables	1
Will you be translating?	No
Title of new work	Selective Nanopore Sensing of miRNA with DNA-based Carrier
Institution name	Imperial College London
Expected presentation date	Jun 2025
Portions	Figure 2
The Requesting Person / Organization to Appear on the License	Liquan Long
Requestor Location	Liquan Long 80 Wood Lane London, United Kingdom
Publisher Tax ID	EU826007151
Total	**0.00 GBP**
Terms and Conditions	

TERMS AND CONDITIONS

This copyrighted material is owned by or exclusively licensed to John Wiley & Sons, Inc. or one of its group companies (each a"Wiley Company") or handled on behalf of a society with which a Wiley Company has exclusive publishing rights in relation to a particular work (collectively "WILEY"). By clicking "accept" in connection with completing this licensing transaction, you agree that the following terms and conditions apply to this transaction (along with the billing and payment terms and conditions established by the Copyright Clearance Center Inc., ("CCC's Billing and Payment terms and conditions"), at the time that you opened your RightsLink account (these are available at any time at http://myaccount.copyright.com).

Approve 3

SPRINGER NATURE LICENSE TERMS AND CONDITIONS

Apr 21, 2025

This Agreement between Liquan Long ("You") and Springer Nature ("Springer Nature") consists of your license details and the terms and conditions provided by Springer Nature and Copyright Clearance Center.

License Number	6013831089053
License date	Apr 21, 2025
Licensed Content Publisher	Springer Nature
Licensed Content Publication	Nature Reviews Materials
Licensed Content Title	Solid-state nanopore sensors
Licensed Content Author	Liang Xue et al
Licensed Content Date	Sep 21, 2020
Type of Use	Thesis/Dissertation
Requestor type	academic/university or research institute
Format	print and electronic
Portion	figures/tables/illustrations
Number of figures/tables/illustrations	1
Would you like a high resolution image with your order?	no
Will you be translating?	no
Circulation/distribution	1 - 29
Author of this Springer Nature content	no
Title of new work	Selective Nanopore Sensing of miRNA with DNA-based Carrier
Institution name	Imperial College London
Expected presentation date	Jun 2025
Portions	Fig. 1
The Requesting Person / Organization to Appear on the License	Liquan Long
Requestor Location	Liquan Long 80 Wood Lane London, United Kingdom
Billing Type	Invoice
Billing Address	Liquan Long 80 Wood Lane London, United Kingdom
Total	**0.00 GBP**

Approve 4

CCC Marketplace

This is a License Agreement between Liquan Long ("User") and Copyright Clearance Center, Inc. ("CCC") on behalf of the Rightsholder identified in the order details below. The license consists of the order details, the Marketplace Permissions General Terms and Conditions below, and any Rightsholder Terms and Conditions which are included below.

All payments must be made in full to CCC in accordance with the Marketplace Permissions General Terms and Conditions below.

Order Date	22-Apr-2025	**Type of Use**	Republish in a thesis/ dissertation
Order License ID	1601857-1		
ISSN	0003-2654	**Publisher**	ROYAL SOCIETY OF CHEMISTRY
		Portion	Image/photo/illustration

LICENSED CONTENT

Publication Title	The Analyst	**Rightsholder**	Royal Society of Chemistry
Article Title	Applications of nanopipettes in the analytical sciences.	**Publication Type**	Journal
		Start Page	2190
		Issue	9
Author / Editor	ROYAL SOCIETY OF CHEMISTRY (GREAT BRITAIN), SOCIETY OF PUBLIC ANALYSTS (GREAT BRITAIN), SOCIETY OF PUBLIC ANALYSTS AND OTHER ANALYTICAL CH, SOCIETY FOR ANALYTICAL CHEMISTRY., CHEMICAL SOCIETY (GREAT BRITAIN), SOCIETY OF PUBLIC ANALYSTS (GREAT BRITAIN).	**Volume**	135
Date	01/01/1876		
Language	English		
Country	United Kingdom of Great Britain and Northern Ireland		

REQUEST DETAILS

Portion Type	Image/photo/illustration	**Distribution**	Worldwide
Number of Images / Photos / Illustrations	1	**Translation**	Original language of publication
Format (select all that apply)	Print, Electronic	**Copies for the Disabled?**	No
		Minor Editing Privileges?	Yes
Who Will Republish the Content?	Academic institution	**Incidental Promotional Use?**	Yes
Duration of Use	Current edition and up to 15 years	**Currency**	GBP
Lifetime Unit Quantity	Up to 9,999		

Approve 5

CCC Marketplace

This is a License Agreement between Liquan Long ("User") and Copyright Clearance Center, Inc. ("CCC") on behalf of the Rightsholder identified in the order details below. The license consists of the order details, the Marketplace Permissions General Terms and Conditions below, and any Rightsholder Terms and Conditions which are included below.

All payments must be made in full to CCC in accordance with the Marketplace Permissions General Terms and Conditions below.

Order Date	22-Apr-2025	Type of Use	Republish in a thesis/ dissertation
Order License ID	1602007-1		
ISSN	0306-0012	Publisher	ROYAL SOCIETY OF CHEMISTRY, ETC.]
		Portion	Image/photo/illustration

LICENSED CONTENT

Publication Title	Chemical Society reviews	Rightsholder	Royal Society of Chemistry
Article Title	Single molecule sensing with solid-state nanopores: novel materials, methods, and applications.	Publication Type	Journal
		Start Page	15
		End Page	28
		Issue	1
Author / Editor	CHEMICAL SOCIETY (GREAT BRITAIN)	Volume	42
Date	01/01/1972		
Language	English		
Country	United Kingdom of Great Britain and Northern Ireland		

REQUEST DETAILS

Portion Type	Image/photo/illustration	Distribution	Worldwide
Number of Images / Photos / Illustrations	1	Translation	Original language of publication
Format (select all that apply)	Print, Electronic	Copies for the Disabled?	No
		Minor Editing Privileges?	Yes
Who Will Republish the Content?	Academic institution	Incidental Promotional Use?	No
Duration of Use	Current edition and up to 15 years	Currency	GBP
Lifetime Unit Quantity	Up to 99,999		
Rights Requested	Main product, any product related to main product, and other compilations/ derivative products		

NEW WORK DETAILS

		Institution Name	Imperial College London
Title	Selective Nanopore Sensing of miRNA with DNA-based Carrier	Expected Presentation Date	2025-06-01
Instructor Name	Dr Aleksandar Ivanov		

ADDITIONAL DETAILS

Order Reference Number	N/A	The Requesting Person / Organization to Appear	Liquan Long

Approve 6

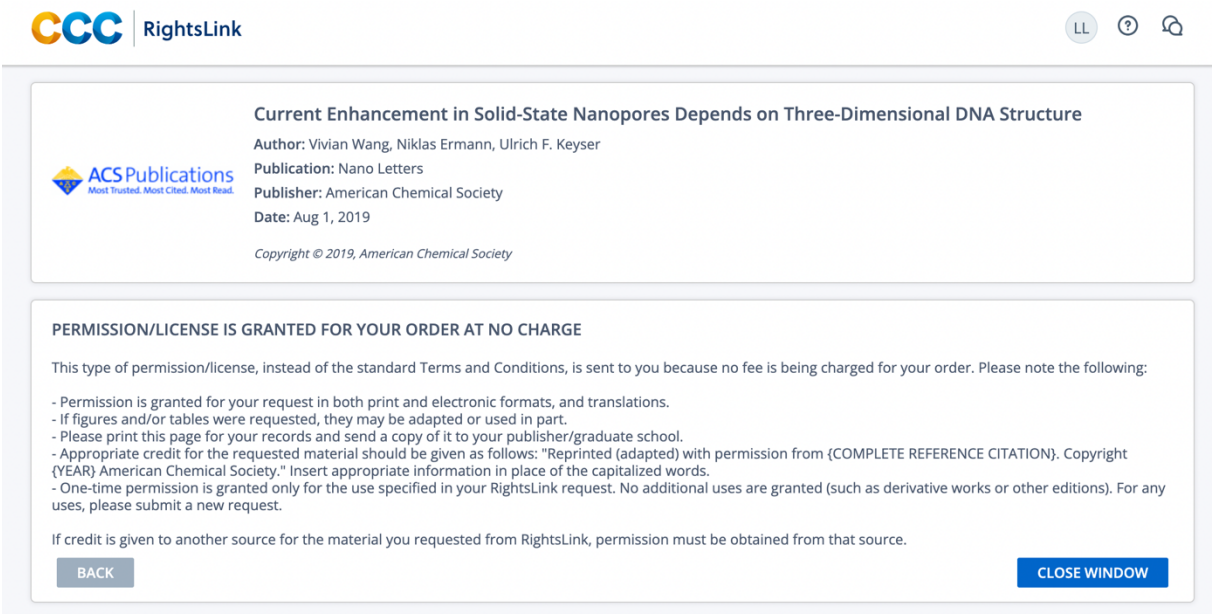
SPRINGER NATURE LICENSE TERMS AND CONDITIONS

Apr 22, 2025

This Agreement between Liquan Long ("You") and Springer Nature ("Springer Nature") consists of your license details and the terms and conditions provided by Springer Nature and Copyright Clearance Center.

License Number	6014471475885
License date	Apr 22, 2025
Licensed Content Publisher	Springer Nature
Licensed Content Publication	Nature Reviews Chemistry
Licensed Content Title	Water at charged interfaces
Licensed Content Author	Grazia Gonella et al
Licensed Content Date	Jun 24, 2021
Type of Use	Thesis/Dissertation
Requestor type	academic/university or research institute
Format	print and electronic
Portion	figures/tables/illustrations
Number of figures/tables/ illustrations	1
Would you like a high resolution image with your order?	no
Will you be translating?	no
Circulation/distribution	1000 - 1999
Author of this Springer Nature content	no
Title of new work	Selective Nanopore Sensing of miRNA with DNA-based Carrier
Institution name	Imperial College London
Expected presentation date	Jun 2025
Portions	Fig. 1
The Requesting Person / Organization to Appear on the License	Liquan Long
Requestor Location	Liquan Long 80 Wood Lane London, United Kingdom
Billing Type	Invoice
Billing Address	Liquan Long 80 Wood Lane London, United Kingdom
Total	**0.00 GBP**

Approve 7



RightsLink

LL

Current Enhancement in Solid-State Nanopores Depends on Three-Dimensional DNA Structure

Author: Vivian Wang, Niklas Ermann, Ulrich F. Keyser

ACS Publications
Most Trusted. Most Cited. Most Read.

Publication: Nano Letters

Publisher: American Chemical Society

Date: Aug 1, 2019

Copyright © 2019, American Chemical Society

PERMISSION/LICENSE IS GRANTED FOR YOUR ORDER AT NO CHARGE

This type of permission/license, instead of the standard Terms and Conditions, is sent to you because no fee is being charged for your order. Please note the following:

- Permission is granted for your request in both print and electronic formats, and translations.
- If figures and/or tables were requested, they may be adapted or used in part.
- Please print this page for your records and send a copy of it to your publisher/graduate school.
- Appropriate credit for the requested material should be given as follows: "Reprinted (adapted) with permission from {COMPLETE REFERENCE CITATION}. Copyright {YEAR} American Chemical Society." Insert appropriate information in place of the capitalized words.
- One-time permission is granted only for the use specified in your RightsLink request. No additional uses are granted (such as derivative works or other editions). For any uses, please submit a new request.

If credit is given to another source for the material you requested from RightsLink, permission must be obtained from that source.

BACK

CLOSE WINDOW

Approve 8

SPRINGER NATURE LICENSE TERMS AND CONDITIONS

Apr 25, 2025

This Agreement between Liquan Long ("You") and Springer Nature ("Springer Nature") consists of your license details and the terms and conditions provided by Springer Nature and Copyright Clearance Center.

License Number	6015910940223
License date	Apr 25, 2025
Licensed Content Publisher	Springer Nature
Licensed Content Publication	Nature Nanotechnology
Licensed Content Title	Stochastic sensing of proteins with receptor-modified solid-state nanopores
Licensed Content Author	Ruoshan Wei et al
Licensed Content Date	Mar 11, 2012
Type of Use	Thesis/Dissertation
Requestor type	academic/university or research institute
Format	print and electronic
Portion	figures/tables/illustrations
Number of figures/tables/illustrations	2
Would you like a high resolution image with your order?	no
Will you be translating?	no
Circulation/distribution	1000 - 1999
Author of this Springer Nature content	no
Title of new work	Selective Nanopore Sensing of miRNA with DNA-based Carrier
Institution name	Imperial College London
Expected presentation date	Jun 2025
Portions	Figure 1, Figure 5
The Requesting Person / Organization to Appear on the License	Liquan Long
Requestor Location	Liquan Long 80 Wood Lane London, United Kingdom
Billing Type	Invoice
Billing Address	Liquan Long 80 Wood Lane London, United Kingdom
Total	**0.00 GBP**

Approve 9

SPRINGER NATURE LICENSE TERMS AND CONDITIONS

Apr 25, 2025

This Agreement between Liquan Long ("You") and Springer Nature ("Springer Nature") consists of your license details and the terms and conditions provided by Springer Nature and Copyright Clearance Center.

License Number	6015901117656
License date	Apr 25, 2025
Licensed Content Publisher	Springer Nature
Licensed Content Publication	Nature Nanotechnology
Licensed Content Title	Solid-state nanopore channels with DNA selectivity
Licensed Content Author	Samir M. Iqbal et al
Licensed Content Date	Apr 1, 2007
Type of Use	Thesis/Dissertation
Requestor type	academic/university or research institute
Format	print and electronic
Portion	figures/tables/illustrations
Number of figures/tables/illustrations	1
Would you like a high resolution image with your order?	no
Will you be translating?	no
Circulation/distribution	1000 - 1999
Author of this Springer Nature content	no
Title of new work	Selective Nanopore Sensing of miRNA with DNA-based Carrier
Institution name	Imperial College London
Expected presentation date	Jun 2025
Portions	Figure 1
The Requesting Person / Organization to Appear on the License	Liquan Long
Requestor Location	Liquan Long 80 Wood Lane London, United Kingdom
Billing Type	Invoice
Billing Address	Liquan Long 80 Wood Lane London, United Kingdom
Total	**0.00 GBP**

Approve 10

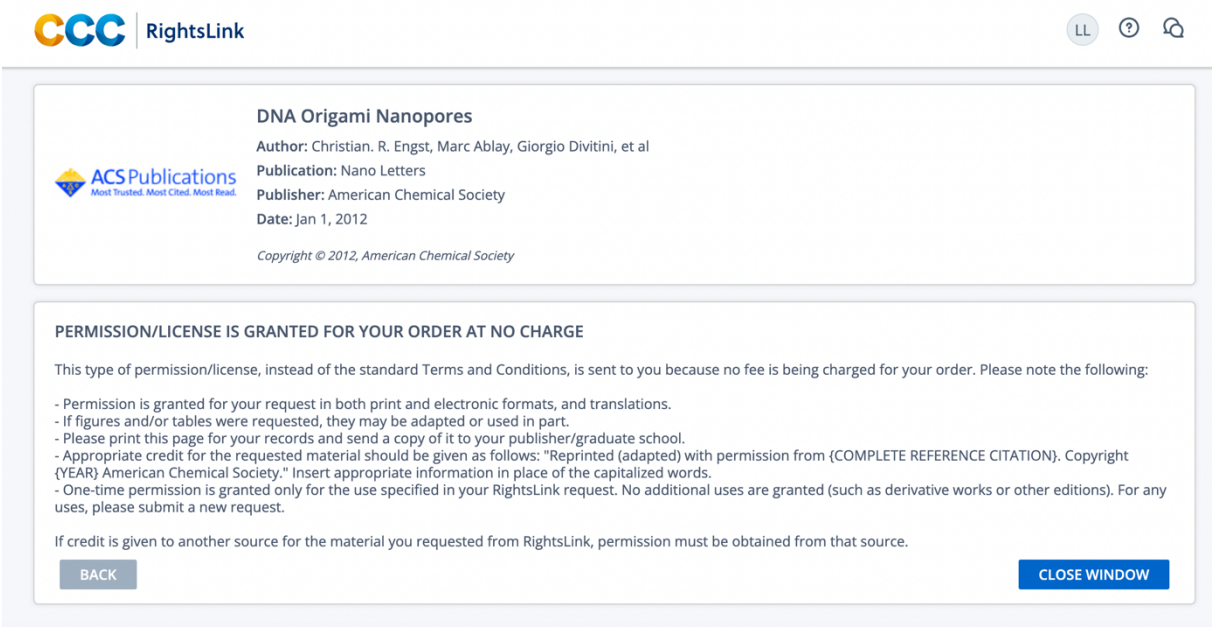
SPRINGER NATURE LICENSE TERMS AND CONDITIONS

Apr 27, 2025

This Agreement between Liquan Long ("You") and Springer Nature ("Springer Nature") consists of your license details and the terms and conditions provided by Springer Nature and Copyright Clearance Center.

License Number	6017210901775
License date	Apr 27, 2025
Licensed Content Publisher	Springer Nature
Licensed Content Publication	Nature Reviews Methods Primers
Licensed Content Title	DNA origami
Licensed Content Author	Swarup Dey et al
Licensed Content Date	Jan 28, 2021
Type of Use	Thesis/Dissertation
Requestor type	academic/university or research institute
Format	print and electronic
Portion	figures/tables/illustrations
Number of figures/tables/ illustrations	1
Will you be translating?	no
Circulation/distribution	1000 - 1999
Author of this Springer Nature content	no
Title of new work	Selective Nanopore Sensing of miRNA with DNA-based Carrier
Institution name	Imperial College London
Expected presentation date	Jun 2025
Portions	Figure 1
The Requesting Person / Organization to Appear on the License	Liquan Long
Requestor Location	Liquan Long 80 Wood Lane London, United Kingdom
Billing Type	Invoice
Billing Address	Liquan Long 80 Wood Lane London, United Kingdom
Total	**0.00 GBP**
Terms and Conditions	

Approve 11



RightsLink

LL

DNA Origami Nanopores

Author: Christian. R. Engst, Marc Ablay, Giorgio Divitini, et al

Publication: Nano Letters

Publisher: American Chemical Society

Date: Jan 1, 2012

Copyright © 2012, American Chemical Society

ACS Publications
Most Trusted. Most Cited. Most Read.

PERMISSION/LICENSE IS GRANTED FOR YOUR ORDER AT NO CHARGE

This type of permission/license, instead of the standard Terms and Conditions, is sent to you because no fee is being charged for your order. Please note the following:

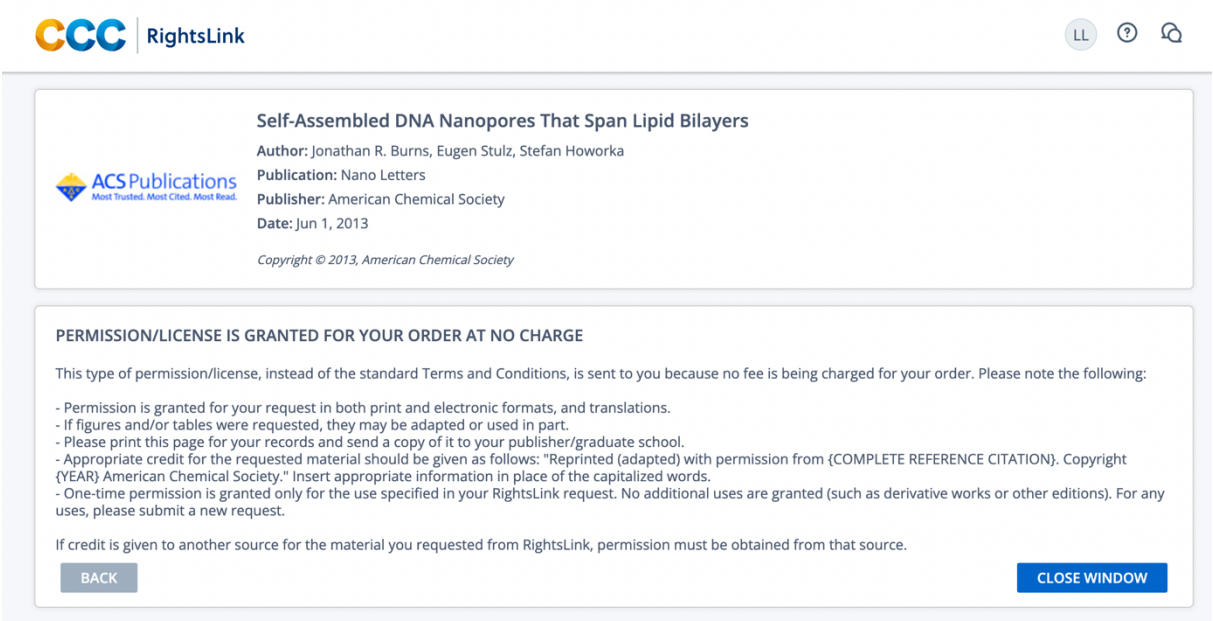
- Permission is granted for your request in both print and electronic formats, and translations.
- If figures and/or tables were requested, they may be adapted or used in part.
- Please print this page for your records and send a copy of it to your publisher/graduate school.
- Appropriate credit for the requested material should be given as follows: "Reprinted (adapted) with permission from {COMPLETE REFERENCE CITATION}. Copyright {YEAR} American Chemical Society." Insert appropriate information in place of the capitalized words.
- One-time permission is granted only for the use specified in your RightsLink request. No additional uses are granted (such as derivative works or other editions). For any uses, please submit a new request.

If credit is given to another source for the material you requested from RightsLink, permission must be obtained from that source.

BACK

CLOSE WINDOW

Approve 12


RightsLink
LL
Self-Assembled DNA Nanopores That Span Lipid Bilayers
Author: Jonathan R. Burns, Eugen Stulz, Stefan Howorka
Publication: Nano Letters
Publisher: American Chemical Society
Date: Jun 1, 2013
Copyright © 2013, American Chemical Society
ACS Publications
Most Trusted. Most Cited. Most Read.
PERMISSION/LICENSE IS GRANTED FOR YOUR ORDER AT NO CHARGE
This type of permission/license, instead of the standard Terms and Conditions, is sent to you because no fee is being charged for your order. Please note the following:
- Permission is granted for your request in both print and electronic formats, and translations.
- If figures and/or tables were requested, they may be adapted or used in part.
- Please print this page for your records and send a copy of it to your publisher/graduate school.
- Appropriate credit for the requested material should be given as follows: "Reprinted (adapted) with permission from {COMPLETE REFERENCE CITATION}. Copyright {YEAR} American Chemical Society." Insert appropriate information in place of the capitalized words.
- One-time permission is granted only for the use specified in your RightsLink request. No additional uses are granted (such as derivative works or other editions). For any uses, please submit a new request.
If credit is given to another source for the material you requested from RightsLink, permission must be obtained from that source.
BACK
CLOSE WINDOW

Appendix 2 Ethics Statement

FDA-approved pooled human serum from human male AB plasma, USA origin, was purchased from Sigma Aldrich, H4522. Consent and ethical approvals were obtained by the provider. No further approvals were required for this study.

Appendix 3 Publication

Part of this thesis is in preparation as Long, L.; Johnson, J. A.; Ren, R.; Michele, L. D.; Edel, J. B.; Ivanov, A. P., Reconfigurable DNA Origami Hinges for Nanopore Detection of microRNA.

Nano Research

Open Access

Research Article

Reconfigurable DNA origami hinges for nanopore detection of microRNA

Liquan Long[1,§], Joshua A. Johnson[1,2,§], Ren Ren[1,3], Lorenzo Di Michele [1,2] ✉, Joshua B. Edel [1] ✉, and Aleksandar P. Ivanov [1] ✉.

[1] *Molecular Sciences Research Hub, Department of Chemistry, Imperial College London, London W12 0BZ, UK*
[2] *Department of Chemical Engineering and Biotechnology, University of Cambridge, Cambridge CB3 0AS, UK*
[3] *Department of Metabolism, Digestion and Reproduction, Imperial College London, London W12 0NN, UK*
[§] *Liquan Long and Joshua A. Johnson contributed equally to this work.*

Received: 19 March 2025; **Revised:** 17 May 2025; **Accepted:** 19 May 2025

✉Address correspondence to Lorenzo Di Michele, ld389@cam.ac.uk; Joshua B. Edel, joshua.edel@imperial.ac.uk; Aleksandar P. Ivanov, alex.ivanov@imperial.ac.uk

Cite this article: *Nano Research*, **2025**, *18*, 94907604. https://doi.org/10.26599/NR.2025.94907604

ABSTRACT: The advancement of biosensor technology is driving the development of ultrasensitive detection methods, with single-molecule sensing emerging as a particularly promising approach. Nanopore sensing enables the detection of biomarkers at the single-molecule level, offering high sensitivity and specificity for biological sample analysis. In this study, we designed a reconfigurable DNA origami hinge as a molecular carrier for nanopore-based detection of miRNA-141-3p, a biomarker associated with prostate cancer. The hinge undergoes a controlled transition from a closed to an extended state upon binding to miRNA-141-3p, with distinct ionic current signatures recorded before and after reconfiguration during nanopore translocation experiments. Our approach demonstrates detection sensitivity down to the nanomolar level and exhibits excellent selectivity, effectively distinguishing miRNA-141-3p from closely related sequences. These findings highlight the potential of DNA nanostructure-based nanopore sensing for ultrasensitive and selective biomarker detection in biological samples.

KEYWORDS: nanopore sensing, DNA origami, microRNA, single-molecule sensing

Not Accepted

1 Introduction

Single-molecule detection techniques hold great promise for advancing diagnostics, particularly when applied directly to patient-derived samples such as blood, saliva, and urine [1-4]. Among these techniques, nanopore sensing stands out for its ability to detect and characterise individual biomolecules with high precision [5-9]. By applying a voltage bias across a nanopore, biomolecules translocate through it, generating ionic current changes governed by electrophoretic, electroosmotic, and diffusive forces [10]. These current fluctuations arise from ion exclusion by the translocating molecule and variations in the surrounding electrolyte composition [11]. This approach enables real-time, single-molecule analysis, providing molecular-level insights that conventional bulk-sensing methods cannot achieve. Nanopore technology has been successfully employed for detecting nanoparticles [12, 13], nucleic acids[14, 15], proteins [16-18], and various other biomolecules [19]. However, its application in early-stage diagnostics remains challenging, as it requires exceptionally high sensitivity, selectivity, and compatibility with complex biological fluids [8]. Achieving a sufficient signal-to-noise ratio (SNR) depends on the nanopore size closely matching that of the target biomolecule [5, 8]. This presents a particular challenge for small biomolecules, such as microRNAs (miRNAs) and small proteins, which often produce low-SNR signals, making detection difficult. Furthermore, nanopore sensing inherently lacks selectivity in biological fluids, which contain several biomolecules of similar size, shape, and charge, further complicating specific target identification. Therefore, enhancing both sensitivity and selectivity is essential to fully realise the diagnostic potential of nanopore technology.

A promising strategy to overcome these challenges is the use of molecular carriers [8, 20]. These carriers are designed to bind target biomolecules, ensuring that their passage through the nanopore generates distinct ionic current events distinguishable from those of the carriers alone [21, 22]. This approach offers several key advantages. First, carriers modulate translocation speed, improving signal resolution by aligning the target's motion with that of the carrier. Second, they enhance the capture rate of target molecules, particularly DNA, due to its linear and elongated structure, thereby boosting sensitivity. Finally, molecular carriers provide versatility, as their receptor components can be readily modified to accommodate various applications.

Previous studies have explored a variety of molecular carriers, including nanoparticles and linear DNA, for nanopore sensing [23-26]. Significant progress has also been